NATIONAL TECHNICAL UNIVERSITY
OF ATHENS
SCHOOL OF CHEMICAL ENGINEERING

Development and Characterization of Chalcopyrite based Thin Film Solar Cells for Photovoltaic Technology Applications

Doctoral Thesis

Konstantina Anestou

Dipl. Applied Physicist NTUA

Supervision Committee: ***Assist. Prof. Dr. Dimitra Papadimitriou (Supervisor)***

Prof. Dr. Ing. Dimitrios Yfantis

Prof. Dr. Christos N. Panagopoulos

ATHENS

2011

NATIONAL TECHNICAL UNIVERSITY
OF ATHENS
SCHOOL OF CHEMICAL ENGINEERING

Development and Characterization of Chalcopyrite based Thin Film Solar Cells for Photovoltaic Technology Applications

Doctoral Thesis

Konstantina Anestou

Dipl. Applied Physicist

Supervisor: ***Assist. Prof. Dr. Dimitra Papadimitriou (NTUA, Physik)***

Co-Supervisors: ***Prof. Dr. D. Yfantis (NTUA, Chem. Eng.)***
Prof. Dr. Ch. N. Panagopoulos (NTUA, Metal. Eng.)
Prof. Dr. M.-Ch. Lux-Steiner (FU-Berlin, Physik)
Priv.Doz.Dr. Th. Schedel-Niedrig (TU-Berlin, Chemie)

ATHENS

2011

«Η έγκριση της διδακτορικής διατριβής από την Ανωτάτη Σχολή Χημικών Μηχανικών του Ε.Μ.Πολυτεχνείου δεν υποδηλώνει αποδοχή των γνωμών του συγγραφέα. (Ν. 5343/1932, ΄Αρθρο 202)»

To my family

"As a blind man has no idea of colors,
so we have no idea of the manner by which
the all-wise God perceives and understands all things."
Isaac Newton

ACKNOWLEDGEMENTS

This thesis entitled "Development and Characterization of Chalcopyrite based Thin Film Solar Cells for Photovoltaic Technology Applications" by Diploma-Physicist NTUA Konstantina Anestou, MSc "Materials Science & Technology" NTUA, has been elaborated under the supervision of Assist. Prof. Dr. Dimitra Papadimitriou, in the frame of her Collaboration with the Helmholtz Zentrum Berlin für Materialien und Energie and the Technical University of Berlin in the field of "Thin Film Photovoltaic Technology", and with the financial support of the PENED-2003 ED248 project entitled "Development of Thin Film Photovoltaic Technology" under the Scientific-Research Responsibility of Assist. Prof. Dr. Dimitra Papadimitriou.

The thesis has been submitted to the NTUA Faculty of Chemical Engineering.

Prof. Dr. Ing. Dimitrios Yfantis is greatly acknowledged for his kind support regarding formal procedures related to the thesis.

Prof. Dr. Christos Panagopoulos is greatly acknowledged for enabling access of Laboratory Facilities at the Faculty of Metal-Engineering and Metallurgy NTUA.

Prof. Dr. Ing. Dimitrios Manolakos is also acknowledged for enabling access of Laboratory Facilities at the Faculty of Mechanical Engineering.

Dr. Stathis Tselepis, Responsible of the Section PV-Systems and Distributed Generation of the Center for Renewable Energy Sources and Saving (CRES), is greatly acknowledged for enabling access of the Sun-Simulator operated at CRES.

Dr. Michael Kompitsas, Scientific Researcher A΄ at the National Hellenik Research Foundation (NHRF) is greatly acknowledged for enabling access of Facilities of the Laboratory "LAser-based Techniques and Applications" (LATA) under his responsibility.

Also, greatly acknowledged are:
Prof. Dr. Martha-Christina Lux-Steiner, Director of Section "Heterogeneous Materials Systems" of the Solar-Energy Research Division (SE2) of the Helmholtz Zentrum Berlin für Materialien und Energie (HZB), Priv. Doz. Dr. Thomas Schedel-Niedrig, Deputy-Head of SE2, HZB, and Prof. Dr. Axel Hoffmann, Director of the Institute of Solid State Physics of the Technical University of Berlin, for their substantial, formal, and moral support throughout the elaboration of this thesis.

The Chalcopyrite absorbers studied and further processed, within the frame of this thesis, have been provided by the work-group of Prof. Dr. M.-Ch. Lux-Steiner (HZB).
Bulk chalcopyrite samples have been provided by Priv. Doz. Dr. U. Pohl (TU-Berlin).

NTUA, December 2011

The present Doctoral Thesis has been elaborated in the frame of the PENED-03 ED248 project entitled:

"Development of Thin Film Photovoltaic Technology"

The project is co-financed 80% of public expenditure through EC - European Social Fund, 20% of public expenditure through Ministry of Development - General Secretariat of Research and Technology and through private sector, under measure 8.3 of OPERATIONAL PROGRAM "COMPETITIVENESS" in the 3rd Community Support Program.

Η παρούσα διδακτορική διατριβή πραγματοποιήθηκε στα πλαίσια του προγράμματος ΠΕΝΕΔ-03, ΕΔ248, με τίτλο:

«Ανάπτυξη της Τεχνολογίας Φωτοβολταϊκών βασισμένων σε Λεπτά Υμένια»

Το πρόγραμμα συγχρηματοδοτείται κατά 80% από το Ευρωπαϊκό Κοινοτικό Ταμείο και κατά 20% από τη Γενική Γραμματεία Έρευνας και Τεχνολογίας του Υπουργείου Ανάπτυξης και Ανταγωνιστικότητας μέσω του προγράμματος «Ανταγωνιστικότητας» του 3^{ου} Κοινοτικού Πλαισίου Στήριξης.

Περίληψη

Στα πλαίσια της παρούσας διδακτορικής διατριβής, αναπτύχθηκαν και μελετήθηκαν Ηλιακές Κυψέλες Χαλκοπυριτικών Ημιαγωγών για τη Φωτοβολταϊκή Τεχνολογία Λεπτών Υμενίων.

Συγκεκριμένα,

χαλκοπυριτικοί απορροφητές αναπτυγμένοι στο Ερευνητικό Κέντρο για Υλικά και Ενέργεια Helmholtz του Βερολίνου (Helmholtz Zentrum Berlin für Materialien und Energie (HZB)) μελετήθηκαν εις βάθος με τεχνικές οπτικού χαρακτηρισμού, στις Εργαστηριακές Εγκαταστάσεις του Εθνικού Μετσόβιου Πολυτεχνείου (ΕΜΠ),

για να αποτελέσουν, στη συνέχεια, τον απορροφητή χαλκοπυριτικών ετεροκυψελών, όπου η μεταβατική στρώση ZnSe και το διαπερατό στην ηλιακή ακτινοβολία «παράθυρο» ZnO της κυψέλης αναπτύχθηκαν με χαμηλού κόστους, μεγάλης επιφανειακής κάλυψης, ταχύρρυθμες χημικές (CBD) και ηλεκτροχημικές (ECD) τεχνικές ενεπόθεσης στο ΕΜΠ.

Η μεταβατική στρώση (buffer-layer) ZnSe αναπτύχθηκε προς αντικατάσταση της στρώσης CdS, η οποία χρησιμοποιείται συνήθως σε ηλιακές κυψέλες χαλκοπυριτών. Ηλιακές κυψέλες απαλλαγμένες από κάδμιο και φιλικότερες προς το περιβάλλον, με συντελεστές απόδοσης 5%, αξιοσημείωτους για εισαγωγή στην Τεχνολογία των Χαμηλού Κόστους – Βέλτιστης Απόδοσης Φωτοβολταϊκών, αναπτύχθηκαν και χαρακτηρίστηκαν δομικά, οπτικά και ηλεκτρικά.

Ακολουθεί σύντομη περιγραφή των κυριοτέρων ενοτήτων της Διδακτορικής Διατριβής με σύγχρονη αναφορά στα αποτελέσματα της κάθε ενότητας:

Μελέτη Χαλκοπυριτικών Απορροφητών με τη μέθοδο της Οπτικής Διαμόρφωσης (Φωτοανακλαστικότητας):

Οι δομικές και οπτικές ιδιότητες χαλκοπυριτικών μονοκρυστάλλων και επιταξιακών υμενίων μελετήθηκαν με μεθόδους Οπτικής Διαμόρφωσης. Με τη μέθοδο της Φωτοανακλαστικότητας διερευνήθηκαν και ποσοτικοποιήθηκαν φαινόμενα ελαστικών τάσεων/παραμορφώσεων καθώς και μεταβολές στη σύσταση τριμερών ($CuGaSe_2$, $CuInSe_2$, $CuGaS_2$, $CuInS_2$) και τετραμερών ($Cu(In,Ga)Se_2$, $Cu(In,Ga)S_2$) χαλκοπυριτικών απορροφητών, στη συνήθη και σε χαμηλές θερμοκρασίες (300-20K). Με αναφορά στους χαλκοπυριτικούς μονοκρυστάλλους, τα επιταξιακά υμένια εμφανίζουν μειωμένη κρυσταλλικότητα κυρίως λόγω της εμφάνισης ελαστικών τάσεων/παραμορφώσεων στις χαλκοπυριτικές ετεροδομές. Οι τάσεις υπολογίστηκαν από την ενεργειακή μετατόπιση των φασμάτων Φωτοανακλαστικότητας (PR) και συγκρίθηκαν με τις τιμές που λήφθηκαν στα ίδια υμένια με Περίθλαση ακτίνων-Χ (XRD).

Το ενεργειακό φάσμα τριμερών σελινιδίων ($CuInSe_2$ και $CuGaSe_2$), μονοκρυστάλλων και επιταχιακών υμενίων, μελετήθηκε σε μεγάλο εύρος θερμοκρασιών από τη συνήθη θερμοκρασία (300K) έως και 10K. Οι ενεργειακές μεταβάσεις E_a, E_b, και E_c καθώς και το εύρος τους προσδιορίστηκαν με ακρίβεια. Από τις ενέργειες μετάβασης υπολογίσθηκε η ενέργεια που οφείλεται στην τετραγωνική παραμόρφωση χαλκοπυριτικών κρυστάλλων και η ενέργεια που οφείλεται στην αλληλεπίδραση της ηλεκτρονιακής ιδιοστροφορμής με τη στροφορμή. Τα αποτελέσματα υποδεικνύουν ιδιόμορφη εξάρτηση (s-shaped) για θερμοκρασίες χαμηλότερες από 100K, η οποία είναι εμφανής κυρίως στους επιταξιακούς απορροφητές $CuGaSe_2$, και «ανώμαλη θερμοκρασιακή εξάρτηση» (anomalous temperature dependence), η οποία εκδηλώνεται ως μετατόπιση-στο-ερυθρό (red-shift) με τη μείωση της θερμοκρασίας, για θερμοκρασίες χαμηλότερες από 50K, στους χαλκοπυριτικούς απορροφητές $CuInSe_2$. Βασιζόμενη στον υπολογισμό των συντελεστών πρόσμιξης, η μη ομαλή εξάρτηση των απορροφητών $CuInSe_2$ αποδίδεται στον κυρίαρχο d-χαρακτήρα του υβριδισμού p-d της ζώνης σθένους. Τα αποτελέσματα της παρούσας μελέτης υποδεικνύουν σημαντικές διαφορές στη θερμοκρασιακή εξάρτηση των ζωνών E_a, E_b, και E_c των μονοκρυστάλλων και των επιταξιακών υμενίων, οι οποίες αποδίδονται κυρίως στην εμφάνιση ελαστικής παραμόρφωσης στα υμένια. Η μελέτη υποδεικνύει, επιπρόσθετα, αξιοσημείωτες διαφορές στη θερμοκρασιακή εξάρτηση των ενεργειακών ζωνών E_a, E_b, και E_c, σε θερμοκρασίες χαμηλότερες των 100K, για υλικό μίας συγκεκριμένης κατηγορίας (μονοκρύσταλλο ή επιταξιακό υμένιο), η οποία σχετίζεται με τους διαφορετικούς

μηχανισμούς σύζευξης ηλεκτρονίων-φωνονίων. Τα πειραματικά αποτελέσματα προσομοιώθηκαν με 6 διαφορετικά μοντέλα και σημαντικές ιδιότητες/παράμετροι ποσοτικοποιήθηκαν, μεταξύ των οποίων είναι η ευκινησία των φορέων μειονότητας (οπών). Οι μέσες φωνονιακές συχνότητες, οι οποίες εξάχθηκαν με χρήση των μοντέλων Varshni, Bose-Einstein, Einstein, thermodynamic, και Manoogian ταυτοποιήθηκαν με βάση τα αποτελέσματα φασματοσκοπίας σκέδασης Raman της παρούσας μελέτης και αποτελέσματα γνωστά από τη βιβλιογραφία.

Τα φαινόμενα ελαστικών τάσεων/παραμορφώσεων αναλύθηκαν σε βάθος και ποσοτικοποιήθηκαν. Η θερμοκρασία στην οποία οι παραμορφώσεις εξαλείφονται είναι σε απόλυτη συμφωνία με τη θερμοκρασία στην οποία τα επιταξιακά υμένια αναπτύσσονται άνευ τάσεων.

Πέραν της θερμοκρασιακής μελέτης των χαλκοπυριτικών απορροφητών, με τη μέθοδο της Φωτοανακλαστικότητας μελετήθηκαν, επίσης, οι οπτικές ιδιότητες τριμερών και τετραμερών χαλκοπυριτών ($CuIn_{1-x}Ga_xSe_2$) σε εξάρτηση από την ποσοστιαία σύσταση.

Αντικατάσταση της μεταβατικής στρώσης CdS από ZnSe

Στην παρούσα εργασία, έμφαση δόθηκε στην αντικατάσταση της μεταβατικής στρώσης του CdS από το φιλικότερο προς το περιβάλλον ZnSe.

Ανάπτυξη μεταβατικής στρώσης ZnSe με τη Μέθοδο της Εξάχνωσης με Δέσμη Ηλεκτρονίων (EBE)

Το παρόν τμήμα αφορά τη Διδακτορική Διατριβή (σε εξέλιξη) του Διπλωματούχου Χημικού Μηχανικού κ. Γ. Ρούπακα. Τα συμπεράσματα παρατίθενται για λόγους σύγκρισης.

Αρχικά πραγματοποιήθηκαν πειράματα ελέγχου. Υψηλής ποιότητας υμένια ZnSe αναπτύχθηκαν με τη μέθοδο της εξάχνωσης με δέσμη ηλεκτρονίων σε υποστρώματα από άμορφο γυαλί, σε θερμοκρασίες που κυμαίνονταν από 300 έως 450^{o}C. Τα υμένια χαρακτηρίσθηκαν δομικά και οπτικά με XRD, EDS, SEM, AFM, φασματοσκοπία Raman και Ελλειψομετρία μηδενισμού. Η πλεγματική σταθερά α υπολογίσθηκε από τις γωνίες περίθλασης Bragg. Εικόνες SEM και AFM

επιδεικνύουν υψηλής ομοιογένειας πολυκρυσταλλική δομή. Η στοιχειακή ανάλυση με EDS υποδεικνύει το σχηματισμό μη-στοιχειομετρικού υμενίου το οποίο τείνει προς τη στοιχειομετρία όσο η θερμοκρασία εναπόθεσης αυξάνει. Ο συντελεστής διάθλασης, ο συντελεστής απορρόφησης και το πάχος των υμενίων μετρήθηκαν με ελλειψομετρία μηδενισμού. Ακολούθως, υψηλής ποιότητας υμένια ZnSe αναπτύχθηκαν με την ίδια μέθοδο σε υποστρώματα χαλκοπυριτικών απορροφητών ($CuGaSe_2$), οι οποίοι χρησιμοποιούνται στη φωτοβολταϊκή τεχνολογία. Τα υμένια υποβλήθηκαν σε θερμική ανόπτηση για βελτίωση της κρυσταλλικότητας και, στη συνέχεια, μελετήθηκαν δομικά και οπτικά με XRD, SEM, AFM, Raman, ελλειψομετρία μηδενισμού και φωτοανακλαστικότητα (PR).

Εφαρμογή χαμηλού κόστους, μεγάλης επιφανειακής κάλυψης, ταχύρρυθμων διαδικασιών ανάπτυξης μεταβατικής στρώσης ZnSe και «παραθύρου» ZnO

Προκειμένου να μειωθεί το κόστος παραγωγής Φωτοβολταϊκών (Φ/Β) βασισμένων σε λεπτά υμένια χαλκοπυριτών και να καταστεί δυνατή η κατευθείαν ανάπτυξη Φ/Β πλαισίων μέσω εναπόθεσης σε μεγάλη επιφάνεια και κυκλωμάτωση των Φ/Β στοιχείων ήδη κατά τη διαδικασία ανάπτυξης, χημικές και ηλεκτροχημικές μέθοδοι εφαρμόσθηκαν για την ανάπτυξη της μεταβατικής στρώσης ZnSe και της εμπρόσθιας ηλεκτρικής επαφής ZnO, διαπερατού στην ακτινοβολία «παραθύρου» ηλιακών κυψελών λεπτών υμενίων χαλκοπυριτών.

Ανάπτυξη μεταβατικής στρώσης ZnSe με τη Μέθοδο της Εναπόθεσης από Χημικό Λουτρό (CBD)

Αρχικά πραγματοποιήθηκε σειρά πειραμάτων ελέγχου. Συγκεκριμένα, υμένια ZnSe αναπτύχθηκαν σε υποστρώματα από άμορφο γυαλί με τη μέθοδο της χημικής εναπόθεσης από λουτρό. Οι χρόνοι εναπόθεσης κυμαίνονταν από 1 έως 6 ώρες και τα υμένια υπέστησαν θερμική ανόπτηση στους 300 ^{o}C για 3 h. Τα υμένια χαρακτηρίσθηκαν δομικά με XRD, SEM, EDS, πριν και μετά την ανόπτηση. Το ενεργειακό χάσμα των υμενίων μελετήθηκε με τη μέθοδο της φασματοσκοπίας απορρόφησης. Η σημαντική παράμετρος του πάχους του υμενίου μετρήθηκε με προφιλομετρία.

Υμένια ZnSe αναπτύχθηκαν επίσης σε υποστρώματα επιταξιακών και πολυκρυσταλλικών χαλκοπυριτικών. Για το χαρακτηρισμό των υμενίων, πραγματοποιήθηκαν μετρήσεις XRD, SEM, EDS, και AFM. Σημαντικές πληροφορίες προέκυψαν αναφορικά με το μέγεθος των κρυσταλλιτών, την εμφάνιση τάσεων/παραμορφώσεων σε εξάρτηση από το χρόνο εναπόθεσης, τη στοιχειακή σύσταση και το πάχος των υμενίων. Σημαντικά διαφορετικοί ρυθμοί εναπόθεσης παρατηρήθηκαν ανάλογα με τη φύση του υποστρώματος.

Ανάπτυξη «παραθύρου» ZnO με τη μέθοδο της εναπόθεσης με παλμικό Laser (PLD)

Προκειμένου να επιτευχθεί ολοκληρωμένη ηλιακή κυψέλη, υμένιο ZnO το οποίο αποτελεί την εμπρόσθια Ωμική επαφή και συγχρόνως το διαπερατό «παράθυρο» της κυψέλης αναπτύχθηκε σε ετεροδομές τύπου: ZnSe/Chalcopyrite/Mo-glass. Λεπτά υμένια ZnO με ενδογενή αγωγιμότητα (i-ZnO) και ZnO με πρόσμιξη In (In:ZnO) αναπτύχθηκαν με τη μέθοδο της εναπόθεσης με παλμικό laser. Μεταλλική επαφή Al/Au εναποτέθηκε στην επιφάνεια του ZnO για τη συλλογή των φορέων. Χαρακτηριστικές καμπύλες I-V καταγράφηκαν υπό σκότος, ενδεικτικές της λειτουργίας της ετεροδομής και της επίτευξης ένωσης p-n.

Ανάπτυξη «παραθύρου» ZnO με τη μέθοδο της Ηλεκτροχημικής Εναπόθεσης (ECD)

Προκειμένου να επιτευχθεί η ολοκλήρωση ηλιακής κυψέλης με χαμηλού κόστους, μεγάλης επιφανειακής κάλυψης, ταχύρρυθμων χημικών και ηλεκτροχημικών μεθόδων, λεπτό παράθυρο ZnO με ενδογενή αγωγιμότητα (i-ZnO) αναπτύχθηκε ηλεκτροχημικά σε ετεροδομή ZnSe/Chalcopyrite/Mo-glass. Με τη μέθοδο ηλεκτραπόθεσης, το ZnO αναπτύχθηκε ακολουθώντας τον προσανατολισμό του υποκείμενου υμενίου ZnSe. Επιτυχώς καταγράφηκαν χαρακτηριστικές καμπύλες I-V α) υπό σκότος και β) σε συνθήκες ακτινοβόλησης, ενδεικτικές της λειτουργίας των ετεροδομών ως ηλιακών κυψελών με συντελεστή πλήρωσης 52.5% και απόδοση 5%.

Ανάπτυξη Αντι-ανακλαστικών Επιστρώσεων βασισμένων σε Νανοδομές ZnO (ZnO-NRs) με τη μέθοδο της Ηλεκτροχημικής Εναπόθεσης (ECD)

Για εφαρμογές σε ηλιακές κυψέλες, αντιανακλαστικές επιστρώσεις νανοδομών ZnO (ZnO-NRs (Nanorods)) αναπτύχθηκαν με ηλεκτροχημικές μεθόδους στο HZB σε υποστρώματα από διαφανές αγώγιμο οξείδιο (TCO). Οι δομικές ιδιότητες των νανοδομών μελετήθηκαν με XRD, SEM και AFM. Οι οπτικές ιδιότητες διερευνήθηκαν με Φασματοσκοπία Διαπερατότητας και Τεχνικές Οπτικής Διαμόρφωσης στο ΕΜΠ. Το ενεργειακό χάσμα των νανοδομών μετρήθηκε με μεγάλη ακρίβεια με Φασματοσκοπία Φωτοανακλαστικότητας. Με τη χρήση των νανοδομών στη θέση του παραθύρου της ηλιακής κυψέλης, επιτεύχθηκε σημαντική μείωση των απωλειών λόγω ανάκλασης σε ηλιακές κυψέλες CIGS. Οι νανοδομές ZnO αυξάνουν το ρεύμα βραχυκύκλωσης χωρίς να επηρεάζουν ουσιαστικά την τάση ανοιχτού κυκλώματος. Μελετήθηκε η μεταβολή του ενεργειακού χάσματος των ZnO-NRs ως συνάρτηση των συνθηκών εναπόθεσης με σκοπό τη βελτιστοποίηση της απόδοσης των ηλιακών κυψελών.

Μελέτη Ηλιακών Κυψελών Λεπτών Υμενίων Χαλκοπυριτών με τη Μέθοδο της Ηλεκτρικής Διαμόρφωσης (Ηλεκτροανακλαστικότητας)

Μετρήσεις ηλεκτρικής διαμόρφωσης σε εξάρτηση από τη θερμοκρασία πραγματοποιήθηκαν σε ηλιακή κυψέλη ZnO/CdS/Cu(In,Ga)S_2/Mo-glass. Οι οπτικές ιδιότητες των επιμέρους στρώσεων της ηλιακής κυψέλης μελετήθηκαν σε μεγάλος εύρος θερμοκρασιών από 300K έως 10K. Οι ενεργειακές μεταβάσεις και το εύρος τους προσομοιώθηκαν με 6 διαφορετικά θεωρητικά μοντέλα. Οι ελαστικές τάσεις / παραμορφώσεις ποσοτικοποιήθηκαν σε εξάρτηση από τη θερμοκρασία.

Με αναφορά σε όλα τα παραπάνω θέματα, η παρούσα διδακτορική διατριβή στοχεύει να συνεισφέρει στη Μελέτη και Ανάπτυξη Χαλκοπυριτικών Ηλιακών Κυψελών για Χαμηλού Κόστους – Βέλτιστης Απόδοσης Φωτοβολταϊκή Τεχνολογία Λεπτών Υμενίων.

Abstract

In the frame of the present doctoral thesis, chalcopyrite based heterojunctions, used in Thin Film Solar Cells (TFSCs) have been further developed and extensively studied.

TFSCs grown at the Helmholtz Zentrum Berlin für Materialien und Energie (HZB) have been exhaustively characterized by Optical Modulation Techniques at the National Technical University of Athens (NTUA). In accordance with the results anticipated, Cd-free chalcopyrite solar cells have been developed and have been structurally, optically, and electrically characterized. The respective buffer- (ZnSe) and window-layers (ZnO) have been grown by low cost chemical (CBD) and electrochemical (ECD) techniques at the NTUA.

In the following, a brief review of the thesis main topics is given:

Optical Modulation (Photoreflectance) Studies:

The structural and optical properties of chalcopyrite single crystals and monocrystalline epitaxial layers have been analyzed by Optical Modulation Techniques. Photoreflectance has been applied at room and low temperatures to quantify elastic strain effects, to determine compositional changes, and to exploit the light interaction probability of ternary ($CuGaSe_2$, $CuInSe_2$, $CuGaS_2$, $CuInS_2$) and quaternary ($CuIn_{1-x}Ga_xSe_2$) chalcopyrite absorbers with applications in solar-cell device technology. With respect to bulk chalcopyrites, epitaxially grown layers exhibit lower crystal quality because of elastic strain effects evolving in semiconductor heterostructures. The mismatch and thermal-strain calculated from the energy-shift of the PR-spectra have been compared to strain values obtained by X-ray Diffraction (XRD) analysis. The dependence of electronic transitions on the polarization state of the excitation light beam and the dependence of chalcopyrite transition energies on anion/cation replacement and temperature has been found in both, bulk crystals and epitaxial layers, to be in agreement with theoretical predictions.

The band gap of ternary chalcopyrite semiconductors, bulk and epitaxially grown selenides $CuInSe_2$ and $CuGaSe_2$, has been studied over a wide temperature

range, from room temperature (300K) down to 10K. Energies and widths of the E_a, E_b, and E_c bands have been determined. The non-cubic crystal field and the spin-orbit interaction have been calculated. The results indicate s-shaped temperature dependence below 100K, most pronounced in $CuGaSe_2$ epitaxial layers, and anomalous temperature dependence below 50K in $CuInSe_2$. Based on the calculation of admixture coefficients, the latter is attributed to the predominant *d*-character of *p*-*d* hybridization of the upper valence band. Besides, the results of the present study point to significantly different temperature dependence of the E_a, E_b, and E_c bands of single crystals and epitaxial layers, which is attributed to incorporation of defects and symmetry breaking in the layers. They also point to significantly different temperature dependence of the E_a, E_b, and E_c bands within one and the same chalcopyrite material dependent on its structural properties (bulk crystal or epitaxial layer), which is associated with different electron-phonon coupling mechanisms dominating electronic transitions at temperatures below 100 K. The experimental results are fitted with 6 different models and important transport properties are calculated, among them minority carrier (hole) mobility. Average phonon frequencies are obtained within the frame of the Varshni, Bose-Einstein, Einstein, thermodynamic, and the Manoogian models and phonon mode assignment is attempted based on the results of this study and also the results of photoluminescence and Raman studies known from the literature. For the epitaxially on GaAs(001) grown $CuInSe_2$ and $CuGaSe_2$ layers, the shear deformation potential is calculated.

Strain/stress effects originating from mismatch- and thermal-strain between substrate and epilayer are quantified and are discussed exhaustively. For full strain relaxation, a temperature is calculated which is in total agreement with the temperature of epitaxial layer growth.

Apart from exhaustive chalcopyrite band gap studies by Photoreflectance techniques, the optical properties of quaternary $CuIn_{1-x}Ga_xSe_2$ epitaxial single-crystal layers were determined by Photoreflectance Spectroscopy (PR) in dependence of composition.

Replacement of CdS- by ZnSe- buffer layer:

Emphasis was given on the replacement of the CdS-buffer layer by the more environmental friendly ZnSe.

ZnSe buffer-layer grown by electron-Beam Evaporation Techniques (EBE)

This topic is dealt with in a PhD-thesis (still processing) by Dipl. Chem. Ing. NTUA, Dipl. Phys. G. Roupakas. For comparison reasons, it is referred in the present PhD-thesis as well.

A series of Control Experiments has been performed at first. High quality ZnSe thin films were deposited by electron-beam evaporation techniques (EBE) on amorphous glass substrates at temperatures ranging from room temperature (RT) to 450^{o}C. The films were structurally and optically characterized by X-Ray Diffraction (XRD), Energy Dispersive Spectrometry (EDS), Scanning Electron Microscopy (SEM), Atomic Force Microscopy (AFM), Raman spectroscopy, and Null-Ellipsometry. Plane spacing d and lattice constant a were calculated from the Bragg-angles. SEM and AFM images demonstrate highly homogenous polycrystalline structure and smooth film surfaces. Compositional analysis by EDS indicates formation of non-stoichiometric Zn-poor films becoming more stoichiometric with the increase of deposition temperature. The Raman LO-phonon width (FWHM) used to calculate crystallite sizes results in size increase with the increase of deposition temperature. Refractive index, absorption coefficient, and film thickness obtained by Null-Ellipsometry at 546nm show weak temperature dependence only in case of absorption. Following that, high quality ZnSe thin films were deposited by EBE on $CuGaSe_2$ (CGS) absorbers used in solar-cell device development. The deposited films act as buffer layers in heterojunction CGS based cells. The films were subjected to post-growth annealing and were structurally and optically characterized by X-Ray Diffraction (XRD), Scanning Electron Microscopy (SEM), Atomic Force Microscopy (AFM), Raman Spectroscopy, Null-Ellipsometry, and Photoreflectance Spectroscopy (PR). SEM and AFM images demonstrate films with highly homogenous structure and small surface roughness. Raman spectra confirm the good crystal quality of the films. In addition, the Raman TO-phonon frequency shift was used to evaluate strain effects. The refractive index n, the absorption coefficient α, and the film thickness d were deduced from the Ellipsometry measurements. The energy band gap of the films was obtained by room temperature (RT) Photoreflectance (PR). The application of PR spectroscopy at RT along with the results of SEM, AFM, XRD, and Raman spectroscopy confirm the excellent quality of the deposited films.

ZnSe buffer-layer grown by Chemical Deposition Techniques (CBD)

To lower the cost of buffer layer growth and to obtain large area deposition, chemical methods were applied for ZnSe thin film deposition and optimization of the deposition process.

A series of Control Experiments has been performed at first. In particular, ZnSe layers were grown on amorphous glass by Chemical Bath Deposition (CBD) at deposition times ranging from one (1) to six (6) hours and were subjected to post growth annealing at 300 ^{o}C for 3 h. The films were structurally characterized by XRD, SEM, EDS, prior and post annealing. The energy band gap was obtained by Absorbance Spectroscopy. The critical parameter of the film thickness in dependence of deposition time was obtained by Profilometry.

ZnSe layers were also grown on epitaxial and polycrystalline Chalcopyrites. XRD, SEM, EDS, and AFM measurements were applied to characterize the samples. Useful information was obtained, concerning the crystallite size, strain/stress evolution dependent on the film deposition time, elemental composition and film thickness. Different growth rates were reported in dependence of substrate nature.

ZnO window-layer grown by Pulsed Laser Deposition (PLD)

To achieve an integrated solar cell, a ZnO window-layer acting as front Ohmic contact was deposited on ZnSe/Chalcopyrite/Mo-glass heterostructures. i-ZnO and In:ZnO were deposited by Pulsed Laser Deposition (PLD). An Al/Au line or point carrier-collector was also deposited on top of the ZnO window layer. I-V characteristics in the dark were successfully recorded showing the achievement of the p-n junction.

ZnO window-layer grown by Electrochemical Deposition (ECD)

To achieve an integrated solar cell processed by low-cost, large-area, fast-deposition-rate chemical and electrochemical techniques, a ZnO window-layer was electrochemically deposited on ZnSe/Chalcopyrite/Mo-glass heterostructure. The ECD grown ZnO window-layer was oriented along the (101) crystallographic plane in coherency with the underlying ZnSe-buffer layer. Pt-point electrodes were deposited as front carrier collector. I-V characteristics of the chalcopyrite heterojunction based TFSC (Pt/i-ZnO/ZnSe/Cu(In,Ga)Se_2/Mo/glass) were successfully recorded in the dark and under illumination.

Antireflective Coating based on ZnO Nanorods grown by Electrochemical Deposition (ECD)

For solar cell device applications, antireflective coatings (ARCS) based on ZnO Nanorods (ZnO-NRs) have been grown at HZB by electrochemical deposition (ECD) techniques. Vertical high quality ZnO nanorods (NRs) have been deposited on glass substrates coated by i-ZnO/TCO. The structural properties of the ZnO NRs have been studied by x-Ray Diffraction (XRD) and microscopy techniques (SEM and AFM). The optical properties have been investigated by Transmittance and Optical Modulation (Photoreflectance) Spectroscopy at NTUA. The energy band gap of the structures has been accurately determined directly from the PR-spectra. By using ZnO nanorods as an antireflective coating (ARC), decrease of the global reflectance of CIGS solar cells has been achieved. The ZnO NRs ARC boosts the solar cells short-circuit current without significant effect on their open-circuit voltage and fill factor. Variation of the band-gap by varying the conditions of growth is foreseen for further development.

Electrical Modulation (Electroreflectance Studies) of Chalcopyrite based Thin Film Solar Cells

Electroreflectance measurements in dependence of temperature were performed on a ZnO/CdS/$CuInGaS_2$/Mo-glass solar cell. The optical properties of all the different layers that constitute the solar cell have been studied over a wide temperature range. Energies and widths of the respective bands of the cell constituents have been determined and were fitted with 6 different models. Important information such as strain/stress evolution dependent on temperature has been quantified.

With reference to the above mentioned topics, the present doctoral thesis aims to contribute to the development of chalcopyrite heterojunction solar cells.

Contents

1. Introduction 31

1.1 History of Photovoltaics 32

1.2 Fundamental properties of semiconductors 34

1.3 pn - junction 37

1.4 Photovoltaic effect 39

1.5 Thin Film Solar Cells (TFSC) 43

1.6 Chalcopyrite-based solar cells 46

1.6.1 The substrate 47

1.6.2 The back ohmic contact 48

1.6.3 The absorber 48

1.6.4 The window layer 49

2. Material properties 51

2.1 Chalcopyrite - Absorber 51

2.1.1 General 51

2.1.2 Structural properties 53

2.1.3 Electronic properties 55

2.1.3.1 Band gap 55

2.1.3.2 Temperature dependence of Semiconductor Band-gap 61

2.1.3.3 Anomalous Temperature dependence of Semiconductor Band-gap 63

2.2 ZnSe - Buffer layer 64

2.2.1 General 64

2.2.2 Structural properties 65

2.2.3 Electronic properties 66

2.3 ZnO - Window layer 67

2.3.1 General 68

2.3.2 Structural properties 69

2.3.3 Electronic properties 70

3. Chalcopyrite Heterostructures 73

3.1 Band Alignment 73
3.2 Mismatch strain and thermal strain 77
3.2.1 Mismatch strain 77
3.2.2 Strain/Stress Analysis by X-ray Diffraction 78
3.2.3 Strain/Stress Analysis by Photoreflectance Spectroscopy 79
3.2.4 Thermal strain 80
4. Growth techniques 83
4.1 Ternary Single Crystal Chalcopyrites grown by CVT 83
4.2 Ternary Epitaxial Chalcopyrites grown on GaAs by MOVPE 84
4.3 Ternary Polycrystalline Chalcopyrites grown on Mo/glass by PVD 85
4.4 Quaternary Epitaxial Chalcopyrites grown on GaAs by MOVPE 86
4.5 ZnSe grown on glass and chalcopyrite substrates by EBE 87
4.6 ZnSe grown on glass and chalcopyrite substrates by CBD 89
4.6.1 Homogeneous process 92
4.6.2 Heterogeneous chemical growth 92
4.7 Au/Al/In:ZnO/i-ZnO grown on ZnSe/$CuGaSe_2$/Mo/glass by PLD 93
4.8 ZnO grown on ZnSe/Cu(In,Ga)S_2/Mo/glass by ECD 94
4.9 ZnO Nanorod ARCs grown on glass substrate by ECD 96
5. Characterization techniques 99
5.1 Structural characterization (XRD, SEM, AFM, RAMAN) 99
5.1.1 X-Ray Diffraction (XRD) 99
5.1.1.1 General 99
5.1.1.2 Experimental set-up 100
5.1.2 Scanning Electron Microscopy (SEM) 100
5.1.2.1 General 100
5.1.2.2 Experimental set-up 102
5.1.3 Atomic Force Microscopy (AFM) 103
5.1.3.1 General 103
5.1.3.2 Experimental set-up 103
5.1.4 Raman Scattering Spectroscopy (RAMAN) 104
5.1.4.1 General 104

5.1.4.2 Theory of Raman scattering in molecules 104
5.1.4.3 Raman tensor in solids 106
5.1.4.4 Experimental set-up 107
5.2 Optical Characterization (SE, PR) 108
5.2.1 Spectroscopic Ellipsometry (SE) 108
5.2.1.1 General 108
5.2.1.2 Null-Ellipsometry 110
5.2.2 Modulation spectroscopy: Photoreflectance(PR) – Electroreflectance(ER) 111
5.2.2.1 General 111
5.2.2.2 Modulation spectra and the dielectric function 112
5.2.2.3 Photoreflectance-spectra in the low-field regime 114
5.2.2.4 Experimental set-up of PR 116
5.2.2.5 Experimental set-up of ER 117
5.3 Electrical characterization 118
6. Results and Discussion 121
A. PROPERTIES STUDIES 122
6.1 Structural properties of chalcopyrite absorbers 122
6.1.1 Epitaxial and polycrystalline $CuGaSe_2$ 122
6.1.1.1 XRD measurements 122
6.1.1.2 Micro-Raman measurements 126
6.2 Optical properties of chalcopyrite absorbers 130
6.2.1 Comparison of bulk and epitaxial absorbers 131
6.2.1.1 Strain-Stress by XRD-analysis Techniques (T=300K). 132
a) $CuGaSe_2$ with [Cu]/[Ga]=1.00. 132
6.2.1.2 Strain-Stress by Optical Modulation Techniques at Low Temperatures (T=20K). 133
6.2.1.3 Strain-Stress by Optical Modulation Techniques at Room Temperature (T=300K). 136
6.2.1.4 Comparison of Strain-Stress by Optical Modulation and XRD Techniques. 137

6.2.1.5 Anion- and/or Cation-Replacement 137
6.2.1.6 Partial Cation Replacement..... 140
6.2.1.7 Temperature Dependence 141
6.2.1.8 Anion/Cation Replacement & Temperature Dependence..... 142
6.2.1.9 Light Polarization..... 142
6.2.2 Temperature dependence of $CuGaSe_2$ chalcopyrite absorbers..... 144
6.2.3 Temperature dependence of $CuInSe_2$ chalcopyrite absorbers 159
6.2.4 Compositional Dependence of $CuGaSe_2$ chalcopyrite absorbers..... 168
6.2.5 Compositional Dependence of $CuIn_{1-x}Ga_xSe_2$ chalcopyrite absorbers.. 170
B. GROWTH & CHARACTERIZATION STUDIES 174
6.3 CBD ZnSe grown on Amorphous Glass substrate..... 174
6.3.1 Structural properties..... 174
6.3.2 Optical properties..... 188
6.4 CBD ZnSe on Epitaxial Chalcopyrite Absorbers 191
6.4.1 Structural properties..... 191
6.5 CBD ZnSe on Polycrystalline Chalcopyrite Absorbers..... 202
6.5.1 Structural properties..... 202
6.6 COMPARISON of EBE ZnSe on Chalcopyrite with CBD ZnSe on Chalcopyrite 208
6.7 PLD Al/In:ZnO/i-ZnO on ZnSe/Polycrystalline-Chalcopyrite Absorbers 211
6.8 ECD ZnO grown on ZnSe/Polycrystalline-Chalcopyrite Absorbers 218
6.9 ECD ZnO Nanorods on glass Substrates 219
6.9.1 Low Dimensional Systems 220
6.9.2 Structural Properties..... 221
6.9.2.1 X-Ray Diffraction (XRD) 221
6.9.2.2 Scanning Electron Microscopy (SEM) 222
6.9.2.3 Atomic Force Microscopy (AFM) 223
6.9.3 Optical Properties..... 225
6.9.3.1 Transmittance..... 225
6.9.3.2 Photoreflectance Spectroscopy 227
6.9.4 Electrical Properties 234

6.10 Chalcopyrite based Thin Film Solar Cells 235
6.10.1 I-V Characteristics of Solar Cells 235
6.10.1.1 with PVD ZnSe/$CuGaSe_2$/Mo/glass 235
6.10.1.2 with CBD ZnSe/$CuGaSe_2$/Mo/glass 236
6.10.2 Electroreflectance(ER)of Al/ZnO/CdS/$CuIn_{1-x}Ga_xSe_2$/Mo/glass Solar Cell 243
6.10.2.1 The $CuIn_{1-x}Ga_xS_2$ absorber 246
6.10.2.2 The CdS buffer layer 252
6.10.2.3 The ZnO Window layer 253
7. Conclusions 255
8. References 261
9. Appendix A 275
10. CURRICULUM VITAE 277

1. Introduction

Nowadays, the biggest challenge for mankind is the protection of the natural environment. This challenge refers to the reservation of the viable development, to the quality of life, even to the future of our planet. The waste of the physical resources (fossil fuels like coal, oil, or natural gas), along with the ongoing environmental pollution, the water supply exhaustion and the green house effect are irreversible, though, they can be diminished. The use of ***Renewable Energy Sources (RES***) is today more demanding than ever. One of the most promising RES is the ***Photovoltaic Technology (PhotoVoltaics - PVs)***. PVs receive a strong appreciation due to their vast (essentially infinite) fuel source, their lack of emissions (no combustion or radioactive fuel for disposal), and the low operating costs along with high reliability in modules. All these advantages, along with others (Table 1.1), make them a versatile form of power production.

Advantages of PVs	*Disadvantages of PVs*
• Fuel source is vast • No emissions, no combustion or radioactive fuel for disposal (does not contribute perceptibly to global climate change or pollution) • Low operating costs • High reliability in modules (over 20 years) • Modular (small or large increments) • Quick installation • Integrated into new or existing building structures • Installed at nearly any point of use • Excellent safety record	• Fuel source is diffuse(sunlight is a low-density energy) • Lack of widespread commercially available system integration and installation (so far)

Table 1.1 Advantages and disadvantages of photovoltaics

Photovoltaic devices generate direct current (DC) electrical power from semiconductors, when they are illuminated by photons (sunlight). The individual PV element is called ***Solar Cell***. PVs aims at tow areas of application: one is the power supply for off-grid professional devices and supply systems (e.g. telecommunication equipment, solar home systems) and the other is large-scale electricity generation as a substitute for and a complement to today's non sustainable energy processes. With respect to the latter, the global potential of PV electricity is of key importance. Table 1.2 shows the technical and the theoretical potential of several renewable energy sources [1.1].

Resource	Current Use	Technical Potential	Theoretical Potential
Hydropower	9	50	147
Biomass	50	>276	2.900
Solar	**0,1**	**>1575**	**3.900.000**
Wind	0,12	640	6.000

**Units: E (J/year)*

Table 1.2 Current use and current potentials of selected renewable sources

Nevertheless, two important conclusions may be drawn from Table 1.2: (a) solar energy conversion, alone, could in principle produce considerably more technical energy than is consumed today, and (b) compared to other renewable energy sources, solar radiation is, by far, the largest. A sustainable global energy system that is strongly based on renewable sources will, in the long run, mainly be a solar energy system.

1.1 History of Photovoltaics

The history of the photovoltaics goes back to the nineteenth century, as shown in Table 1.3. The first functional, intentionally made PV device was by Fritts in 1883. He melted Se into a thin shit of metal substrate and pressed an Au-leaf as the top contact. It was nearly 30cm^2 in area. He noted, *"... the current, if not wanted immediately, can be either stored where produced, in storage batteries, ... or transmitted a distance and there used"*. This man foresaw today's PV technology and applications over a hundred years ago.

History of PVs
• 1839: Becquerel (FR) discovered photo galvanic effect in liquid electrolytes
• 1873: Smith (UK) discovered photoconductivity of solid Se
• 1883: Fritts (US) makes the first large area solar cell using Se film
• 1954: First 6% efficient Si and Cu_2S/CdS solar cells reported
• 1958: NASA Vanguard satellite with Si backup solar array
• 1963: Sharp Corp (JP) produces first commercial Si modules
• 1970: First GaAs heterostructure solar cells by Alferov (USSR)
• 1973: Worldwide oil crisis spurs many nations to consider renewable energy including PVs; World's first solar powered residence built with Cu_2S solar modules (Delaware, USA)
• 1980: First thin-film solar cell, using Cu_2S/CdS (USA)
• 1985: High-efficient (>20%) Si solar cells under standard sunlight
• 1986: First commercial thin-film power module, the a-Si G4000 from Arco Solar (USA)
• 1994: GaInP/GaAs 2-terminal concentrator multijunction >30% (USA)
• 1995: German demonstration project "1000 roofs" to install PVs on houses
• 1998: Cu(InGa)Se_2 thin-film solar cell reaches 19% efficiency, comparable with multicrystalline Si
• 1999: Cumulative worldwide installed PVs reaches 1000MW
• 2000: Olympics in Australia highlight wide range of PV applications
• 2002: Cumulative worldwide installed PVs reach 2000MW. **It took 25 years to reach the first 1000MW and only 3 years to double it!!**

Table 1.3 Notable events in the history of photovoltaics

The modern era of PVs started in 1954 when researchers at Bell Labs in the USA, accidentally, discovered that pn-junction diodes generated voltage, when the room lights were on. Within a year, they had produced a 6% efficient Si pn-junction solar cell [1.2]. A year later, a 6% GaAs pn-junction solar cell was reported by RCA Lab in US [1.3]. By 1960, 6% efficient CdTe based thin film solar cells were produced [1.4]. By this time, the US space program, was utilizing Si PV cells for powering satellites. In 1970, a group at

the Ioffe Institute, in the USSR, developed a heterojunction GaAlAs/GaAs solar cell and pointed the way to new device structures. A significant improvement in performance, occurring in 1973, was the "violet cell" having an improved short wavelength response, leading to a 30% relative increase in efficiency over the state-of-the-art Si cells [1.5]. In the 1980s, the industry began to mature. Manufacturing facilities for producing PV modules from Si wafer pn-junction solar cells were built in the USA, Japan, and Europe. Companies attempted to scale up the thin-film PV technologies like a-Si and $CuInSe_2$, which had achieved efficiency greater than 10% for small area ($1cm^2$) devices, made with carefully controlled laboratory scale equipment. Meanwhile, the Japanese PV industry began to take off. Production of c-Si modules and intensive research on thin-film technology, led to many innovative device designs, improved materials processing, and growing dominance in the world PV market.

Along with the maturing of the solar cell technology, many products, like inverters (which convert the DC- to AC-power) and sun trackers needed to grow. An early development, that helped many companies, was to sell PV cells for consumer-sized, small-scale power applications. Another application was the rural electrification of remote villages, in an attempt to help, roughly one third of the world's citizens to gain access to modern communication systems and lighting. Yet another important development in the application of PV in the late 1990s, was building integrated PV, where PV cells are incorporated into a standard building product, such as a window or a roof shingle. In 2001, the success has been even bigger in Japan, where homebuilders receive rebate from the government for about 30% of the PV system cost. Their electric bill is determined by the utility, using the "net metering", where the customer pays only the net difference between what they used and what they generated. Rebates and net metering are also available in some of the states in the USA since 2002.

1.2 Fundamental properties of semiconductors

Electronic grade semiconductors are very pure crystalline materials. Their atoms are aligned in a regular periodic array. This periodicity, coupled with the atomic properties of the component elements, is that gives to semiconductors their very useful electronic properties. An abbreviated periodic table of elements is given in Table 1.4.

I	II	III	IV	V	VI
		B	C	N	O
		Al	Si	P	S
Cu	Zn	Ga	Ge	As	Se
Ag	Cd	In	Sn	Sb	Te

Table 1.4 Abbreviated periodic table of elements

When the semiconductor is in thermal equilibrium (i.e. at a constant temperature with no external injection or generation of carriers), the Fermi function determines the ratio of filled states to available states at each energy, and is given by Eq.(1.1) [1.6]

$$f(E) = \frac{1}{1 + e^{(E - E_F)/kT}} \tag{1.1}$$

where E_F is the Fermi energy, k is the Boltzmann's constant, and T is the temperature in Kelvin. The Fermi function depends strongly on temperature. At absolute zero, it is a step function and all the states below E_F are filled with electrons, whereas those above E_F are completely empty. As the temperature increases, thermal excitation will leave some states below E_F empty, and the corresponding number of states above E_F will be filled with the excited electrons (Figure 1.1).

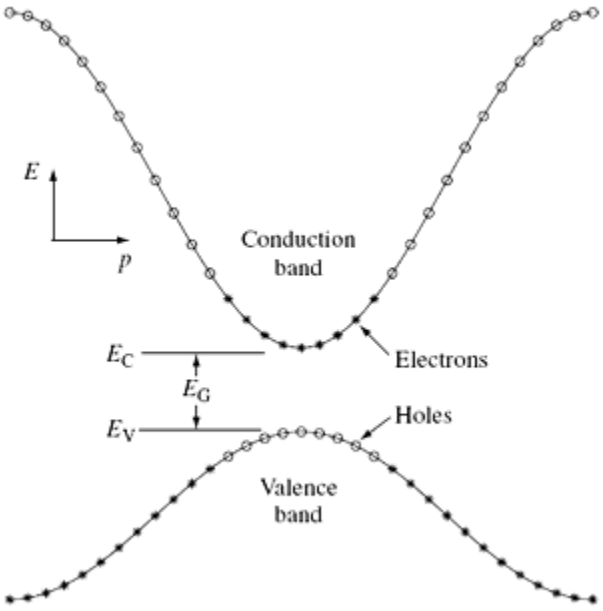

Figure 1.1 A simplified energy band diagram at T>0 K for a direct semiconductor

The conduction-band and valence-band effective densities of states, N_C and N_V, respectively, are given by Eq.(1.2):

$$N_C = 2\left(\frac{2\pi m_e^* kT}{h^2}\right)^{3/2}$$
$$N_V = 2\left(\frac{2\pi m_h^* kT}{h^2}\right)^{3/2} \tag{1.2}$$

where m_e^* and m_h^* are the electron- and hole-effective mass, respectively. When the Fermi energy is sufficiently far (>3kT) from either band-edge, the carrier concentrations can be approximated as

$$n_0 = N_C e^{(E_F - E_C)/kT}$$
$$p_0 = N_v e^{(E_V - E_F)/kT} \tag{1.3}$$

And the semiconductor is called ***nondegenerate***. In nondegenerate semiconductors, the product of the equilibrium electron and hole concentrations is independent of the location of the Fermi energy and is just

$$p_0 n_0 = n_i^2 = N_C N_V e^{(E_V - E_C)/kT} = N_C N_V e^{-E_g/kT} \tag{1.4}$$

In intrinsic (undoped) semiconductors, in thermal equilibrium, the number of electrons, in the conduction band, and the number of holes, in the valence band, is equal.

$$n_0 = p_0 = n_i \tag{1.5}$$

where n_i is the intrinsic carrier concentration.

The Fermi energy in an intrinsic semiconductor ($E_i = E_F$) is given by Eq.(1.6), which is typically very close to the middle of the band gap.

$$E_i = \frac{E_V + E_C}{2} + \frac{kT}{2} ln\left(\frac{N_V}{N_C}\right) \tag{1.6}$$

The intrinsic carrier concentration is typically very small. This is the reason that semiconductors behave as insulators. The number of electrons and holes in their respective bands, and hence the conductivity of the semiconductor, can be controlled through the introduction of specific impurities, or dopands, called ***donors*** and ***acceptors***. For example, when semiconductor *Si* is doped with *P*, one electron is donated to the

conduction band for each atom of *P* introduced. From Table 1.4, it can be seen that *P* is in the column V of the periodic table of elements, and thus has five valence electrons. Four of these are used to satisfy the four covalent bonds of *Si* and the fifth is available to fill an empty state in the conduction band. If *Si* is doped with *B* (tree valence electrons, since it is in column III), each *B*-atom accepts an electron from the valence band, leaving behind a hole. All impurities introduce additional localized electronic states into the band structure, often even between E_C and E_V, as illustrated in Figure 1.2.

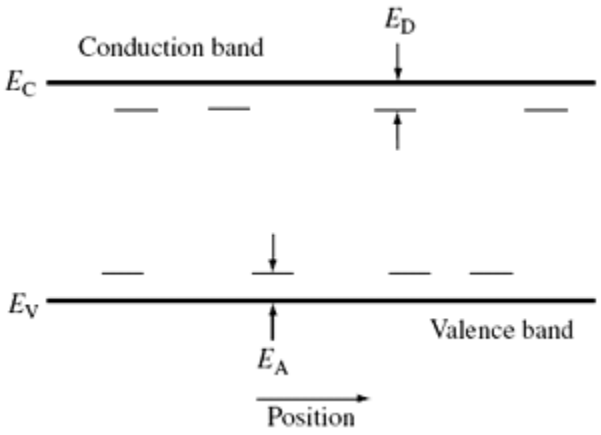

Figure 1.2 Donor and acceptor states in a semiconductor

The controlled production of donor and acceptor impurities into a semiconductor allows the creation of the ***n-type*** (electrons are the primary source of electrical conduction) and ***p-type*** (holes are the primary source of electrical conduction) semiconductors, respectively. This is the basis for the construction of all semiconductor devices, including solar cells.

1.3 pn - junction

At the heart of any solar cell is the pn-junction. Modeling and understanding a solar cell is much simplified by using the pn-junction concept. When the impurity concentration in a semiconductor changes abruptly from acceptor impurities N_A (*p-type*) to donor impurities N_D (*n-type*), as shown in Figure 1.3, one obtains an abrupt junction.

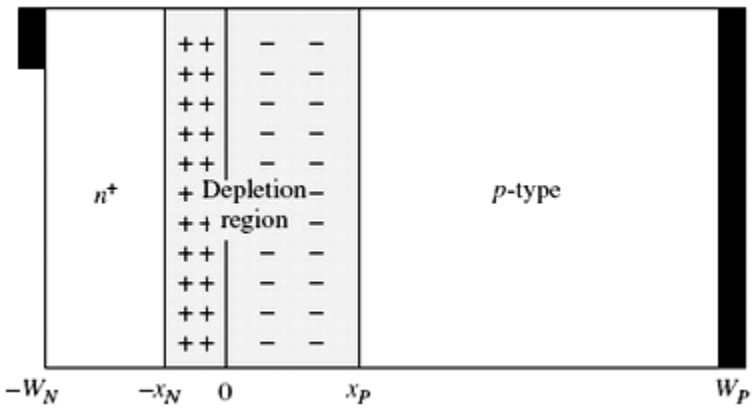

Figure 1.3 Simple solar cell structure

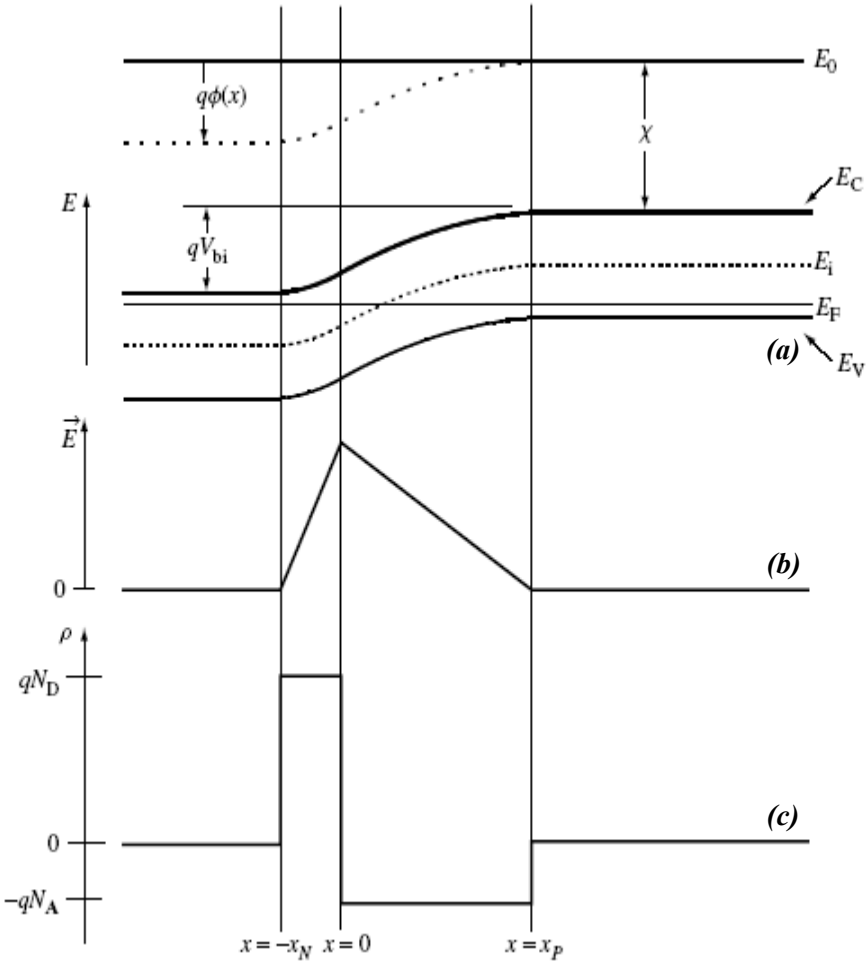

Figure 1.4 Equilibrium conditions in a solar cell:(a) energy band formation, (b) electric field distribution, and (c) charge density distribution

In thermal equilibrium, there is no current flow and by definition, the Fermi energy must be independent of position. Since there is a concentration difference of holes and electrons between the two types of semiconductors, holes diffuse from the *p-type* region into the *n-type* region and similarly, electrons diffuse from the *n-type* region to the *p-type* region. As the carriers diffuse, the charged impurities are no longer screened by the majority of carrier, and, subsequently, an electric field is produced, which limits the diffusion of the holes and electrons. In thermal equilibrium, the diffusion and drift currents for each carrier type balance, so there is no current flow. The transition region between the *n-type* and the *p-type* semiconductors is called s***pace-charge region***. It is also called ***depletion zone***, since it is effectively depleted of both holes and electrons. The electrostatic potential difference, resulting from the junction formation, is called the ***built-in voltage*** (V_{bi}). Figure 1.4 shows the equilibrium energy band diagram, electric filed, and charge density, for a simple abrupt pn-junction silicone diode, in the vicinity of the depletion region.

The basic solar cell structure, which has been demonstrated in Figure 1.3, is simply a pn-junction diode, consisting of two quasi-neutral regions on either side of a depletion region, with an electrical contact made to each quasi-neutral region. Typically, the more heavily doped quasi-neutral region is called the ***emitter*** (the *n-type* region in Figure 1.3) and the more lightly doped region is called the ***absorber*** (the *p-type* region in Figure 1.3). The *p-type* region is referred as "the absorber", since the emitter is usually very thin and the most of the light absorption occurs in the *p-type* region.

1.4 Photovoltaic effect

The radiative energy output from the sun derives from a nuclear fusion reaction. In every second about 6×10^{11} kg of H_2 is converted to He, with a net mass loss of about 4×10^{3} kg, which is corresponds to 4×10^{20} J. this energy is emitted primarily as electromagnetic radiation in the ultra-violet (UV) to infra-red (IR) and radio spectral regions (0.2 to 3μm).

Figure 1.5 shows three curves related to solar spectral irradiance (power per unit area per unit wavelength). The upper curve is the radiation spectrum of a 5762K black

body. The middle curve represents the solar spectrum outside the earth's atmosphere, where the air mass is zero (AMO). This spectrum is the relevant one for satellite and space-vehicle applications. The AM1.5 (sun at 45^{o} above horizon) spectrum represents a satisfactory energy weighted average for terrestrial applications.

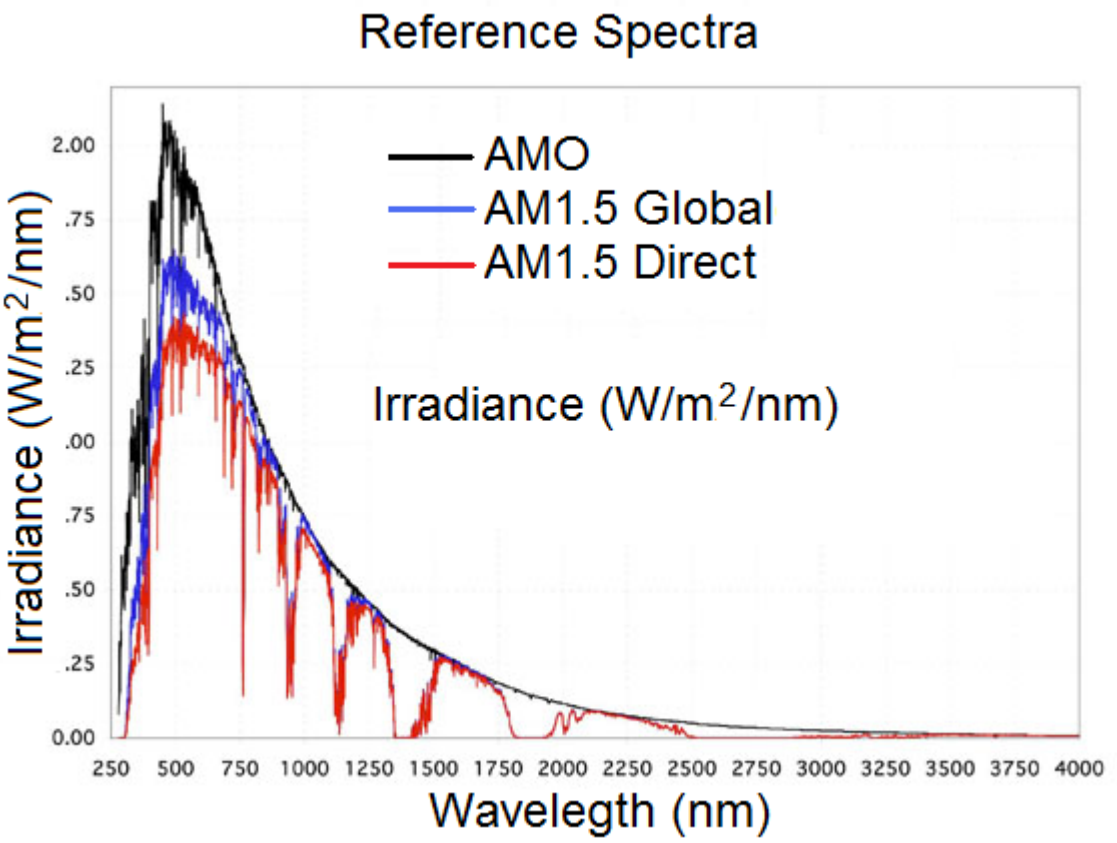

Figure 1.5 The solar radiation spectrum for a black body at 5762K, an AM0 spectrum, and an AM1.5 global spectrum

The conventional solar cell (e.g. a pn-junction) has a band-gap energy abbreviated E_g. When the cell is exposed to solar radiation, a photon with energy (hv) less than the E_g makes no contribution to the cell output. A photon with energy greater than E_g contributes an energy E_g to the cell output, and the excess over E_g is wasted as heat. Incident photon illumination can create electron-hole pairs in the space charge region. Under closed circuit conditions, the minority carriers, if generated within a certain distance of the junction (called ***diffusion length***) can diffuse to the junction, be swept to the other side (due to electric field in the depletion region) producing the photocurrent I_L (Figure 1.6) in the reverse-bias direction, and be collected by appropriate contacts. The

photocurrent I_L produces voltage drop V across the resistive load R, which forward biases the pn-junction. The forward-bias voltage V produces a forward-bias current:

$$I_F = I_S(e^{eV/kT} - 1) \tag{1.7}$$

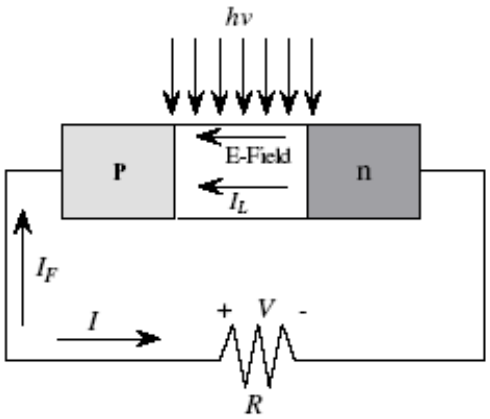

Figure 1.6 A pn-junction solar cell under illumination

The net pn-junction current, in reverse-bias direction is:

$$I = I_L - I_F = I_L - I_S(e^{qV/kT} - 1) \tag{1.8}$$

Where I_S is the reverse-bias diode saturation, q is the electron charge, k is the Boltzmann's constant and T is the temperature. The photocurrent is always in the reverse-bias direction and the net solar cell current is also always in the reverse hole direction.

In a short circuit condition (R=0, V=0), the current is called ***short-circuit current*** (I_{SC}) and is equal to I_L. In an open circuit condition (R→∞, I=0) the voltage is called ***open-circuit voltage*** (V_{OC}), and is given by Eq.(1.9).

$$V_{OC} = V_T \, ln\left(1 + \frac{I_L}{I_S}\right) \tag{1.9}$$

where V_T is the thermal voltage, given in [1.7] as:

$$V_T = \frac{kT}{q} \tag{1.10}$$

A plot of the diode current as function of the diode voltage, known as ***I-V characteristi***c, in the dark and under illumination is shown in Figure 1. 7. The efficiency

of the cell can be expressed in terms of the short-circuit current (I_{SC}) and the open-circuit voltage (V_{OC}) of the device, once the ***fill factor*** ff is defined [1.6]:

$$ff = \frac{I_m V_m}{I_{SC} V_{OC}} \tag{1.11}$$

where I_m and V_m represent the current and voltage for the conditions of maximum output power of the device (inset in Figure 1. 7)

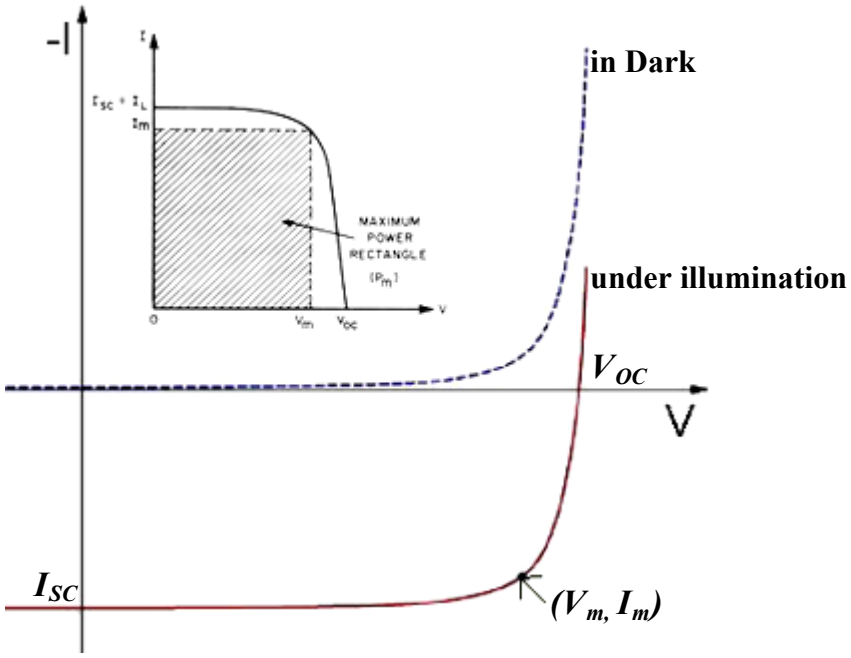

Figure 1. 7 I-V characteristics of a solar cell in the dark and under illumination.

The cell ***conversion efficiency*** η, defined as the ratio of the generated power with respect to the power of the incident radiation output (P_{in}), may be written as:

$$\eta = \frac{P_m}{P_{in}} = \frac{ff \cdot I_{SC} \cdot V_{OC}}{P_{in}} \tag{1.12}$$

For a common solar cell, the forward current can be dominated by the recombination current in the depletion region. The efficiency, then, is generally reduced, compared to that of an ideal diode. Furthermore, for solar cells having mixtures of diffusion and recombination current, or containing many defects, the forward current,

may show an exponential dependence of the forward voltage, leading also to decreased efficiency.

1.5 Thin Film Solar Cells (TFSC)

Since the discovery of a pn-junction Si photovoltaic device, reported in 1954 (as already shown in §1.1), the science and technology of PV devices (solar cells) and systems, have undergone revolutionary developments. One key to the development of any photovoltaic technology is the cost reduction. This has been evident in the case of crystalline Si (c-Si) PVs. Today, the best single crystal Si solar cells have reached an efficiency of 25% [1.8], compared with the theoretical maximum value of 30%.

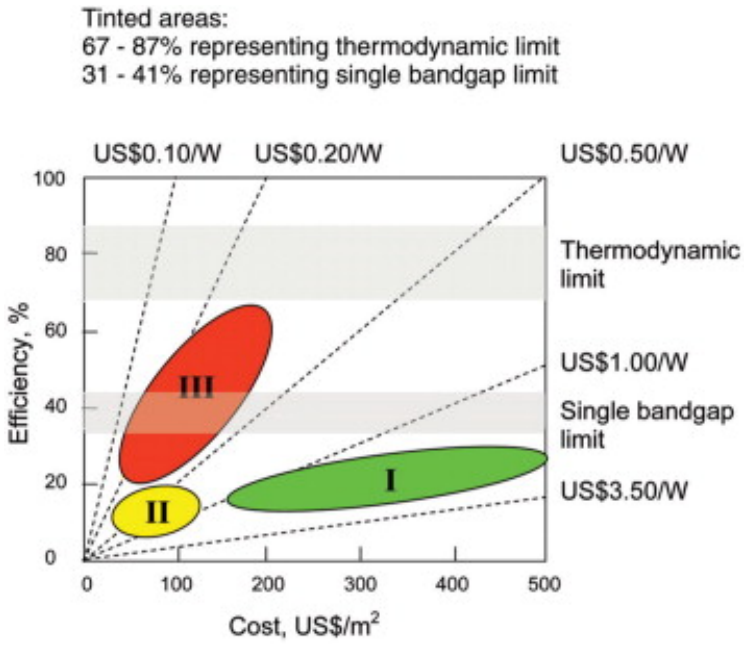

Figure 1.8 Cost-efficiency analysis for first- (I), second- (II), and third- (III) generation PV technologies

First-generation technologies are primarily based on c-Si (including large-grain, poly- and single-crystalline). The current technologies are rapidly evolving towards costs of 1-2$/Wp (Wp stands for watt peak). Key issues are Si feedstock supply, losses involved in preparing Si-wafers, and the development of lower cost/high-throughput processing.

Second-generation technologies are those that have demonstrated practical conversion efficiencies and potentially lower costs per watt, than crystalline Si, but have no significant market penetration at present. Commercialization of these approaches is typically in the early manufacturing face. This group represents a fairly broad base of technologies, including thin film photovoltaics, solar concentrators, solar thermal conversion and the emerging field of organic photovoltaics, which is the transition from second-generation to ***third-generation*** technologies (ultimate thin film solar cell, with high efficiency, made of abundant, non toxic, durable materials).

Thus, over the past decade, there has been considerable effort in advancing thin film, "second-generation" technologies, that do not require the use of silicon wafer substrates, and can, therefore, be manufactured at significantly reduced cost. Steady progress has been made in laboratory efficiencies, as can be seen in Figure 1.9 [1.9], for chalcopyrite-based devices (red circles).

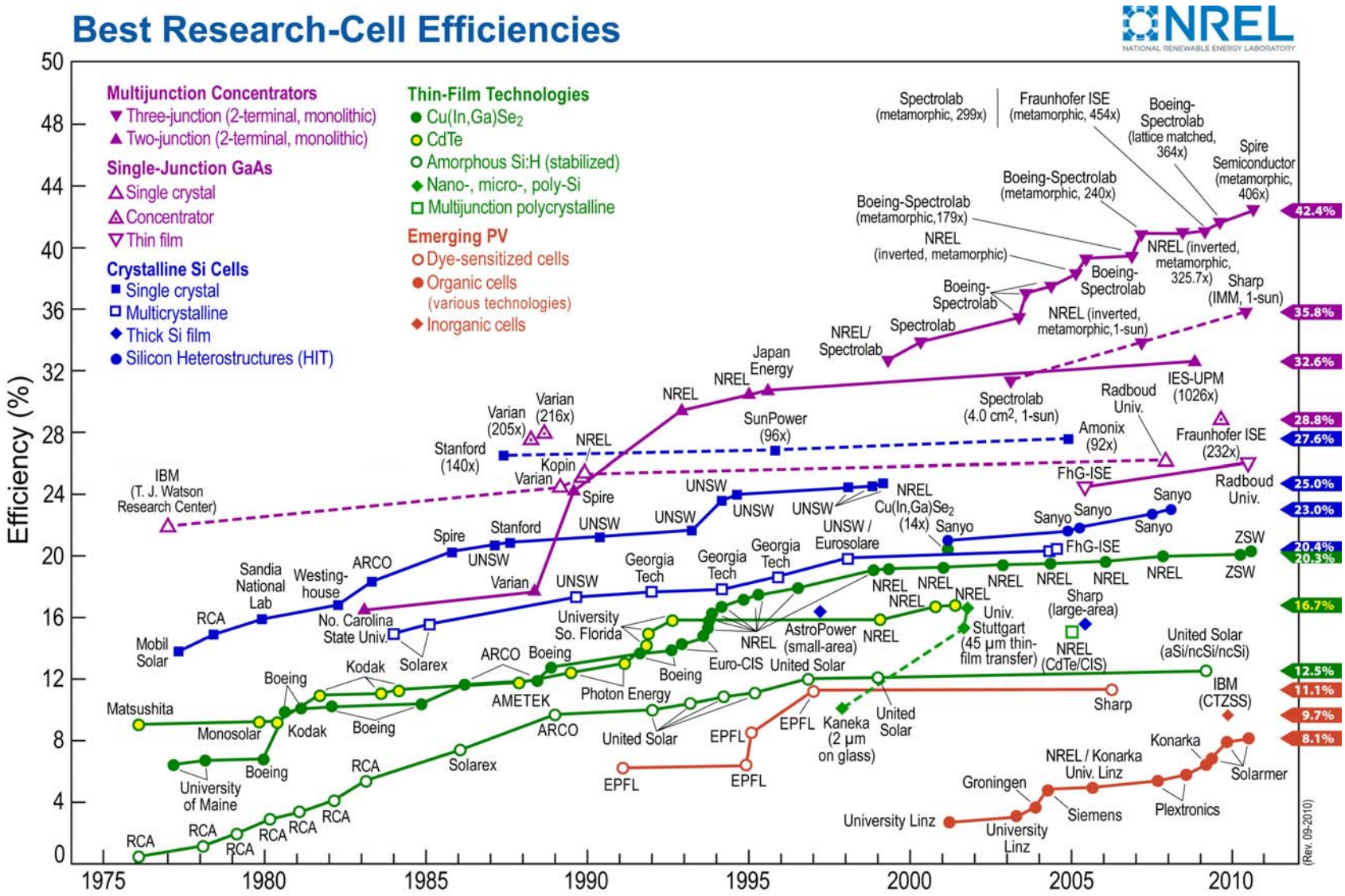

Figure 1.9 Progress of research –scale photovoltaic device efficiencies, under AM1.5 simulated solar illumination, for a variety of technologies [1.9]

1.6 Chalcopyrite-based solar cells

A very challenging technology is based on ternary compound semiconductors ***$CuInSe_2$, $CuGaSe_2$, $CuInS_2$, $CuGaS_2$*** and their multinary alloys ***$Cu(In,Ga)(S,Se)_2$*** (CIGS). The first results of single crystal work on $CuInSe_2$ (CIS) [1.10] were extremely promising, but also showed the complexity of the thin film technology and the material itself. However, pioneering work [1.11] later on showed immediate success. It became evident that CIS process technology is very flexible with respect to process conditions.

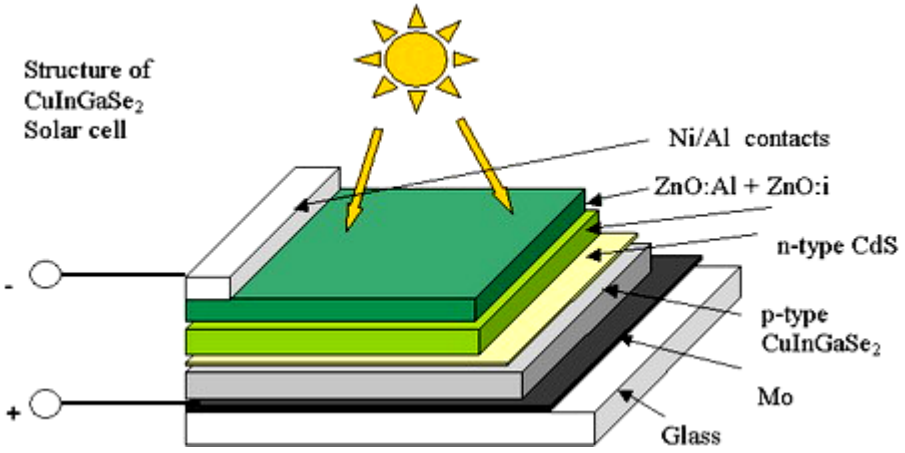

Figure 1.10 Typical structure of a chalcopyrite-based solar cell

In principle, a solar cell is a pn-junction, as has already been mentioned in §1.3. A typical chalcopyrite solar cell is demonstrated in Figure 1.10. The solar cell consists of:

1. the substrate (glass/polymer, or flexible conducting substrates as Ti-foil, which serve also as the back ohmic contact)
2. the back ohmic contact (Mo on glass substrates)
3. the absorber, which constitutes the p-type semiconductor of the junction
4. the window layer (the buffer layer: CdS or ZnSe along with the transparent conducting oxide: ZnO)
5. the front ohmic collection grid

For every part of the solar cell, follows a brief description.

1.6.1 The substrate

Thin film solar cell devices are configured in either substrate or superstrate configuration (Figure 1.11) [1.12]. For substrate configuration, the substrate is metal or metallic coating on a glass/polymer substrate, which also acts as the contact. For superstrate configuration, the substrate is transparent and the contact is made by a conducting oxide coating on the substrate. Substrate is a passive component in the device and is required to be mechanically stable, matching thermal expansion coefficient with deposited layers and inert during the device fabrication. Suitable substrates as selected in the basis of these criteria.

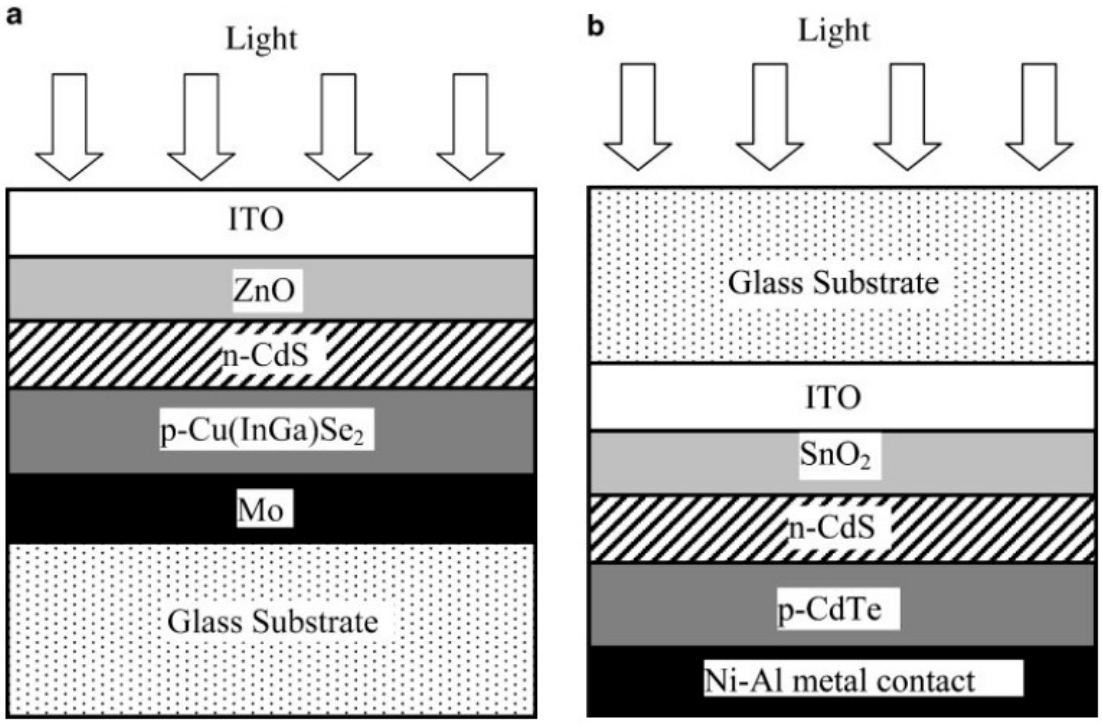

Figure 1.11 Typical TFSC structures for a single-junction: a) substrate CIGS, and b) superstrate CdTe solar cell devices

Flexible substrates, stainless steel foils/polymer films, are suitable for roll-to-roll deposition enabling a compact deposition system design as well as flexibility in device handling. Electrically conductive substrates enable the fabrication of front and rear-side conduction cells, whereas insulating substrates enable fabrication of monolithically interconnected cells for modules.

Both superstrate and substrate device structures are currently being pursued for CIGS solar cell fabrication. The film growth and interdiffusion and, hence, the device properties are dependent on the device structure. The CIGS solar cells, based on superstrate structure is inferior to substrate structure, because of the interdiffusion of the buffer layer (CdS or ZnSe) during high-temperature CIGS film growth. Solar cell (CIGS/ZnO) grown on superstrate configuration reached a 10.2% efficiency [1.13], whereas, solar cell (ZnO/CdS/CIGS) grown on substrate configuration reached efficiencies beyond 20% [1.14]. Also, efficiencies of 19.9% have been reported for CIGS devices with fill-factor 81.2% [1.15]. The substrate appears to play an active role in improving the photovoltaic performance of the CIGS absorber materials.

Na, in the soda-lime glass substrate has been considered as a key prerequisite for efficient CIGS device fabrication. Na diffuses into CIGS absorber, improves the grain growth performance. Sodium is inherently present in soda-lime glass and in the case of Na free substrate, Na precursors are intentionally incorporated in the device fabrication.

1.6.2 The back ohmic contact

For CIGS devices, the back contact is applied to the p-type semiconductor in both superstrate and substrate configurations (Figure 1.11). In order to form an ohmic contact, the metal used for contact should have a work function higher than that of the p-type semiconductor (CIGS). This aligns the metal Fermi level with the upper valence band edge. In the substrate configuration of CIGS solar cells, Mo is used as the contacting material because of its inert nature during the highly corrosive CIGS deposition conditions. Mo forms an ohmic contact via the formation of a thin intermediate $MoSe_2$ layer, formed during CIGS deposition conditions.

1.6.3 The absorber

I-III-VI chalcopyrite materials have desirable properties for photovoltaic applications. $CuInS_2$, having a band-gap of 1.5eV is considered an ideal material for photovoltaic application. The difficulties in controlling the sulfur during deposition, and the relative rapid diffusion of metals and impurity species, even at low temperatures, slow down the development of this material. However, devices with efficiency 11.4% have been reported [1.16].

On the other hand, $CuInSe_2$, with band-gap of 1.0eV, has proved to be a leading candidate for photovoltaic applications. Due to its rather low band-gap, a common practice has evolved, where Ga is added to obtain a quaternary alloy $CuIn_{1-x}Ga_xSe_2$, with a wider band-gap. According to the Ga concentration in the quaternary chalcopyrite, the bang-gap of the chalcopyrite can range from 1.0 to 2.5 eV, taking full advantage of the solar spectrum (Figure 1.12).

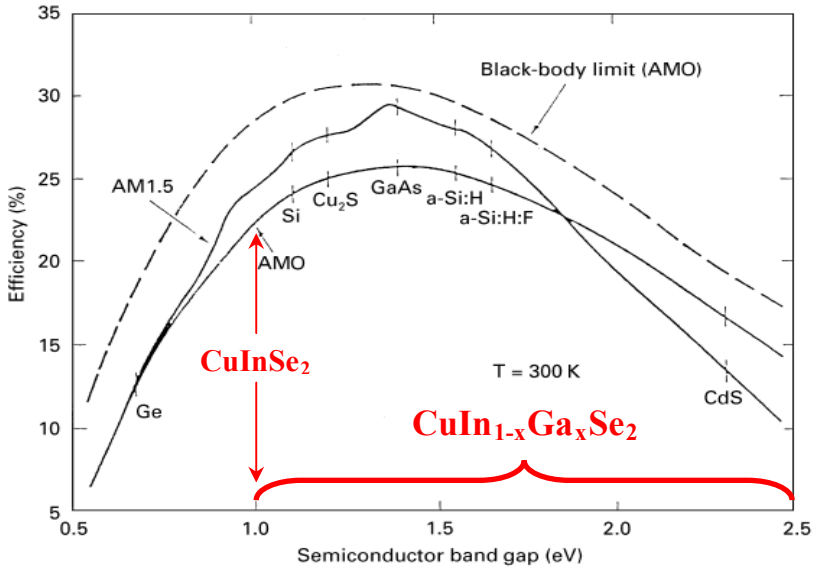

Figure 1.12 Efficiency versus band-gap for the most common solar cell absorbers

1.6.4 The window layer

The window layer in a solar cell device consists of the buffer layer and the transparent conductive oxide (TCO). The primary function of the buffer layer in a heterojunction is to form a junction between the TCO and the absorber layer, while admitting a maximum amount of light to the junction region and absorber layer. For high optical throughput with minimal resistive loss, the band-gap of the window layer should be as wide as possible to maintain low series resistance. It is also important that the band-offset is rewarding for optimal carrier transport.

The CIGS solar cells typically use a CdS buffer layer and a transparent conducting oxide, which both form the window layer of the device. However, buffer

layers are being investigated to replace CdS, because of the concern about the toxicity of Cd, and also to improve the blue response in devices.

Transparent conducting oxides (TCO) in general are n-type degenerate semiconductors, with good electrical conductivity and high transparency in the visible spectrum. Thus, a low-resistance contact to the device and transmission of most of the incident light to the absorber layer is ensured. The conductivity of a TCO depends on the carrier concentration and mobility. An increase in the carrier concentration may result in enhanced free carrier absorption, which reduces the transparency of the TCO in the high-wavelength region. Table 1.5 shows alternative materials used as window layers for Thin Film Solar Cell (TFSC) applications. The most common material, used in a solar cell device, is a ZnO layer. In particular, the transparent conductive oxide consists of two separate layers. An intrinsic layer (undoped) deposited right after the buffer layer, followed by an n-doped ZnO layer. Al is the most common dopant for ZnO.

Material	Resistivity ($\times 10^{-4}\Omega$ cm)	Transparency (%)
SnO_2	8	80
In_2O_3:Sn/Ga	2	85
In_2O_3:F	2.5	85
Cd_2SnO_4	2	85
Zn_2SnO_4	100	90
ZnO:Al	8.5	90
ZnO:In	8	85

Table 1.5 Typical resistivity and transmission (in visible)

for various TCO materials for TFSC applications[1.17], [1.18]

2. Material properties

The understanding of the materials used in photovoltaic devices, is of great importance for the experimental investigation and the following inference. The present doctoral thesis treats materials used in a thin film solar cell device:

i. **the Chalcopyrite absorber**
ii. **the ZnSe buffer layer, and**
iii. **the ZnO window layer**

Optical and Electrical properties of solar cell devices are also investigated.

In the following section, the structural, electrical, and optical properties of the above mentioned materials are presented.

2.1 Chalcopyrite - Absorber

2.1.1 General

Chalcopyrite is a copper-iron-sulfite mineral, which crystallizes in the tetragonal system, and it has the chemical composition of $CuFeS_2$. In general, the crystal structure of I-III-VI_2 ($A^{I}B^{III}X^{VI}{}_2$) ternary compound semiconductors belongs to the non-symmorhic space group D_{2d}^{12} (eight atoms per primitive unit cell), which is a superlattice of zinc-blende (ZB) structure T_d^2 (two atoms per primitive unit cell), as shown in Figure 2.1. Each anion (X) is coordinated by two A- and two B-cations, whereas each cation is tetrahedrally coordinated by four anions [2.1].

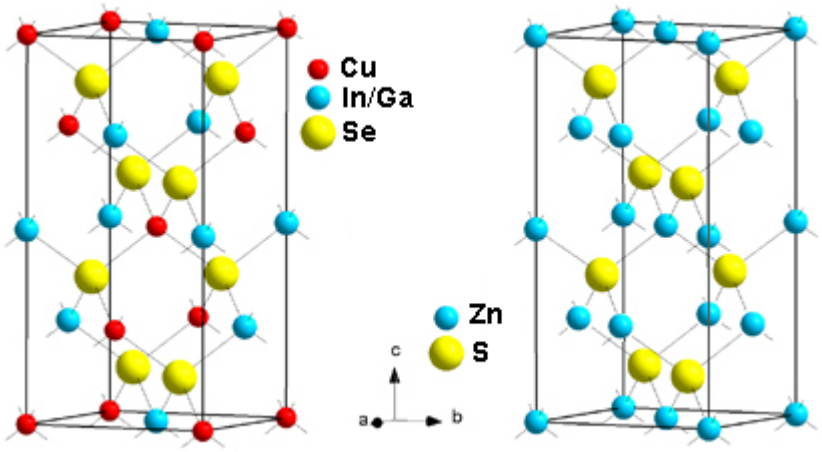

Figure 2.1 Crystal structure of chalcopyrite (left) and zinc-blende (right) lattices

There are three significant structural differences with respect to the zinc-blende structure. First, there are two cation sublattices rather than one, leading to the existence of two basic near-neighbor chemical bonds A-X and B-X, with generally unequal bond lengths $R_{A-X} \neq R_{B-X}$. Second, the unit cell is tetragonally distorted with a distortion parameter $\eta \equiv c/2\alpha \neq 1$. Third, the anions are displaced from the ideal tetrahedral site by an amount u. The two near-neighbor bond distances are given by Eq.(2.1)

$$R_{AX} = \alpha[u^2 + (1+\eta^2)/16]^{1/2}$$
$$R_{BX} = \alpha[(u-1/2)^2 + (1+\eta^2)/16]^{1/2} \quad (2.1)$$

where α is the cubic lattice constant. The bond length mismatch is hence:

$$\mathrm{a} = R_{BX}^2 - R_{AX}^2 = (u-1/4)a^2 \quad (2.2)$$

and vanishes for a zinc-blende-like undistorted anion sublattice, where $u \equiv 1/4$.

Chalcopyrite	α (Å)	c(Å)	u	$\mathrm{a} = R_{BX}^2 - R_{AX}^2$
$CuInSe_2$	5.580	11.595	0.226	-0.747
$CuGaSe_2$	5.606	11.008	0.248	-0.063
$CuInS_2$	5.521	11.104	0.215	-1.067
$CuGaS_2$	5.351	10.465	0.263	0.372

Table 2.1 Chalcopyrite α and c lattice constants, anion displacement u, and bond length mismatch a.

As already mentioned, the crystal structure of an $A^{I}B^{III}X^{VI}_2$ semiconductor is closely related to that of the zinc blende binary analogs, but with non-ideal tetragonal

strain parameter $\eta \equiv c/2\alpha \neq 1$ and anion displacement parameter $u \neq$ ¼ reflecting the unequal cation-anion bond length. Remarkably, however, despite this close structural resemblance to zinc blende semiconductors, the observed optical band gaps of the $A^{I}B^{III}X^{VI}_2$ semiconductors are more than 50% smaller than their binary analogs[2.2]. This difference is known as **band-gap anomaly** ΔE_g [2.3], and it is the one that makes some of the ternary chalcopyrites (e.g. $CuInSe_2$) among the strongest known absorbers in the solar spectrum. The band-gap anomaly is produced both by a purely electronic factor: the repulsive *p-d* interactions in the valence band associated with the A-atom *d*-orbitals, and by a pure structural factor: the anion distortions, reflecting the classical atomic size mismatch in the A-X and B-X bonds.

2.1.2 Structural properties

The structural properties of chalcopyrite semiconductors have been studied by Raman scattering [2.4], [2.5], [2.6].

There is a four-to-one relationship between the Brillouin Zone (BZ) and the unrelaxed (n=1 and u=0.25) chalcopyrite structure compounds and the BZ of the corresponding ZB-structure materials, because of the two types of cations and the volume of the unit cell which is four times larger than that of ZB materials. Thus, points X(0,0,2π/α), W(2π/α,0,π/α), and W(0,2π/α,π/α) of the ZB-structure materials are folded to the central point Γ of the BZ of the chalcopyrite-structure compounds (Figure 2.2). For better understanding, they are often labeled by Γ[X] and Γ[W], and are distinguished from Γ[Γ], which is the Brillouin Zone Center for both materials.

The chalcopyrite-structure compounds have eight atoms per primitive unit cell. Therefore, 24 vibrational eigenmodes are expected: 6 zone-centered (Γ-like) modes, as in the cubic compounds, 6 Γ[X] and 12 Γ[W] modes:

$$1\Gamma_1 + 2\Gamma_2 + 3\Gamma_3 + 4\Gamma_4 + 7\Gamma_5 \qquad (2.3)$$

where all the Γ_5 modes are doubly degenerated [2.7]. These modes include three acoustic modes Γ_4+Γ_5 and 21 optic modes $1\Gamma_1 + 2\Gamma_2 + 3\Gamma_3 + 3\Gamma_4 + 6\Gamma_5$. Taking off two silent modes $2\Gamma_2$ and taking into account the splitting of doubly degenerated (longitudinal

optical (LO) and transversal optical (TO) modes due to the long-range electrostatic interaction) $3\Gamma_4+6\Gamma_5$ modes, chalcopyrite compounds have 22 Raman active modes:

$$\underbrace{1A_1}_{1\Gamma_1}+\underbrace{3B_1}_{3\Gamma_3}+\underbrace{6B_2}_{3\Gamma_4(LO)+3\Gamma_4(TO)}+\underbrace{12E}_{6\Gamma_5(LO)+6\Gamma_5(TO)} \tag{2.4}$$

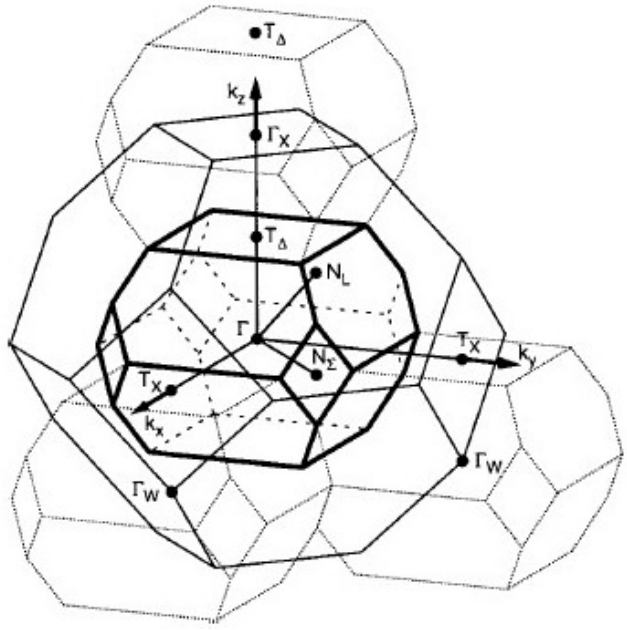

Figure 2.2 Brillouin Zone (BZ) of chalcopyrite and its relationship to that of the zinc blende (ZB) compound. The volume of the former is four times smaller than that of the latter. The doted polyhedra show the ZB reciprocal-space regions that fold into the chalcopyrite BZ. Symmetry points are labeled A_B, where A and B refer to the chalcopyrite ZB symmetries, respectively.

In Table 2.2 the vibrational frequencies of $CuInSe_2$, $CuGaSe_2$, $CuInS_2$, and $CuGaS_2$ are shown. In a Raman spectrum of $A^IB^{III}X^{VI}_2$ chalcopyrite compounds, the A_1 mode is the most intensive line generally observed. This mode results from the motion of the X^{VI} atom, with the A^I and B^{III} atoms remaining at rest [2.11]. This explains the fact,

that the selenides ($CuInSe_2$, $CuGaSe_2$) have similar vibrational frequencies (178cm^{-1} and 183cm^{-1}, respectively). The same behavior is observed for the sulfides too.

Modes		$CuInSe_2$	$CuGaSe_2$	$CuInS_2$	$CuGaS_2$
Γ_1	A_1	178	183	294	312
Γ_3	$^1B_1$	229	263	-	358
	$^2B_1$	179	165	-	202
	$^3B_1$	67	76	-	99
Γ_4 (TO)	$^1B_2$	217	252	323	368
	$^2B_2$	177	187	234	258
	$^3B_2$	70	98	79	95
Γ_4 (LO)	$^4B_2$	233	278	352	399
	$^5B_2$	200	-	266	278
	$^6B_2$	72	98	79	95
Γ_5 (TO)	^1E	217	-	321	364
	^2E	227	219	295	332
	^3E	211	170	244	258
	^4E	188	140	140	165
	^5E	78	-	88	116
	^6E	61	58	67	74
Γ_5 (LO)	^7E	233	273	339	387
	^8E	230	243	314	348
	^9E	216	187	260	271
	^{10}E	188	140	140	165
	^{11}E	78	-	88	116
	^{12}E	60	58	67	74
Ref.		[2.6]	[2.8]	[2.9]	[2.10]

Table 2.2 Vibrational frequencies (in cm^{-1}) of $CuInSe_2$, $CuGaSe_2$, $CuInS_2$, and $CuGaS_2$

2.1.3 Electronic properties

2.1.3.1 Band gap

The dielectric function of a semiconductor is closely linked to its electronic band structure [2.12]. The linear response of a nonmagnetic medium to transverse electromagnetic radiation ($\nabla \cdot D = 0, \nabla \cdot B = 0$) is completely described by the dielectric tensor ε or by the conductivity tensor $\sigma = -(i\omega/4\pi)(\varepsilon - 1)$, where ω is the angular frequency. These tensors depend, in general, on the frequency and the wave-vector of the radiation. The causal nature of the response to an electromagnetic field imposes a relationship between the real $\varepsilon_r(\omega)$ and the imaginary $\varepsilon_i(\omega)$ parts of ε: no response to an

applied field can appear before the field is applied. This relationship is, in the absence of magnetic fields:

$$\varepsilon_r(\omega)-1=\frac{2}{\pi}P\int_0^{\infty}\frac{\omega'\varepsilon_i(\omega)}{\omega'^2-\omega^2}d\omega' \tag{2.5}$$

and its inverse:

$$\varepsilon_i(\omega)=\frac{2\omega}{\pi}P\int_0^{\infty}\frac{\varepsilon_r(\omega)}{\omega^2-\omega'^2}d\omega' \tag{2.6}$$

where $P\int$ designates the Cauchy principal part of the integral. Eqs. (2.5) and (2.6) are called the *Kramers-Kronig relations*.

For isotropic and cubic materials, ε and σ reduce to scalars. The propagation of a plane electromagnetic wave is isotropic and is determined by the scalar complex refractive index:

$$n=n_r(\omega)+in_i(\omega)=\varepsilon(\omega)^{1/2} \tag{2.7}$$

The real and imaginary parts of n are related to those of ε by:

$$\begin{aligned}\varepsilon_r(\omega)&=n_r^2(\omega)-n_i^2(\omega)\\ \varepsilon_i(\omega)&=2n_r(\omega)n_i(\omega)\end{aligned} \tag{2.8}$$

where the real part of the refractive index $n_r(\omega)$ is the refractive index $n(\omega)$, while the imaginary part $n_i(\omega)$ is the extinction coefficient $k(\omega)$. Using these notations, Eqs. (2.8) give the $n(\omega)$ and $k(\omega)$ [2.13]:

$$n=\frac{\sqrt{\varepsilon_r+|\varepsilon|}}{\sqrt{2}},\quad k=\frac{\sqrt{-\varepsilon_r+|\varepsilon|}}{\sqrt{2}}. \tag{2.9}$$

The electric field E of a plane wave propagating along the x direction has the form:

$$\vec{E}(x,t)=\vec{E}_0e^{i[(n_c\omega/c_0)x-\omega t]}=\vec{E}_0e^{-(2\pi k/\lambda)x}e^{i(\kappa x-\omega t)} \tag{2.10}$$

The expression $2\pi k/\lambda$ describes the attenuation of the field. Since the absorption coefficient is usually defined by the attenuation in intensity written in the form of Lambert's law:

$$I(x)=\vec{E}\vec{E}^{*}=I_0e^{-\alpha x} \tag{2.11}$$

one obtains for the relationship between k and α:

$$\alpha = \frac{4\pi k}{\lambda} \tag{2.12}$$

where the α^{-1} is known as the optical penetration depth [2.14].

The features observed in $\varepsilon(\omega)$ in the optical range are related to the inter-band transitions originated by large or singular values of the joint valence and conduction density of states. These points of the band structure are also known as critical points. The behavior of the dielectric function near a critical point is given by Eq. (2.13)

$$\varepsilon(\omega) = C - Ae^{i\phi}(\omega - E + i\gamma)^n \tag{2.13}$$

where A is the amplitude, ϕ the phase angle, E the energy threshold, and γ the broadening. The exponent *n* takes the values -½ , 0, and ½ for one- (1D), two- (2D), and three-dimensional (3D) critical points, respectively. Discrete excitons (0D) are represented by n= -1. Conclusions about the bands can be drown by evaluating experimental $\langle \varepsilon(\omega) \rangle$ spectra using Eq. (2.13) to determine critical point parameters. Usually, fitting procedures are run on numerically calculated derivatives of $\langle \varepsilon(\omega) \rangle$. In particular, fitting of the second derivative of the dielectric functions $d^2 \langle \varepsilon \rangle / d\omega^2$ of the chalcopyrite compounds give the critical-point energies.

The structure of the fundamental absorption edge of chalcopyrites is well known [2.1], [2.15]. These crystals are semiconductors with a direct gap at the Brillouin Zone Center Γ. The three-fold valence-band maximum is composed of three nondegenerate states, giving rise to three transitions called E_a, E_b, and E_c from smaller to larger energies. Experimental measurements of these transition energies and of their selection rules allow us to determine the symmetry of the three valence states and to calculate the crystal-field Δ_{cf} and the spin-orbit Δ_{so} parameters, using the quasi-cubic model. The polarization selection rules can be understood in relationship to their well-known binary analogues, as described in [2.2] and depicted in Figure 2.3.

Starting from a threefold-degenerate Γ_{15} state in zinc blende, the introduction of a tetragonal crystal field gives rise to one Γ_4 plus a twofold-degenerate Γ_5 level. The possible dipolar interband transitions to the Γ_1 conduction-band minimum are $\Gamma_4 \rightarrow \Gamma_1$, allowed in $\vec{E} \parallel c$, and $\Gamma_5 \rightarrow \Gamma_1$ allowed in $\vec{E} \perp c$. Spin-orbit interaction further splits the

Γ_5 levels and the selection rules are somewhat relaxed, as given in Figure 2.3. Although only one of the transitions ($\Gamma_6 \rightarrow \Gamma_6$ in the double group) has a pure $\vec{E} \perp c$ polarization and the other two are mixed, it is approximately true that each transition keeps its original polarization, i.e. before introducing the spin-orbit interaction. Also, even if all three transitions result from two simultaneous interactions, in the present compounds, where $\Delta_{cf} < \Delta_{so}$, it is useful to make a simplification. In the simplified view, E_a and E_b can be regarded as a crystal-field-split gap, where each of these transitions has a different polarization as determined by the sign of Δ_{cf}. The most usual situation in chalcopyrite compounds is that $\Delta_{cf} < 0$ and then E_a is allowed in $\vec{E} \parallel c$ and E_b in $\vec{E} \perp c$. This is the case in CGS. However, in CIS $\Delta_{cf} > 0$ and the situation is reversed: E_a is allowed in $\vec{E} \perp c$ and E_b in $\vec{E} \parallel c$. In this simplified schema, the higher transition energy E_c corresponds to the spin-orbit-split gap.

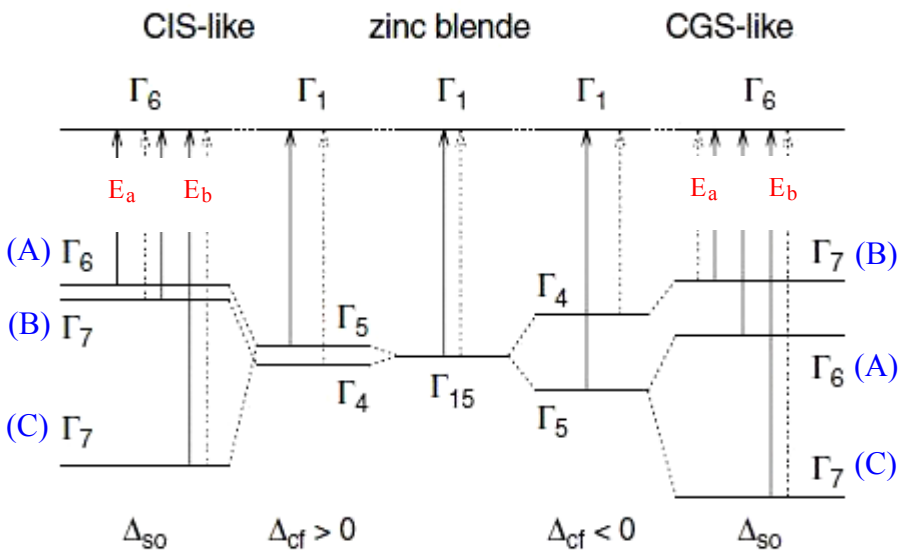

Figure 2.3 Schematic evolution of the energy states at the band gap of chalcopyrite, starting from a zinc blende-like gap without spin–orbit coupling. Solid (dashed) arrows represent transitions allowed by symmetry in $E \perp c$ ($E \,//\, c$) polarization, respectively. Note that the ordering of the topmost valence bands is different in CIS and CGS [2.2]

Within the so-called quasi-cubic model, the energies of the Γ_7 levels relative to the Γ_6 level in the valence band of the chalcopyrite crystal, are given in [2.1]:

$$E_{1,2} = \frac{1}{2}\left(\Delta_{so} + \Delta_{cf}\right) \pm \frac{1}{2}\left[\left(\Delta_{so} + \Delta_{cf}\right)^2 - \frac{8}{3}\Delta_{so} \cdot \Delta_{cf}\right]^{1/2} \tag{2.14}$$

where $E_{1,2}$ are the energies of the Γ_7 valence band relative to the Γ_6 conduction band in chalcopyrite, obtained using observations from the PR-spectra. The component E_1 is referred to the energy difference between B(Γ_7)-A(Γ_6) bands, and the component E_2 is referred to the energy difference C(Γ_7)-A(Γ_6), as shown in Figure 2.3. Consequently, for the CGS-like chalcopyrites $E_1 = E_a - E_b$, and $E_2 = E_c - E_b$, whereas, for the CIS-like chalcopyrites, $E_1 = E_b - E_a$, and $E_2 = E_c - E_a$.

The ratio of strengths of transitions from a given Γ_7 valence band to the Γ_6 conduction band for light polarized parallel and perpendicular to the optical axis, respectively, is given by Eq. (2.15):

$$\frac{I_{\parallel}}{I_{\perp}} = \left(2 + 3\frac{E}{\Delta_{so}}\right)^2 \tag{2.15}$$

Eq. (2.14) has been used to deduce the valence band parameters of many $A^{I}B^{III}X^{VI}_2$ crystals from electroreflectance measurements and the results are summarized in Table 2.3 *[2.1]*.

Chalcopyrite	Energy gaps (eV)			$-\Delta_{cf}$ (eV)		Δ_{so} (eV)		Estimated
	E_a	E_b	E_c	Theor.	Exp.	Theor.	Exp.	% d-like
$CuInSe_2$	1.04	1.04	1.27	0.04	-0.006	0.48	0.23	34
$CuGaSe_2$	1.68	1.75	1.96	0.03	0.090	0.44	0.23	36
$CuInS_2$	1.53	1.53	1.53	0.05	0.005	0.17	-0.02	45
$CuGaS_2$	2.43	2.55	2.55	0.12	0.120	0.13	0.00	35

Table 2.3 Valence band parameters of $A^{I}B^{III}X^{VI}_2$ crystals [2.1]

The corresponding wave functions of the three valence bands are given by:

$|A\rangle : S_+ \uparrow,$

$|B\rangle : a_B S_- \uparrow + a_C S_0 \downarrow,$

$|C\rangle : a_C S_- \uparrow + a_B S_0 \downarrow$

where $\uparrow$ and $\downarrow$ represent spin up and down, respectively, and S_+, S_-, and S_0 are functions defined by *p*-like basis functions. The admixture coefficients a_B and a_C can now be written [2.16]:

$$a_B = \left[1+\frac{1}{2}\left(2-\frac{3}{\Delta_{SO}}E_1\right)^2\right]^{-1/2} \tag{2.16}$$

$$a_C = \left[1+\frac{1}{2}\left(2-\frac{3}{\Delta_{SO}}E_2\right)^2\right]^{-1/2} \tag{2.17}$$

where $a_B^2 + a_C^2 = 1$.

The corresponding interband transition strengths between the p-like valence and the s-like conduction bands can be calculated from Eq.(2.18):

$$C_{0A\perp} : C_{0B\perp} : C_{0C\perp} : C_{0A\|} : C_{0B\|} : C_{0C\|} = 1 \ : \ a_B^2 \ : \ a_C^2 \ : \ 0 \ : \ 2a_C^2 : 2a_B^2 \tag{2.18}$$

The proposed [2.3] assignments and notations of the main optical transitions are given in the generic band structure displayed in Figure 2.4.

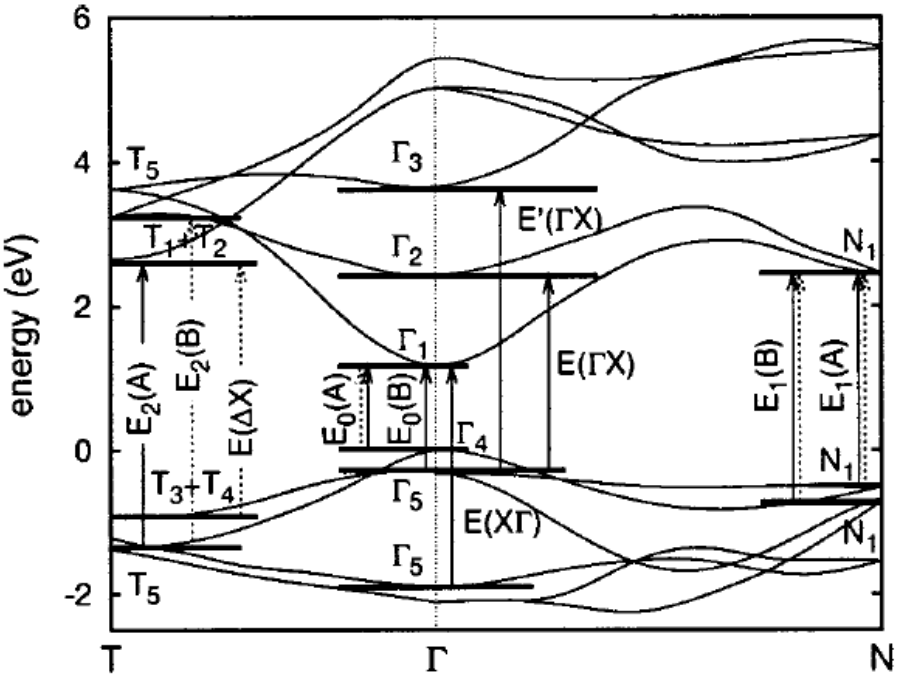

Figure 2.4 Proposed assignments and notations for the transitions observed in $CuB^{III}X^{VI}{}_2$ chalcopyrites in the optical range, depicted on the generic band structure. Dashed and solid arrows represent optical transitions allowed in $\vec{E} \| c$ and $\vec{E} \perp c$, respectively[2.3].

2.1.3.2 Temperature dependence of Semiconductor Band-gap

Semiconductors exhibit large shifts of the fundamental absorption edge with temperature. Part of these shifts is due to the thermal expansion and the concomitant changes in the band structure with volume, which usually accounts only for a fraction (¼ or ½) of the observed shift. The remaining temperature dependence of band-gap energies arises from the renormalization of the band energies by electron-phonon interactions. The electron-phonon interactions in turn are of two types: The first-order interaction considered in second-order (self-energy term) [2.17], and b) the quadratic interaction taken in the first-order (Debye-Waller term) [2.18].

In this thesis, the temperature dependence of the energy gap is studied using Varshni's empirical model, a thermodynamic model, the Einstein model, and the Pässler model, briefly summarized below:

A. Approximating the two basic features of experimental $E_g(T)$ curves, ***Varshni*** [2.19] observed an almost quadratic dependence at low temperatures and a linear dependence at high temperatures and suggested an empirical description of $E_g(T)$ dependence according to Eq.(2.19):

$$E_g(T) = E_g(0) - \frac{aT^2}{(T+\beta)} \tag{2.19}$$

where $E_g(0)$ represents the band-gap at zero temperature, $-\alpha$ the ($T \to \infty$) limit of $dE_g(T)/dT$, and β is a temperature parameter.

B. Using the Einstein representation of the total thermal energy of the solid, the temperature dependence of the energy band-gap can be expressed by the ***Einstein*** model [2.20]:

$$E_g(T) = E_g(0) - \frac{K}{e^{\Xi/T} - 1} \tag{2.20}$$

where K is a temperature-independent constant, and Ξ is the Einstein temperature.

C. The temperature dependence of the interband transitions can be described with an equation (Eq.(2.21)) containing the ***Bose-Einstein*** occupation factor for phonons [2.21]:

$$E_g(T) = E_B - a_B\left[1 + \frac{2}{e^{\Theta_B/T} - 1}\right] \tag{2.21}$$

Besides the changes of the band structure by thermal expansion of the lattice, the temperature dependence is mainly due to the electron-phonon interaction. The parameter Θ_B ($\Theta_B = h \cdot v / k_B$) describes an average frequency of both acoustic and optical phonons involved and corresponds to the Debye Temperature, α_B is the strength of the interaction, and (E_B-α_B) is the transition energy at 0K.

D. It is well known that both the thermal dilation of the lattice and the electron-phonon interaction will contribute to the temperature variation of the band gap energy. For many semiconductors the first component can usually be neglected due to its limited contribution. Hence, the electron-phonon coupling is dominant and can be described by a three-parameter ***thermodynamic model*** [2.22]:

$$E_g(T) = E_g(0) - S\langle\hbar\omega\rangle\left[\coth\left(\frac{\langle\hbar\omega\rangle}{2k_BT}\right) - 1\right] \tag{2.22}$$

where $E_g(0)$ represents the band-gap at zero temperature, $\langle\hbar\omega\rangle$ is an effective phonon energy, and S is a dimensionless constant related to the electron-phonon coupling.

E. ***Pässler*** proposed [2.23] an analytical description of Eg in dependence of T, within the regime of dominant electron-phonon interaction. According to his theory, the variation can be expressed by Eq.(2.23):

$$E_g(T) = E_g(0) - \delta\frac{\Theta}{2}\left\{\left[1 + \left(\frac{2T}{\Theta}\right)^p\right]^{1/p} - 1\right\} \tag{2.23}$$

where δ is equal to the high-temperature limit of the associated entropy, Θ is the effective phonon temperature, and the parameter $p=n+1$; the exponent n governs the shape of the spectral function.

F. ***Manoogian*** [2.24] proposed an empirical method for separating the energy band gab versus temperature curves of semiconductors into their constituent dilation and vibration parts:

$$E_g(T) = E_g(0) + UT^x + \frac{V}{e^{\Theta/T} - 1} \tag{2.24}$$

where U, V, x are fitting parameters and Θ is the effective temperature of phonons that interact with electrons.

Broadening parameter temperature dependence of the interband transitions is described by the Eq.(2.25) [2.25]:

$$\Gamma(T) = \Gamma(0) + \frac{\Gamma_{ep}}{e^{\Theta_{LO}/T} - 1} \tag{2.25}$$

Γ(0) represents the broadening due to the temperature independent mechanisms, such as impurities, dislocations, and surface scattering, and Γ_{ep} the strength of the exciton-LO-phonon coupling. Here, Θ_{LO} is the average frequency of the longitudinal optical phonons. It should be noted, that the optical phonons are the main contributors to the broadening of critical points.

2.1.3.3 Anomalous Temperature dependence of Semiconductor Band-gap

In most semiconductors, for temperature above 100K the energy band-gap decreases with the increase of temperature. The temperature dependence of the lowest band-gaps of some chalcopyrite compounds ($AgGaS_2$ [2.26], [2.27], [2.28], $AgGaSe_2$ [2.27], $CuInS_2$ [2.29], [2.30], and $CuInSe_2$ [2.31], [2.32]) show anomalies in the temperature region below 100K. In this region, the energy-gap slightly increases with the increase of the temperature.

Shay and Kasper [2.33] have attributed these effects to the contribution of the d-levels in the upper valence band. Jaffe and Zunger [2.34] have proposed a theory for the band-gap anomaly: this anomaly can be analyzed in terms of a chemical factor and a structural factor. The chemical contribution to the band-gap anomaly consists partly of a p-d hybridization effect and partly of a cation electronegativity effect. The structural contribution has a smaller contribution to the band-gap anomaly due to variations in the tetragonal symmetry. Similar to the chalcopyrite compounds, anomalies have been also observed for the cuprous halides [2.35].

2.2 ZnSe - Buffer layer

2.2.1 General

Most of the semiconductors of interest for device applications crystallize in diamond, zinc-blende (sphalerite), or wurzite structures. In the case of II-VI compounds, it is very common to obtain both the cubic (zinc blende) and hexagonal (wurzite) structures, depending on growth conditions. The zinc blende structure has two face centered cubic (fcc) sublattices, one of which is formed by cations and the other by anions. The dimensions of the unit cell are defined in terms of the lattice parameter a. The wurzite structure presents similar bonding to the zinc blende. The only difference is that the wurzite structure has a hexagonal closed pack lattice instead of the fcc.

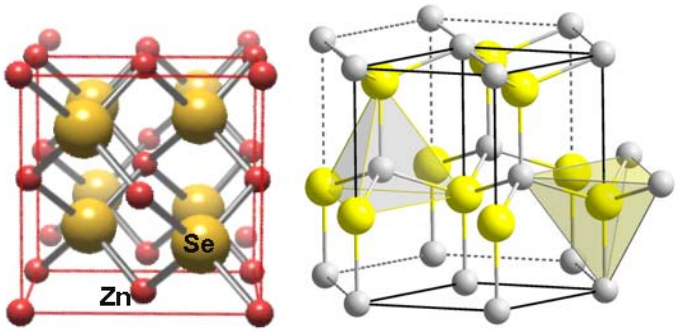

Figure 2.5 Cubic (left) and Hexagonal (right) ZnSe crystal structure

ZnSe semiconductor crystallizes in the zinc blende structure as shown in Figure 2.5. The unit cell vectors for the ZB structure are:

$$\begin{aligned} \mathrm{a} &= \left(0, \frac{1}{2}, \frac{1}{2}\right) a \\ \mathrm{b} &= \left(\frac{1}{2}, 0, \frac{1}{2}\right) a \\ \mathrm{c} &= \left(\frac{1}{2}, \frac{1}{2}, 0\right) a \end{aligned} \tag{2.26}$$

where α is the cubic lattice constant. There are two atoms per unit cell: Zn at $(0,0,0)a$ and Se at $\left(\frac{1}{4}, \frac{1}{4}, \frac{1}{4}\right)a$. The lattice constant for ZnSe is found [2.38] to be 5.618 Å.

2.2.2 Structural properties

The structural properties of the ZnSe semiconductor compound were studied by Raman scattering [2.39].

The calculated [2.39] dispersion curves along some important symmetry directions for ZnSe are shown in Figure 2.6. The symmetry points are Γ(0, 0, 0), X(π/α, 0, 0), K(3π/4α, 3π/4α, 0), L(π/2α, π/2α, π/2α), and W(π/α, π/2α, 0).

At the Γ(0, 0, 0) symmetry point, the lowest valence state at -13.36eV arises from the bonding Zn(*4s*)–Se (*4s*) singlet. The top of the valence band originates from the Zn(*4p,3d*)–Se(*4p*)-like orbitals possessing triply degenerate character in an anti-bonding manner. The bottom of the conduction band appearing at 1.04eV is comprised of the anti-bonding *4s* states of the Zn and Se atoms.

At the X(π/α, 0, 0) point, the valence states appear either from the Zn(*4s,3d*)–Se(*4p*)-like orbitals or from the Zn(*4p,3d*)–Se(*4p*)-like orbitals just below the valence-band edge. The semicore Se(*3d*) states appear much lower, around -47.06eV. Table 2.4 shows the phonon frequencies for ZnSe.

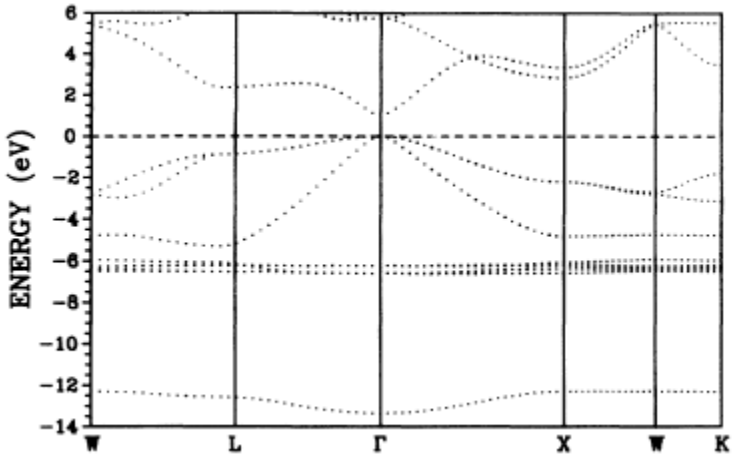

Figure 2.6 Dispersion curves for ZnSe [2.39]

	Vibrational Frequencies (cm^{-1})
Γ (TO)	224
X (TO)	203
X (TA)	79
X_1 (LA)	173
X_2 (LA)	158

Table 2.4 ZnSe phonon frequencies in cm^{-1}

f ZnSe [2.40] corresponds to direct transitions from the highest valence band to the lowest conduction band at the Γ point ($\Gamma_{15}^{v} \rightarrow \Gamma_{1}^{c}$). The spin orbit interaction splits the Γ_{15}^{v} valence band into Γ_{8}^{v} and Γ_{7}^{v} (splitting energy Δ_0) and the Γ_{15}^{c} conduction band into Γ_{8}^{c} and Γ_{7}^{c} (splitting energy $\Delta_0^{'}$). The corresponding optical transitions at or near $\vec{k} = 0$ are, respectively, labeled E_0 $\left[\Gamma_{8}^{v}(\Gamma_{15}^{v}) \rightarrow \Gamma_{6}^{c}(\Gamma_{1}^{c})\right]$, $E_0 + \Delta_0$ $\left[\Gamma_{7}^{v}(\Gamma_{15}^{v}) \rightarrow \Gamma_{6}^{c}(\Gamma_{1}^{c})\right]$, $E_0^{'}$ $\left[\Gamma_{8}^{v}(\Gamma_{15}^{v}) \rightarrow \Gamma_{7}^{c}(\Gamma_{15}^{c})\right]$, $E_0^{'} + \Delta_0$ $\left[\Gamma_{7}^{v}(\Gamma_{15}^{v}) \rightarrow \Gamma_{7}^{c}(\Gamma_{15}^{c})\right.$, dipole forbidden $\left.\right]$, $E_0^{'} + \Delta_0^{'}$ $\left[\Gamma_{8}^{v}(\Gamma_{15}^{v}) \rightarrow \Gamma_{8}^{c}(\Gamma_{15}^{c})\right]$, and $E_0^{'} + \Delta_0^{'} + \Delta_0$ $\left[\Gamma_{7}^{v}(\Gamma_{15}^{v}) \rightarrow \Gamma_{8}^{c}(\Gamma_{15}^{c})\right]$.

The spin-orbit interaction also splits the L_{3}^{v} valence band into $L_{4.5}^{v}$ and L_{6}^{v}, and the L_{3}^{c} conduction band into L_{6}^{c} and $L_{4.5}^{c}$. The corresponding transitions are, respectively, labeled E_1 $\left[L_{4.5}^{v}(L_{3}^{v}) \rightarrow L_{6}^{c}(L_{1}^{c})\right]$, $E_1 + \Delta_1$ $\left[L_{6}^{v}(L_{3}^{v}) \rightarrow L_{6}^{c}(L_{1}^{c})\right]$, $E_1^{'}$ $\left[L_{4.5}^{v}(L_{3}^{v}) \rightarrow L_{6}^{c}(L_{3}^{c})\right]$, and $E_1^{'} + \Delta_1^{'}$ $\left[L_{4.5}^{v}(L_{3}^{v}) \rightarrow L_{4.5}^{c}(L_{3}^{c})\right]$ [2.41].

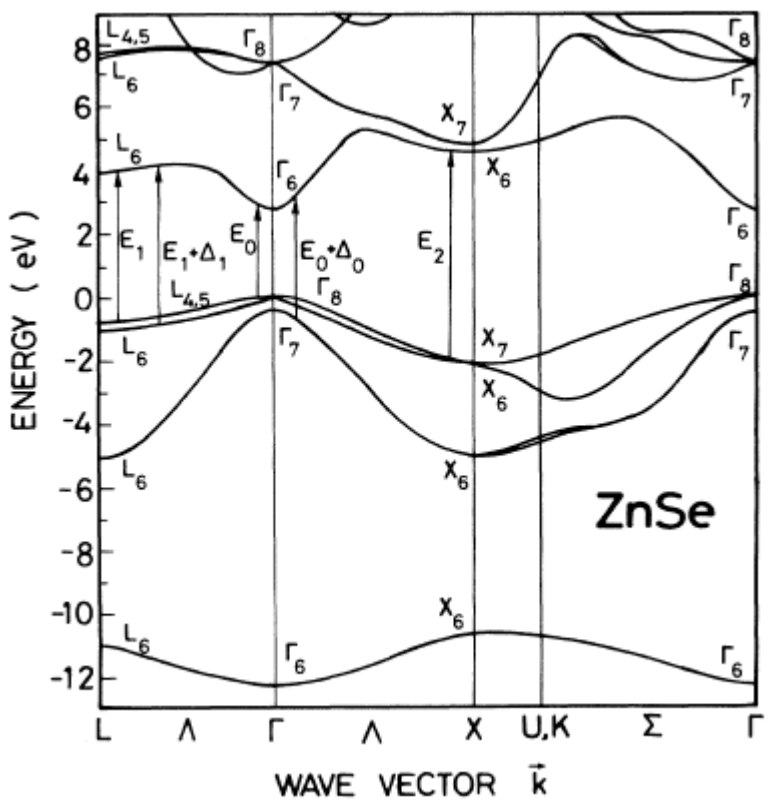

Figure 2.7 Electronic energy band structure of ZnSe [2.42]

The E_2 transitions are expected to take place along the [110] (Σ) or near X, and occur in ZnSe for energies between the $E_1\ (E_1+\Delta_1)$ and the $E_1'\ (E_1'+\Delta_1')$ critical points. At higher energies one expects structure in the optical spectrum due to excitation from the atomic *d*-levels into the conduction bands.

2.3 ZnO - Window layer

Recently, zinc oxide (ZnO) has attracted much attention within the scientific community as a 'future material'. The renewed interest in this material has arisen out of the development of growth technologies for the fabrication of high quality single crystals and epitaxial layers allowing for the realization of ZnO-based electronic and optoelectronic devices.

With a wide bandgap of 3.4 eV and a large exciton binding energy of 60 meV at room temperature, ZnO is important for blue and ultra-violet optical devices. Other

favorable aspects of ZnO include its broad chemistry leading to many opportunities for wet chemical etching, low power threshold for optical pumping, radiation hardness and biocompatibility. Together, these properties of ZnO make it an ideal candidate for a variety of devices

2.3.1 General

At ambient pressure and temperature, ZnO crystallizes in the wurtzite (B4 type) structure. This is a hexagonal lattice, belonging to the space group P63mc, and is characterized by two interconnecting sublattices of Zn^{2+} and O^{2-}, such that each Zn ion is surrounded by tetrahedra of O ions, and vice-versa (Figure 2.8).

This tetrahedral coordination gives rise to polar symmetry along the hexagonal axis. This polarity is responsible for a number of the properties of ZnO, including its piezoelectricity and spontaneous polarization, and is also a key factor in crystal growth, etching and defect generation. The four most common face terminations of wurtzite ZnO are the polar Zn terminated (001) and O terminated $(00\bar{1})$ faces (c-axis oriented), and the non-polar $(11\bar{2})$ (a-axis) and $(10\bar{1})$ faces which both contain an equal number of Zn and O atoms. The polar faces are known to posses different chemical and physical properties, and the O-terminated face possess a slightly different electronic structure to the other three faces.

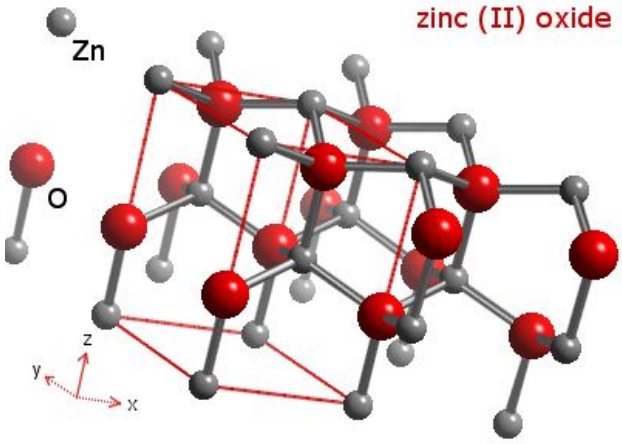

Figure 2.8 The hexagonal wurzite structure of ZnO. O atoms are shown as large red spheres, Zn atoms as smaller grey spheres. One unit cell is outlined for clarity.

Aside from causing the inherent polarity in the ZnO crystal, the tetrahedral coordination of this compound is also a common indicator of sp^3 covalent bonding. However, the Zn–O bond also possesses very strong ionic character, and thus ZnO lies on the borderline between being classed as a covalent and ionic compound, with an ionicity of f_i =0.616 on the Phillips ionicity scale [2.43]. The lattice parameters of the hexagonal unit cell are a=3.2495Å and c=5.2069 Å, and the density is 5.605 g cm^{-3} [2.44].

In an ideal wurtzite crystal, the axial ratio c/a and the u parameter (which is a measure of the amount by which each atom is displaced with respect to the next along the c-axis) are correlated by the relationship uc/a=(3/8)1/2, where c/a=(8/3)1/2 and u=3/8 for an ideal crystal. ZnO crystals deviate from this ideal arrangement by changing both of these values. This deviation occurs such that the tetrahedral distances are kept roughly constant in the lattice. Additional to the wurzite phase, ZnO is also known to crystallize in the cubic zincblende and rocksalt (NaCl) structures.

2.3.2 Structural properties

In single crystal wurtzite ZnO, there are 4 atoms per unit cell, giving rise to 12 phonon modes. These modes are important for understanding the thermal, electrical and optical properties of the crystal, and are as follows: one longitudinal acoustic (LA), two transverse-acoustic (TA), three longitudinal-optical (LO) and six transverse-optical (TO) branches.

The A_1 and E_1 branches are Raman and infrared active, while the two E_2 branches (non-polar) are only Raman active. The E_2^{low} mode is associated with the vibrations of the Zn sub-lattice, whilst the E_2^{high} mode is associated with the oxygen atoms only. The B_1 branches are always inactive. The phonon modes of ZnO have been extensively studied and modeled [2.45]. Table 2.5 gives a list of the experimental values for the most common phonon modes visible at 300 K [2.46].

Phonon mode	Value (cm^{-1})
E_2^{low}	101
E_2^{high}	437
TO (A_1)	380
LO (A_1)	574
TO (E_1)	591

Table 2.5 Principal phonon modes of wurzite ZnO at 300 K

2.3.3 Electronic properties

The electronic band structure of ZnO has been extensively investigated. The results of a band structure calculation using the Local Density Approximation (LDA) and incorporating atomic self-interaction corrected pseudopotentials (SIC-PP) to accurately account for the Zn 3d electrons is shown in Figure 2.9 [2.47].

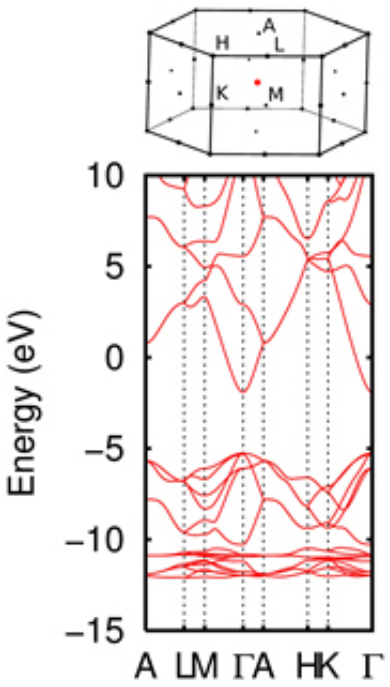

Figure 2.9 The band structure of bulk wurzite ZnO calculated using dominant atomic self-interaction-corrected pseudopotentials.

The band structure is shown along high symmetry lines in the hexagonal Brillouin zone. Both the valence band maxima and the lowest conduction band minima occur at the point k=0 indicating that ZnO is a direct band gap semiconductor. The bottom 10 bands (occurring around −9 eV) correspond to Zn 3d levels. The next 6 bands from −5 eV to 0 eV correspond to O 2p bonding states. The first two conduction band states are strongly Zn localized and correspond to empty Zn 3s levels. The band gap as determined from this calculation is 3.44 eV.

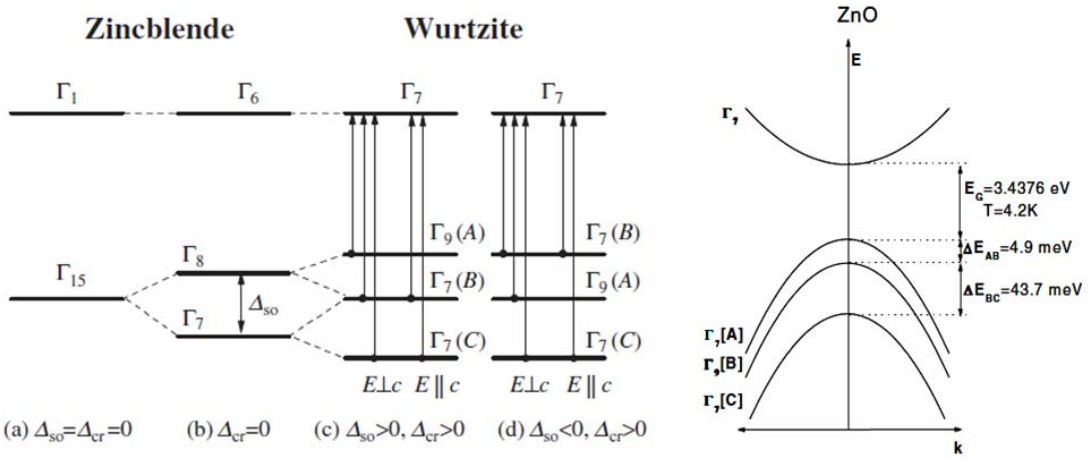

Figure 2.10 Valence band splitting in the zinc blende and wurzite structures due to the interaction of the spin-orbit (Δ_{SO}) and the crystal field (Δ_{CF}). (b) splitting due to the spin-orbit interaction, and (c), (d) splitting found in the wurzite crystals under the combined interaction of spin-orbit and crystal-field effects for $\Delta_{SO}>0$ and $\Delta_{SO}<0$, respectively. Note that the E_A transitions are dipole forbidden for $E \| c$ *[2.48]. Right: Band Structure and symmetries of hexagonal ZnO[2.49]*

As shown schematically in Figure 2.10, the valence band maxima of materials with wurzite structure can be obtained from that of materials with zinc blende structure due to the action of a small hexagonal crystal field [2.50]. The combined effect of spin-orbit (Δ_{SO}) and hexagonal crystal-field perturbations (Δ_{CF}), in the wurzite lattice, splits the Γ_{15} valence band into Γ_9(A), Γ_7(B), and Γ_7(C) valence bands. The hexagonal wurzite ZnO crystal thus, exhibits three excitonic states E_{0A}(ex), E_{0B}(ex), and E_{0C}(ex), at the fundamental band edge E_0. The optical-transition selection rules suggest that the structures of Γ_7 symmetry (E_{0B} and E_{0C}) can be observed for both $E \perp c$ and $E \| c$,

while that of Γ_9 symmetry (E_{0A}) can only be observed for $E \| c$. This is known as the "quasi- cubic" model [2.51], [2.52]. Transition energies of ZnO are shown in Table 2.6.

Table 2.6 ZnO Transition energies [2.49]

Transition Energies (eV)	
Ea	3.437
Eb	3.443
Ec	3.481

3. Chalcopyrite Heterostructures

As already mentioned, high efficiencies have been reached for chalcopyrite heterojunction solar cells [3.1], [3.2]. A significant part of photogeneration in a homojunction solar cell takes place close to the surface of the emitter. Avoiding current losses, therefore, requires a careful design of the emitter properties. In a heterojunction solar cell, the generation maximum is shifted to the pn-junction, where the electrical field is at its maximum and contributes to the collection of the photogenerated carriers. Due to the high band gap window, only a few carriers are generated close to the surface, and the influence of surface recombination can thus be neglected. In contrast to the homojunction, the heterojunction may exhibit a high density of states at the interface. Nevertheless, highly efficient chalcopyrite-based solar cells are dominated by bulk, rather than interface recombination.

3.1 Band Alignment

The bucking current due to recombination at the interface has to be minimized to achieve high open circuit voltages. The recombination rate R within the field zone of the diode is approximated by

$$R = \frac{np}{\tau(n+p)} \tag{3.1}$$

where n and p denote the concentrations of electrons and holes, respectively, and where τ is the carrier lifetime.

The current losses at the interface can be neglected if the doping is such, that the interface is inverted. For a chalcopyrite based solar cell with a p-type absorber, this means that the Fermi-level (E_F) at the interface should be close to the conduction band. In this case, the minority carriers collected from the bulk are majority carriers at the interface and are not subject to significant recombination. In consequence, the performance of a carefully designed heterojunction solar cell is almost independent from the interface recombination.

The situation changes if the conduction bands are not aligned at the interface. A small ***spike*** ($\Delta E_C>0$) can be beneficial, because it tends to increase the inversion. On the other hand, a ***cliff*** ($\Delta E_C<0$) is undesirable because it reduces the inversion and it also opens a recombination path with decrease barrier E_b (Figure 3.1).

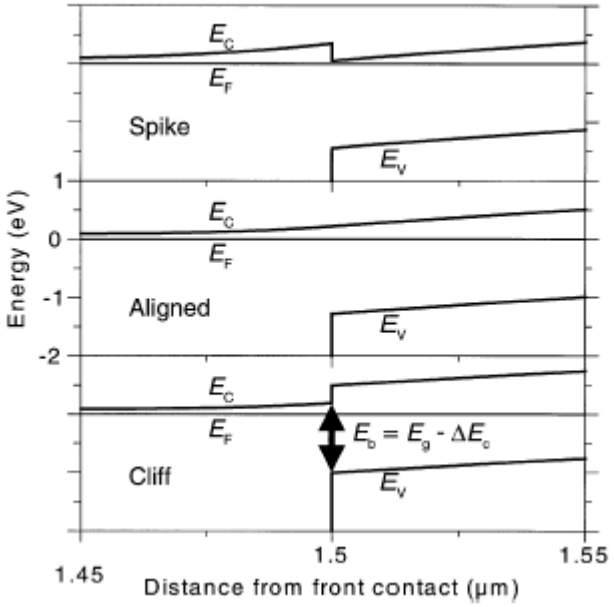

Figure 3.1 Band diagrams in the vicinity of the interface

The best efficiency solar cells are realized as heterojunctions, containing a CIGS absorber, a 50nm-thick CdS buffer layer and a ZnO window layer. However, with the increase of the Ga content, lower solar cell efficiencies have been observed [3.3]. This fact is attributed to the CdS buffer layer. The increase of the energy band gap changes the band alignment in the vicinity of the interface absorber/CdS. As shown in Figure 3.2, in the case of $CuInSe_2$/CdS, the band offset is positive ($\Delta E_C>0$, *spike*), whereas, with the increase of the Ga content, the band offset increases. In the case of $CuGaSe_2$/CdS, the band offset becomes negative ($\Delta E_C<0$, *cliff*).

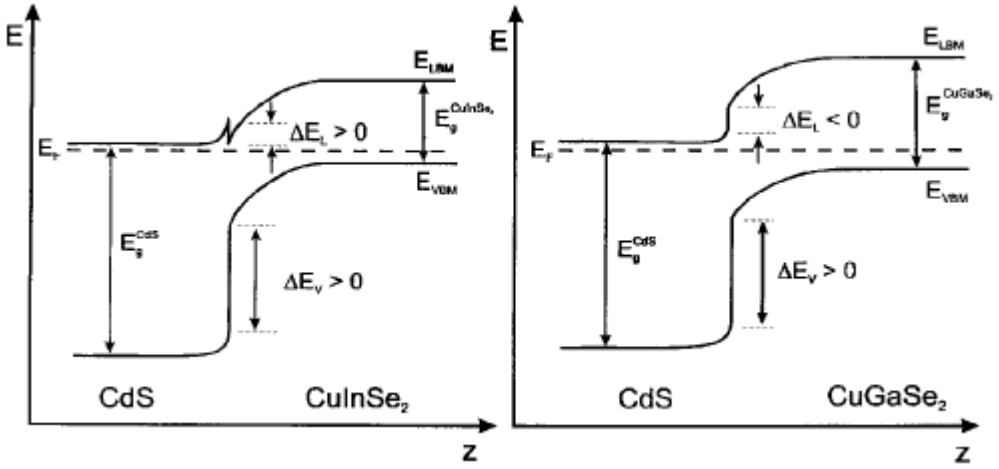

Figure 3.2 $CuInSe_2$/CdS (left) and the $CuGaSe_2$/CdS (right) band diagrams in the vicinity of the interface

To avoid such a behavior, the buffer layer should have small band offset and/or higher band gap. ZnSe fulfills the above conditions and, for this reason, is an ideal buffer layer for high efficiency solar cells (Figure 3.3).

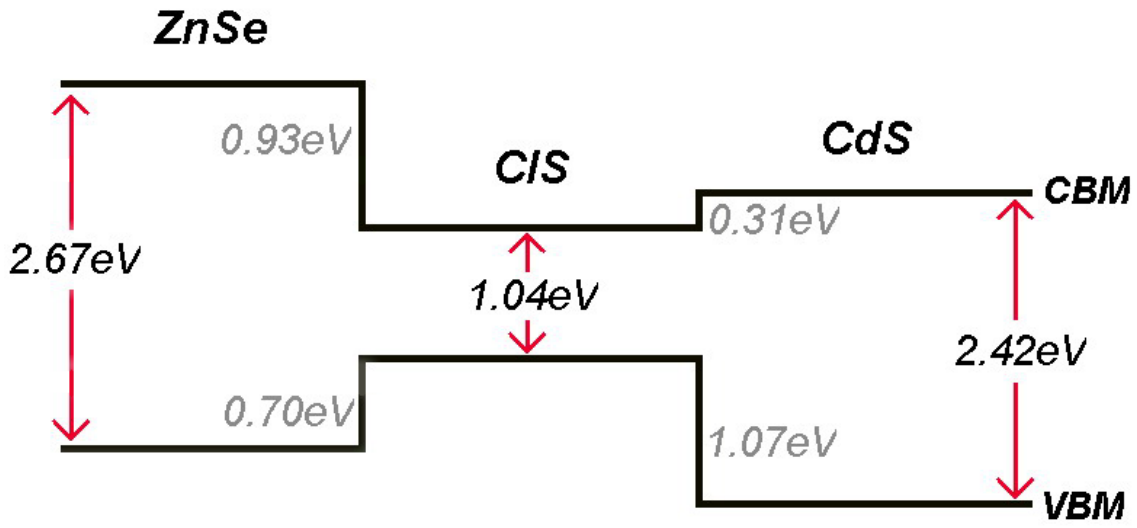

Figure 3.3 Schematic of the calculated band lineup of the ZnSe/$CuInSe_2$ and CdS/$CuInSe_2$ heterojunctions [3.4]

The band bending in the substrate induced by the formation of the ZnSe layer is given by the shift in the substrate core level positions during the first deposition steps. The valence band bends downwards from the Fermi level, while the magnitude strongly

depends on the position of the Fermi level in the band gap, and therefore on the doping of the substrate (Figure 2.11).

For the near-stoichiometric substrates, the band bending is (0.4 ± 0.1)eV for the (112) surface of $CuInSe_2$. The valence band offset at the $CuInSe_2$/ZnSe interface is given by the difference of the corresponding valence band maxima, corrected by the band bending in the substrate. When the ZnO forms, a band bending in the ZnSe layer is not observed, which is also unlikely due to its thinness. The binding energy shift in the Zn core levels is at least partially due to a chemical shift from ZnSe to ZnO and cannot be used to determine the band bending in ZnO. The total valence band offset across the heterojunction amounts to (2.15 ± 0.2)eV in (112) surface [3.5].

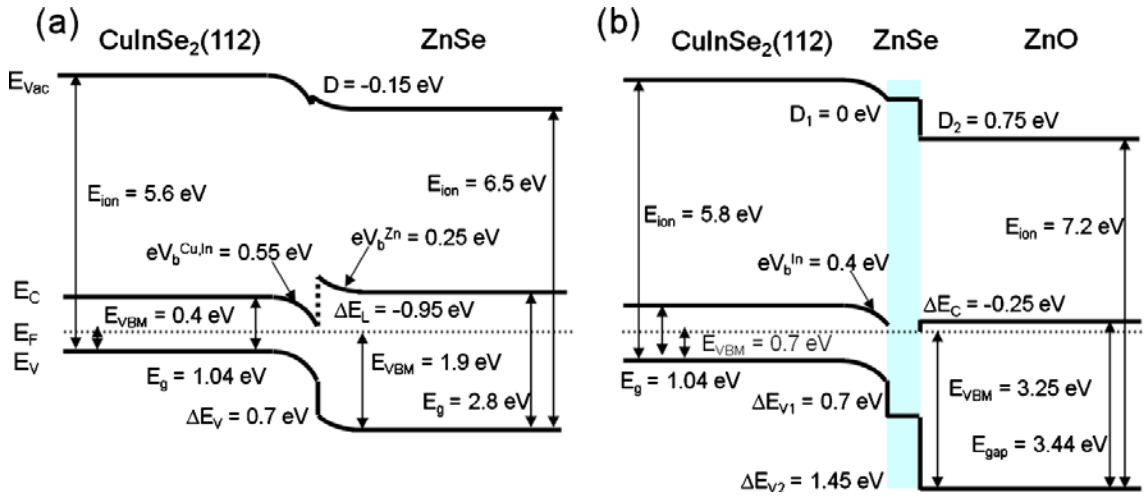

Figure 2.11 Band alignment illustrations for (a) a $CuInSe_2$(112)/ZnSe heterojunction and (b) a $CuInSe_2$(112)/ZnSe/ZnO heterojunction [3.5]

3.2 Mismatch strain and thermal strain

3.2.1 Mismatch strain

In a heterostructure system, the lattice matching conditions should be satisfied in order to obtain good quality heterostructures. The lattice mismatch introduces undesirable lattice defects, such as misfit dislocations and internal strains in the epilayers [3.6].

With respect to the misfit parameter f_m, which represents the lattice mismatch between the substrate and the epilayer, the mismatch strain ε is defined as:

$$\varepsilon = f_m = \frac{\Delta a}{a_{epi}} = \frac{a_{sub} - a_{epi}}{a_{epi}} \tag{3.2}$$

where a_{sub} and a_{epi} are the lattice constants of the substrate and the epilayer, respectively.

According to Hooke's law, the strain ε is related to the stress σ [3.7] by:

$$\sigma_i = C_{ij}\varepsilon_j \tag{3.3}$$

where the constants C_{ij} represent the elastic stiffness of the material.

Mismatch strain is usually generated by a planar stress defined [3.8] as:

$$\begin{aligned} &\sigma_{xx} = \sigma_{yy} = \sigma, \quad \sigma_{zz} = 0 \\ &\sigma_{xy} = \sigma_{yz} = \sigma_{zx} = 0 \end{aligned} \tag{3.4}$$

For materials of cubic symmetry, the strain tensor ε due to an in-plane biaxial stress with two equal components (a so called bisotropic stress, $\sigma_{xx}=\sigma_{yy}=\sigma$) has the following elements:

$$\begin{aligned} &\varepsilon_{xx} = \varepsilon_{yy} = \varepsilon, \\ &\varepsilon_{zz} = -\frac{2C_{12}}{C_{11}}\varepsilon_{xx} = -\frac{2C_{12}}{C_{11}}\varepsilon \end{aligned} \tag{3.5}$$

In this case, the strain ε and the stress σ are related to one another as follows:

$$\sigma_{xx} = \left[C_{11} + C_{12} - \frac{2C_{12}^2}{C_{11}} \right] \varepsilon \tag{3.6}$$

3.2.2 Strain/Stress Analysis by X-ray Diffraction

Once the lattice spacing d is obtained, according to Braggs' law ($d = n\lambda / 2\sin\theta$), from the position of the diffraction peak θ for a given reflection *hkl*, the strain along z may be obtained from the formula [3.10]:

$$\varepsilon_{zz} = \frac{d - d_0}{d_0} \tag{3.7}$$

where d_0 is the unstressed lattice spacing.

Uniform stress σ results in uniform lattice strain ε, which causes angular peak displacement, while non-uniform stress distorts peak shape as well. If the stress tensor existing in the irradiated layers is biaxial:

$$\begin{pmatrix} \sigma_{xx} & 0 & 0 \\ 0 & \sigma_{yy} & 0 \\ 0 & 0 & 0 \end{pmatrix}$$

then a simplified x-ray residual stress equation can be derived:

$$\frac{d - d_0}{d_0} = \frac{1+\nu}{E}\left(\sigma_{xx}\cos^2\varphi + \sigma_{yy}\sin^2\varphi\right)\sin^2\psi - \frac{\nu}{E}\left(\sigma_{xx} + \sigma_{yy}\right) \tag{3.8}$$

where E and ν are the Young's modulus and Poisson's ratio, respectively, φ is the angle of a given direction of incidence relative to the surface of the specimen and ψ the angle between the normal to the surface and the normal to the *hkl* planes.

For a bisotropic stress ($\sigma = \sigma_{xx} = \sigma_{yy}$), Eq. (3.8) yields:

$$\frac{d - d_0}{d_0} = \frac{1+\nu}{E}\sin^2\psi - \frac{\nu}{E}2\sigma \tag{3.9}$$

If the epilayer is known to be coherent and is grown on a surface that is parallel to the symmetry plane (usually (001)), as in case of the epitaxial on GaAs(001) grown chalcopyrite layers [3.11] studied in this work, then ψ=0 and Eq.(3.9) is rewritten as:

$$\frac{d - d_0}{d_0} = -\frac{\nu}{E}2\sigma \tag{3.10}$$

For materials of cubic symmetry, Young's modulus and Poisson's ratio are expressed in terms of the elastic stiffness components C_{ij} as follows:

$$E = \frac{\left(C_{11} + 2C_{12}\right)\left(C_{11} - C_{12}\right)}{C_{11} + C_{12}} \tag{3.11}$$

$$\nu = \frac{C_{12}}{C_{11} + C_{12}} \tag{3.12}$$

Inserting Eqs. (3.11) and (3.12) into (3.10), the latter becomes:

$$\sigma = \frac{1}{2}\left(2C_{12} - C_{11} - \frac{C_{11}^2}{C_{12}} \right)\varepsilon_{zz} \tag{3.13}$$

3.2.3 Strain/Stress Analysis by Photoreflectance Spectroscopy

In the ternary chalcopyrites [3.9], the upper valence band is split into three sub-bands labeled E_a, E_b and E_c due to the combined effects of the non-cubic crystal-field and the spin-orbit interaction. Stresses induce additional shifts of the three split valence bands resulting in significant changes of the energy band structure.

The crystallographic orientation of chalcopyrite heteroepitaxial layers is strongly depended on substrate type. Ternary chalcopyrites on GaAs(001) substrates are grown highly orientated with their c-axis normal-to-the-plane of growth [3.11]. Under the application of a bisotropic stress parallel to the [100] and [010] crystallographic directions, the calculated energy-shift of the two upper-most valence bands at k=0, designated ΔE_a and ΔE_b, is given, in the quasi-cubic approximation, by [3.12], [3.13]:

$$\begin{aligned}
\Delta \mathrm{E_a} &= \left[-2\alpha \left(\frac{\mathrm{C_{11} - C_{12}}}{\mathrm{C_{11}}} \right) + \mathrm{b} \left(\frac{\mathrm{C_{11} + 2C_{12}}}{\mathrm{C_{11}}} \right) \right] \varepsilon_{zz} \\
\Delta \mathrm{E_b} &= \left[-2\alpha \left(\frac{\mathrm{C_{11} - C_{12}}}{\mathrm{C_{11}}} \right) - \mathrm{b} \left(\frac{\mathrm{C_{11} + 2C_{12}}}{\mathrm{C_{11}}} \right) \right] \varepsilon_{zz}
\end{aligned} \tag{3.14}$$

where, in case of the strain-free and strained epilayers,

$$\begin{aligned}
\Delta \mathrm{E_a} &= \mathrm{E_a^{bulk}} - \mathrm{E_a^{strained\ layer}} \\
\Delta \mathrm{E_b} &= \mathrm{E_b^{bulk}} - \mathrm{E_b^{strained\ layer}}
\end{aligned} \tag{3.15}$$

$\mathrm{E_a^{bulk}}$ and $\mathrm{E_b^{bulk}}$ represent the transition energies of the strain-free lattice, $E_a^{strained\ layer}$ and $E_b^{strained\ layer}$ are the band energies of the strained layer. ε_{zz} is the normal-to-the-plane component of elastic strain. C_{11}, C_{12} are the elastic stiffness constants and α, b are the hydrostatic and shear deformation potentials of the chalcopyrite, respectively.

Combining Eqs.(3.14) and (3.15), the strain normal-to-the-plane of growth is calculated from the energy shift of the strained compared to the strain-free chalcopyrite, using both, E_a and E_b transition energies, according to:

$$\Delta E_{split} = \Delta E_b - \Delta E_a = (E_b^{bulk} - E_a^{bulk}) - (E_b^{strained\ layer} - E_a^{strained\ layer}) =$$
$$= -2b\left(\frac{C_{11}+2C_{12}}{C_{11}}\right)\varepsilon_{zz} \qquad (3.16)$$

Taking into account the relationship between ε_{zz} and $\varepsilon_{xx}=\varepsilon_{yy}$ in Eq.(3.5), Eq.(3.16) is equivalent to Eq. (3.13), previously derived.

3.2.4 Thermal strain

With the temperature varying, the misfit parameter includes changes of the lattice constants induced by thermal effects. Two different models have been used for the temperature change of the epilayer and the substrate lattice constants [3.14]:

1st model

This model assumes pseudomorphic growth, in which the epilayer has lattice constant a, equal to that of the substrate. In this case, the thermal expansion coefficient of the lattice constants of both the epilayer and the substrate can be given by:

$$a_T = a_{RT}(1+\alpha_a \cdot \Delta T) \qquad (3.17)$$

Where a_{RT} is the lattice constant at room temperature (RT), α_a is the linear expansion coefficient of the material, and ΔT is the difference between the temperature of the measurement and RT.

2nd model

This model assumes the development of thermal stresses after growth; strain is fully relaxed at the growth temperature and the epilayer is elastically strained during cooling due to mismatch in the thermal expansion coefficients between the epilayer and the substrate. In this case, changes in the lattice constant of the epilayer at RT are given by:

$$\Delta a_{epi} = a_{epi}^{RT}\left(\frac{1-\alpha_{epi}^{a}\Delta T}{1+\alpha_{sub}\Delta T}-1\right) \qquad (3.18)$$

where a_{epi}^{RT} is the lattice constant of the epilayer at RT, α^{a}_{epi} is the thermal expansion coefficient of the epilayer, α_{sub} is the thermal expansion coefficient of the substrate, and ΔT is the difference between the growth temperature and the RT.

4. Growth techniques

The ternary $CuInS_2$, $CuInSe_2$, $CuGaS_2$, and $CuGaSe_2$ bulk (single-crystal) chalcopyrites studied in this thesis were provided by Priv. Doz. Dr. Udo Pohl at the Technical University of Berlin. The ternary $CuInS_2$, $CuInSe_2$, $CuGaS_2$, and $CuGaSe_2$ and quaternary $CuIn_{1-x}Ga_xSe_2$ epitaxial chalcopyrite layers were provided by Prof. Dr. M.-Ch. Lux-Steiner and her work-group at the Helmholtz-Centre Berlin for Materials and Energy (HZB). The ZnSe films were deposited on glass and chalcopyrite substrates using e-beam Evaporation (EBE) and Chemical Bath Deposition (CBD) techniques of the laboratory for Material Growth and Optical Characterization of Assist Prof. Dr. D. Papadimitriou at the National Technical University (NTUA) of Athens. Au/Al contacts and In:ZnO/i-ZnO layers were deposited by Pulsed Laser Deposition (PLD) in the laboratory of Dr. M. Kompitsas at the National Hellenic Research Foundation (NHRF). Antireflective Coatings (ARCs) of ZnO nanorods were provided by Prof. Dr. M.-Ch. Lux-Steiner and her work-group at the Helmholtz-Centre Berlin for Materials and Energy (HZB).

4.1 Ternary Single Crystal Chalcopyrites grown by CVT

The ternary $CuInS_2$, $CuInSe_2$, $CuGaS_2$, and $CuGaSe_2$ bulk (single-crystal) chalcopyrites were grown by ***Chemical Vapor Transport (CVT)*** with iodine [4.1]. Crystals were grown from presynthesized chalcopyrite source material that was solidified from stoichiometric melt. Source material and crystallized iodine were placed in one end of a cleaned quartz ampoule. The end was immersed in liquid nitrogen as the ampoule was evacuated and fused for sealing. The sealed ampoule was placed in a furnace and was subjected to a time temperature program. The growth zone was kept hotter than the source zone during heat-up. Afterwards, the temperatures were reversed to initiate growth.

4.2 Ternary Epitaxial Chalcopyrites grown on GaAs by MOVPE

The ternary $CuInS_2$, $CuInSe_2$, and $CuGaSe_2$ epitaxial layers were grown on GaAs (001) substrates by ***Metal-Organic Vapor Phase Epitaxy (MOVPE)*** in a horizontal quartz reactor (AIX 200 SC), see Figure 4.1 [4.2] - [4.4]. The precursors were *CpCuCNtB* ($C_5H_5CuCNC(CH_3)_3$), *TEGa* ($Ga(C_2H_5)_3$), and *DTBSe* ($(((CH_3)_3C)_2Se$), which were transferred into the reactor chamber by the hydrogen carrier gas. These molecules decompose at 570°C substrate temperature and 50 *mbar* reactor pressure. The metals (Cu, Ga/In) and Se/S are deposited on the substrate and contribute to the chalcopyrite film growth, while the rest organics are removed by an exhaust cleaner.

MOVPE offers the possibility of highly controlled composition variation by changing the input molar flow ratio of the precursors. Aiming to a controlled variation of the chemical composition of the epilayers, two different approaches were chosen: a) In a series of MOVPE experiments the input molar flow ratio CpCuCNtB/TEGa (p_I /p_{III}-ratio) was varied at an excess of DTBSe(p_{VI}), while the $p_{VI}/(p_I+p_{III})$-ratio was kept constant [4.5]. These growth experiments were performed with the substrate rotating. b) Without the substrate rotation and at fixed p_I /p_{III} and p_{VI} /(p_I+p_{III}) ratio, a gradient composition sample was obtained in one single run due to the depletion of the Cu precursor in the gas phase.

By the heteroepitaxial growth on GaAs-(001), the chalcopyrite $CuGaSe_2$-layers are grown highly oriented with their *c*-axis in the direction of the surface-normal of the GaAs-substrate [4.2].

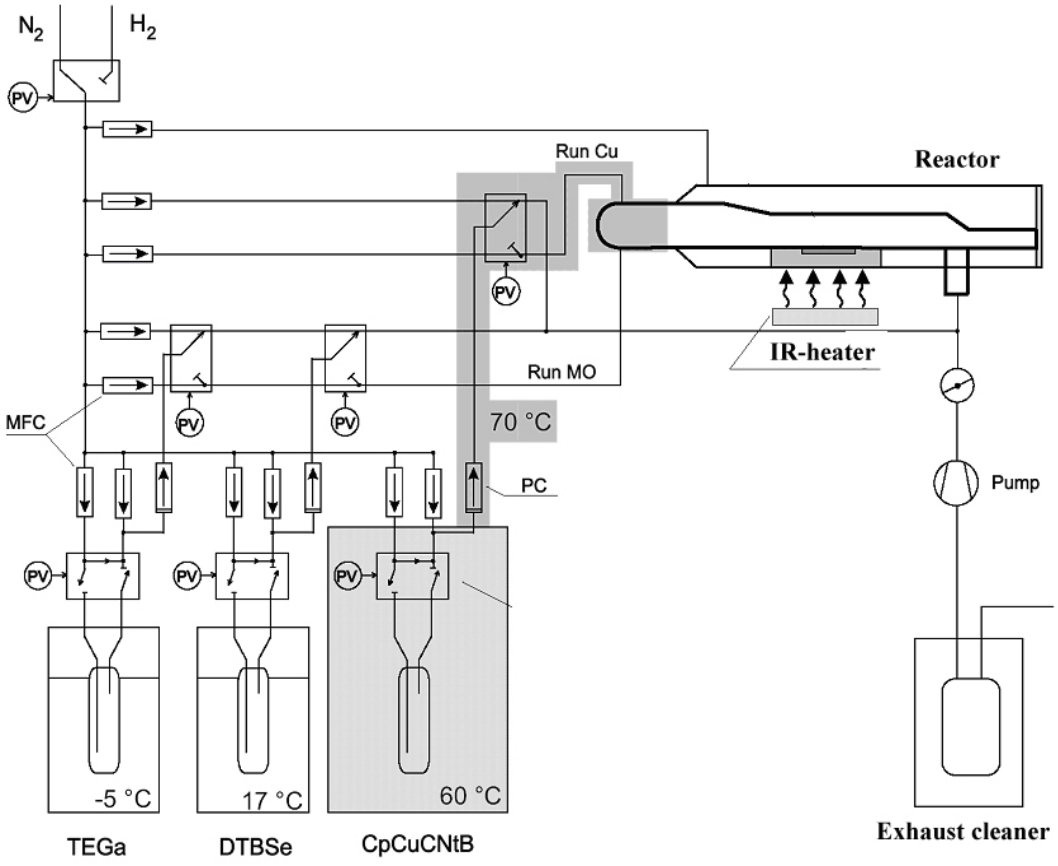

Figure 4.1 The MOVPE set-up for ternary epitaxial layer growth[4.2], [4.3].

4.3 Ternary Polycrystalline Chalcopyrites grown on Mo/glass by PVD

The Physical Vapor Deposition (PVD) system for $CuGaSe_2$ thin-film preparation was equipped with two thermally stable effusion cells filled with Cu and Ga. Se was evaporated from a tungsten boat, and the Se-flux was regulated by a quartz crystal monitor controlling the power supplied to the source. The base pressure in the evaporation chamber was below 10^{-6} *mbar*; during the growth process, the pressure was below $5x10^{-6}$ *mbar*. A 10 *kW* halogen heater system was used for fast heating ramps of the soda-lime-glass (SLG) substrates. For preparing homogeneous films, the substrate holder was rotated. 16 homogeneous 2.5x2.5 cm^2 samples can be prepared in one evaporation process. $CuGaSe_2$ absorber layers were deposited on SLG/Mo for solar cell devices.

4.4 Quaternary Epitaxial Chalcopyrites grown on GaAs by MOVPE

The quaternary $CuIn_{1-x}Ga_xSe_2$ epitaxial layers were grown by ***Metal-Organic Vapor Phase Epitaxy (MOVPE)*** on GaAs (001) substrates [4.5]. The EPICHEM metalorganic precursors were: TriMethyl Gallium, ($(CH_3)_3Ga$, TMGa), TriMethyl Indium ($(CH_3)_3In$, TMI), Di-TertiaryButyl-Selenium ($(C_4H_9)_2Se$, DTBSe) and Cyclopentadienyl Copper TriEthyl Phosphine ($C_5H_5CuP(C_2H_5)_3$, CpCuTEP). During the process 5 l/min Pd-purified H_2 was used as a carrier gas at a pressure of 30mbar. The growth temperature was 500 °C or 570 °C. The amount of deposited material was controlled by the flux of H_2 through the precursors and by their vapor pressure. Due to its low vapor pressure, CpCuTEP has to be heated to 60°C. The other precursors may be used at room temperature or below. The Cu-precursor was kept at maximum output and the Se-precursor was provided at 10 times the concentration of the other precursors. The composition of the films was controlled by the ratio of the Ga and In fluxes, [Ga]/([Ga]+[In]). The deposition time was 4 h. There is a linear dependence between the [Ga]/([Ga]+[In]) flux ratio during the process and the EDX measured [Ga]/([Ga]+[In]) ratio, x, in the film. Changes of temperature do not affect this dependence much. The EDX measurements were performed in an Oxford IMCA system within a LEO440 SEM. An electron beam at 7 keV was used to avoid signals from the underlying GaAs, since the CIGS layers are only 250-450 nm thick (see Table 4.1.1). No As signal was detected at this excitation energy. The measurements were calibrated with a polycrystalline $Cu(In,Ga)Se_2$ standard from NREL. The error is about 1 %.

The optimizing of the growth process of $CuIn_{1-x}Ga_xSe_2$ started with the parameter set known for $CuGaSe_2$, which is grown in high quality at 570 °C. High quality $CuInSe_2$ can be grown at 500 °C without measurable Ga diffusion from the substrate. Therefore, various growth temperatures were used to obtain CIGS with different Ga contents: low temperatures (500 °C) for low Ga ($x<0.3$) and high temperatures (570 °C) for high Ga ($x>0.3$) content. Each sample is grown in such conditions to establish ***slightly Cu-rich*** CIGS layers with a ratio of [Cu]/([Ga]/+[In])=1.0-1.1.

4.5 ZnSe grown on glass and chalcopyrite substrates by EBE

Even though, the best efficiency of 19.9% for CIGS solar cells has been achieved with CdS as a buffer layer prepared by CBD, concerns with small amounts of cadmium have lead towards the investigation of Cd-free buffer layers [4.6], [4.7]. ZnSe is one of the materials alternately used. ZnSe is deposited by ***Physical Vapor Deposition (PVD)*** in the e-beam evaporation (EBE) technique on PVD grown Ga-rich $CuGaSe_2$ polycrystalline films. The absorber films were deposited on molybdenum coated soda lime glass substrates and on $CuGaSe_2$ chalcopyrite absorbers. The ZnSe deposition takes place in a Veeco VE-770 Chamber (Figure 4.2) equipped with a quartz crystal monitor-detector for controlling the deposition rate. The substrate can be heated up to 1200 ^{o}C, while the temperature is electronically controlled with an accuracy of 0.1 ^{o}C. In our case, the substrate temperature was 400 ^{o}C, while the e-beam power was 11 KW. The deposition process is followed by annealing at 250 ^{o}C for 30 min. The quartz crystal frequency deviation during the growth process was 1 KHz, corresponding to a layer thickness in the order of 100 nm.

Figure 4.2 The e-beam evaporation (EBE) chamber.

For the CIS, CIGS solar cell technology, the thickness of the buffer layer is of great importance, and should not exceed the critical value of 50nm. The control of the thickness is performed *insitu* with a crystal monitor detector. The eigenfrequency of the quartz crystal is modulated according to the material deposited on its surface. Thus the quartz crystal is placed beside the substrate, the quantity of ZnSe deposited on the crystal is indicative of that deposited on the substrate. The configuration is calibrated such as change of 1 Hz in the frequency corresponds to 1 Å thickness. The relationship between the layer thickness and the quartz crystal frequency is given by Eq. (4.1):

$$g \cdot t = \frac{m}{A} = \frac{\delta f}{k} \tag{4.1}$$

where t is the layer thickness, m is the layer mass, A is the layer surface, δf is the frequency difference, and $k = 0.474 \times 10^8$ Hz cm^2/g is a constant given by Eq. (4.2):

$$k = f^2 \cdot \frac{A'}{N \cdot g_q \cdot A} \tag{4.2}$$

where f is the quartz crystal frequency, A' is the deposition surface, A is the quartz crystal surface, N is a frequency constant, and g_q is the quartz crystal density.

Initially, the deposition rate is low (10-20 Hz/s), corresponding to 10-20 Å/s. Thereafter, the deposition rate increases rapidly reaching the 300 Hz/s, a fact that needs to be taken into account in order to stop the procedure on time and achieve the desirable thickness of 30-40nm.

It should be noted, that for the solar cell with EBE grown ZnSe studied in the present work, the ZnO window layer was deposited by PLD at 300 ^{o}C temperature and 0.2mbar O_2 (gas carrier) pressure, as described in section 3.7. The Al front ohmic contacts were also deposited by PLD with the use of a proper mask.

4.6 ZnSe grown on glass and chalcopyrite substrates by CBD

High efficiency solar cells are known from the literature to be fabricated using CdS buffer layers. However, since cadmium is a toxic material, other, more environmentally friendly Cd-free buffer layers have been processed. ZnSe is an important semiconductor material with a large bandgap (2.7eV), which has vast potential use in thin film solar cells. A very attractive method for producing ZnSe thin films, due to the possibility of large area deposition at low cost, is the ***Chemical Bath Deposition (CBD)*** method.

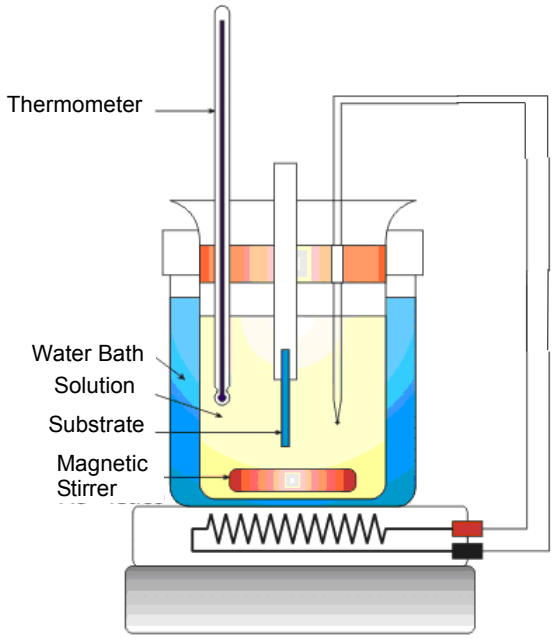

Figure 4.3 Schematic diagram of the Chemical Bath Deposition Apparatus

The CBD apparatus (Figure 4.3) consists of: a) a beaker in which the solution is inserted, b) a magnetic stirrer (with PVC magnet) to keep the solution under stirring during the deposition, c) a hotplate to moderate the desired temperature, d) a water bath to maintain the temperature of the solution homogenous, e) a temperature detector, and f) a holder for the substrate. The pH was measured during deposition with a pH-meter.

The procedure followed for CBD growth of ZnSe thin films starts with a 0,4M Zn^{+2} ($ZnSO_4$) solution with 25% ammonia (NH_3) and 25% Hydrazine (NH_2NH_2) as complexing agents, to which are added: 0,08M selenourea ($SeC(NH_2)_2$) as selenide precursor and 0,08M sodium sulfite (Na_2SO_3) as an antioxidant, to initiate the CBD reaction. At the same time, the substrate is immersed in the bath. The bath is maintained at a constant temperature (70^{o}C) [4.8] and is kept under stirring with a magnet. Substrates are previously cleaned in an ultrasonic bath with ethanol for 30min.

Specifically, for chalcogenide deposition (CdS, ZnSe, ZnS, etc) at least two different mechanisms are present, which yield different compositions and morphology of the films. A heterogeneous mechanism occurs due to the reaction of cation precursors adsorbed on the substrate surface. This mechanism proceeds through the formation of an adsorbed intermediate complex of the type $Me(OH)_x(NH_3)_y$ [4.9]-[4.10], which reacts with the chalcogenide precursor. A side-reaction to the chalcogen-film growth is the

deposition of $Me(OH)_2$, which explains the amount of oxide and hydroxide encountered some times.

On the other hand, a homogeneous mechanism occurs due to the deposition of colloid aggregates formed in the bulk of the solution, which yields more stoichiometric and porous films.

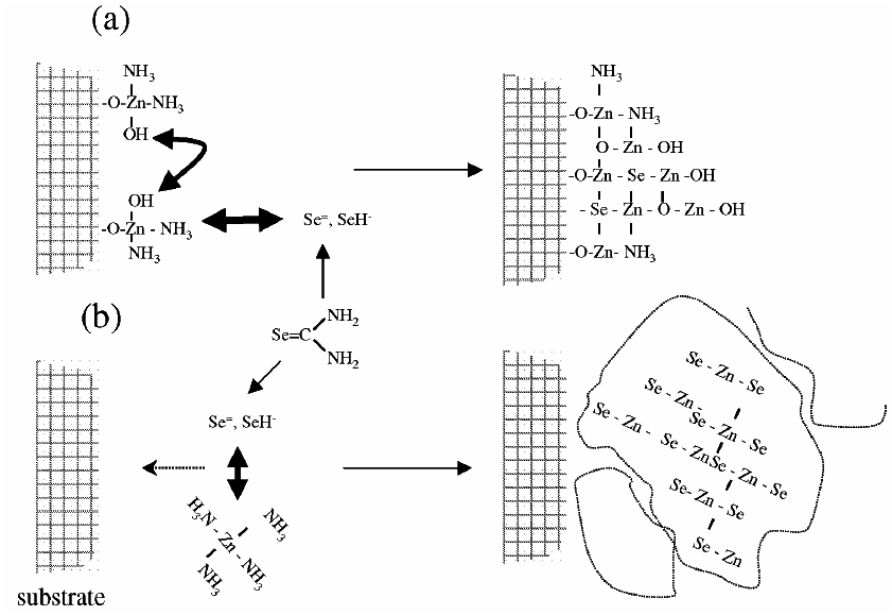

Figure 4.4 Scheme of the two main reaction mechanisms present in the chemical bath: a) heterogeneous mechanism, and b) homogeneous mechanism

Both mechanisms, as shown in Figure 4.4, coexist in the bath, but the predominance of the one or the other may be induced, to some extent, by the experimental conditions. Moreover, the predominant mechanism changes during the CBD process, heterogeneous deposition being more important at the beginning but with increasing influence of homogeneous deposition with the time upon exhaustion of reactants and growth of colloids [4.9], [4.11].

4.6.1 Homogeneous process

The determining species for this process are selenourea ($SeC(NH_2)_2$), ammonia (NH_3), and $ZnSO_4$. During the induction, the reaction of selenourea with ammonia and hydroxide, must occur to generate the selenide ions:

$$NH_2CSeNH_2 + OH^- \rightarrow NH_2C(O)NH_2 + HSe^- \quad (4.3)$$

Zn+ cations participate in two main equilibria, with ammonia and hydroxide

$$Zn^{2+} + 4NH_3 \leftrightarrow Zn(NH_3)_4^{2+} \quad (4.4)$$

$$Zn^{2+} + 4OH^- \leftrightarrow ZnOH_2^{2-} + 2H_2O \quad (4.5)$$

$Zn(NH_3)_4^{2+}$ being predominant at the ammonia concentrations used in the bath. Once biselenide species are formed after Reaction (4.3), they may react with SO_3^{2-} (Reactions (4.6) and (4.7)) and with $Zn(NH_3)_4^{2+}$ (Reaction (4.8)):

$$HSe^- + \frac{1}{2}O_2 \rightarrow Se + OH^- \quad (4.6)$$

$$Se + SO_3^{2-} \rightarrow SeSO_3^{2-} \quad (4.7)$$

$$Zn(NH_3)_4^{2+} + HSe^- + OH^- \rightarrow ZnSe + 4NH_3 + H_2O \quad (4.8)$$

where in red are the solid compounds that contribute to the growth of the film. Reaction (4.8) is favored by the high insolubility of ZnSe and is responsible for the appearance of the first solid ZnSe particles.

4.6.2 Heterogeneous chemical growth

This mechanism is observed after 20 – 25 min deposition [4.12]. The predominant selenide precursor in solution is selenosulphate, formed after reactions (4.6) and (4.7), while hydrolysis liberates the biselenide anions:

$$SeSO_3^{2-} + [OH^-]_S \rightarrow SO_4^{2-} + [HSe^-]_S \quad (4.9)$$

$$Zn(NH_3)_4^{2+} + [HSe^-]_S + [OH^-]_S \rightarrow ZnSe + 4NH_3 + H_2O \quad (4.10)$$

The adsorbed species are tentatively introduced to account for the heterogeneous character of this mechanism. The overall reaction is:

$$Zn(NH_3)_4^{2+} + SeSO_3^{2-} + 2[OH^-]_S \rightarrow 4NH_3 + H_2O + SO_4^{2-} + ZnSe \quad (4.11)$$

4.7 Au/Al/In:ZnO/i-ZnO grown on ZnSe/CuGaSe$_2$/Mo/glass by PLD

The ZnO window layer and the Al front ohmic contact were deposited using the method of ***Pulsed Laser Deposition (PLD)***. This method is particularly flexible, mostly because the laser used in the layer deposition is placed outside the deposition chamber and may be applied in both, vacuum and carrier gas environment. Additionally, the pulsed laser technique allows the growth of multilayer structures.

Layer growth in the presence of carrier gas can lead to controlled material properties, such as composition, optical and magnetic properties. A typical PLD configuration is shown in Figure 4.5.

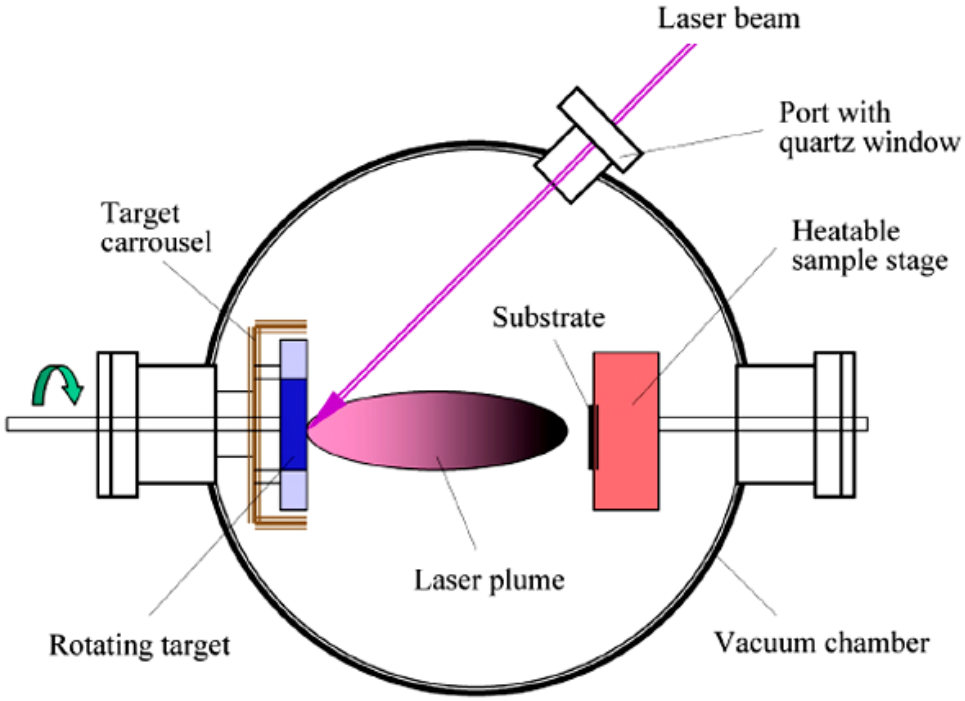

Figure 4.5 PLD deposition configuration.

The window of the solar cell consists of two layers. An ultra thin (50nm) intrinsic ZnO (i-ZnO) layer and an Indium doped ZnO (In:ZnO) layer with 3% In, with approximately 700 – 1000nm thickness.

The deposition conditions remained the same during the preparation of all solar cell samples: The chamber was under 20Pa O_2 (gas carrier) pressure. Substrate temperature was set to 300^{o}C and measured with a thermocouple. Two different targets

were used for the two different layers: a ceramic ZnO and a 3% ceramic In:ZnO target, mounted at a carousel. During deposition, the ablated targets were in continuous movement, to avoid target penetration. For the excitation of the targets an excimer laser at 248nm with pulse frequency of 10Hz was used. The fluence of the laser was 2.4J/cm^2.

The Al-front ohmic contact is deposited in vacuum using an Al foil as target. The substrate is not heated for this procedure. Additionally, an Au-thin film is deposited on top of Al to avoid oxidation.

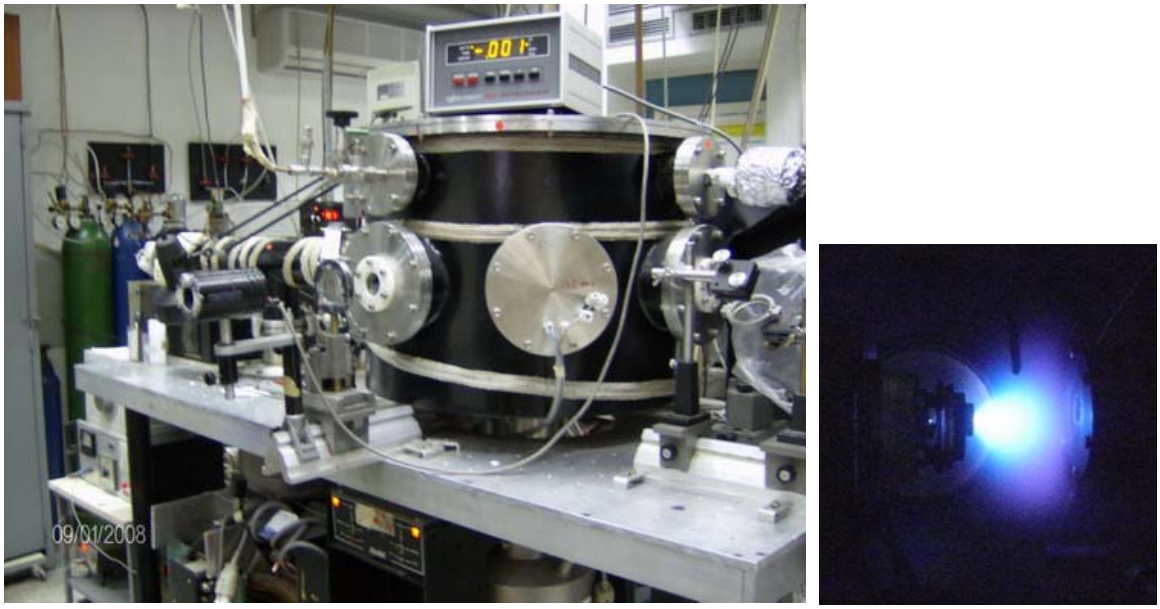

Figure 4.6 The PLD chamber (left) and the plasma generated during deposition (right)

4.8 ZnO grown on ZnSe/Cu(In,Ga)Se$_2$/Mo/glass by ECD

ZnO thin films were deposited by Electrochemical Deposition (ECD), initially on Mo coated glass substrate (Control Experiments), and then on ZnSe/Cu(In,Ga)Se_2/Mo/glass under potentiostatic cathodic conditions in a zinc nitrate solution. The electrochemical cell (Figure 4.7) has a standard three electrode geometry with substrate (working electrode), pure Zn (counter electrode), and a KCl saturated calomel electrode (reference electrode).

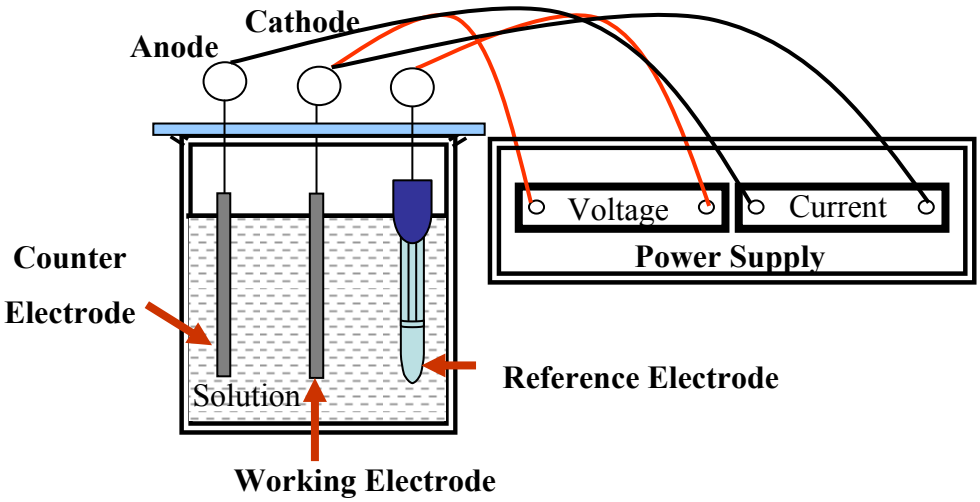

Figure 4.7 Schematic representation of an electrochemical cell

Prior to ZnO deposition, the Mo coated glass substrates were cleaned in an ultrasonic ethanol bath and a cyclic voltammogram (Figure 4.8) was recorded to obtain the optimum cathodic potential E_o= -650mV.

The ZnO films were recorded in the potentiostatic mode under magnetic stirring (100cycles/min) in a 0.05M $Zn(NO_3)_2$ solution at 80°C. After deposition, the samples were rinsed with deionised water and dried in air.

The general scheme of ZnO electroprecipitation from nitrate baths is assumed to occur according to the following Reaction sequence:

$$Zn(NO_3)_2 \rightarrow Zn^{+2} + 2NO_3^- \qquad (4.12)$$

Electroreduction of nitrate ions generates hydroxide ions at the cathode:

$$NO_3^- + H_2O + 2e^- \rightarrow NO_2^- + 2OH^- \qquad (4.13)$$

Zinc ions interact with the hydroxyl anions producing zinc hydroxyl. From this, ZnO and H_2O are formed:

$$Zn^{+2} + 2OH^- \rightarrow Zn(OH)_2 \rightarrow ZnO + H_2O \qquad (4.14)$$

The overall reaction results in the formation of ZnO:

$$Zn^{+2} + NO_3^- + 2e^- \rightarrow ZnO + NO_2^- \qquad (4.15)$$

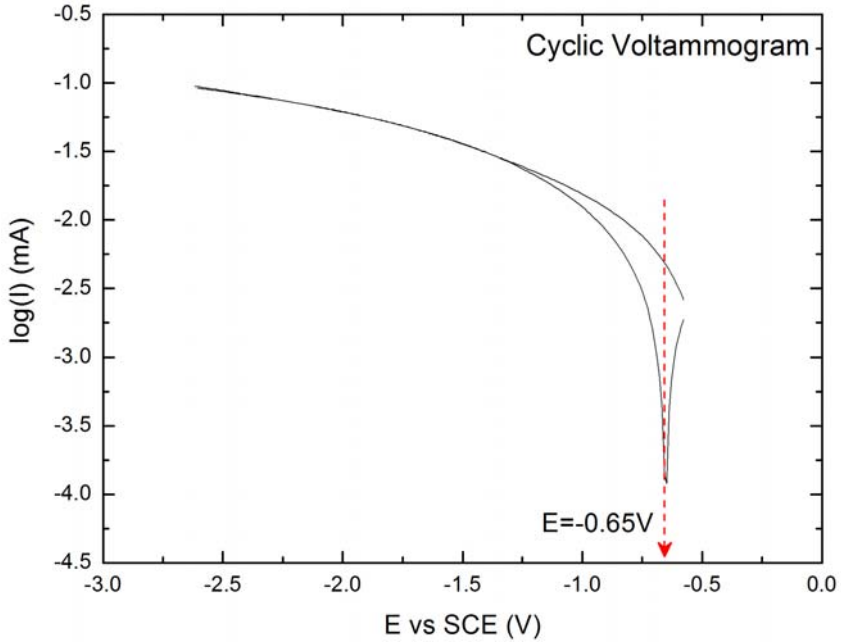

Figure 4.8 Cyclic Voltamperogram of ZnO on Mo-glass substrate

4.9 ZnO Nanorod ARCs grown on glass substrate by ECD

Alternatively to PLD deposited ZnO window layer, another configuration of the window layer is also investigated. ZnO-nanorods serve not only as the window layer but also as an Anti-Reflective Coating (ARC), making them perfect candidates for solar cells devices.

The ZnO-nanorods were grown by ***Electro-Chemical Deposition (ECD) Techniques*** on intrinsic i-ZnO films (40-50nm) electrodeposited on fluorine doped SnO_2-coated glass (named: FTO glass). The substrates are cut into small 2.5x2.0 cm^2 rectangles and then cleaned in an ultrasonic bath of acetone and ethanol with subsequent rinsing in distilled water. The ZnO-nanorods/i-ZnO samples are deposited in a three-electrode electrochemical cell with Pt counter and pseudoreference electrodes. The electrodeposition was carried out at potential −1.35 V versus Pt. The electrochemical cell was placed in a thermoregulated bath and the deposition temperature was adjusted to 75 °C. An aqueous solution of $Zn(NO_3)_2$ with molarity 7 m*M* was used. The solution was stirred during the deposition process. Typical deposition current densities were 0.3–0.5 mA/cm^2. The deposition time was 3000-3600s in the potentiostatic mode. The deposited samples were washed with distilled water to remove any residual salt.

ZnO formation takes place on the cathode side. The possible chemical reactions can be described as follows [4.13]:

$$\begin{aligned} &Zn(NO_3)_2 \leftrightarrow Zn^{2+} + 2NO_3^- \\ &NO_3^- + H_2O + 2e^- \rightarrow NO_2^- + 2OH^- \\ &Zn^{2+} + OH^- \leftrightarrow Zn(OH)_2 \\ &Zn(OH)_2 \rightarrow ZnO + H_2O \end{aligned} \qquad (4.16)$$

In the present work, three different kinds of samples have been studied:

a) 0719-1: ZnO nanorods prepared in a 7mM $Zn(NO_3)_2$ bath,

b) 0719-2: ZnO nanorods prepared in a 7mM $Zn(NO_3)_2$ and 70mM HNO_3 bath. The nitrate ions served as an oxidant for the preparation of ZnO. The HNO_3 decreases the *p*H value of the solution which leads to a significant decrease of the defect emission [4.14], and

c) 0719-3: ZnO nanorods prepared in 7mM $Zn(NO_3)_2$ and 5mM NH_4NO_3 bath. The use of NH_4NO_3 leads to an increase of the vertical growth rate of the ZnO nanorods [4.15].

Two different substrates, i.e., solar thermal absorber substrates provided by the Almeco-TiNOX GmbH (TiNOX substrate) and copper indium gallium (di)selenide (CIGS) solar cells, were used. The dimensions of the deposited ZnO-nanorods (NRs, Figure 4.9) were: D=40-50nm, D_b=150-180nm, H=500nm, and L=200-220nm which corresponds to a surface packing density in the order of 10^8 NRs/cm^2.

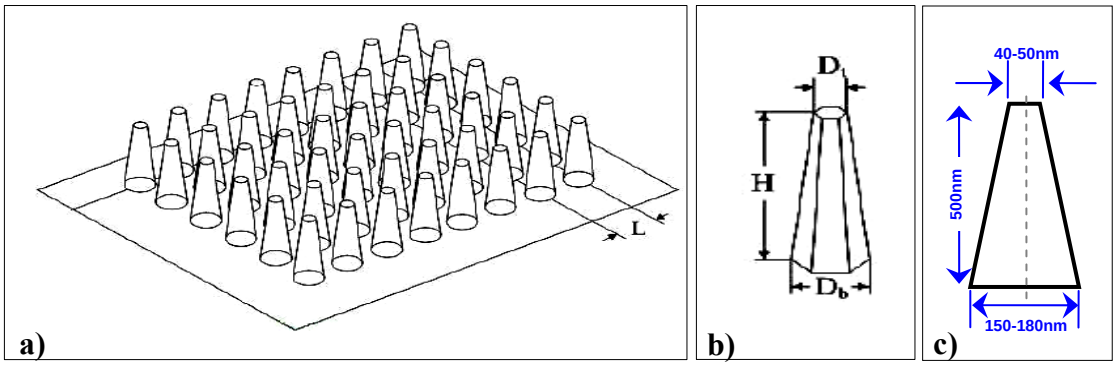

Figure 4.9 Schematic drawing of : a) a ZnO NR Array, b) a single ZnO NR, and c) cross-section of a ZnO NR

5. Characterization techniques

5.1 Structural characterization (XRD, SEM, AFM, RAMAN)

5.1.1 X-Ray Diffraction (XRD)

5.1.1.1 General

X-ray diffraction (XRD) is a versatile, non-destructive technique that reveals detailed information about the chemical composition and crystallographic structure of natural and manufactured materials.

When a monochromatic X-ray beam with wavelength λ is projected onto a crystalline material at an angle θ, part of the beam is reflected, while the rest is scattered by the crystal structure [5.1]. Diffraction occurs only when the optical distance traveled by the reflected rays differs by a complete number n of wavelengths ($AB + BC = n\lambda$).

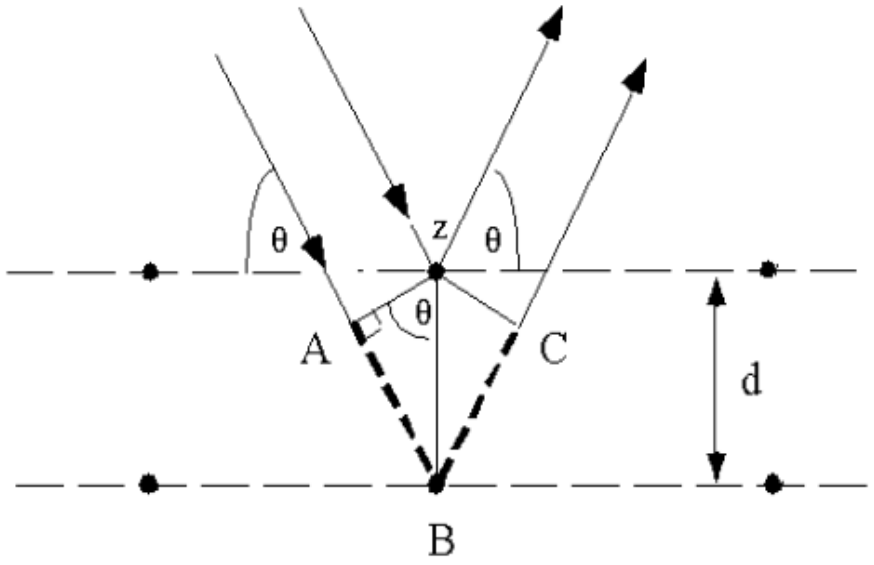

Figure 5.1 X-Ray reflection geometry.

As shown in Figure 5.1, the reflection geometry results in:

$$AB + BC = 2AB = 2d \sin\theta$$
$$n\lambda = 2d \sin\theta \quad (5.1)$$

The latter relationship is called **Bragg's law**.

5.1.1.2 Experimental set-up

In the present thesis, the XRD analysis is performed by an XRD D8 type Focus Bruker instrument with Cu filter, like the one shown in Figure 5.2.

Figure 5.2 The XRD instrument used in the present thesis.

5.1.2 Scanning Electron Microscopy (SEM)

5.1.2.1 General

The scanning electron microscope (SEM) is a type of electron microscope that images the sample surface by scanning it with a high-energy beam of electrons in a raster scan pattern. The electrons interact with the atoms that make up the sample producing

signals that contain information about the sample's surface topography, composition and other properties such as electrical conductivity.

In a typical SEM (Figure 5.3), an electron beam is thermionically emitted from an electron gun fitted with a tungsten filament cathode. Tungsten is normally used in thermionic electron guns because it has the highest melting point and lowest vapor pressure of all metals, thereby allowing it to be heated for electron emission. The electron beam, which typically has an energy ranging from a few hundred eV to 40 keV, is focused by one or two condenser lenses to a spot about 0.4 nm to 5 nm in diameter. The beam passes through pairs of scanning coils or pairs of deflector plates in the electron column, typically in the final lens, which deflect the beam in the *x* and *y* axes so that it scans in a raster fashion over a rectangular area of the sample surface.

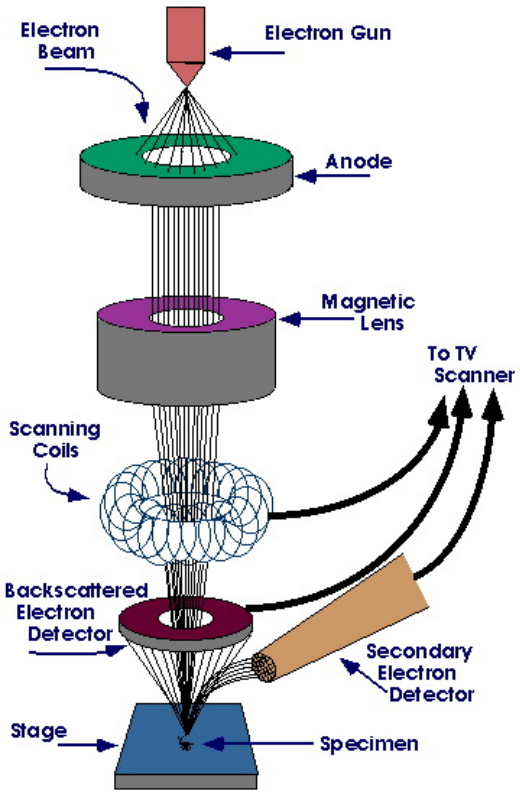

Figure 5.3 Schematic diagram of a typical SEM chamber

When the primary electron beam interacts with the sample, the electrons lose energy by repeated random scattering and absorption within a teardrop-shaped volume of the specimen known as the interaction volume, which extends from less than 100 nm to around 5 μm into the surface. The size of the interaction volume depends on the electron's landing energy, the atomic number of the specimen and the specimen's density.

The energy exchange between the electron beam and the sample results in the reflection of high-energy electrons by elastic scattering, emission of secondary electrons by inelastic scattering and the emission of electromagnetic radiation, each of which can be detected by specialized detectors. The beam current absorbed by the specimen can also be detected and used to create images of the distribution of specimen current. Electronic amplifiers of various types are used to amplify the signals which are displayed as variations in brightness on a cathode ray tube. The raster scanning of the CRT display is synchronized with that of the beam on the specimen in the microscope, and the resulting image is, therefore, a distribution map of the intensity of the signal being emitted from the scanned area of the specimen. The image is digitally captured and displayed on a computer monitor.

5.1.2.2 Experimental set-up

In the present thesis, the SEM-images were taken by a JEOL JSM 6380-LV Scanning Electron Microscope, like the one shown in Figure 5.4.

Figure 5.4 The Scanning Electron Microscope (SEM) setup (left) and chamber (right) used in the present thesis.

5.1.3 Atomic Force Microscopy (AFM)

5.1.3.1 General

Atomic force microscopy (AFM) is a method of measuring surface topography on a scale from angstroms to 100 microns. The AFM consists of a microscale cantilever with a sharp tip (probe) at its end that is used to scan the specimen surface. The cantilever is typically silicon or silicon nitride with a tip radius of curvature on the order of nanometers. When the tip is brought into proximity of a sample surface, forces between the tip and the sample lead to a deflection of the cantilever according to Hooke's law. Depending on the situation, forces that are measured in AFM include mechanical contact force, Van der Waals forces, chemical bonding, electrostatic forces, magnetic forces, etc. As well as force, additional quantities may simultaneously be measured through the use of specialized types of probe. Typically, the deflection is measured using a laser spot reflected from the top surface of the cantilever into an array of photodiodes.

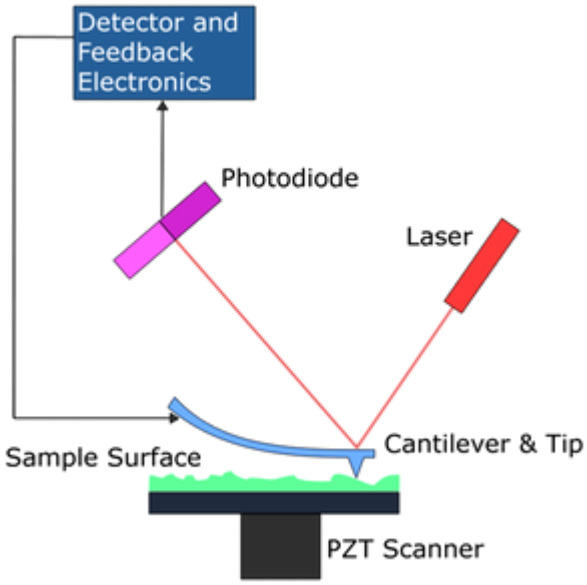

Figure 5.5 Operation principle of an Atomic Force Microscope (AFM).

5.1.3.2 Experimental set-up

In the present thesis, the AFM-images were taken with a DME Dualscope DS95 Atomic Force Microscope, like the one shown in Figure 5.6.

Figure 5.6 The Atomic Force Microscope (AFM) used in the present thesis.

5.1.4 Raman Scattering Spectroscopy (RAMAN)

5.1.4.1 General

Raman spectroscopy (RAMAN) is a spectroscopic technique used to study vibrational, rotational, and other low-frequency modes in a system [5.2]. It relies on inelastic scattering, or Raman scattering, of monochromatic light, usually from a laser in the visible, near infrared, or near ultraviolet range. The laser light interacts with phonons or other excitations in the system, resulting in the energy of the laser photons being shifted. The shift in energy gives information about the phonon modes in the system. Infrared spectroscopy (IR) yields similar, but complementary, information.

5.1.4.2 Theory of Raman scattering in molecules

The classical theory of Raman scattering is based on the idea that, in a diatomic molecule, the electromagnetic field $\vec{E} = \vec{E}_0 \cos \omega_L t$ of the incident light induces a time dependent dipole moment $\vec{P} = \alpha \vec{E}$, where α is the electronic polarizability which depends on the electric charge distribution of the dipole. For sufficiently small displacements of nuclei from their equilibrium position, α changes linearly with the

normal coordinate $Q = \sqrt{\mu}(u_2 - u_1)$ (μ: reduced mass, u_1, u_2: displacements of molecules) and can be expanded in Taylor's series as:

$$\alpha = \alpha_0 + \left(\frac{\partial \alpha}{\partial Q}\right)_0 Q + \frac{1}{2}\left(\frac{\partial^2 \alpha}{\partial Q^2}\right)_0 Q^2 + \ldots \tag{5.2}$$

The first-order Raman Effect is determined by the term linear in Q. If the molecule vibrates with the frequency ω_S, then $Q = Q_0 \cos \omega_S t$. In this case, the total dipole moment has the form:

$$\vec{P}(\omega) = \left(\alpha_0 + \left(\frac{\partial \alpha}{\partial Q}\right)_0 Q_0 \cos \omega_S t\right) \vec{E}_0 \cos \omega_L t \tag{5.3}$$

With the application of trigonometric sum rules, the above relation yields:

$$\vec{P}(\omega) = \alpha_0 \vec{E}_0 \cos \omega_L t + \frac{1}{2}\left(\frac{\partial \alpha}{\partial Q}\right)_0 Q_0 \vec{E}_0 \left[\cos(\omega_L + \omega_S)t + \cos(\omega_L - \omega_S)t\right] \tag{5.4}$$

This equation shows that the induced dipole moment $\vec{P}$ vibrates not only at the frequency ω_L, but also at the frequencies $\omega_L \pm \omega_S$.

The intensity of scattered light per unit solid angle $I(t)$ is given by:

$$\begin{aligned} I(t) &= A|P(t)|^2 \\ &= AE_0{}^2\left[k_0{}^2 \cos^2 \omega_L t + k_1{}^2 \cos^2(\omega_L - \omega_S)t + k_2{}^2 \cos^2(\omega_L + \omega_S)t\right] \\ &\quad + \textit{cross terms} \end{aligned} \tag{5.5}$$

where $k_0{}^2 = \alpha_0{}^2 \omega_L{}^4$, $k_1{}^2 = \frac{1}{4}\left(\frac{\partial \alpha}{\partial Q}\right)_0^2 Q_0{}^2 (\omega_L - \omega_S)^4$, and $k_2{}^2 = \frac{1}{4}\left(\frac{\partial \alpha}{\partial Q}\right)_0^2 Q_0{}^2 (\omega_L + \omega_S)^4$.

The first term in Eq. (5.5) is known as ***Rayleigh scattering***, the second and third terms represent Raman scattering at the *Stokes* ($\omega_L - \omega_S$) and *anti-Stokes* frequency ($\omega_L + \omega_S$), respectively [5.3].

The first-order Raman scattering process can be virtually decomposed into three electronic transitions: The interaction with an incident photon ($\hbar\omega_L$) results in the simultaneous excitation of a phonon ($\hbar\omega_S$) and the inelastic scattering of the photon ($\hbar\omega_{SC}$ at frequency $\omega_{SC} = \omega_L \pm \omega_S$) as shown in Figure 5.7. The Stokes and anti-Stokes

scattering can be described by *Feynman graphs* indicating that in the Stokes process, a phonon is created, while in the antiStokes process, the phonon is annihilated.

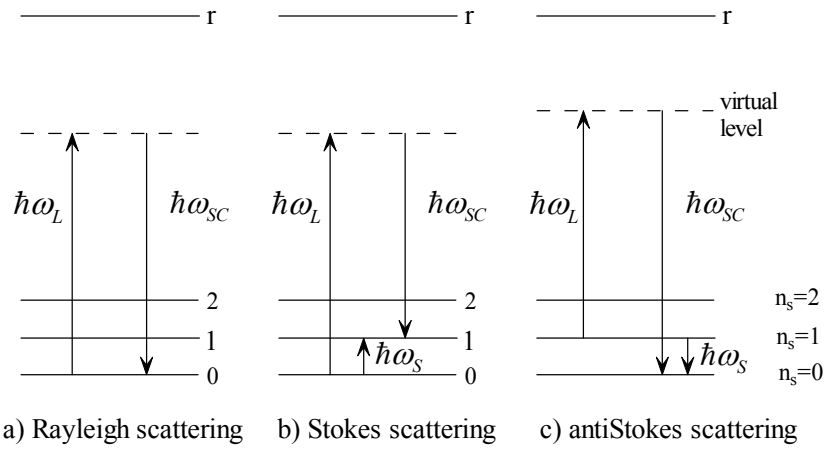

Figure 5.7 Transitions for a) Rayleigh scatting,

b) first-order Stokes scatting and c) first-order antiStokes scatting [5.3]

In Stokes scattering, excitation starts at the ground state, while, in antiStokes scattering, an excited state is the starting state (Figure 5.7 b) and c)). For optical phonons and not too high temperatures, the population of the ground vibrational level ($|0\rangle$) is much greater than that of excited vibrational levels ($|1\rangle$).

5.1.4.3 Raman tensor in solids

In case of crystals, the susceptibility tensor χ_{jl} is used rather than the scalar polarizability α. The susceptibility can be expanded in analogy to α in Eq. (5.6) according to [5.2]:

$$\chi_{jl} = \left(\chi_{jl}\right)_0 + \sum_q \left(\frac{\partial \chi_{jl}}{\partial Q_q}\right)_0 Q_q + \sum_{q,m} \left(\frac{\partial^2 \chi_{jl}}{\partial Q_q \partial Q_m}\right)_0 Q_q Q_m + \cdots, \qquad (5.6)$$

where the sum runs over all normal coordinates. $\partial\chi_{jl}/\partial Q_q$ is a component of the derived polarizability tensor, which is known as the Raman tensor and written as $\left(\chi_{jl}\right)_q$, or χ_{jlq} .or $\chi_{jl,q}$. The components of the tensor have three indices. *j* and *l* extend over the coordinates 1 to 3 and *q* runs over the 3N-3 normal coordinates for the vibrations, where

N is the number of atoms in the unit cell. In other words, q runs over all optical modes with wave vector k=0. Thus, the Raman tensor which refers to all zone-center vibrations has rank three. For an individual mode, this tensor is given by a matrix with three rows and three columns determined from the derived susceptibilities. This quantity is called the Raman tensor of a particular mode with its distinct symmetry.

The scattering geometry can be described by the Porto notation as: a(bc)d, where the letters refer to Cartesian coordinates x,y,z. a and d give the directions of the incident and scattered light wavevector, respectively, b and c give the directions of the corresponding polarizations[5.2]. In Table 5.5.1, the Raman tensors and their symmetries A, B, E are given for the point group D_{2d} in the orthogonal system O: [100], [010], [001] [5.4].

When the energy of photons used to excite Raman scattering in a medium is resonant with some electronic transitions of the medium, one expects in general the Raman cross sections to be enhanced. This phenomenon is known as Resonance Raman scattering (RRS) [5.5].

Table 5. 1 Raman tensors and their symmetries for the point group D_{2d} ($\bar{4}2m$) in the orthogonal system O: [100], [010], [001] [5.3].

A_1	B_1	$B_2(z)$	E(y)	E(x)
$\begin{bmatrix} a & 0 & 0 \\ 0 & a & 0 \\ 0 & 0 & b \end{bmatrix}$	$\begin{bmatrix} c & 0 & 0 \\ 0 & -c & 0 \\ 0 & 0 & 0 \end{bmatrix}$	$\begin{bmatrix} 0 & d & 0 \\ d & 0 & 0 \\ 0 & 0 & 0 \end{bmatrix}$	$\begin{bmatrix} 0 & 0 & e \\ 0 & 0 & 0 \\ e & 0 & 0 \end{bmatrix}$	$\begin{bmatrix} 0 & 0 & 0 \\ 0 & 0 & e \\ 0 & e & 0 \end{bmatrix}$

5.1.4.4 Experimental set-up

In the present thesis, the Raman spectra were taken with a Renishaw RM1000 Confocal Raman Instrument. The excitation source was a 632.8nm He-Ne laser beam, and the detection was performed with a Charged Couple Device (CCD). The system was also equipped with a Leica optical microscope.

Figure 5.8 The RAMAN Scattering Microscope used in the present thesis.

5.2 Optical Characterization (SE, PR)

5.2.1 Spectroscopic Ellipsometry (SE)

5.2.1.1 General

Ellipsometry is a versatile and powerful optical technique for the investigation of the dielectric properties (complex refractive index or dielectric function) of thin films. Upon the analysis of the change of polarization of light upon reflection on a sample, ellipsometry can yield information about layers that are thinner than the wavelength of the probing light itself, even down to a single atomic layer. Ellipsometry can probe the complex refractive index or dielectric function tensor, which gives access to fundamental physical parameters and is related to a variety of sample properties, including morphology, crystal quality, chemical composition, or electrical conductivity. It is commonly used to characterize film thickness for single layers or complex multilayer stacks ranging from a few angstroms or tenths of a nanometer to several micrometers with an excellent accuracy.

In the most common experimental configuration for Spectroscopic Ellipsometry (SE), linearly polarized light is incident on a surface and the polarization state of the reflected light, which is in general elliptically polarized (Figure 5.9) is analyzed.

Knowing the polarization states, the Fresnel coefficients ratio -the *p- (parallel)* and *s-* (*senkrecht, perpendicular)* complex reflectances r_p and r_s, respectively- can be derived:

$$\rho = \frac{r_p}{r_s} = \tan\Psi e^{i\Delta}, \tag{5.7}$$

since the polarization is determined by the ratio of the components of the electric field vector. The parameter Ψ corresponds to the ratio of the magnitude of the total reflection coefficient and Δ is the phase shift in *p*- and *s*- waves due to the reflection. Ψ and Δ are known as the Ellipsometry parameters [5.6].

Using the Fresnel equations, ρ can be directly translated into a complex dielectric function $\varepsilon(\hbar\omega)$. Depending on the photon energy $E = \hbar\omega$ of the incident light, $\varepsilon(\hbar\omega)$ is the bulk dielectric function of the material under study provided the sample is homogeneous. However, the presence of surface layers or roughness results in inaccurate values for the bulk dielectric function and care has to be taken in the preparation of the samples. In case of inhomogeneity in the samples, $\varepsilon(\hbar\omega)$ is an average over the region penetrated by the incident light and is then a so-called pseudodielectric function or effective dielectric function, written as $<\varepsilon(\hbar\omega)>$. From this effective dielectric function $<\varepsilon(\hbar\omega)>$ and appropriate models, layer properties, such as thickness or layer dielectric functions, can be derived. Using this analysis two experimental parameters-the real and imaginary part of $<\varepsilon>$ - (per photon energy) are determined [5.7].

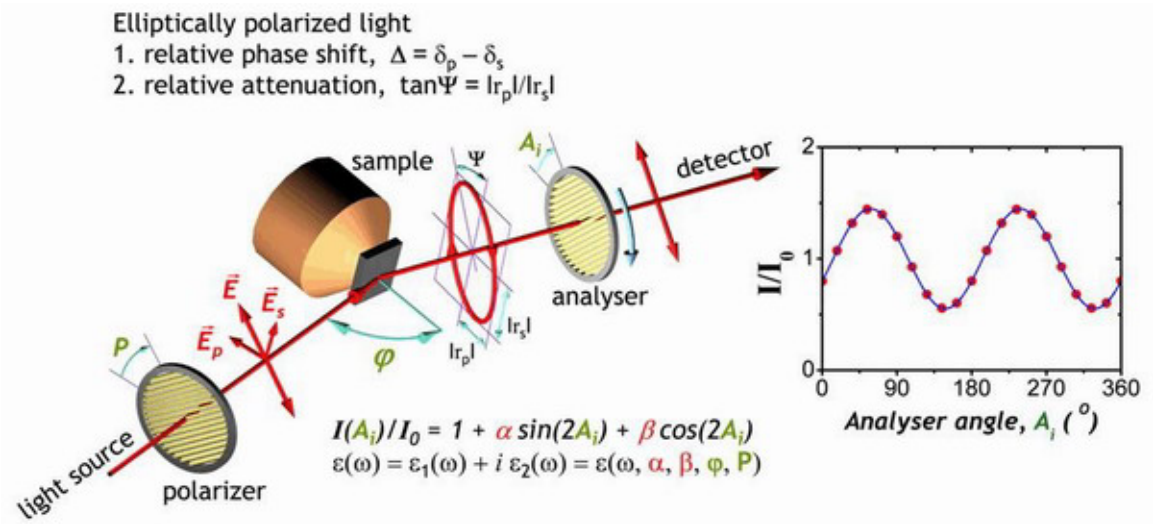

Figure 5.9 Principle of ellipsometric measurements

Since Ellipsometry is measuring the ratio (or difference) of two values (rather than the absolute value of either), according to Eq.(5.7), it is very robust, accurate, and reproducible. For instance, it is relatively insensitive to scatter and fluctuations, and requires no standard sample or reference beam.

An ellipsometer consists of a light source, a polarizer to fix the polarization of the incident light, an analyzer to measure the polarization state of the reflected light and a detector. With these basic components, the ellipsometer can be configured in a large number of modes: null, rotation analyzer, rotation polarizer and polarization modulation.

5.2.1.2 Null-Ellipsometry

In null-ellipsometry, the polarization state of the incident and the reflected light can be accessed by varying the angles of two of the three elements, polarizer (P), compensator (C), and analyzer (A) until the intensity measured by the detector is minimized [5.7]. The Fresnel ratio ρ can then be calculated according to:

$$\rho = \frac{\tan A[\tan Q + \rho_c \tan(P - Q)]}{\rho_c \tan Q \tan(P - Q) - 1} \tag{5.8}$$

$\rho_c = T_c e^{-i\Delta_c}$, $T_c=1$, $\Delta_c=90^o$

The experimental setup used for null-ellipsometric measurements is a Rudolph Instruments PCSA-439 (Figure 5. 10), at 546 nm.

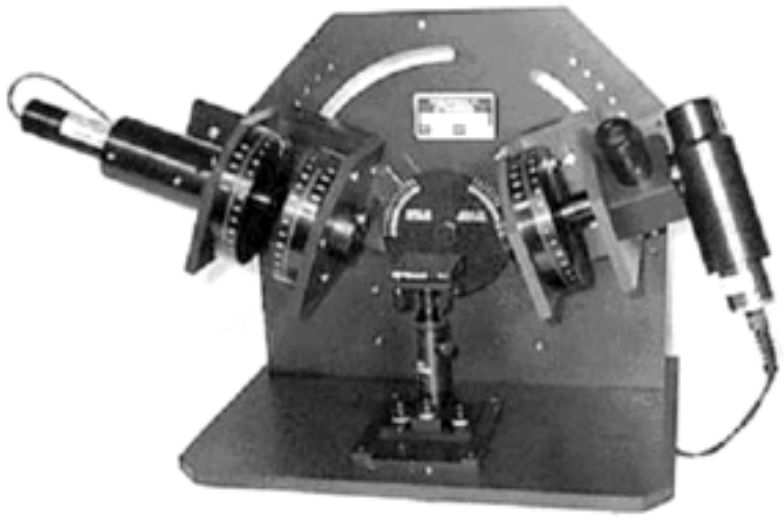

Figure 5. 10 Null-ellipsometer

5.2.2 Modulation spectroscopy: Photoreflectance(PR) – Electroreflectance(ER)

5.2.2.1 General

Modulation spectroscopy is a powerful and versatile optical technique for obtaining valuable information about a large variety of semiconductor systems, including bulk and thin films, surfaces, the effects of growth/processing, as well as the characterization of actual device structures.

Modulation spectroscopy is an analog method for taking the derivative of the optical spectrum (reflectance or transmittance) of a material by periodically modifying the measurement conditions. The basic principle of this optical technique is as follows: by applying a repetitive perturbation, such as an electric field (photo-/electromodulation), heat pulse (thermomodulation), or stress (piezomodulation), some property of the measuring system is also periodically varied and the corresponding normalized change in the reflectance R is determined.

The periodic variation of the measurement conditions gives rise to sharp, differential-like spectra in the region of interband (intersubband) transitions. Therefore, modulation spectroscopy emphasizes relevant spectral features and suppresses uninteresting background effects. It is possible to account for the line shapes to yield accurate values of important parameters such as the energies and broadening functions of interband (intersubband) transitions. Even at 300 K the energy of a particular feature can be obtained to within a few meV.

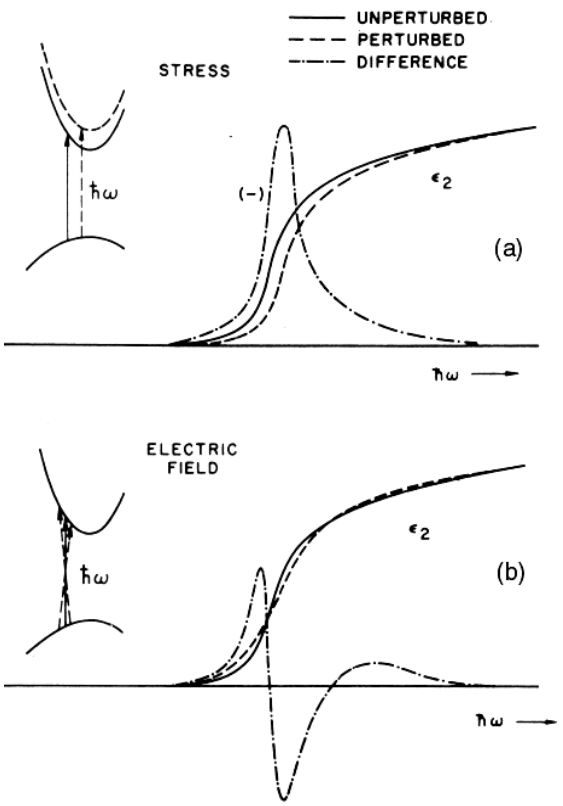

Figure 5.11 (a) Schematic diagram of the change in the imaginary part of the dielectric function expected for a first-derivative modulation process, where lattice periodicity is preserved. (b) Similar diagram for electric field modulation, where lattice periodicity is not preserved. The effect of the perturbation on the energy band structure and optical transition is shown at the left side in each case [5.8].

Modulation spectroscopy can be also employed to investigate the effects of static perturbations such as electric and magnetic fields, hydrostatic pressure, stress/strain (external and/or internal), temperature, composition, etc.

5.2.2.2 Modulation spectra and the dielectric function

The perturbation induced change ΔR in the reflectance R produces a change in the intensity reflected by the sample as: $\Delta I / I = \Delta R / R$. The experimental modulation spectra show $\Delta R / R$ as a function of energy.

In a two-phase system (material-ambient), the relationship between R and the dielectric function of the material $\varepsilon = \varepsilon_r + i\varepsilon_i$ is:

$$R = \left| \frac{n - n_a}{n + n_a} \right|^2 \quad , \qquad n^2 = \varepsilon, \quad {n_a}^2 = \varepsilon_a \tag{5.9}$$

where n is the (real part of the) refractive index of the material, n_a and ε_a are the (real parts of the) refractive index and the dielectric function of the ambient, respectively.

The differential changes in reflectance are related to the perturbation of the complex dielectric function in a simple manner, expressed as [5.9]:

$$\begin{aligned} \frac{\Delta R}{R} &= \mathrm{Re}\left[\frac{2n_a}{n(\varepsilon - \varepsilon_a)} \right] \\ &= \mathrm{Re}\left[(\alpha - i\beta)\Delta\varepsilon \right] \\ &= \alpha\Delta\varepsilon_r + \beta\Delta\varepsilon_i \end{aligned} \tag{5.10}$$

where $\Delta\varepsilon_r$ and $\Delta\varepsilon_i$ are the modulation induced changes in the complex dielectric function $\varepsilon = \varepsilon_r + i\varepsilon_i$; α and β are the Seraphin coefficients, which depend on the unperturbed dielectric function. The quantities $\Delta\varepsilon_r$ and $\Delta\varepsilon_i$ are related by a Kramers-Kronig inversion. Near the fundamental gap of bulk materials $\beta \approx 0$ and $\frac{\Delta R}{R} \approx \alpha\Delta\varepsilon_1$ is the only important term. However, in multilayer structures, interference effects may play a significant role, so both $\Delta\varepsilon_r$ and $\Delta\varepsilon_i$ have to be considered. The functional form of $\Delta\varepsilon_r$ and $\Delta\varepsilon_i$ can be calculated for a given perturbation provided that the dielectric function and critical points are known [5.10], [5.11].

The general expression for ε is:

$$\varepsilon(E, \Gamma) = 1 + \frac{4\pi i e^2 \hbar}{m^2 E^2} \int_{BZ} d^3k \int_0^\infty dt \left| \hat{e} \cdot \vec{p}_{cv} \right|^2 \times \exp \int_{-t/2}^{t/2} dt' \frac{i[E - E_{cv}(\vec{k}) + i\Gamma]\, t'}{\hbar} \tag{5.11}$$

where E is the photon energy, Γ is a phenomenological broadening parameter, BZ is the abbreviation of the Brillouin Zone, c and v denote conduction (empty) and valence (filled) bands, respectively, $\hat{e}$ is the unit polarization vector of the photon electric field; the momentum matrix element $\vec{P}_{cv}$ is independent of the wave vector $\vec{k}$; $E_{cv}(\vec{k}) = E_c(\vec{k}) - E_v(\vec{k})$ is the interband energy.

The physical mechanism responsible for electric field modulation is the coupling of the field to the electrons, causing them to accelerate through the lattice. Under the application of the electric field $\vec{F}$, the complex dielectric function $\varepsilon(E,\vec{F},\Gamma)$ is usually written as a sum of the dielectric constant $\varepsilon(E,0,\Gamma)$ without a field and the change of the dielectric constant $\Delta\varepsilon(E,\vec{F},\Gamma)$ due to the electric field. The dielectric function under the application of an electric field $\vec{F}$ becomes [5.12]:

$$\begin{aligned}\varepsilon(E,\vec{F},\Gamma) &= \varepsilon(E,0,\Gamma) + \Delta\varepsilon(E,\vec{F},\Gamma) \\ &= 1 + \frac{iA'}{E^2}\int_{BZ} d^3k \int_0^\infty dt \exp\left[\frac{i(E - E_{cv} + i\Gamma)t + i\Omega t^3/3}{\hbar}\right]\end{aligned} \qquad (5.12)$$

where $A' = \dfrac{4\pi e^2\hbar\left|\hat{e}\cdot\vec{p}_{cv}\right|^2}{m^2}$, $(\hbar\Omega)^3 = e^2\hbar^2F^2/8\mu = (\hbar\theta)^3/4$, $\hbar\theta$ is the electro-optical energy, and μ is the effective mass, defined as $\dfrac{1}{\mu} = \dfrac{1}{m_e} + \dfrac{1}{m_h}$ (m_e and m_h are the electron and hole mass, respectively).

The resulting line shapes vary according to the applied electric fields. Generally, two distinct regions of field strength exist:

1) the high-field region where the Franz-Keldysh effect is observed and
2) the low-field region where broadening effects dominate.

In the first case, the electromodulation (EM) spectrum exhibits, above the band-gap, oscillatory features called Franz-Keldysh oscillations (FKOs), which are a direct measure of the relevant electric field (built-in and/or applied) [5.10]. The second case will be discussed in detail right below.

5.2.2.3 Photoreflectance-spectra in the low-field regime

In the low-field regime, the homogenous broadening Γ is large, i.e., $\Gamma t >> \Omega t^3$. In this case, we expand $\exp(i\Omega t^3/3\hbar) \approx 1 + i\Omega t^3/3\hbar$ in Eq.(5.12), which results in the Aspnes' low-field limit expression [5.10]:

$$\varepsilon(E,\vec{F},\Gamma) = 1 + \frac{A'}{E^2}\int_{BZ} d^3k \int_0^\infty dt\left(1 + \frac{i\Omega t^3}{3\hbar}\right)\exp\left[\frac{i(E - E_{cv} + i\Gamma)t}{\hbar}\right] \qquad (5.13)$$

Integrating the above equation yields the final form:

$$\varepsilon(E,\vec{F},\Gamma)=1+\frac{iA'}{E^2}\int_{BZ}d^3k\frac{1}{E-E_{cv}+i\Gamma}+\frac{2iA'}{E^2}\int_{BZ}d^3k\frac{(\hbar\Omega)^3}{(E-E_{cv}+i\Gamma)^4} \quad (5.14)$$

In the low-field regime, the modulated PR lineshape is related to the third-derivative of the unperturbed dielectric function.

The structures observed in the PR spectra are attributed to interband critical points (CPs), which can be analyzed in terms of standard analytic line shapes [5.11]:

$$\varepsilon\left(E,\Gamma\right)=A\Gamma^{-n}e^{i\varphi}\left(E-E_g+i\Gamma\right)^n, \quad (5.15)$$

which depends upon 5 parameters: amplitude A, phase projection factor φ, threshold (bandgap) energy E_g, broadening parameter Γ, and exponent n. It is useful to define the overall amplitude $A\Gamma^{-n}$ rather than A, so that the coefficient A is independent of the broadening parameter. For undifferentiated spectra the exponent n has the value of –1/2 for one-dimensional (*1D*), 0 for *2D*, and 1/2 for *3D* critical points. Discrete excitons can be included if we allow n to take the value (*-1*). Thus only one functional form covers everything.

In the low-field regime, the broadening parameter Γ is larger than the electro-optical energy $\hbar\theta$ ($\Gamma >> \hbar\theta$ or $\Gamma >> \hbar\Omega$). In this case, only the peak at E_g remains; all other oscillations should be largely washed out. The PR line-shape for band-to-band transitions is related to the third derivative of ε according to $\Delta\varepsilon \approx \left(\hbar\Omega\right)^3 \frac{\partial^3\left(\varepsilon E^2\right)}{\partial E^3}$.

In this case, the experimental modulation spectra of $\Delta R/R$ can be given as:

$$\begin{aligned}\frac{\Delta R}{R}&=\mathrm{Re}\left[\frac{2n_a}{n\left(\varepsilon-\varepsilon_a\right)}\Delta\varepsilon\right]\\&=\mathrm{Re}\left[\frac{2n_a}{n\left(\varepsilon-\varepsilon_a\right)}\left(\hbar\Omega\right)^3\frac{\partial^3\left(\varepsilon E^2\right)}{\partial E^3}\right],\\&=\mathrm{Re}\left[A\Gamma^m e^{i\varphi}\left(E-E_g+i\Gamma\right)^{-m}\right]\end{aligned} \quad (5.16)$$

where m=2.5 for 3D critical points. This equation is the well-known ***Aspnes' Third Derivative Functional Form*** (TDFF) [5.11].

5.2.2.4 Experimental set-up of PR

The experimental set-up of the PR (Figure 5.12) consists of a spectral lamp (XBO, 100 W or Tungsten/halogen lamp 75 or 100 W), a single diffraction grating monochromator (CVI, 1200/grate, 0.25 m), set in the path of the incident light beam, several mirrors and lenses to guide the incident and reflected light, and a semiconductor detector (Si- or InGaAs-diode). The modulation source is an Ar^+- or Kr^+-laser chopped by a mechanical chopper at a frequency of 10 Hz. Laser light scattered on the sample is spectrally separated by a second monochromator (SPEX 1704, 1600/grate, 1 m) set in the path of the reflected light. The detected light is amplified by lock-in techniques. For scans in the energy region above 1.5 eV, the XBO lamp and the Si-detector may be used. Below 1.5 eV, the halogen lamp and the InGaAs detector should be used instead. For low temperature measurements, samples are cooled down to 10 K in a closed-cycle He-cryostat.

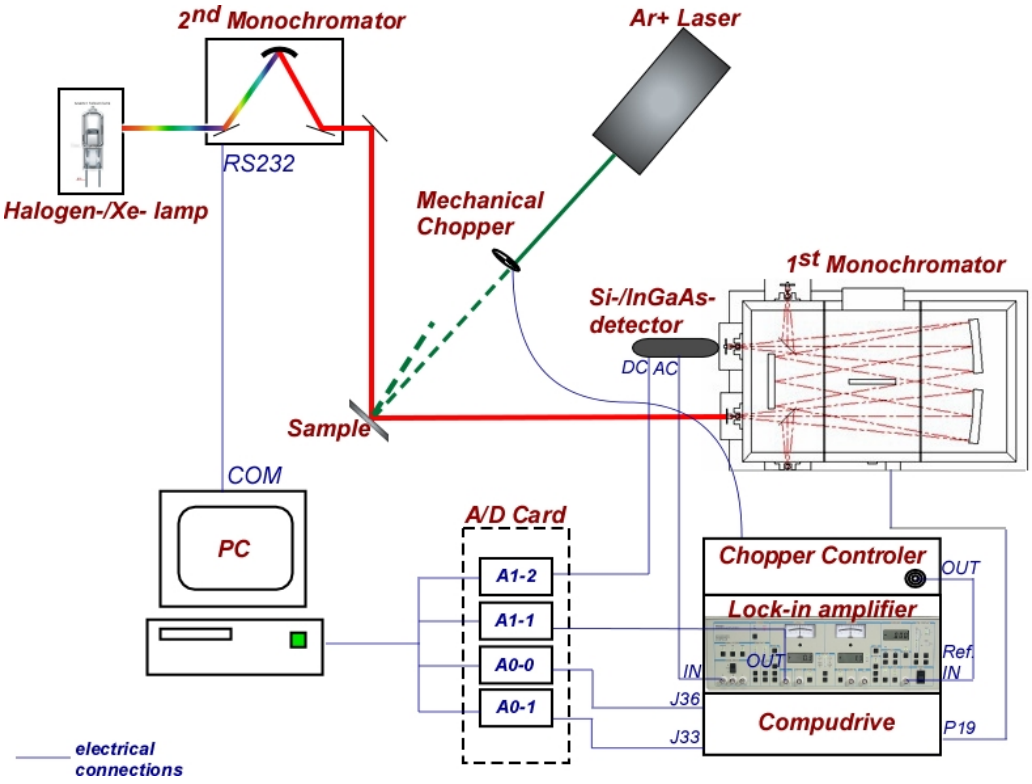

Figure 5.12 Schematic diagram of the PR- set-up.

Depending on the absorption properties of the investigated samples, PR spectra were excited by the irradiation of a tungsten-halogen or a Xe spectral-lamp. The sample properties were modulated by the 488nm line of Ar^+-laser or the 356.4nm line of Kr^+-

laser at chopping frequencies in the range 10-30 Hz. The incident light beam and the laser beam were focused on the same spot of the sample surface. The reflected light was spectrally analyzed by a single-grating monochromator and detected by a Si-diode detector. Alternately, an InGaAs-detector was used.

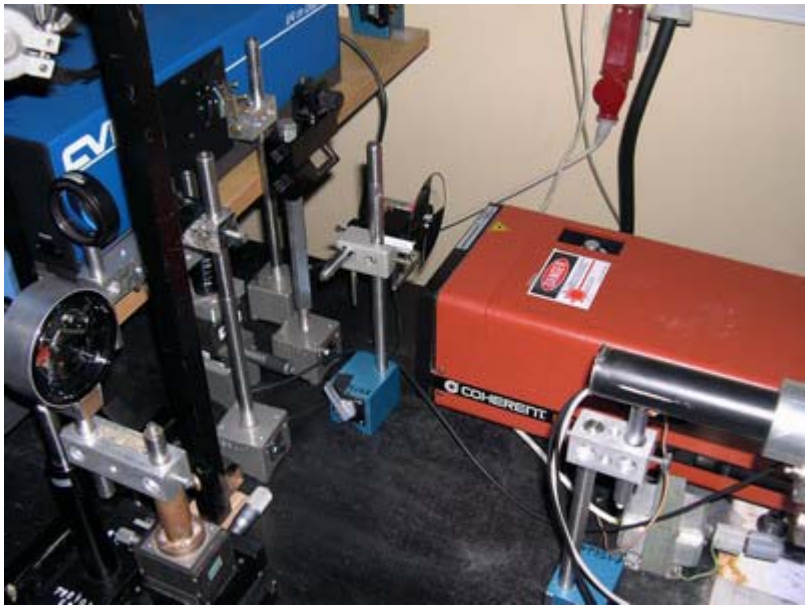

Figure 5.13 The PR- set-up used in the present thesis.

5.2.2.5 Experimental set-up of ER

The experimental set-up for ER is the same as for PR operation. The main difference in this method is the excitation source, which is an electric pulse, generated by a pulse voltage generator. Electroreflectance (ER) measurements were performed on thin film solar cells, in particular on a ZnO/CdS/$CuGaSe_2$/Mo/glass solar cell in dependence of the temperature. The voltage pulse was applied on the front ohmic contact of the solar cell, whereas the back ohmic contact was connected to the ground electrode. The output of the pulse generator was set to 10Hz, with the amplitudes in the range from 0 to +1.5V. A schematic diagram of the ER set-up is shown in Figure 5.14.

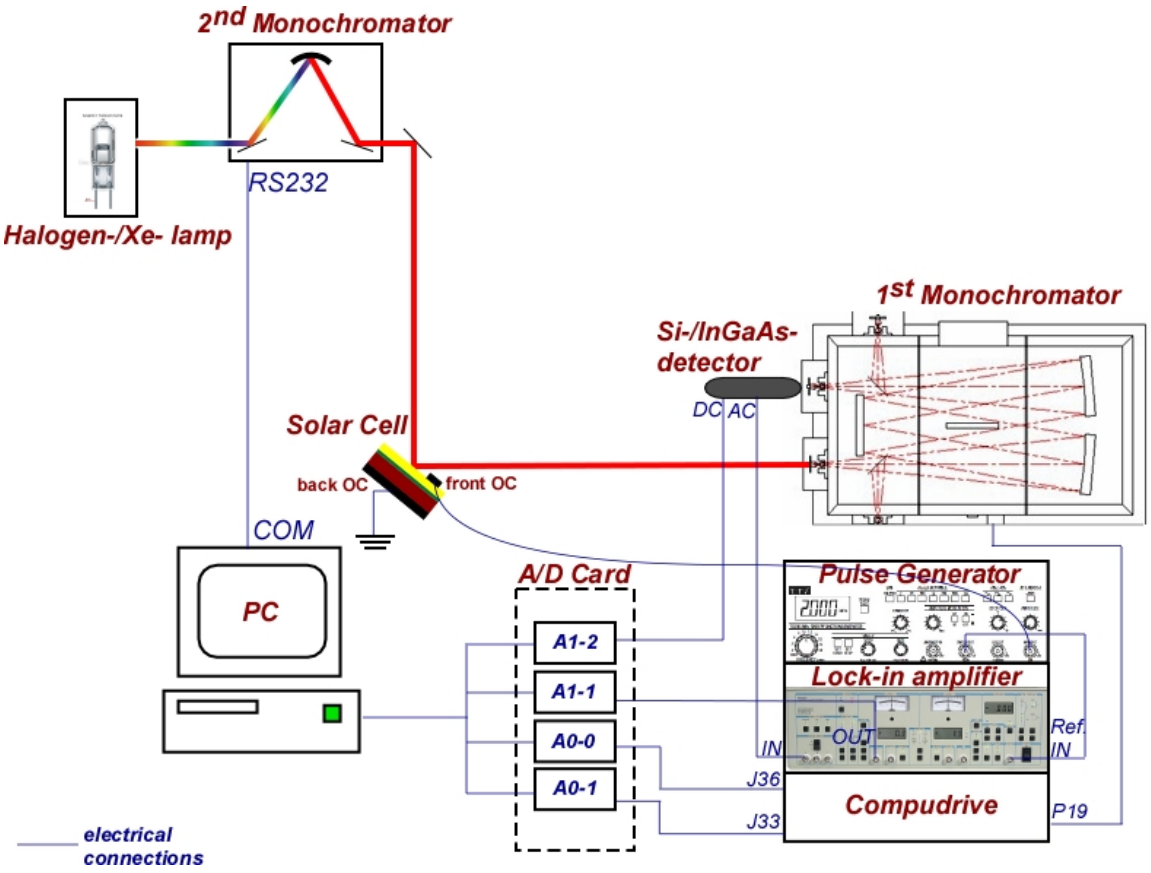

Figure 5.14 Schematic diagram of the ER- set-up.

5.3 Electrical characterization

The electrical properties of the solar cells (I-V characteristics, efficiency η, and Fill Factor *FF*) were measured with a Sun Simulator at the Center for Renewable Energy Sources and Saving (CRES).

Figure 5.15 Sun simulator at the Center for Renewable Energy Sources and Saving (CRES)

6. Results and Discussion

In the present thesis, a systematic study of the chalcopyrite structural and optical properties is realized. Knowing the properties of ternary chalcopyrite absorbers is of great importance, not only because the photogeneration in solar cells takes place in the absorber, but also because ternary chalcopyrites are used, in this work, to develop Cd-free chalcopyrite based thin film solar cells with ZnSe buffer. In fact, ZnSe buffer layers are processed by vacuum (EBE) as well as low low-cost chemical (CBD) techniques and conclusive results are extracted referred to the quality of the deposited layers.

Besides ternary, quaternary chalcopyrites are also studied. From the physical point of view, these extended studies aim to generalization of the results for chalcopyrite semiconductors, while from the technological point of view, ternary CIS and quaternary CIGS chalcopyrites are the most promising candidates for efficient solar cell devices applications.

In the following sections, the structural properties of $CuGaSe_2$ ternary chalcopyrites, studied by X-Ray Diffraction (XRD) and Raman Spectroscopy, are presented. A systematic study of the optical properties of both, bulk- and epitaxial chalcopyrite absorbers, is included. The optical properties are investigated by Modulation Spectroscopy (Photoreflectance) and Spectroscopic Ellipsometry.

Once the structural and optical properties of the chalcopyrite layers are exactly known, the layers are selected for ZnSe buffer-layer growth.

For growth control, ZnSe was initially deposited on glass substrates and the thickness of the deposited layers was calibrated. Following this, ZnSe was deposited on a $CuGaSe_2$ chalcopyrite absorber by Electron-Beam Evaporation Techniques (EBE). The structural and optical properties of the buffer layer were studied using a variety of experimental techniques, such as XRD, SEM, AFM, Raman, and PR.

Following ZnSe deposition, ZnO was deposited on ZnSe/$CuGaSe_2$/Mo/glass by Pulsed Laser Deposition Techniques (PLD).

After the solar cell was readied by depositing a ZnO window-layer and Al-front ohmic contacts, its electrical properties were studied using a Sun Simulator. In particular, the I-V characteristics and the efficiency η of the solar cell were measured.

A. PROPERTIES STUDIES

6.1 Structural properties of chalcopyrite absorbers

Structural characterization of the chalcopyrite absorbers before buffer-layer deposition is of great importance, since the orientation and the crystal quality of the deposited film depend strongly on the underlying absorber properties. Therefore, several chalcopyrite absorbers grown by different methods and with different compositions ([Cu]/[Ga] or [Cu]/[In]) have been processed. The techniques applied in chalcopyrite growth have already been described in § 4.2 and § 4.3.

6.1.1 Epitaxial and polycrystalline $CuGaSe_2$

6.1.1.1 XRD measurements

For the XRD measurements, the Cu-K_{a1} (λ=1.5406 Å) line was used. All XRD-spectra were fitted with Lorenzians. Indicative, Figure 6.1 shows a fitted XRD-spectrum of a ternary polycrystalline $CuGaSe_2$ chalcopyrite on Mo/glass.

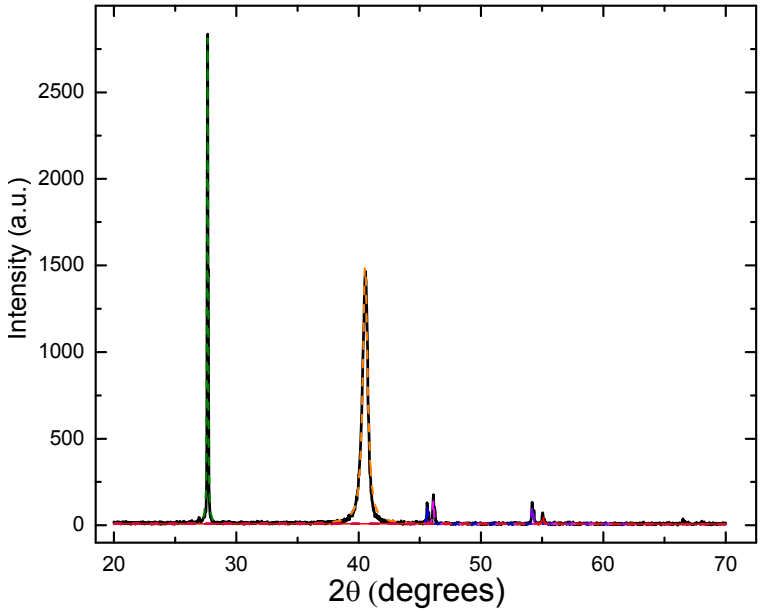

Figure 6.1 Indicative fitting of an XRD-spectrum

In Figure 6.2, the XRD-spectra of $CuGaSe_2$ epitaxial layers with compositions [Cu]/[Ga] = 0.96, 1.10, 1.12, 1.13, and 1.180 are shown. The sharp lines, in the spectra, are related to both, the $CuGaSe_2$ absorber and the GaAs substrate. The XRD data show that the chalcopyrite grows with the same orientation as GaAs. The most intense peak at $2\theta = 68.33^o$ is Bragg-reflection at the (008) crystallographic plane, whereas the less intense peak at $2\theta = 32.64^o$ originates from the (004) crystallographic plane. For GaAs substrate, the peaks for (002) and (004) Bragg-reflections appear at $2\theta = 31.66^o$ and 65.99^o, respectively.

Noteworthy is that, for Cu-rich chalcopyrite layers, secondary microcrystalline Cu-Se phases are formed preferentially on the chalcopyrite surface. These phases are initially observed on the $CuGaSe_2$ layer with [Cu]/[Ga]=1.12 and become distinct for layers with [Cu]/[Ga]=1.8. In particular, the XRD-peaks at $2\theta = 29.23^o$ and 65.83^o are assigned, according to XRD-data known from the literature, to the (101)- and (004)-reflection peaks of Cu_3Se_2 and $Cu_{1-x}Se$ ($0.1<x<0.4$) microcrystalline phases, respectively.

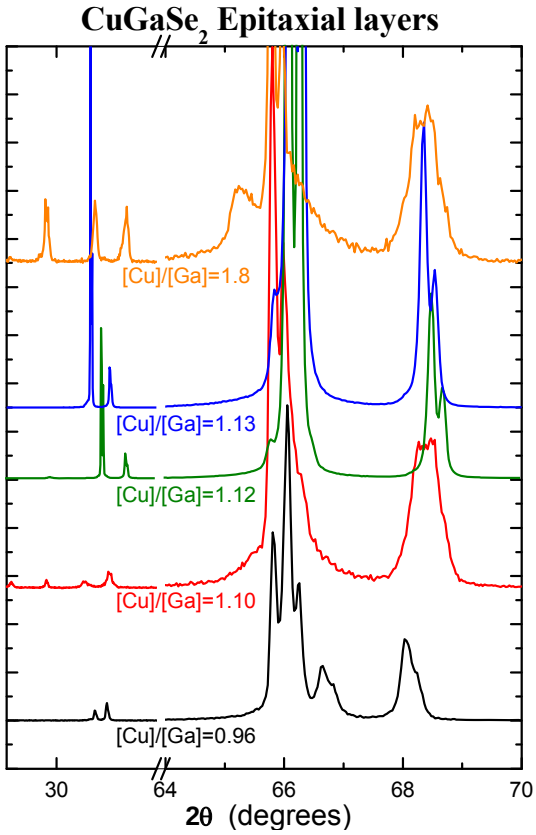

Figure 6.2 XRD-spectra of $CuGaSe_2$ epitaxial layers

with compositions [Cu]/[Ga] = 0.96, 1.10, 1.12, 1.13, and 1.80.

In Figure 6.3, the XRD-spectra of $CuGaSe_2$ polycrystalline layers with compositions [Cu]/[Ga] = 0.89, 1.00, and 1.13, are shown. The sharp peaks observed are assigned to the $CuGaSe_2$ layer and the back ohmic contact Mo. The most intense chalcopyrite peak at $2\theta = 27.67^o$ is Bragg-reflection at the (112) crystallographic plane. Reflections from the (220)-, (204)-, (312)-, and (116)-crystallographic planes are observed at $2\theta = 45.63^o$, 46.13^o, 54.21^o, and 55.08^o, respectively. The peak at $2\theta = 40.51^o$ is (110)-reflection peak of the Mo substrate.

The presence of one intense and four less intense peaks in the XRD-spectra is indicative of the oriented polycrystalline structure of the PVD-grown chalcopyrite layers. The studied polycrystalline chalcopyrites are mainly (≈85%) orientated along the [112] crystallographic direction.

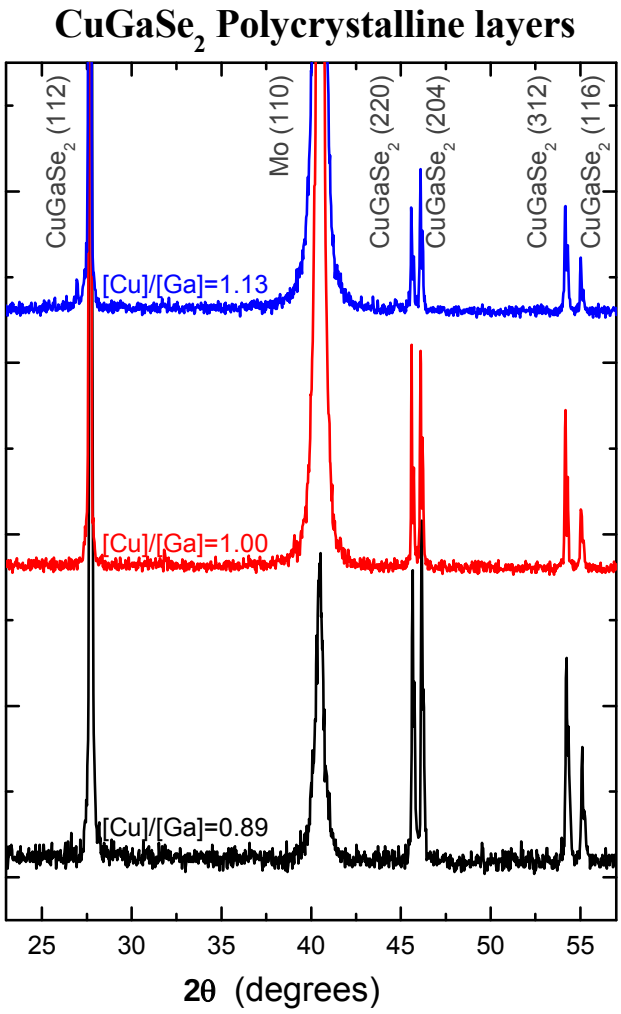

Figure 6.3 XRD-spectra of $CuGaSe_2$ polycrystalline layers with compositions [Cu]/[Ga] = 0.89, 1.00, and 1.13.

The fitted parameters of the above XRD-spectra, in particular, the Bragg angle 2θ, the Full Width at Half Maximum (FWHM), and the intensity of the peak, have been entered in the collective diagrams, shown in Figure 6.4. As mentioned above, the preferential orientation of the $CuGaSe_2$ epitaxial layers is the [008] and appears at $2\theta = 65.83^o$, whereas that of the $CuGaSe_2$ polycrystalline layers is the [112] and appears at $2\theta = 27.67^o$. The orientation of both, the epitaxial and the polycrystalline layers, does not depend significantly on the Ga fraction. Furthermore, the epitaxial layers with [Cu]/[Ga] near stoichiometry are of better quality as indicated by the decrease of the FWHM and the increase of the intensity of the XRD-spectra in Figure 6.4. For very Cu-rich chalcopyrites, the crystal quality is drastically reduced.

Observations similar to prior ones imply that the crystal quality of polycrystalline $CuGaSe_2$ chalcopyrites is reduced with the increase of the Ga-fraction and is low for Ga-rich absorbers. Generally, Ga-rich chalcopyrites exhibit extensive defects in the crystal structure as demonstrated in Ref. [6.1].

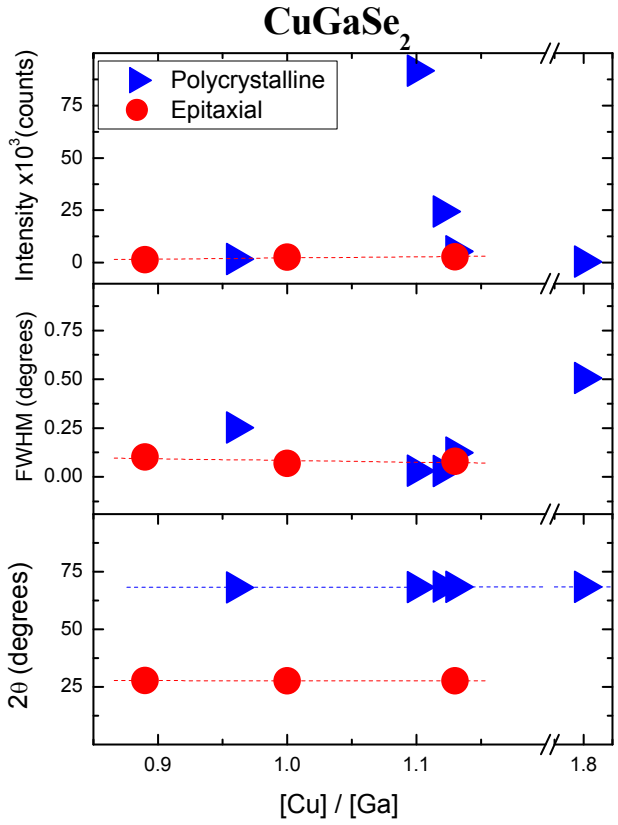

Figure 6.4 Bragg angle, FWHM, and Intensity drawn from fitting the XRD-spectra:

(Red circles designate epitaxial layers, blue triangles, polycrystalline ones)

6.1.1.2 Micro-Raman measurements

Structural characterization of $CuGaSe_2$ epitaxial and polycrystalline layers has also been performed by micro-Raman spectroscopy. Micro-Raman spectra were fitted with Lorentzians. An indicative fitting is shown in Figure 6.5.

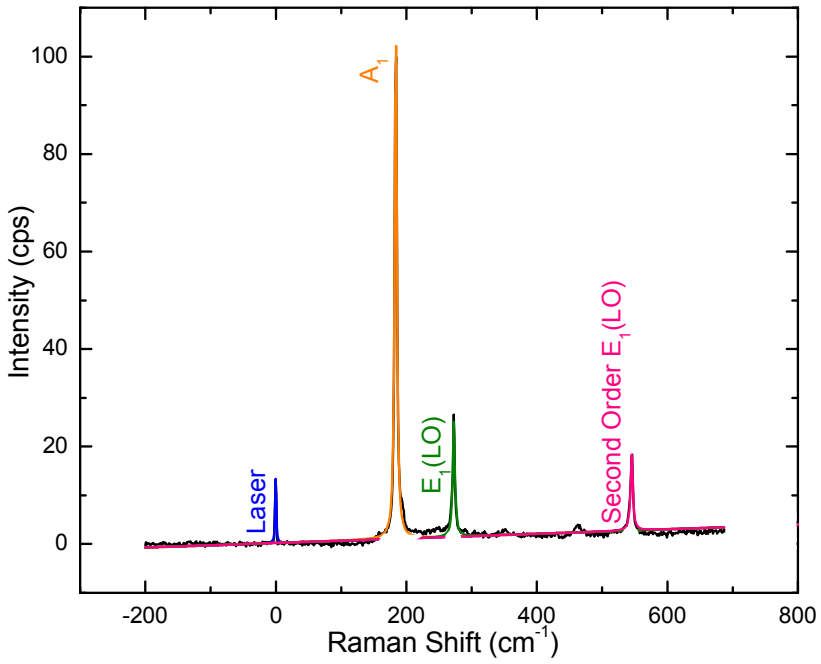

Figure 6.5 Indicative fitting of a micro-Raman spectrum

As already mentioned in § 2.1.2, the tetragonal distorted chalcopyrite absorbers have 22 Raman-active vibrational modes. For the investigation of structural properties of epitaxial (Figure 6.6) and polycrystalline (Figure 6.7) $CuGaSe_2$ films, the most intense Raman modes, A_1 at 183.85 cm^{-1} and $E_1(LO)$ at 272.76 cm^{-1}, are used as indicators. The A_1 mode corresponds to phonon excitation from the Γ_1 Brillouin-zone-center and the E_1 longitudinal optical (LO) mode corresponds to phonon excitation from the Γ_5 point of the Brillouin-zone. In all the micro-Raman spectra, the second order of the A_1-mode is also observed. The identification of the peaks has been performed according to [6.2].

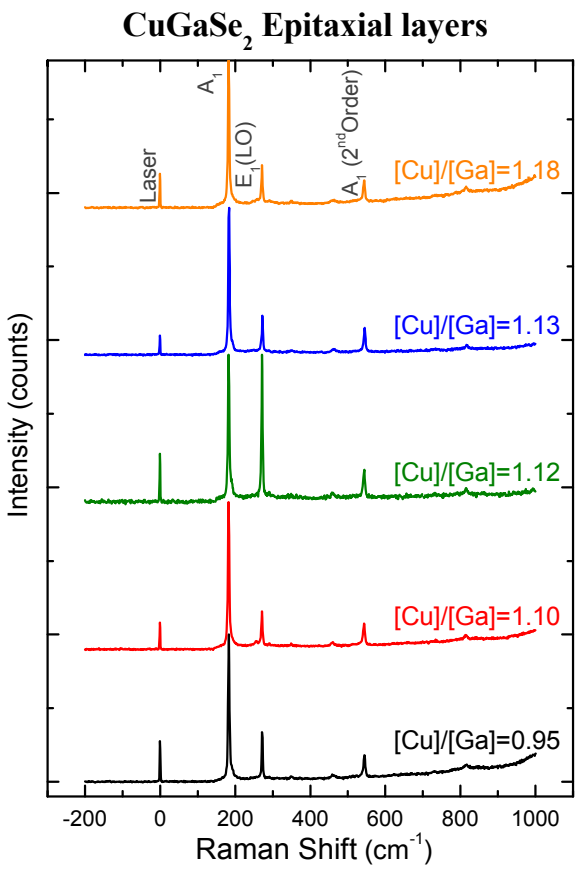

Figure 6.6 micro-Raman -spectra of $CuGaSe_2$ epitaxial layers with compositions [Cu]/[Ga] = 0.95, 1.10, 1.12, 1.13, and 1.80.

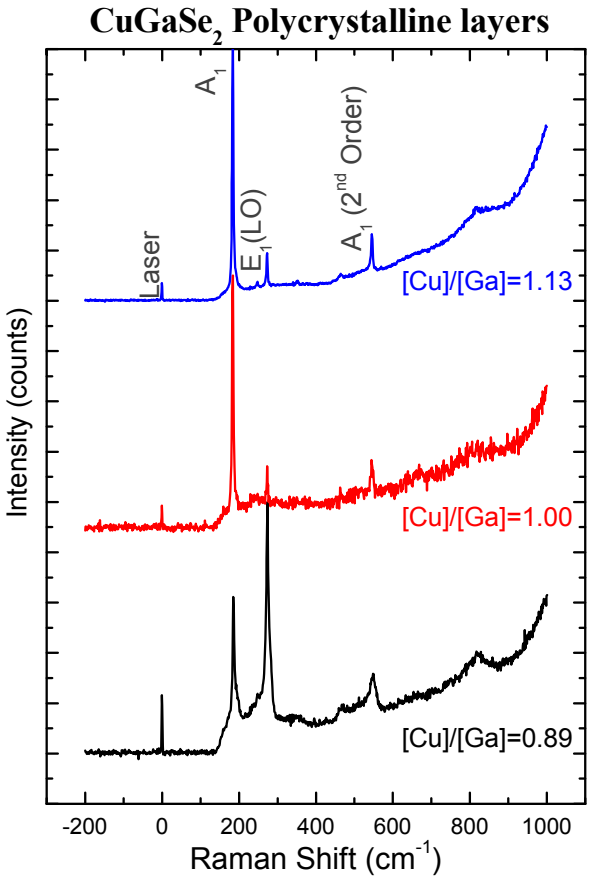

Figure 6.7 micro-Raman -spectra of $CuGaSe_2$ polycrystalline layers with compositions [Cu]/[Ga] = 0.89, 1.00, and 1.13.

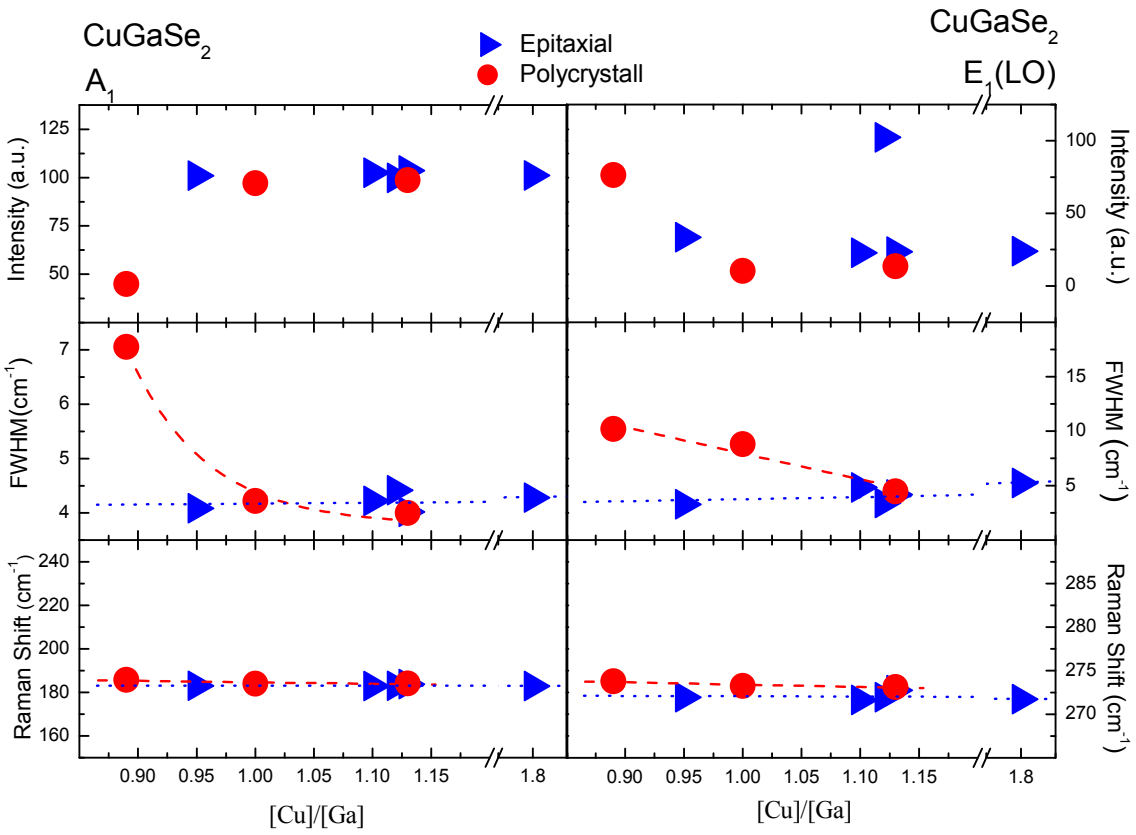

Figure 6.8 Raman-Shift, FWHM, and Intensity, of both A_1 and E_1 Raman modes, for epitaxial (blue triangles) and polycrystalline (red circles) chalcopyrite layers.

With increasing the Ga content, the A_1-mode frequency, intensity and band-width of epitaxial grown samples remain almost unchanged as demonstrated in Figure 6.8. The same observation is made for both, A_1- and E_1-modes. Contrary to the epitaxial, with increasing the Ga content, in the polycrystalline $CuGaSe_2$ absorbers, the Raman-shift is almost the same. The width of both, A_1- and E_1-modes, is increased for Ga-rich absorbers, whereas the intensity is decreased. This behavior indicates that Ga-rich $CuGaSe_2$ absorbers exhibit reduced crystal quality.

The results of the Raman and XRD measurements are in total agreement.

6.2 Optical properties of chalcopyrite absorbers

The optical properties of chalcopyrites have been studied with two complementary techniques, Photoreflectance and Ellipsometry, both of which have been already described in § 5.2.

6.2.1 Comparison of bulk and epitaxial absorbers

Systematic comparative studies of chalcopyrite single crystals grown by Chemical Vapor Transport (CVT, § 4.1) and monocrystalline epitaxial layers grown by Metal-Organic Vapor Phase Epitaxy (MOVPE, § 4.2) are presented. Photoreflectance spectroscopy (PR) is applied at room and low temperatures to investigate the structural and optical properties of ternary ($CuGaSe_2$, $CuInSe_2$, $CuGaS_2$, $CuInS_2$) and quaternary ($CuIn_{1-x}Ga_xSe_2$) chalcopyrite absorbers with applications in solar-cell device technology.

By applying PR spectroscopy, strain/stress effects can be quantified, structural changes due to anion/cation replacement in ternary and quaternary chalcopyrites can be identified, and light polarization effects promoting the chalcopyrite ability to absorb solar radiation can be sensed. In accordance, the observed changes of (optical) transition energies due to strain, anion/cation replacement, and temperature, and the selection rules for optical transitions as a result of light polarization are used to identify and, so far it is possible, to quantify these effects. Apart from this, the results of strain quantification by PR are compared with the results obtained independently by application of standard strain characterization X-ray Diffraction (XRD) Techniques.

i) The effect of elastic strain on the crystal quality of chalcopyrite heterostructures. It is demonstrated that mismatch and thermal strain can be quantified by using the energy shift of the PR-bands of epitaxial layers with respect to the PR-bands of the bulk at room (RT) and lower temperatures (20K). The results of strain analysis by PR techniques are consistent with those indicated by XRD analysis of strain. Moreover, optical modulation techniques have been recently shown to provide higher-resolution compared to Raman analysis of strain in the respective structures [6.3]. It should be noted, that Raman spectroscopy, a well established experimental tool, is based on the detection of strain induced phonon frequency shifts [6.4]. Optical Modulation techniques, such as piezoreflectance spectroscopy and piezoelectroreflectance, on the other hand, are applied to investigate the effect of strain on the electronic bands [6.5].

ii) The effect of cation- and/or anion-replacement, temperature, and polarization of the incident light beam on the chalcopyrite optical properties. There are three types of replacement, that directly affect interband transitions in the vicinity of the chalcopyrite optical gap: 1) cation-replacement in $CuInSe_2$ (or $CuInS_2$) absorbers, with

In cations replaced by Ga to form $CuGaSe_2$ (or $CuGaS_2$), 2) anion-replacement in $CuGaSe_2$ (or $CuInSe_2$) absorbers, with Se-anions replaced by S to form $CuGaS_2$ (or $CuInS_2$), and 3) partial cation-replacement, with part of the In-atoms in $CuInSe_2$ absorbers substituted by Ga to form quaternary $CuIn_{1-x}Ga_xSe_2$ chalcopyrites (x represents the Ga-fraction). Substitution induced band energy shifts are found to be in agreement with theoretical predictions [6.6] and semi-empirical calculations [6.7]. Agreement between theory and experiment is also found in the temperature dependence of energy bands. At moderate temperatures, light absorption is governed by E_a and E_b transitions. At lower temperatures, transitions are facilitated due to the lack of interferences and the E_c transition emerges. Apart from this, it is demonstrated, that the efficiency of interband transitions depends directly on the polarization state of the incident light-beam and that orientation effects influence significantly the interaction of light with the chalcopyrite absorber.

As far as chalcopyrite material properties are investigated, though there have been already a lot of literature reports on this topic, the most significant ones referred in [6.5]-[6.9], the present analysis is the first one that directly links the properties of monocrystalline (epitaxial) layers of several ternary and quaternary chalcopyrites with those of chalcopyrite bulk crystals.

6.2.1.1 Strain-Stress by XRD-analysis Techniques (T=300K).

a) $CuGaSe_2$ with [Cu]/[Ga]=1.00.

The XRD-diffractograms of a stoichiometric ([Cu]/[Ga]=1.00) $CuGaSe_2$ single crystal and an epitaxial layer of equal stoichiometry are shown in Figure 6.9. In the XRD-diffractogram of the $CuGaSe_2$ single crystal, the peak at $2\theta=32.61^o$ is assigned to the Bragg reflection on the $CuGaSe_2$ (004) crystallographic plane. In the XRD-diffractogram of the epitaxial layer, the peaks at $2\theta=68.33^o$ and 32.64^o are assigned to the (008) and (004) Bragg reflections, respectively. For the GaAs substrate, the peaks at $2\theta=31.66^o$ and 65.99^o are (002) and (004) reflections, respectively. The mismatch strain normal-to-the-plane (ε_{zz}) was calculated according to Eq.(3.7) using Bragg's law (with d_0 spacing of the single crystal (unstrained) and d spacing of the epitaxial layer (strained)), and the (004) Bragg reflections of single crystal and epitaxial layer. The calculation

yields ε_{zz} = -0.0009. The corresponding in-plane stress was calculated to σ =+76MPa by inserting the elastic stiffness components of $CuGaSe_2$: C_{11}=112.2GPa and C_{12}=66.4GPa [6.10] in Eq.(3.13). The positive sign depicts tensile stress.

b) $CuGaSe_2$ with [Cu]/[Ga]=1.10.

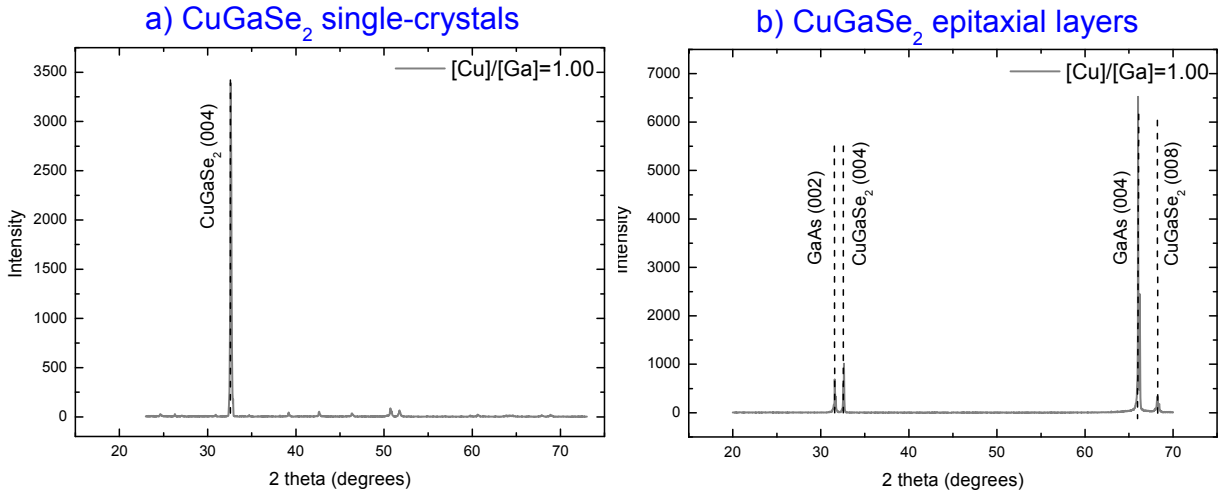

Figure 6.9 XRD-spectra of single-crystal (a) and epitaxial (b) $CuGaSe_2$ with [Cu]/[Ga]=1.00

The XRD-diffractograms of a slightly Cu-rich ([Cu]/[Ga]=1.10) $CuGaSe_2$ single crystal and an epitaxial layer with the same composition have also been measured. Bragg peaks appear at 32.57° ((004) reflection of the $CuGaSe_2$ bulk crystal) and at 32.64° and 68.33° ((004) and (008) reflections of the $CuGaSe_2$ epitaxial layer, respectively). Similar to the above, the normal-to-the-plane strain and the corresponding planar stress were calculated to ε_{zz} = -0.002 and σ = +176MPa.

6.2.1.2 Strain-Stress by Optical Modulation Techniques at Low Temperatures (T=20K).

a) $CuGaSe_2$ with [Cu]/[Ga]=1.00.

In Figure 6.10, the PR-spectra of both, a $CuGaSe_2$ single crystal a) and an epitaxial layer b) with [Cu]/[Ga]=1.00 are shown. The PR-spectra were fitted using a Third Derivative Functional Form (TDFF) derived by Aspnes [6.11]. The fitting results are represented by dashed-lines in the experimental spectra. Referred to fundamental-gap energies of chalcopyrite single crystals, the E_a transition energy of the epitaxial layer, in

the PR-spectra, is shifted. The Photoluminescence (PL) spectra of epitaxial layers appear also shifted compared to the PL-spectra of the bulk [6.12]. The energy shift of both, PR- and PL-spectra, is mostly due to mismatch strain effects.

A common observation is the line broadening of the PR-spectra of Cu-rich samples compared to the spectra of stoichiometric samples. The line-width of the PR-spectra of ternary and quaternary chalcopyrites can be explained as originated by compositional effects and limitations in structural ordering. It has been found [6.13]-[6.14], that the broadening parameter Γ in the PR-spectra of $CuGaSe_2$ depends strongly on the [Cu]/[Ga] ratio in the material, while transition energies are not significantly affected. On the other hand, transition energies are always shifted by elastic strain, while line broadening occurs only in the presence of large amounts of strain. In accordance with these observations, it is assumed that the line-width of the single crystals and epitaxial layers studied depends on compositional effects and effects of structural disorder, while band-energy shifts are generated by elastic-strain effects. Based on this assumption, the experimentally measured values of the E_a and E_b transitions are used, in the following, to quantify the effects of mismatch strain in epitaxial grown layers of ternary chalcopyrites.

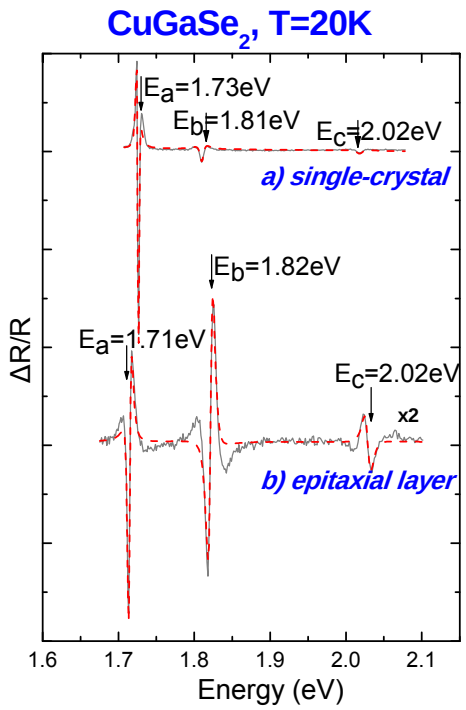

Figure 6.10 PR-spectra of stoichiometric ([Cu]/[Ga]=1.00) single-crystal (a) and epitaxial (b) $CuGaSe_2$ at 20K.

The mismatch strain (ε_{xx}) in the stoichiometric ([Cu]/[Ga]=1.00) epitaxial $CuGaSe_2$ layer, at low temperatures (T=20K), was calculated with Eq.(3.5) via Eq.(3.16) using the values of the optical transitions E_a and E_b determined from fitting the PR spectra and the shear deformation potential of $CuGaSe_2$ (*b=-2.7eV* [6.15]). The component of mismatch strain normal-to-the-plain (ε_{zz}), calculated from the energy-shift of the PR-spectra of $CuGaSe_2$ (Eq.(3.16)), is ε_{zz} = -0.0043 and that of the strain parallel to-the-plane (ε_{xx}), ε_{xx} = +0.0037 (Eq.(3.5)). The in-plane stress calculated with Eq.(3.6) is σ = +366MPa. The positive sign depicts tensile stress.

b) $CuGaSe_2$ with [Cu]/[Ga]=1.10.

For Cu-rich ([Cu]/[Ga]=1.10) $CuGaSe_2$, the components of mismatch strain normal- and parallel-to-the-plain (ε_{zz}), calculated from the energy-shift of the PR-spectra, are ε_{zz} = -0.0058 and ε_{xx}= +0.0049. The in-plane stress is σ = +488MPa.

Evaluation of strain at 20K by inserting the lattice constants of the GaAs substrate and the $CuGaSe_2$ epilayer known from the literature (Table 6.1) directly in Eq.(3.2), under consideration of Eq.(3.17), and calculating the corresponding stress with Eq.(3.6) (or alternately Eq.(3.13)) results in σ= +1035MPa, in case of stoichiometric $CuGaSe_2$.

The value obtained by optical modulation techniques on the stoichiometric $CuGaSe_2$ sample (σ = +366MPa) seems to be almost by factor 3 (2.8) underestimated from the calculated one. Divergences to this extend could be possibly explained by adaption of quasi-cubic model in the description of initially tetragonally distorted chalcopyrite lattice and the disregard of the temperature dependence of the thermal expansion coefficients of $CuGaSe_2$ and GaAs in Eq.(3.17).

It should be noted, that for another member of the chalcopyrite-type ternary semiconductors, $CuInSe_2$, the linear thermal expansion coefficient α_a [6.16] decreases up to 116% in the range from 300 to 40K. Assuming that the thermal expansion coefficient of $CuGaSe_2$ follows a similar trend, thus being α_a= -2.15 10^{-6} K^{-1} at 40K, the in-plane strain calculated with Eq.(3.2), under consideration of Eq.(3.17), is ε_{xx}= +0.0059. The stress calculated to σ=+594MPa deviates by factor less than 2 (1.7) from the stress obtained by means of Optical Modulation Techniques. This deviation can be further reduced by the use of the thermal expansion coefficient at T=20K instead of 40K, provided that adequate data are given in the literature.

Table 6.1 Lattice constants a_{REF} referred in the literature at room temperature, lattice constants a^{LT} at low temperature (LT), and thermal expansion coefficients α_a of both $CuGaSe_2$ epilayer and GaAs substrate at 300K.

Compound	**a_{REF} (Å)**	**a^{LT} (Å)**	**α_a (10^{-6} K^{-1})**
$CuGaSe_2$	5.607 [6.17]	5.586	13.45 [6.19]
GaAs	5.653 [6.18]	5.644	5.87 [6.18]

6.2.1.3 Strain-Stress by Optical Modulation Techniques at Room Temperature (T=300K).

a) $CuGaSe_2$ with [Cu]/[Ga]=1.10.

It was possible to obtain PR-spectra of Cu-rich bulk and epitaxial chalcopyrites also at room temperature (300 K). The components of mismatch strain normal- and parallel-to-the-plain (ε_{zz}), calculated from the energy-shift of the PR-spectra, are ε_{zz} = -0.0014 and ε_{xx}= +0.0012. The in-plane stress is σ = +122MPa. With the increase of temperature, stresses decrease and are expected to diminish at growth temperatures. The epitaxial layer is grown free of strain at elevated temperatures and becomes elastically strained during cooling because of the mismatch in the thermal expansion coefficients between epilayer and substrate [6.20].

6.2.1.4 Comparison of Strain-Stress by Optical Modulation and XRD Techniques.

By comparison, the strain/stress analysis results obtained at 300K by application of Optical Modulation (σ = +122MPa) and XRD (σ = +176MPa) Techniques on Cu-rich $CuGaSe_2$ samples with [Cu]/[Ga]=1.10 differ by factor 1.4 (30%) only; this difference is tentatively attributed to simplifications adapted in the evaluation of residual stress by using Eq.(3.10) instead of Eq.(3.9) for standard XRD analysis as well as experimental and fitting errors.

6.2.1.5 Anion- and/or Cation-Replacement

The effects of full or partial replacement of the In-cation by Ga and the S-anion by Se are analyzed in the following sections. The PR-spectra of both single-crystals and epitaxial layers are shown in Figure 6.11 and Figure 6.12, at 20 and 300K respectively. The optical transition energies determined for each chalcopyrite material by PR analysis are summarized in Table 6.2.

Table 6.2 Band gap energies of ternary chalcopyrite absorbers

obtained from the PR-spectra shown in Figure 6.11 and Figure 6.12

	Compound	**E_a (eV)**	**E_b (eV)**	**E_c (eV)**	**T (K)**
single crystals	$CuGaSe_2$	1.73	1.81	2.02	20
	$CuInSe_2$	1.04	1.05	1.26	
	$CuInS_2$	1.53	1.56	1.57	
epitaxial layers	$CuGaSe_2$/GaAs	1.68	1.77	1.96	300
	$CuInSe_2$ /GaAs	1.02	1.04	-	
	$CuGaS_2$ /GaAs	2.47	2.58	-	
	$CuIn_{0.81}Ga_{0.19}Se_2$/GaAs	1.12	1.16	-	

Cation Replacement

In the ternary chalcopyrites, cation replacement affects significantly the absorber energy-gap. As demonstrated in Figure 6.11, for the single-crystals at 20K, and in Figure 6.12, for the epitaxial layers at 300K, in $CuInSe_2$, the transition energies E_a, and E_b are lower than the energies in $CuGaSe_2$, which can be explained as originating from the energy dependence of the Cu *d*-character in the upper valence band [6.6]. According to J. E. Jaffe [6.6], the Cu centered *d*-contribution to the density of states reaches its maximum at 3-4 eV below the valence band maximum (VBM), has a double-structure peak, and the distance between this peak and the VBM increases in the sequence Ga → In. The electronic structure of the upper valence band is dominated by the Cu *d* – Se *p* interactions, with the strongest interaction for gallium compounds. This is the most significant difference between the structure of the upper valence band of the binary and ternary semiconductors.

Another issue emerging is the splitting of E_a and E_b bands. In $CuInSe_2$, the E_a and E_b bands are so close that band separation is almost impossible (Figure 6.11a, and Figure 6.12a), whereas in $CuGaSe_2$, the two bands are clearly separated (Figure 6.11c, and Figure 6.12b). This fact can be also explained [6.21] as originated by the evolution of the energy states at the band-gap of the chalcopyrites. With the introduction of the tetragonal crystal field and the spin orbit interaction, the threefold-degenerate Γ_{15} state in zinc blende splits in three levels ($2\Gamma_7+\Gamma_6$). The ordering of the topmost valence bands, along with the distance between Γ_6 and the upper Γ_7 band, are different in $CuInSe_2$ and $CuGaSe_2$ (Figure 2.3).

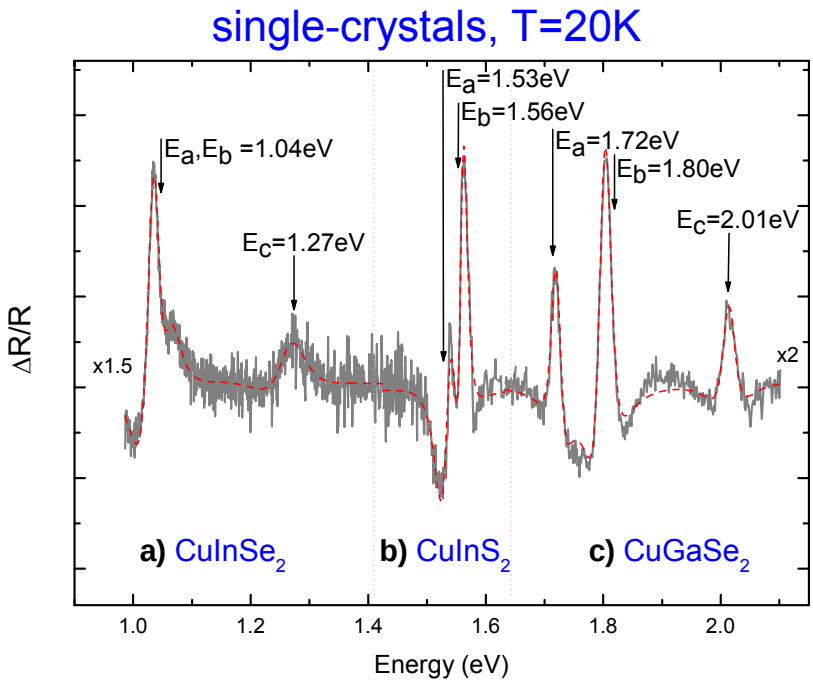

Figure 6.11 PR-spectra of single-crystal chalcopyrite absorbers at 20K; (a) and (b) indicative of anion replacement, and (a) and (c) indicative of cation replacement

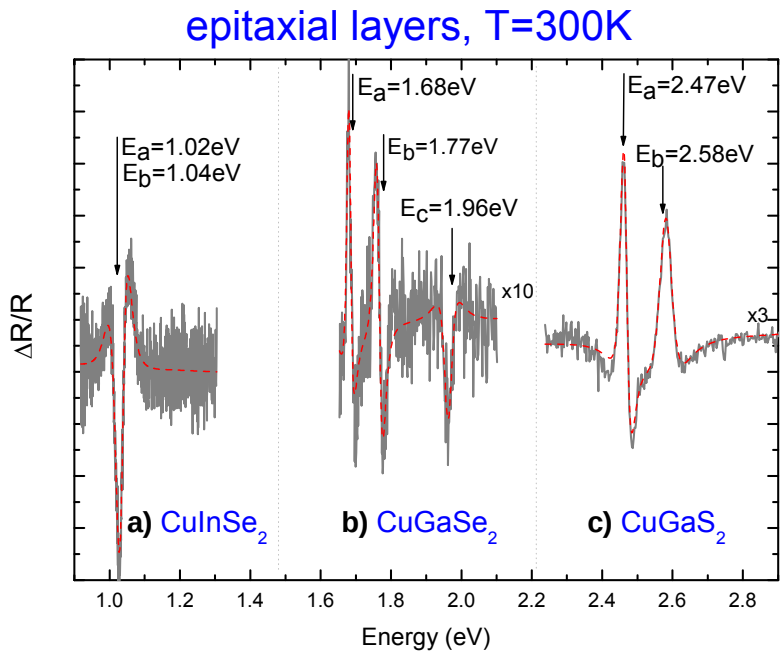

Figure 6.12 PR-spectra of epitaxial chalcopyrite absorbers at 300K; (a) and (b) indicative of cation replacement, and (b) and (c) indicative of anion replacement

Anion Replacement

Anion replacement in chalcopyrite absorbers is also of great significance [6.6]. The existence of the Cu *d*-character in the upper valence band has an immense consequence for the optical band-gaps. The Γ_{15} *d*-like combinations of the *d*-orbitals interact with the Γ_{15} *p*-like combinations of the anion *p*-orbitals at the VBM. The strength of this interaction depends inversely on the energy separation between the Cu *d*- and the anion *p*-orbitals. It is expected hence to be stronger for the sulfides than for the selenides, which accounts for the higher energy gap of $CuInS_2$ compared to the gap of $CuInSe_2$ (Figure 6.11a and b) in the chalcopyrite single crystals and for the higher energy gap of $CuGaS_2$ compared to the gap of $CuGaSe_2$ (Figure 6.12b and c) in the epitaxial chalcopyrite layers.

6.2.1.6 Partial Cation Replacement

Since $CuInSe_2$ has band-gap energy of only ~1eV, which is lower than the ideal value for photovoltaic energy conversion, it has been suggested, that Ga addition to $CuInSe_2$ (partial replacement of the cation In by Ga) to form the $CuIn_{1-x}Ga_xSe_2$ alloy would raise the band-gap energy.

The compositional dependence of band gap energies of $CuIn_{1-x}Ga_xSe_2$ alloys at 300 and 20 K has been discussed extensively in one of our previous publications [6.22]. In the present work, the room temperature PR spectra of an epitaxial quaternary $CuIn_{1-x}Ga_xSe_2$ layer, with Ga fraction x= 0.19, and the spectra of the ternary end-members of the series, with x= 0.00 and 1.00, are presented (Figure 6.13). With the increase of Ga-content, the E_a and E_b band energies of the ternary compounds shift to higher energies, varying from E_a=1.02eV and E_b=1.04eV for $CuInSe_2$ (x=0.00) to E_a=1.68eV and E_b=1.77eV for $CuGaSe_2$ (x =1.00). The E_a and E_b band energies of the quaternary, E_a=1.12eV and E_b=1.16eV, lay in between, as expected. Apart from this, with the increase of the Ga-fraction, the PR-spectra show band broadening as a result of increasing disorder.

The band-gap E_g of $CuIn_{1-x}Ga_xSe_2$ alloys can often be described by an empirical relationship utilized in Eq. (6.1) [6.7]:

$$E_g(x) = (1-x)E_g(CIS) + xE_g(CGS) - bx(1-x) \qquad (6.1)$$

where b is an optical bowing parameter. The E_a and E_b transition energies for the quaternary $CuIn_{1-x}Ga_xSe_2$ with Ga fraction x=0.19 were calculated to E_a=1.11eV and E_b=1.15eV by inserting in Eq. (6.1) the experimentally measured values of the E_a and E_b gaps for $CuInSe_2$ and $CuGaSe_2$, and the bowing parameter given in [6.7]. The experimental values for $CuIn_{1-x}Ga_xSe_2$ (x=0.19), E_a=1.12eV and E_b=1.16eV, differ from the calculated ones only by 1%.

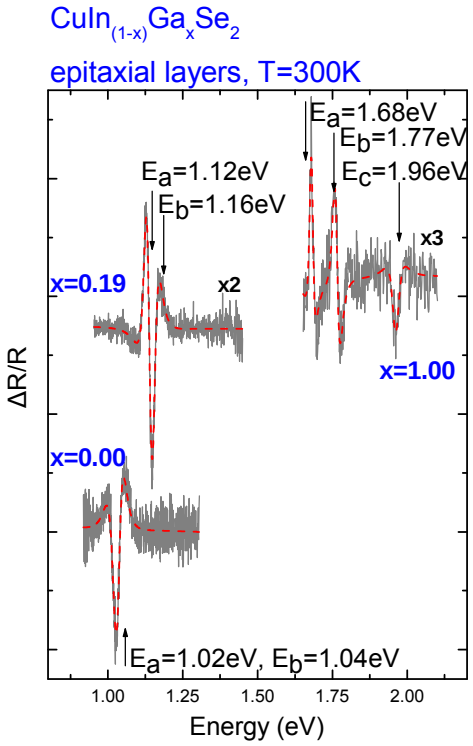

Figure 6.13 Compositional dependence of the PR-spectra of $CuIn_{1-x}Ga_xSe_2$ epitaxial layers at 300K (x = 0.00, 0.19, and 1.00) indicative of the band energy-shift with partial anion replacement.

6.2.1.7 Temperature Dependence

The temperature dependence of the semiconductor band-gap has been described by an empirical formula (Eq.(2.19)) derived by Varshni [6.23], as described in §2.1.3.2. In Figure 6.11c and Figure 6.12b, the temperature dependence of the $CuGaSe_2$ single crystals and epitaxial layers at room- (300K) and low- (20K) temperatures is demonstrated. Using Eq.(2.19) and values of $\alpha=3\ 10^{-4}$eV/K and b=277K published for

$CuGaSe_2$ [6.24], the calculated value of the band-gap energy at 300K is E_g^{calc}=1.66eV. Though the energy band-gap of $CuGaSe_2$, for temperatures below 100K, tends to acquire a constant value [6.25], for consistency reasons, instead of E_g at 0K, the corresponding value at 20K has been used for the calculation. The measured band-gap energy of both, the epitaxial layer and the single-crystal, at 300K (E_g=1.68eV) deviates from the calculated one by 0.6% only.

6.2.1.8 Anion/Cation Replacement & Temperature Dependence

As already stated, cation replacement shifts the E_a, E_b, and E_c transitions to higher energies. Comparing the PR-spectra of $CuInSe_2$ and $CuGaSe_2$ at 20K (Figure 6.11a and c) and 300K (Figure 6.12a and b), it is obvious that the E_a and E_b transition energies for $CuInSe_2$ are lower than the transition energies for $CuGaSe_2$. Besides, at lower temperatures, where degrees of freedom are frozen and interferences are being radically reduced, the E_c transition of $CuInSe_2$ is also observed (Figure 6.11a). Nevertheless, the decrease of temperature did not result in separation of the E_a and E_b bands in $CuInSe_2$.

Similar holds for the PR-spectra of $CuInSe_2$ and $CuInS_2$ absorbers at 20K (Figure 6.11a and b). As already stated, anion replacement shifts the E_a, E_b, and E_c transitions to higher energies. This is due to the interaction between the Cu *d*- and the anion *p*-orbitals. At low temperatures, the E_a and E_b bands of sulfides are fully separated in contrast to those of selenides, which, even at the lowest temperature of 20K, overlap. However, the E_b and E_c bands of sulfides are not separated even at the lowest temperature of 20K, which is in agreement with the results of both, Photoreflectance Spectroscopy measurements [6.26] published in the past and recent Spectroscopic Ellipsometry measurements [6.27].

6.2.1.9 Light Polarization

The selection rules of light polarization referred in section § 2.1.3 are of great significance for interband transitions. It has been experimentally observed [6.28], that in CGS-like materials light polarization parallel to the optical axis c ($\vec{E} \parallel \vec{c}$) favors the E_a

transition, contrary to light polarization perpendicular to the optical axis c ($\vec{E} \perp \vec{c}$), which allows occasionally a rather weak E_a transition.

In Figure 6.14, the PR-spectra of a $CuGaSe_2$ epitaxial layer at 300K, for incident light without polarization and light with vertical- and horizontal-polarization orientation are presented.

For a non-polarized light beam, the E_a transition appears to be slightly more intense than the E_b transition.

When the light beam is polarized vertically, the electric field $\vec{E}$ is perpendicular to the optical axis of the sample ($\vec{E} \perp \vec{c}$), leading to a slightly dominant E_b transition and a weak E_a transition.

When the light beam is polarized horizontally, the electric field $\vec{E}$ has both, parallel ($\vec{E} \parallel \vec{c}$) and perpendicular ($\vec{E} \perp \vec{c}$) components, leading to a slightly dominant E_a transition, in the same manner as for a non-polarized light beam. As indicated in Figure 2.3, this should be expected for a CGS-like absorber, in the presence of large Δ_{SO}: the E_a and E_c transitions are for both polarization orientations, $\vec{E} \perp \vec{c}$ and $\vec{E} \parallel \vec{c}$, allowed. The E_b transition is absent only in case of a pure parallel to the optical axis polarized light beam ($\vec{E} \parallel \vec{c}$).

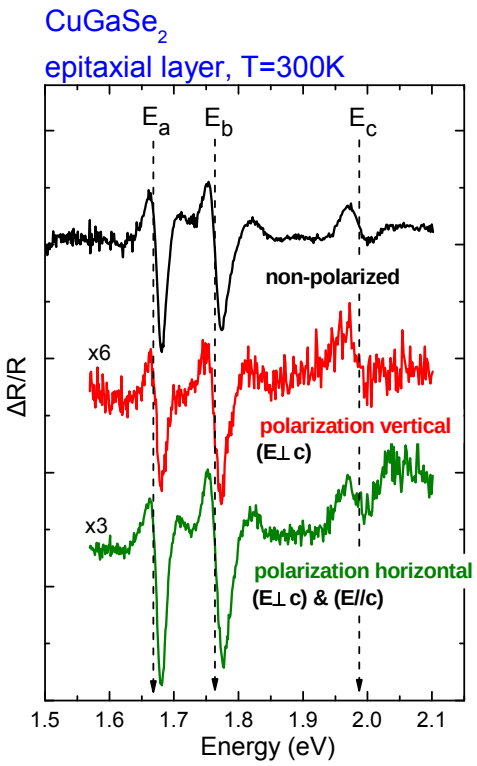

Figure 6.14 PR-spectra of $CuGaSe_2$ epitaxial layer at 300K for incident light without polarization and light with vertical- ($\vec{E} \perp \vec{c}$) and horizontal-polarization ($\vec{E} \perp \vec{c}$ and $\vec{E} \parallel \vec{c}$)

6.2.2 Temperature dependence of $CuGaSe_2$ chalcopyrite absorbers

The PR-spectra recorded, in the temperature range 10 – 300K, on a bulk- and an epitaxial [6.13] $CuGaSe_2$ chalcopyrite absorber, are shown in Figure 6.15a) and b), respectively. With the increase of temperature, the spectral bands appear less intense, red shifted and broadened, which, at temperatures up to 150K, is attributed to electron scattering on phonons. Generally, it is contributed by the thermal lattice expansion and the dependence of mismatch stain on temperature.

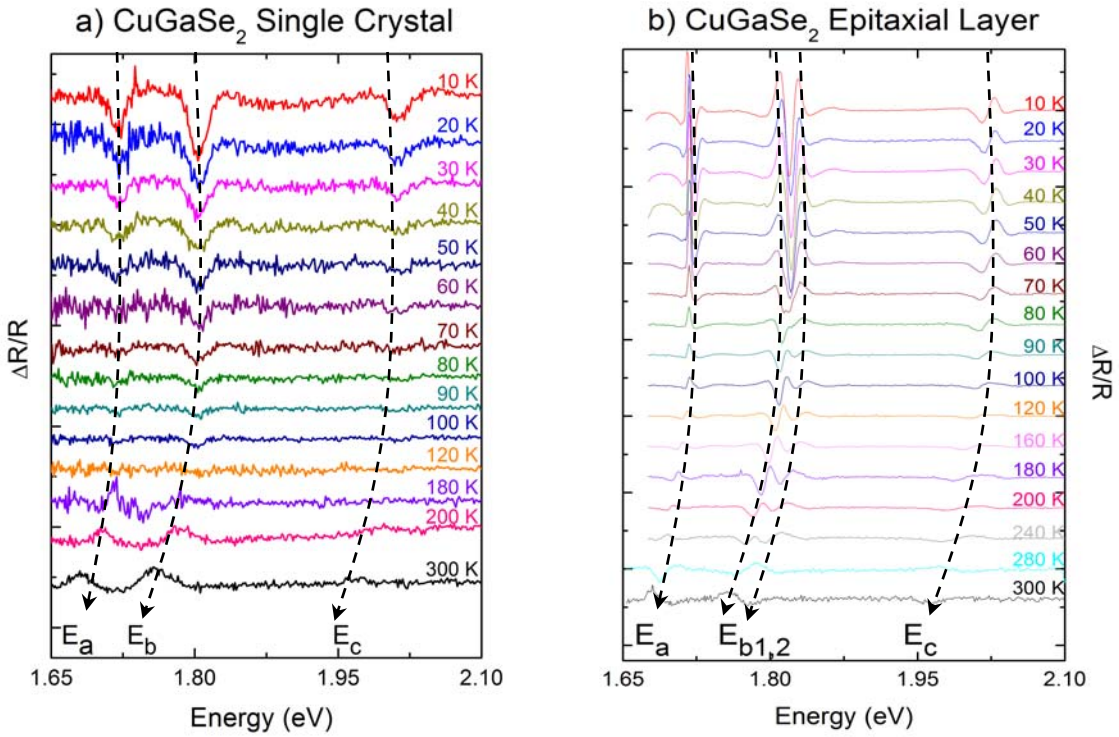

Figure 6.15 Photoreflectance spectra of $CuGaSe_2$: a) single crystal and b) epitaxial layer recorded in the temperature range 10 - 300K

The temperature dependence of all three (E_a, E_b, and E_c) transition energies of both, the bulk- and epitaxial-chalcopyrites, is shown in Figure 6.16. Transition energies have been extracted by TDFF fitting of the recorded PR-spectra.

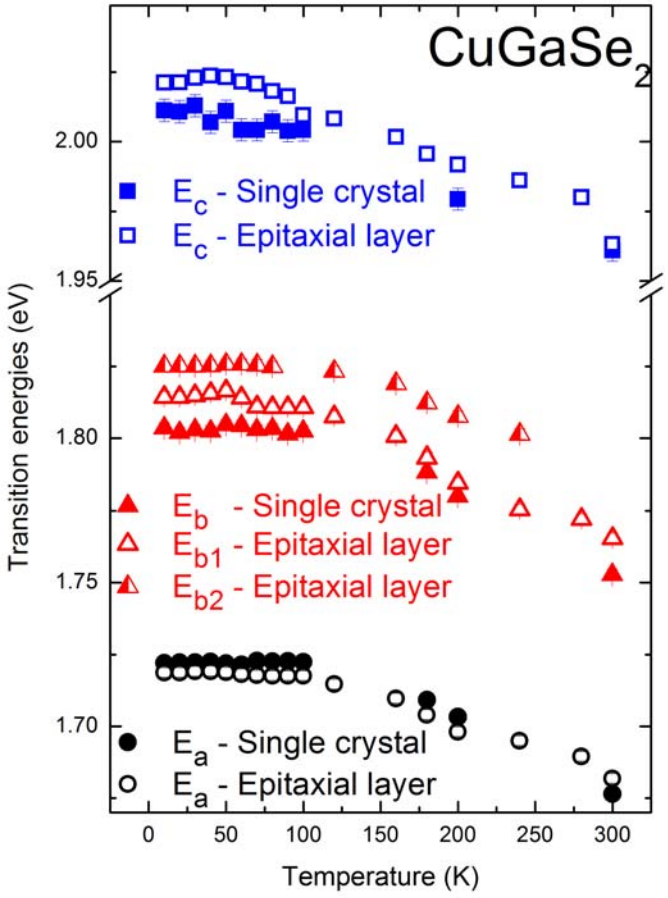

Figure 6.16 $CuGaSe_2$ temperature dependence of the E_a, E_b, and E_c-bands.

Transition energies (E_a, E_b, and E_c) in dependence of temperature, for $CuGaSe_2$ single crystal and epitaxial layer, are shown in Figure 6.17-Figure 6.19, and each one can be fitted with the models presented in § 2.1.3.2. From the fitting results, several parameters, e.g. the transition energy at 0K, the strength of the interaction and the effective energy, have been quantified and are listed in Table 6.3.

In the temperature range 0 - 240K (Figure 6.17), the E_a-valence band of the epitaxial layer appears slightly red-shifted with respect to the E_a-band of the single crystal, while the E_b and E_c bands appear blue-shifted compared to the respective bands of the bulk. This effect indicates strain development in epitaxial $CuGaSe_2$. Bearing in mind, that the band-gap is narrowed (widened-up) in the presence of tensile (compressive) strain-stress, the red-shift (blue-shift) is indicative of tensile (compressive) strain.

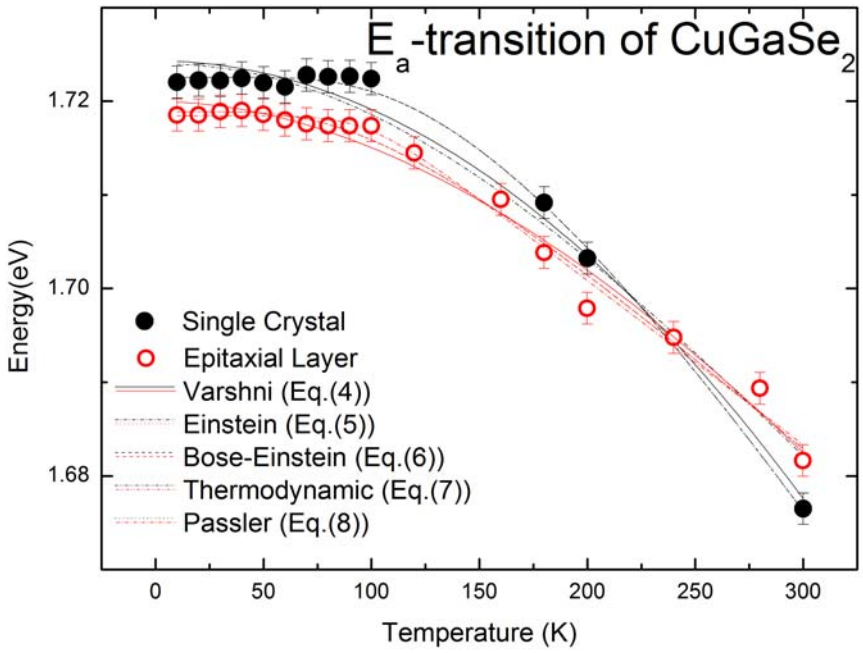

Figure 6.17 $CuGaSe_2$ E_a transition energy in dependence of the temperature. The experimental data of both single crystal and epitaxial layer were fitted with five different models

The temperature dependence of the E_b transition energy of $CuGaSe_2$ is shown in Figure 6.18. The line-shape of the PR-spectra, assigned to the E_b transition of the epitaxial layer, is more complex than that of the single crystal. In particular, two spectral functions (TDFF) were needed to fit the PR-bands below 240K. The contribution of two different functional terms is more apparent at intermediate temperatures, between 100 and 240K. These two functions are designated in both, Figure 6.16 and Figure 6.18, as E_{b1} and E_{b2}. The two contributions are tentatively explained as originating from the two different sources of mismatch strain, e.g. the strain between the $CuGaSe_2$-epitaxial layer and the GaAs-substrate and the strain between the $CuGaSe_2$-epitaxial layer and the Cu_xSe-crystallites dispersed on the film surface. The line-shape, at each temperature, is modified, in the same way as the band energy, by the electron-phonon interaction and the thermal strain.

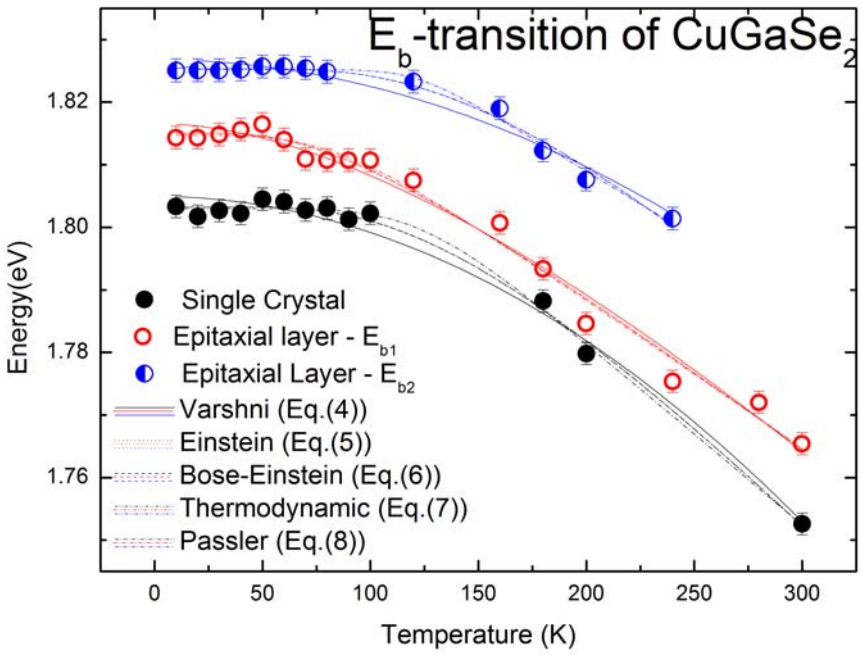

Figure 6.18 $CuGaSe_2$ E_b transition energy in dependence of the temperature. The experimental data of both single crystal and epitaxial layer were fitted with five different models

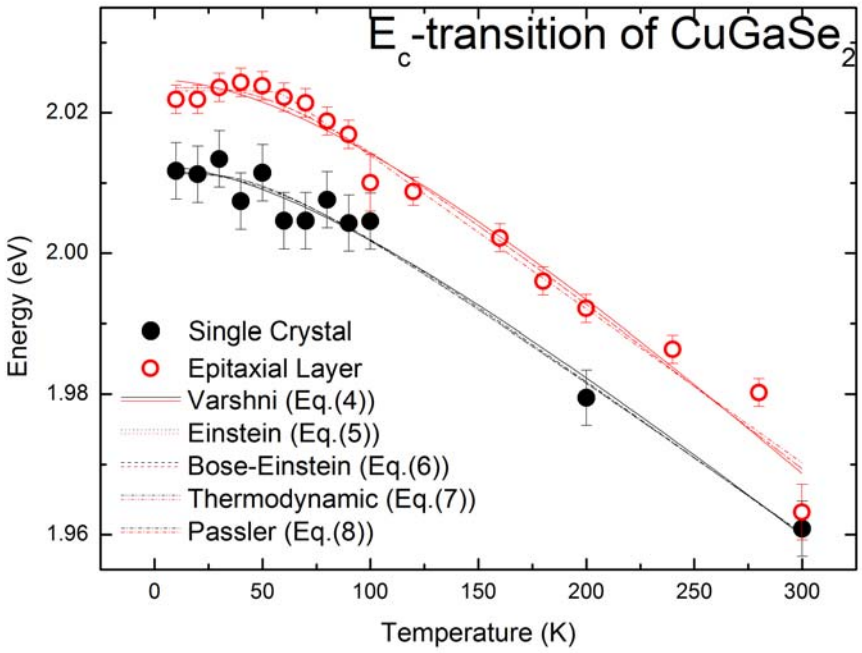

Figure 6.19 $CuGaSe_2$ E_c transition energy in dependence of the temperature. The experimental data of both single crystal and epitaxial layer were fitted with five different models

The temperature dependence of the E_c-energy band of both single crystal and epitaxial $CuGaSe_2$ is shown in Figure 6.19.

The results of the bandgap dependence on temperature are discussed in the frame of the five models used for the fitting of data in Figure 6.17-Figure 6.19. The effective phonon temperature (Ξ: obtained by Einstein model (Eq.(2.20)), Θ_B: obtained by Bose-Einstein model (Eq.(2.21)), Θ: obtained by the Pässler model (Eq.(2.23))), is expected to be smaller ($\Theta \approx 2\Theta_D/3$ [6.29]) than the Debye temperature. The Debye temperature for $CuGaSe_2$ calculated by various techniques ranges from 195 to 288K [6.30] and is consequently higher than the average obtained effective phonon temperature Θ listed in Table 6.3.

The electron-phonon coupling parameter S, obtained by Eq.(2.22), ranges from 1.29 to 2.22 for bulk and from 1.23 to 1.91 for the epitaxial $CuGaSe_2$ and its lower value is in accordance with the parameter S (=1.29) reported elsewhere [6.31] for monocrystalline $CuGaSe_2$. It can be concluded that the interaction between band-edge states and the phonon system is stronger in the bulk than in the epitaxial $CuGaSe_2$.

Further, from Eq. (2.20) or (2.22), it can be extracted:

$$\frac{dE_g}{dT} = -\frac{S}{2k_B}\frac{\left\langle (\hbar\omega)^2 \right\rangle}{T^2}\frac{1}{\sinh^2\left(\left\langle \hbar\omega \right\rangle / 2k_BT\right)} \tag{6.2}$$

At high temperatures $k_BT \gg \langle \hbar \cdot \omega \rangle$, the slope of the E_g(T) curve approaches its limit value [6.31]:

$$-\left[\frac{dE_g}{dT}\right]_{\max} = 2Sk_B \tag{6.3}$$

Comparing the above given $T \to \infty$ of Eq. (2.20) or (2.22) with its counterpart due to Eq. (2.23), the following correlations between different model parameters are found: $2Sk_B = \frac{K}{\Xi} = \delta$ for the magnitude of the limiting slope and $\frac{\langle \hbar \cdot \omega \rangle}{k_B} = \Xi = \Theta = \Theta_B$ for the effective phonon temperature. Comparing the parameter values listed in Table 6.3, it is concluded that these theoretical relations are fulfilled within deviations of max. 5%.

Table 6.3 Fitting parameters of the E_a, E_b, and E_c-bands of both bulk and epitaxial $CuGaSe_2$, with five different models: Varshni, Einstein, Bose-Einstein, Thermodynamic, and Pässler.

		Varshni			Einstein			Bose-Einstein				Thermodynamic			Pässler				$-\left[\frac{dE_g}{dT}\right]_{max}$	$\frac{\langle\hbar\cdot\omega\rangle}{k_B}$
		$E_g(0)$ (eV)	a (meV/K)	b (K)	$E_g(0)$ (eV)	K (meV)	Ξ (K)	E_B (eV)	a_B (meV)	Θ_B (K)	$E_g(0)=E_B-a_B$ (eV)	$E_g(0)$ (eV)	S	$\langle\hbar\cdot\omega\rangle$ (meV)	$E_g(0)$ (eV)	δ (meV/K)	Θ (K)	p	(meV/K)	(K)
Single Crystal	E_a	1.724	0.227	396	1.722	101	381	1.814	92	381	1.722	1.722	2.220	32.8	1.724	0.274	380	2.15	0.380	381
	E_b	1.805	0.278	251	1.803	72	230	1.885	81	230	1.804	1.803	2.196	19.8	1.803	0.292	227	2.74	0.378	230
	E_c	2.012	0.260	145	2.011	33	150	2.028	17	150	2.011	2.011	1.283	12.9	2.012	0.224	152	2.50	0.221	150
Epitaxial layer	E_a	1.720	0.256	271	1.719	67	316	1.752	34	316	1.718	1.719	1.233	27.3	1.718	0.205	311	2.66	0.213	318
	E_{b1}	1.817	0.278	213	1.815	66	249	1.848	33	249	1.815	1.815	1.524	21.5	1.815	0.239	243	2.72	0.263	249
	E_{b2}	1.827	0.240	337	1.826	114	377	1.917	91	377	1.826	1.825	1.913	32.6	1.825	0.309	398	2.44	0.330	378
	E_c	2.026	0.247	187	2.024	41	170	2.044	21	170	2.023	2.024	1.316	13.5	2.024	0.229	168	2.72	0.244	157

The calculated value of $-(dE_g/dT)_{max}$ is also listed in Table 6.3 and is close to the parameters a obtained by the Varshni model and δ obtained by the Pässler model. Assuming that mobility μ is determined by lattice scattering, its value can be expressed by Eq.(6.4) [6.32]:

$$\mu = \frac{48}{9\pi}\left(\frac{3}{4\pi}\right)^{1/3}\left(\frac{\pi}{2}\right)^{1/2}\frac{e\hbar^2 k_B}{\Omega^{1/3}\left(m^*\right)^{3/2}\left(k_B T\right)^{3/2}\left(dE_g/dT\right)} \tag{6.4}$$

where Ω is the volume of the unit cell and m* is the effective mass.

The hole mobility was calculated at Room Temperature (T=300K) assuming that $m_h^* = 1.2 \cdot m_e$ [6.33]. The calculated hole mobility, by applying results from Varshni, Einstein, Thermodynamic, and Pässler models, is listed in Table 6.4.

Table 6.4 Hole mobility calculated from parameters of four different models (Varshni, Einstein, Thermodynamic, and Pässler)

		Varshni		**Einstein**		**Thermodynamic**		**Pässler**	
		a (meV/K)	μ_h (cm^2/V s)	K/Ξ (meV/K)	μ_h (cm^2/V s)	S k_B (meV/K)	μ_h (cm^2/V s)	δ (meV/K)	μ_h (cm^2/V s)
Single Crystal	E_a	0.227	43.0	0.265	36.9	0.380	25.7	0.274	35.7
	E_b	0.278	35.1	0.313	31.2	0.378	25.8	0.292	33.5
	E_c	0.260	37.6	0.220	44.4	0.221	44.4	0.224	43.6
Epitaxial layer	E_a	0.256	38.1	0.212	46.1	0.213	45.9	0.205	47.7
	E_{b1}	0.278	35.1	0.265	36.9	0.263	37.2	0.239	40.9
	E_{b2}	0.340	28.7	0.302	32.3	0.330	26.6	0.309	31.6
	E_c	0.247	39.6	0.241	40.5	0.244	40.0	0.229	42.7

The hole mobility of single crystal $CuGaSe_2$ are close to previously reported data (μ_h=20-30cm^2/Vs) [6.33] for the room temperature Hall mobility obtained on similar grown CVT single crystals. The hole mobility of the epitaxial $CuGaSe_2$ layers are closer to the values of the single crystal than those reported [6.34] (μ_h=100-170cm^2/Vs) on

epitaxially grown $CuGaSe_2$, which demonstrates the high crystal quality of the epitaxial layers used in the present work.

At room temperature, nine optical phonon modes in $CuGaSe_2$ have been reported [6.35] by means of Raman spectroscopy. The frequencies of these modes vary from the lowest value at $60cm^{-1}$ (7meV) up to the highest value at $273cm^{-1}$ (34meV). Using infrared reflectivity spectroscopic data, Bodnar et al [6.36] have reported on eight optical phonon modes in $CuGaSe_2$.The frequencies of these modes vary from the lowest value at $170cm^{-1}$ (21meV) to the highest value at $278cm^{-1}$ (34meV). From fitting with the Pässler model, effective phonon energies $\langle \hbar\omega \rangle$ have been calculated and range from 12.9 to 32.8meV for the single crystal, and from 13.5 to 32.6meV for the epitaxial $CuGaSe_2$ layer (Table 6.3). These effective phonon energies are closer to the highest frequency modes observed in the Raman and IR spectra, and the difference is within the accuracy of the data. Further, the phonon energy originating from the E_a band of the single crystal is close to the experimentally determined energy separation of the observed LO-phonon replica of the DA transition (34±2meV). In $CuGaSe_2$, the $193cm^{-1}$ (24meV) and $199cm^{-1}$ (25meV) modes appear to be much more intense in epitaxially grown samples [6.37]. For this reason, in the epitaxial $CuGaSe_2$ layer, phonons interacting with electrons in the E_a, and E_{b1} bands have energies in this region. The phonon energy 32.6meV, associated with the E_{b2} band, can be assigned to the $263cm^{-1}$(33meV) mode of the Cu_2Se crystallites [6.38].

Temperature dependence of the width (Full Width at Half Maximum = FWHM) of all three transition energies in both single crystal and epitaxial $CuGaSe_2$ is shown in Figure 6.20. Each diagram has been fitted with Eq.(2.25). It is noted [6.39] that the optical phonons are the main contributors to the broadening of critical points. This leads to a higher average phonon effective energy (Figure 6.5) obtained by the broadening parameters than the values obtained for the electron-phonon contribution to the energy band shifts with temperature. The values calculated for the effective phonon energies, though close to the ones calculated from fitting the band energies, appear lower than those. On the contrary, the phonon energy associated with the E_{b2} band energy of the epitaxial $CuGaSe_2$ layer is almost zero, which may be indicative of TO-phonon contribution.

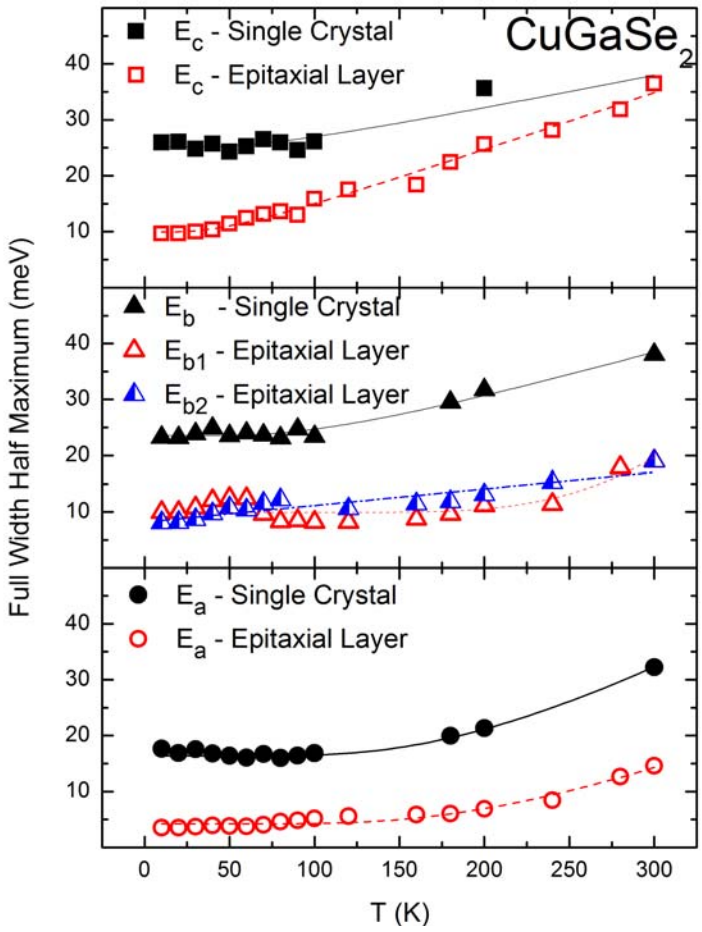

Figure 6.20 $CuGaSe_2$ temperature dependence of band width (FWHM) for all three transition energies.

Table 6.5 FWHM Fitting parameters of the E_a, E_b, and E_c-bands of both, bulk and epitaxial $CuGaSe_2$. The fitting revealed the phonon effective energy

		Bose-Einstein			
		$\Gamma(0)$ (meV)	Γ_{ep} (meV)	Θ_{LO} (K)	$\Theta_{LO}k_B$ (meV)
Single Crystal	E_a	16	135	495	30.7
	E_b	24	29	321	20.0
	E_c	25	13	204	12.7
Epitaxial layer	E_a	4	112	448	27.9
	E_{b1}	10	65	326	20.3
	E_{b2}	8	0	0	0
	E_c	10	13	130	8.1

By using the values (Table 6.3) extracted from the PR-spectra shown in Figure 6.16, the spin orbit interaction Δ_{SO} and the non-cubic crystal field Δ_{CF} of both, the single crystal and the epitaxial layer, have been quantified as a function of the temperature according to Eq.(2.14). The results are shown in Figure 6.21. For the E_b-band, which is decomposed into two sub-bands attributed to the $CuGaSe_2$/GaAs-strain and the $CuGaSe_2$/Cu_xSe-strain, the band energy of the lowest energy side of the overall band was used in the calculations. The spin orbit interaction, in single crystal $CuGaSe_2$, at Room Temperature (RT), is Δ_{SO}=294meV; it tends to increase at lower temperatures with a rate of $25x10^{-6}$eV/K. In the epitaxial layer, the spin orbit interaction at RT is Δ_{SO}=287meV and increases at lower temperatures with a rate of $54x10^{-6}$eV/K. The calculated spin orbit interaction, in this work, is close to values (Δ_{SO}=227meV) reported elsewhere [6.40].

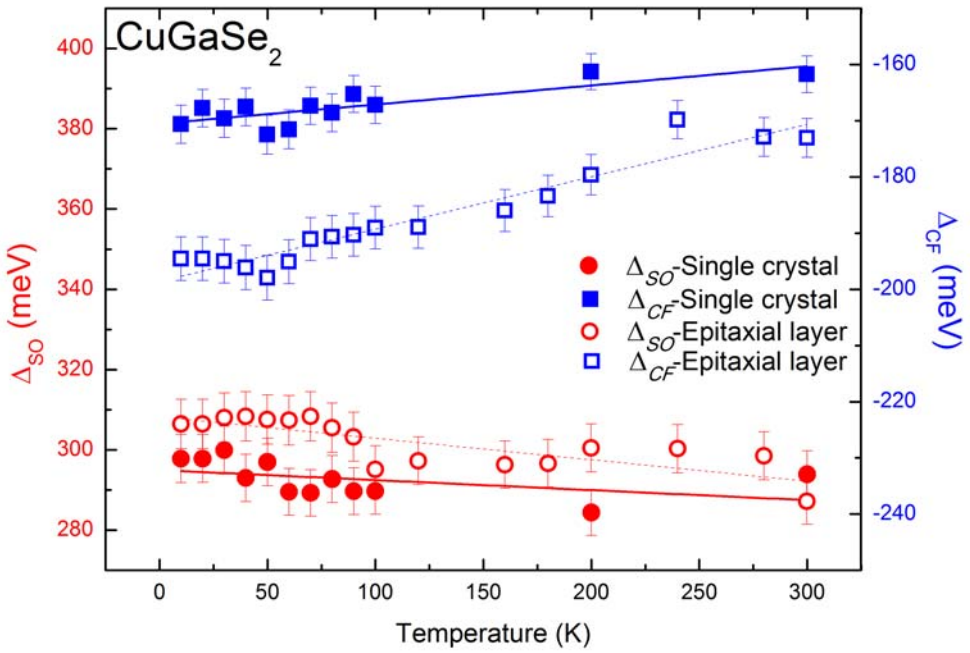

Figure 6.21 Temperature dependence of the spin-orbit interaction (Δ_{SO}) and the non-cubic crystal field (Δ_{CF}) of a $CuGaSe_2$ single crystal and an epitaxial layer (lines serve as guide to the eye)

For compounds of I-III-VI_2 group, it is suggested [6.41] that the *p-d* hybridization influence on the spin-orbit splitting is determined by [6.42]:

$$\Delta_{SO} = a\Delta_p + (1-a)\Delta_d \qquad (6.5)$$

where α is the fractional admixture of *p*-levels and (1-a) is the fractional admixture of *d*-levels in the uppermost valence bands. Artus et al. [6.43] have proposed a method to determine the Δ_p splitting of the *p*-orbitals for I-III-VI_2 compounds using the expression:

$$\Delta_p = \frac{29}{20}\left(0.2\Delta_p(III) + 0.8\Delta_p(VI)\right) \qquad (6.6)$$

where Δ_p(III), and Δ_p(VI) are the spin orbit splittings for III and VI atoms, respectively. In $CuGaSe_2$ compounds, using Δ_p(Ga)=0.12 [6.44] and Δ_p(Se)=0.29 [6.45], the splitting of the *p*-orbitals via Eq.(6.6) is found to be Δ_p =0.37eV. Based on this along with Δ_d=-0.13eV [6.46], the *p*-orbital contributions for both, single-crystal and epitaxial $CuGaSe_2$, are calculated with Eq.(6.5) and are found to be α_{sc}=84.8% and α_{epi}=83.4% for the single crystal and the epitaxial layer, respectively. These values are in agreement with the value 80.1% reported in [6.45]. Consequently, the *d*-level contribution is (1-α_{sc})=15.2% and (1-α_{epi})=16.6% for the single crystal and the epitaxial layer, respectively.

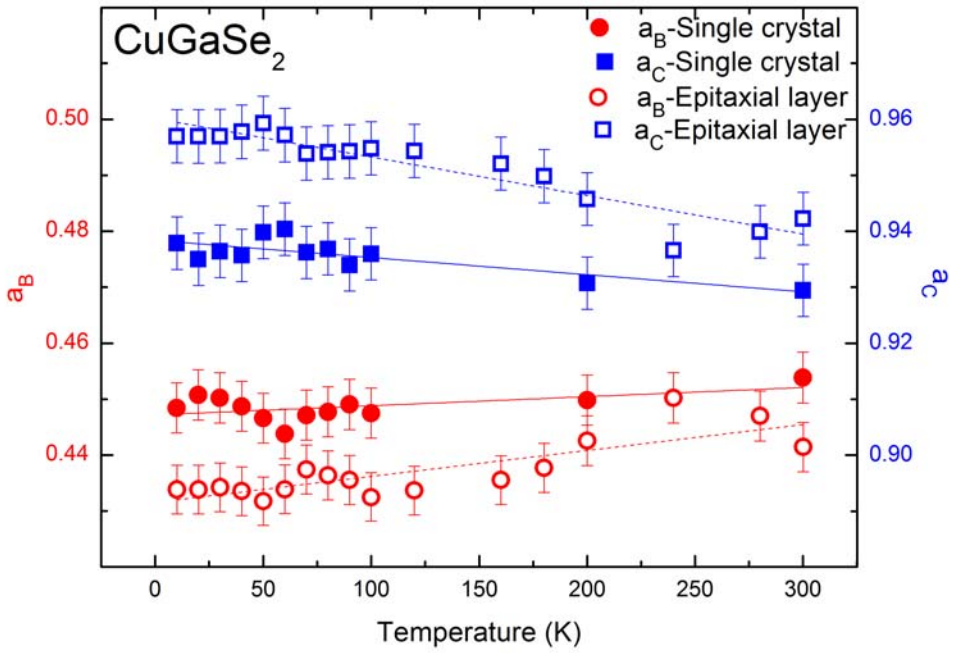

Figure 6.22 Temperature dependence of the admixture coefficients a_B and a_C of a $CuGaSe_2$ single crystal and an epitaxial layer (lines serve as guide to the eye)

The admixture coefficients a_B and a_C for both, single crystal and epitaxial $CuGaSe_2$, have been calculated via Eq.(2.16) and Eq.(2.17), respectively, using the spin orbit interaction Δ_{SO} experimentally obtained. The dependence of the admixture

coefficients a_B and a_C on temperature is shown in Figure 6.22. The values obtained at RT for the single crystal $CuGaSe_2$ are a_B=0.454 and a_C=0.929, whereas for the epitaxial $CuGaSe_2$ layer, are a_B=0.441 and a_C=0.942. Those values are close to previously reported a_B=0.442 and a_C=0.897 [6.47].

The crystal field interaction in single crystal $CuGaSe_2$, at RT, is also determined to Δ_{CF}=-162meV. The absolute value of Δ_{CF}, at low temperatures, is increased with a rate of $34x10^{-6}$ eV/K. In epitaxial $CuGaSe_2$, the crystal field interaction, at RT, is Δ_{CF}=-173meV and its absolute value increases, at lower temperatures, with a rate of $93x10^{-6}$ eV/K. The crystal field values of the single crystal are lower than those of the epitaxial layer, which may be attributed to the fact that single crystals are strain-free in comparison to the strained epitaxial layers; a strain field may overlapp to the non-cubic crystal field, in the latter case.

The value of the crystal field is calculated by Eq.(6.7) [6.9]:

$$\Delta_{CF} = \frac{3}{2}\mathrm{b}\left(2 - \frac{c}{\mathrm{a}}\right) \tag{6.7}$$

where a and c are the crystal lattice constants and b is the shear deformation potential of the lattice. For the shear deformation potential b of all I-III-VI_2 compounds, appropriate values have been reported [6.45]:

$$\begin{aligned} \mathrm{b}_p &= (-0.8 \pm 0.2)\ \mathrm{eV} \\ \mathrm{b}_d &= (-4.3 \pm 1.5)\ \mathrm{eV} \end{aligned} \tag{6.8}$$

where b_p and b_d are the deformation potentials associated with the *p*- and *d*-orbitals, respectively. These two deformation potentials can be combined in Eq.(6.9) [6.48]:

$$\mathrm{b} = a\mathrm{b}_p + (1-a)\mathrm{b}_d \tag{6.9}$$

where α is the fractional admixture of *p*-levels and (1-α) is the fractional admixture of *d*-levels in the uppermost valence bands.

Having already estimated the *p*-orbital contribution α_{sc}=84.8% and α_{epi}=83.4% for the single crystal and the epitaxial layer, respectively, the shear deformation potentials obtained by Eq.(6.9) are: b_{sc}=-1.33eV, for the single crystal, and b_{epi}=-1.38eV, for the epitaxial $CuGaSe_2$. It is known from literature, that for I-III-VI_2 compounds, the shear deformation potential is close to -1eV [6.42].

Taking into consideration that, for $CuGaSe_2$, c/a=1.960 (a=5.607Å, and c=10.990Å [6.49]), then the crystal field interactions, calculated from Eq.(6.7) via Eq.(6.8) and Eq.(6.9), are Δ_{CF}=-79.8meV, for the single crystal, and Δ_{CF}=-82.8meV, for the epitaxial layer. The calculated values of the crystal field interaction are in agreement with values reported by Shay et all [6.50]. However, the values obtained experimentally by Eq.(2.14) and calculated by Eq.(6.7) deviate by factor 2 for both, single crystal and epitaxial layer.

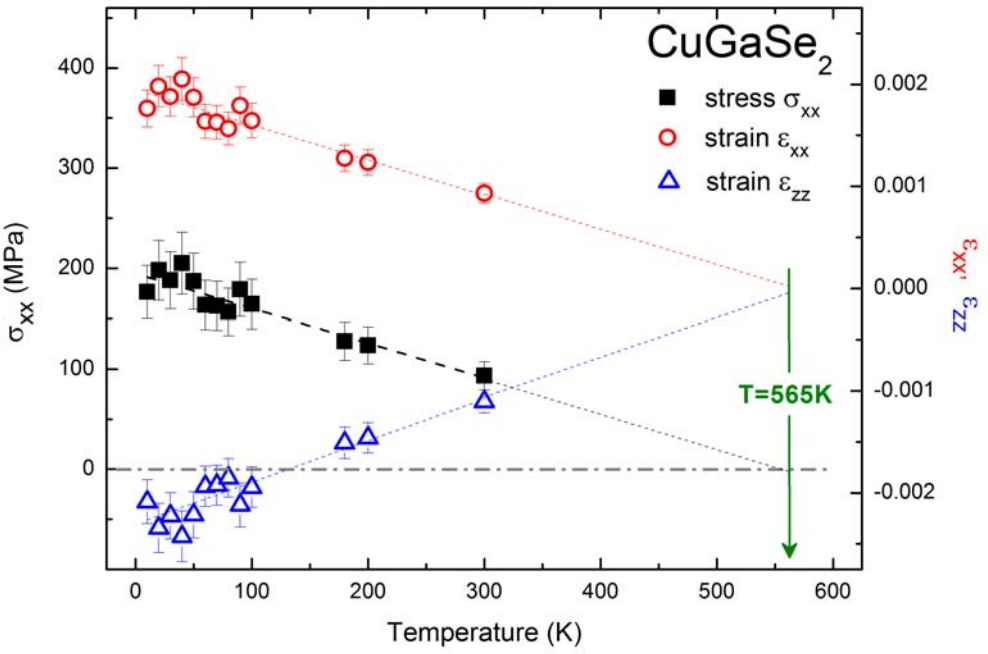

Figure 6.23 Stress σ_{xx}, strains ε_{xx} and ε_{zz} of the epitaxial $CuGaSe_2$ as a function of the temperature

Strain effects on $CuGaSe_2$ epitaxial layer were studied with reference to the strain-free $CuGaSe_2$ single crystal. Based on the cubic approximation, the strain ε_{zz} can be calculated from the energy-shift of the PR-spectra (Eq.(3.16)). Strain ε_{xx} can be quantified via Eq.(3.5) and stress σ_{xx} via Eq.(3.6). In the aforementioned calculations, the shear deformation potential of the epitaxial layer b_{epi}=-1.38eV obtained in this work and the elastic stiffness components C_{11}=112.2GPa and C_{12}=66.4GPa [6.10] of $CuGaSe_2$ have been used. The quantification of strain effects, in the films studied, is expected to be most important for photovoltaic device development. Figure 6.23 demonstrates the

temperature dependence of σ_{xx} stress and ε_{xx}, ε_{zz} strains for an epitaxial grown $CuGaSe_2$ layer. The stress values vary from σ_{xx} =+205MPa (T=10K) to σ_{xx} =+91MPa (T=300K). The positive sign depicts tensile stress, as initially suggested with respect to the red energy-shift of the E_a electronic band experimentally observed in section 6.2.2. The neto-strain effect is assumed to be a result of electronic band deformation and band shift under the application of tensile stress. This effect is manifested by the down-shift of the E_a energy band (fundamental band-gap) of the epitaxial $CuGaSe_2$ layer, in Figures 6.16 and 6.17, as expected under the application of tensile stress. The E_b and E_c energy bands of the epitaxial layer, however, lie energetically higher than the respective bands of the bulk (Figures 6.16, 6.18, and 6.19). Since the overall band-shift is contributed by three factors, e.g. 1) band-gap renormalization due to the electron-phonon interaction, 2) spin-orbit splitting, and 3) strain/stress effects, it is presumably the renormalization or the combination of both, renormalization and spin-orbit interaction (Fig. 6.21), which counterbalance the effect of tensile stress and make the E_b- and E_c- bands finally appear up-shifted.

The strains ε_{xx}, ε_{zz} and the stress σ_{xx} show almost linear dependence on the temperature. The linear equations that have been fitted to the experimental data are:

$$\begin{aligned} \varepsilon_{xx} &= -3.45 \cdot 10^{-6} T + 0.002 \\ \varepsilon_{zz} &= +4.08 \cdot 10^{-6} T + 0.002 \\ \sigma_{xx} &= -34.5 \cdot 10^{-2} T + 194.7 \end{aligned} \qquad (6.10)$$

With the increase of temperature, stresses decrease and are expected to diminish at growth temperatures. The epitaxial layer is grown free of strain at elevated temperatures and becomes elastically strained during cooling because of the mismatch in the thermal expansion coefficients between epilayer and substrate [6.51]. Therefore, the temperature at which the epitaxial layer is stress-free is assumed to be the growth temperature. Using Eq.(6.10), the $CuGaSe_2$ epitaxial layer appears to be free of stresses at almost 565K, which is in total agreement (error < 1%) with the growth temperature (570K) of the $CuGaSe_2$ epitaxial layer reported in [6.52].

6.2.3 Temperature dependence of $CuInSe_2$ chalcopyrite absorbers

The PR-spectra of single crystal and epitaxial $CuInSe_2$ chalcopyrite absorber as a function of the temperature are presented in Figure 6.24. In the epitaxial $CuInSe_2$ layer, it is evident that the separation energy of E_a and E_b bands is decreasing with the increase of the temperature. The increase in the split energy is assumed to be due to the increase of the biaxial compressive strain owing to the mismatch of the thermal expansion coefficients of the $CuInSe_2$ layer and the GaAs substrate.

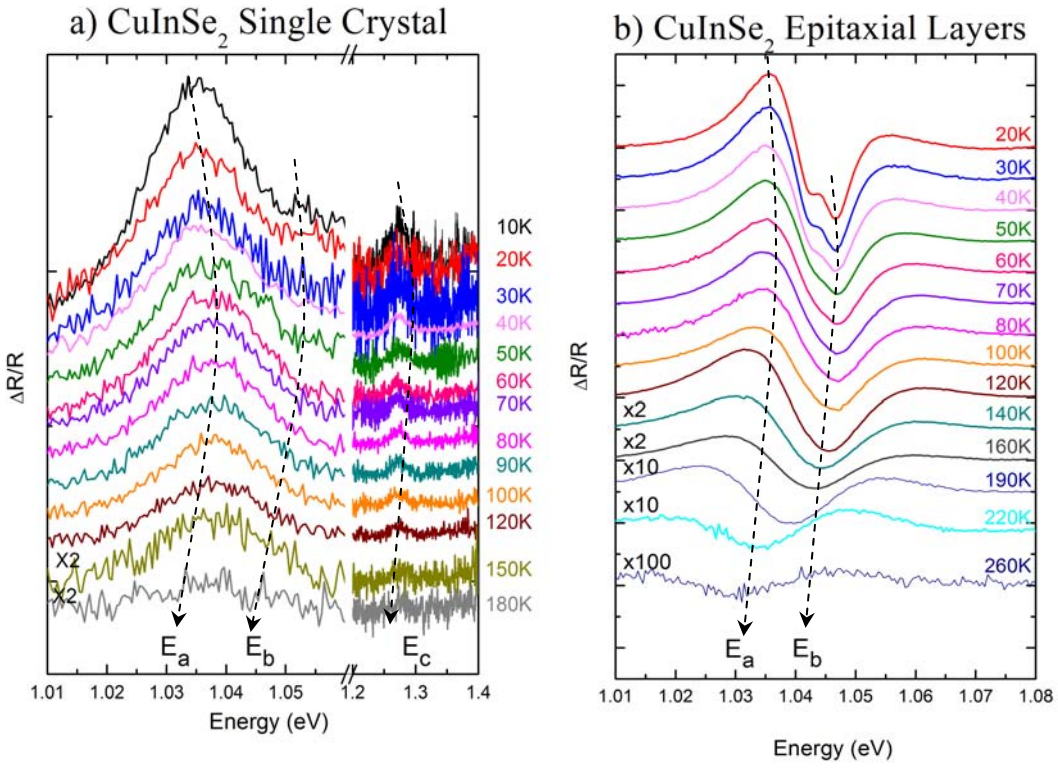

Figure 6.24 Photoreflectance spectra of $CuInSe_2$: a) single crystal in the temperature range 10 – 180K, and b) epitaxial layer in the temperature range 10 - 260K

The intensity of both, the bulk and the epitaxial layer decreases with the increase of the temperature. The PR-spectra were fitted with TDFFs and the gap energies were obtained for each temperature. The result of the fittings is shown in Figure 6.25. It must be noted, that, for the single crystal, the E_c transition was also recorded and is projected in Figure 6.25. It is obvious, that both, E_a and E_b transitions, increase slightly with the increase of the temperature, in the low temperature regime, and reach a maximum value at 100K; from 120 to 260K, transition energies decrease continuously with the temperature. This behavior is in agreement with the results obtained from piezoelectric-opticoacoustic (PPA) measurements [6.53], and the results of photoluminescence [6.54] and optical absorption measurements [6.55].

Such anomalous temperature behavior of the energy band gap can originate from the combined effect of the lattice thermal expansion and the electron–phonon interaction. In [6.55], it has been associated with the temperature variation of the thermal expansion coefficient of $CuInSe_2$, which in [6.56] was found to be negative below 80 K. In [6.57], the model used to describe the anomalous temperature dependence of the band gap, in the copper halides, has dealt with the effects of both, temperature and mass changes as being the result of the change in lattice constant and the renormalization of the band-gap by electron–phonon interaction. Two oscillators with opposite values of electron–phonon coupling coefficients A_i, for the i-oscillator, were drawn to describe changes in the gap energies. The anomalous positive slope for T<100K has been assigned to copper vibrations ($A_{Cu}>0$), whereas the decrease in slope for T>100K has been assigned to vibrations of the halogen, which have negative values of A.

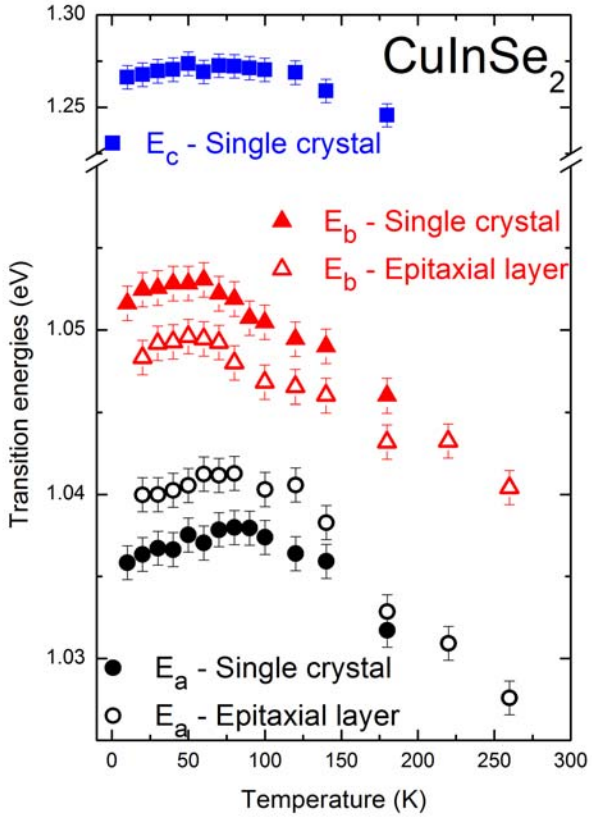

Figure 6.25 $CuInSe_2$ temperature dependence of the E_a, E_b, and E_c-bands

Taking into account this anomalous temperature dependence of $CuInSe_2$, the experimental data of the E_a, E_b, and E_c transition energies of both, the single crystal and the epitaxial $CuInSe_2$, were fitted preferentially with the Manoogian model (Eq.(2.24)), instead of being fitted with the six models used for $CuGaSe_2$. The results of the fitting are shown in Figure 6.26-Figure 6.28 and are summarized in Table 6.6.

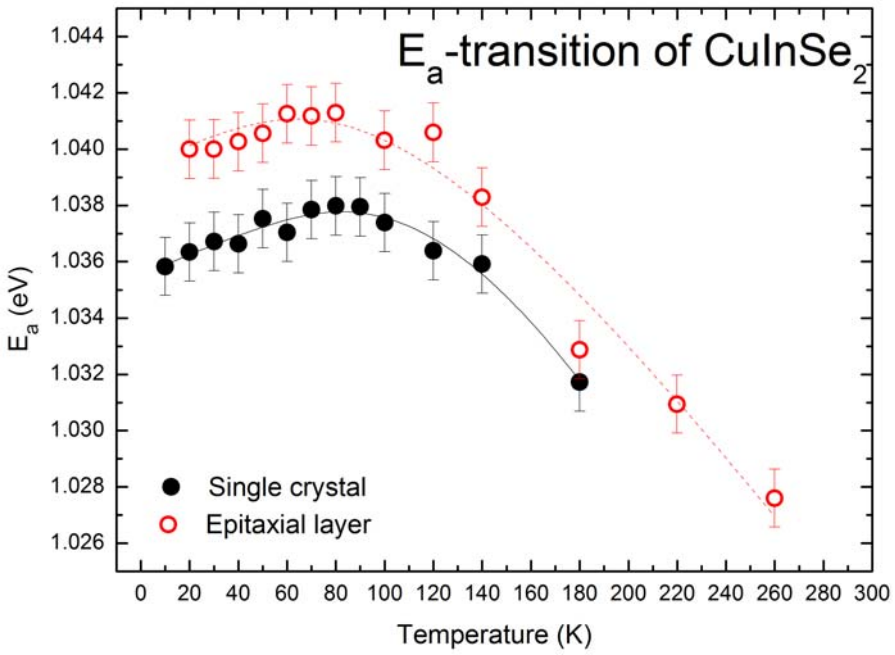

Figure 6.26 $CuInSe_2$ E_a transition energy in dependence of the temperature. The experimental data of both, single crystal and epitaxial layer, were fitted with the Manoogian model

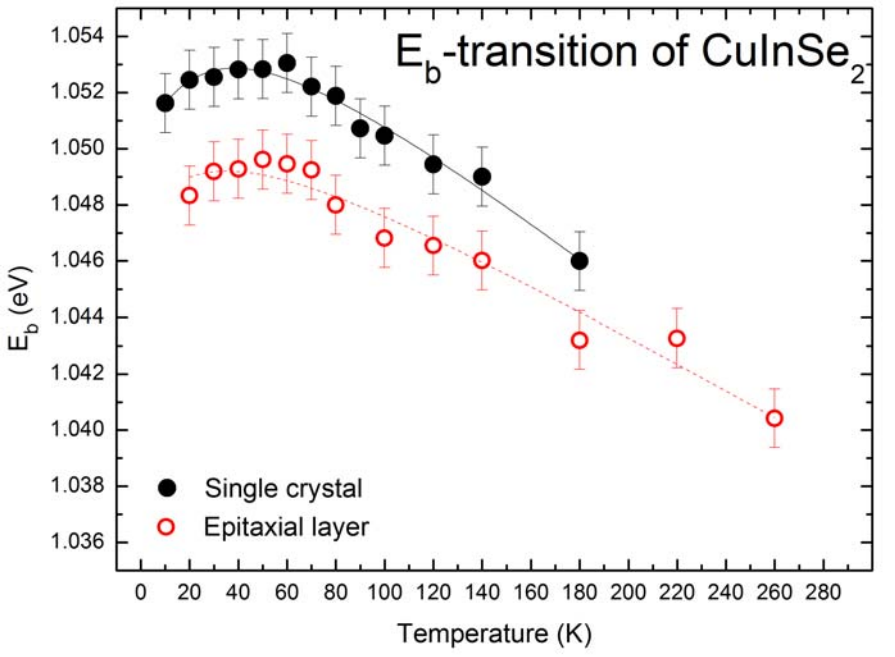

Figure 6.27 $CuInSe_2$ E_b transition energy in dependence of the temperature. The experimental data of both, single crystal and epitaxial layer, were fitted with the Manoogian model

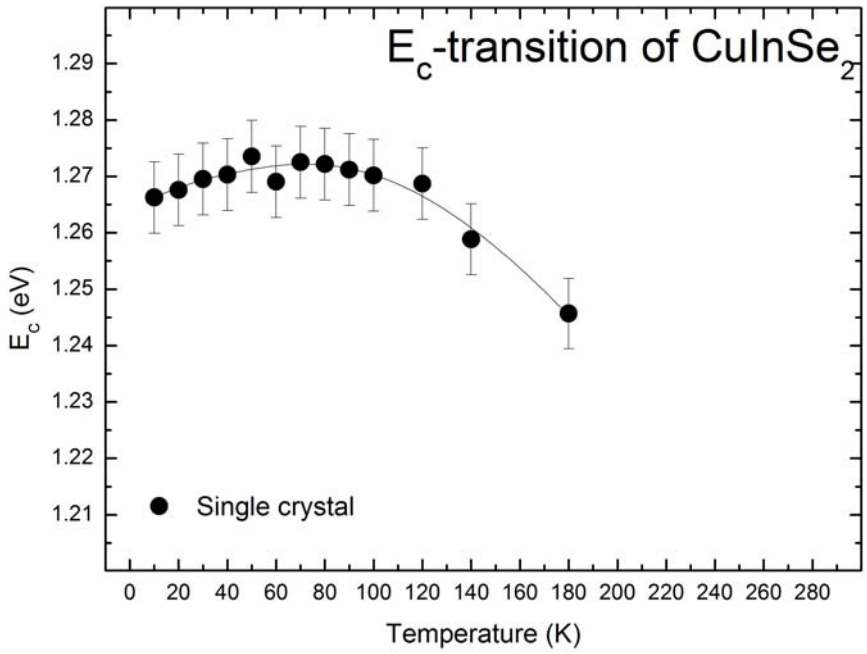

Figure 6.28 $CuInSe_2$ E_c transition energy in dependence of the temperature. The experimental data of both, single crystal and epitaxial layer, were fitted with the Manoogian model

Table 6.6 Fitting of the E_a, E_b, and E_c-bands of the bulk and E_a, and E_b-bands of the epitaxial $CuInSe_2$ with the Manoogian model revealed the phonon effective energy

		Manoogian					
		E(0) (eV)	U (eV/K)	X	V (eV/K)	Θ (K)	Θk_B (meV)
Single Crystal	E_a	1.035	0.001	0.83	-0.10	351	30.3
	E_b	1.049	0.001	0.34	-0.02	157	13.5
	E_c	1.259	0.003	0.34	-0.04	337	29.1
Epitaxial layer	E_a	1.039	0.001	0.37	-0.05	330	28.5
	E_b	1.048	0.002	0.25	-0.01	119	10.3

At room temperature, optical phonon modes in $CuInSe_2$ have been reported [6.58] by means of Raman spectroscopy. The frequencies of these modes vary from the lowest value at $58cm^{-1}$ (7meV) up to the highest value at $233cm^{-1}$ (29meV). At low temperature (T=100K), Tanino et. al. [6.58] have reported on more optical phonon modes in $CuInSe_2$. From fitting with the Manoogian model, effective phonon energies $\langle \hbar\omega \rangle = \Theta k_B$ have been calculated and range from 13.5 to 30.3meV, for the single crystal, and from 10.3 to 28.5meV, for the epitaxial $CuInSe_2$ layer (Table 6.6). These effective phonon energies are close to the frequency modes observed in the Raman spectra and any difference is within the accuracy of the data. Further, the phonon energy originating from the E_a and E_c bands of the single crystal is close to the experimentally determined energy separation of the observed LO-phonon replica of the DA transition (29±2meV).

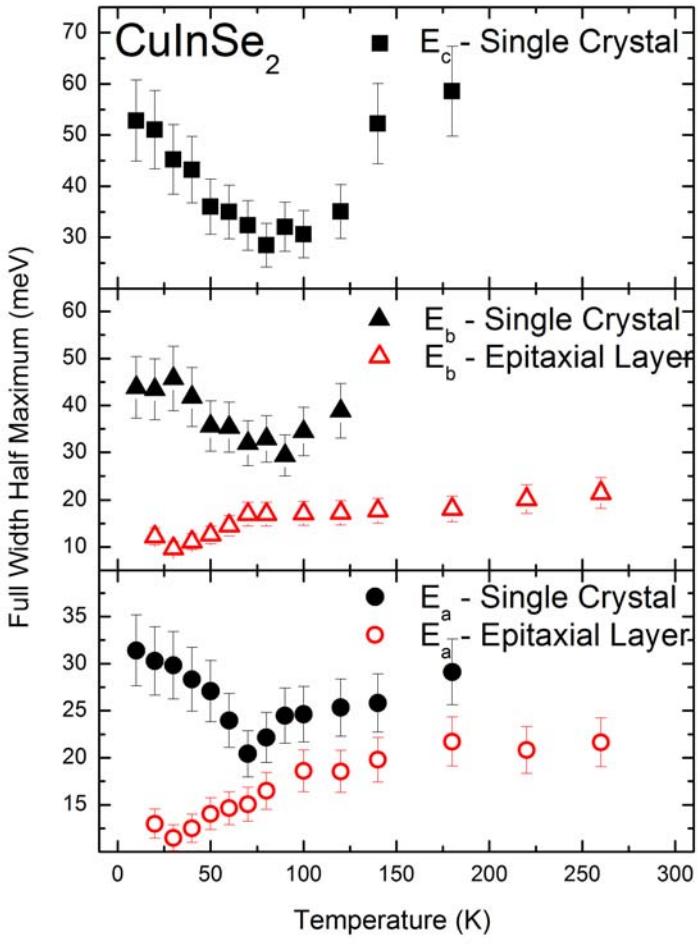

Figure 6.29 $CuInSe_2$ temperature dependence of band width (FWHM) of all three band transitions

As it can be seen in Figure 6.29, except from the transition energies, the FWHM of energy bands in $CuInSe_2$ also appears to have anomalous temperature dependence. The FWHM decreases in the temperature range 10-80K. This anomaly is rather obvious in the single crystal $CuInSe_2$ and refers to all three energy bands. Due to this anomalous behavior, Eq.(2.25) is not suitable for the fitting of the width.

By using the results of the PR-spectra shown in Figure 6.25, the spin orbit interaction Δ_{SO} and the non-cubic crystal field Δ_{CF} of the $CuInSe_2$ single-crystal have been quantified as a function of the temperature according to Eq.(2.14). The calculation of Δ_{SO} and Δ_{CF} could only be performed for the single crystal $CuInSe_2$ since the E_c-transition energy is necessary for this calculation (Eq. (2.14)). The spin orbit interaction obtained experimentally at T=180K is Δ_{SO}=239meV. The variation rate of the spin orbit interaction is $26x10^{-6}$eV/K; it is increased at lower temperatures, as shown in Figure 6.30, and calculated to be Δ_{SO}=237meV at RT, which is in total agreement with previously reported values (235meV) [6.40], [6.54]. The absolute value of the crystal field interaction decreases with increased temperature, which is in agreement with the behavior of the $CuGaSe_2$ semiconductors discussed above.

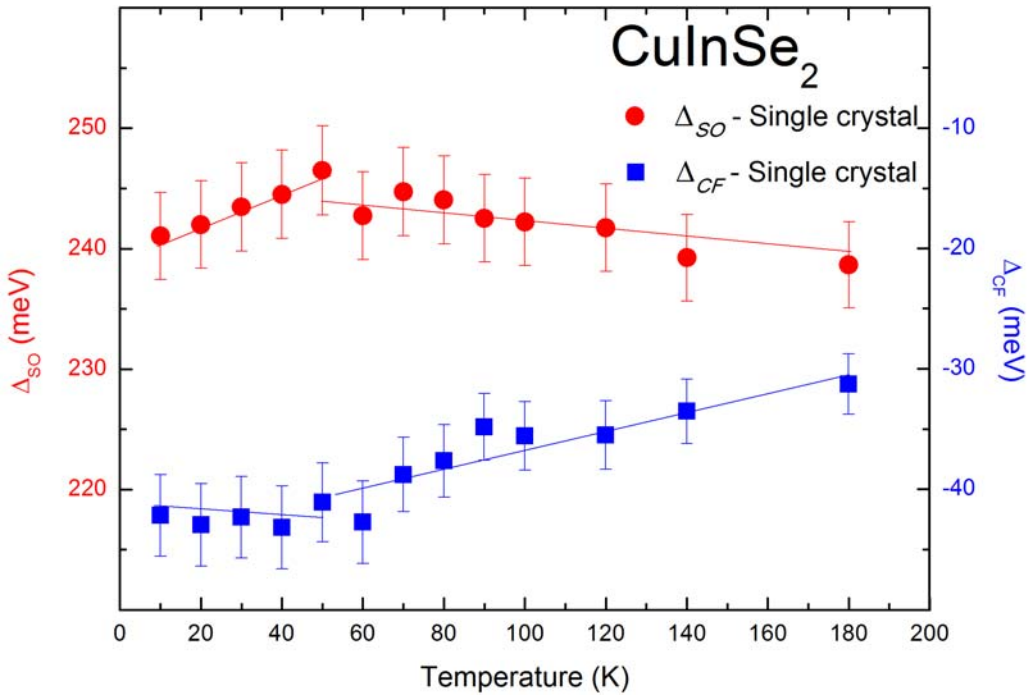

Figure 6.30 Temperature dependence of the spin-orbit interaction (Δ_{SO}) and the non-cubic crystal field (Δ_{CF}) of a $CuInSe_2$ single crystal.

The *p*-orbital contribution in $CuInSe_2$ can be obtained via Eq.(6.6). Using Δ_p(In)=0.27 [6.44] and Δ_p(Se)=0.29 [6.45], the Δ_p splitting is found to be 0.41eV. Based on this and along with Δ_d=-0.13eV [6.46], the *p*-orbital contribution for single-crystal $CuInSe_2$ is calculated with Eq.(6.5) to α_{sc}=68.3%. This value is in agreement with the value 74.5% reported in [6.45]. Consequently, the *d*-level contribution in $CuInSe_2$ is (1-α_{sc})=31.7%. The *d*-level contribution in $CuInSe_2$ is twice as large as the contribution in $CuGaSe_2$, which accounts for the anomalous temperature dependence of the energy band gap in $CuInSe_2$.

The admixture coefficients a_B and a_C, for the single crystal $CuInSe_2$ compound, can be calculated via Eq.(2.16) and Eq.(2.17), respectively, using the spin orbit interaction Δ_{SO}. The dependence of the admixture coefficients a_B and a_C on temperature is shown in Figure 6.31. Thus, the calculated values at T=180K are: a_B=0.606 and a_C=0.849; they increase at lower temperatures with rates of $7x10^{-5}$/K and $3x10^{-5}$/K, respectively. Therefore, the admixture coefficients are expected to be a_B=0.596 and a_C=0.843, at RT, and are close to previously reported a_B=0.587 and a_C=0.807 at RT [6.47]; the rather small deviation is attributed to differences in the ambient temperature (RT: nominal 300 K) at which the measurements have been performed.

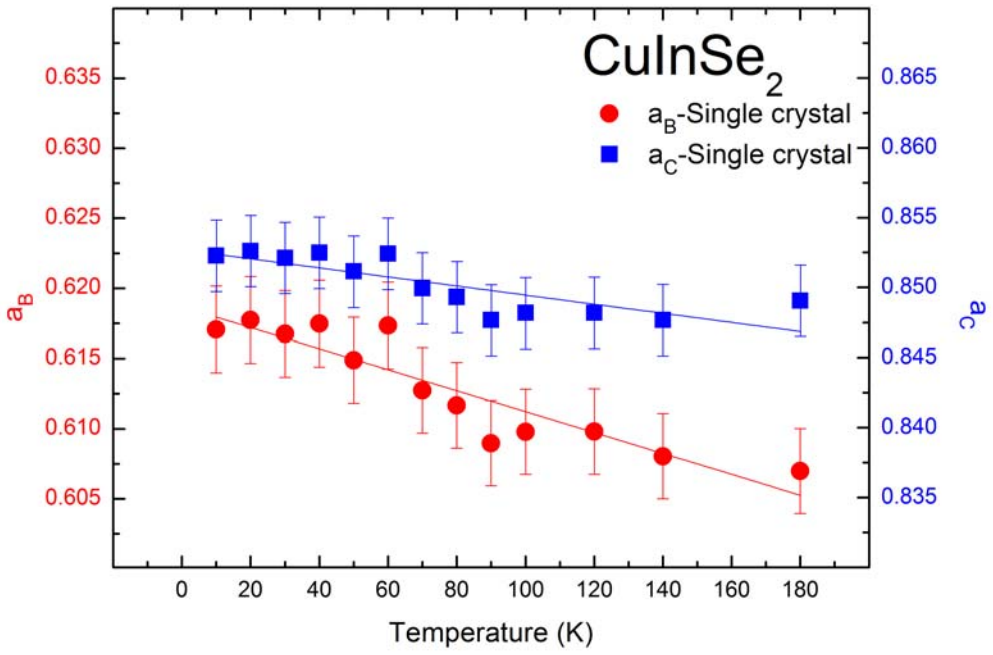

Figure 6.31 Temperature dependence of the admixture coefficients a_B and a_C of a $CuInSe_2$ single crystal

The crystal field interaction obtained at T=180K is Δ_{CF} =-31meV and its absolute value increases at lower temperatures (Figure 6.30) with a rate approaching $78x10^{-6}$eV/K, thus it is expected to be Δ_{CF} =-21meV at RT. The crystal field interaction is expected to be positive in CIS-like compounds, however, negative values of crystal field interaction (Δ_{CF}=-20meV) for $CuInSe_2$ chalcopyrite have been previously reported in [6.59] and are in absolute agreement with the experimentally obtained values in the present work.

The crystal field interaction Δ_{CF} can also be calculated via Eq.(6.7). Having estimated the *p*-orbital contribution α_{sc}=68.3% for the single crystal $CuInSe_2$, the shear deformation potential obtained by Eq.(6.9) is b_{sc}=-1.91eV. Taking, also, into consideration that, for $CuInSe_2$, c/a=2.001 (a=5.773Å, and c=11.550Å [6.49]), the calculated value is Δ_{CF}=+3meV. The calculated value of the crystal field interaction is in agreement with theoretical values reported by Shay et all [6.50]. However, the values obtained experimentally with Eq.(2.14) and those calculated with Eq.(6.7) deviate strongly, for both single crystal and epitaxial layer, probably because other effects than the p-orbital character dominate Δ_{CF}.

Strain effects on $CuInSe_2$ epitaxial layer were studied with reference to the strain-free $CuInSe_2$ single-crystal. As already mentioned, the strain ε_{zz} can be calculated from the energy-shift of the PR-spectra (Eq. (3.16)). Strain ε_{xx} can be quantified via Eq.(3.5) and stress σ_{xx} via Eq.(3.6). In the above mentioned calculations, the shear deformation potential b=-1.91eV and the elastic stiffness components C_{11}=96.8GPa, C_{12}=60.9GPa [6.10] of $CuInSe_2$ have been used. The quantification of strain effects in the studied films is expected to be most important for photovoltaic device development.

Figure 6.32 demonstrates the temperature dependence of σ_{xx} stress and ε_{xx}, ε_{zz} strains for an epitaxial grown $CuInSe_2$ layer. The stress values vary from σ_{xx} =-58MPa (T=20K) to σ_{xx} =-35MPa (T=180K). The negative sign depicts compressive stress. Under the influence of compressive stress, the band-gap is widened-up as demonstrated by the up-shift of the (fundamental) energy-gap E_a of the epitaxial layer with respect to the E_a gap of the bulk, in Figures 6.25 and 6.26. This shift is counterbalanced in case of the higher gaps, as has been already pointed out in the previously discussed case of $CuGaSe_2$ (CGS compound), and the E_b band of the layer appears in case of $CuInSe_2$ (CIS compound) down-shifted with respect to the E_b band of the bulk. The E_b gap narrowing

of the epitaxial layer is tentatively attributed to the dominating character of band-gap renormalization by the electron-phonon interaction and the spin-orbit splitting.

The strains ε_{xx}, ε_{zz} and the stress σ_{xx} show almost linear dependence on the temperature. The linear equations that have been fitted to the experimental data are:

$$\varepsilon_{xx} = +1.46 \cdot 10^{-6} T - 7.11 \cdot 10^{-4}$$
$$\varepsilon_{zz} = -1.84 \cdot 10^{-6} T + 8.96 \cdot 10^{-4} \qquad (6.11)$$
$$\sigma_{xx} = +11.34 \cdot 10^{-2} T - 57.14 \cdot 10^{-4}$$

Using Eq.(6.11), the $CuInSe_2$ epitaxial layer appears to be free of stresses at almost T=504K which is in total agreement with the reported [6.60] growth temperature 500K.

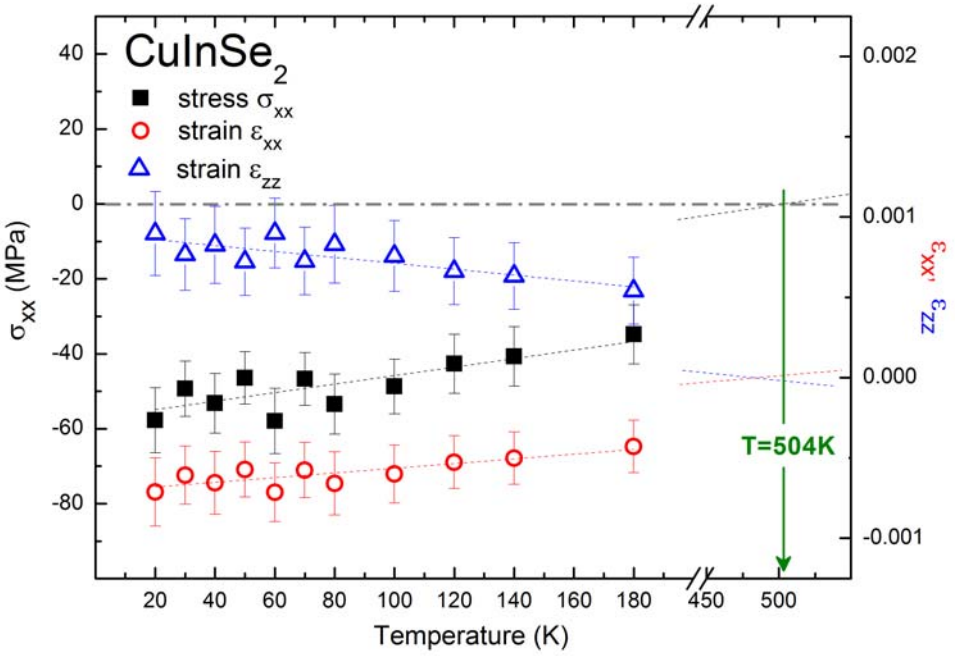

Figure 6.32 Stress σ_{xx}, strains ε_{xx} and ε_{zz} of the epitaxial $CuInSe_2$ as a function of the temperature

6.2.4 Compositional Dependence of $CuGaSe_2$ chalcopyrite absorbers

Figure 6.33 shows the compositional dependence of the PR spectra of MOVPE $CuGaSe_2$ layers at 20K, with [Cu]/[Ga] varying from 0.95 to 1.18. With increasing [Cu]/[Ga] ratio, the red energy-shift of the three valence-split bands, E_a, E_b and E_c, and the band broadening increase. Both effects are considered to be due to a secondary

microcrystalline Cu_xSe-phase formed from the Cu-excess on the $CuGaSe_2$ layer surface of Cu-rich modifications. Similar results were reported in [6.62] for the dependence of band energies on strain.

The three valence band splitting can be only weakly observed in the PR spectra of Ga-rich layers at 20 K. The low spectral intensity of the Ga-rich modifications, even at 20K, is a result of "shifting and mixing" of the three valence-split bands because of potential fluctuations [6.61] and increasing disorder.

The three valence-split bands, E_a, E_b and E_c, were fitted with TDFF functions. The fitting results are presented in Figure 6.34.

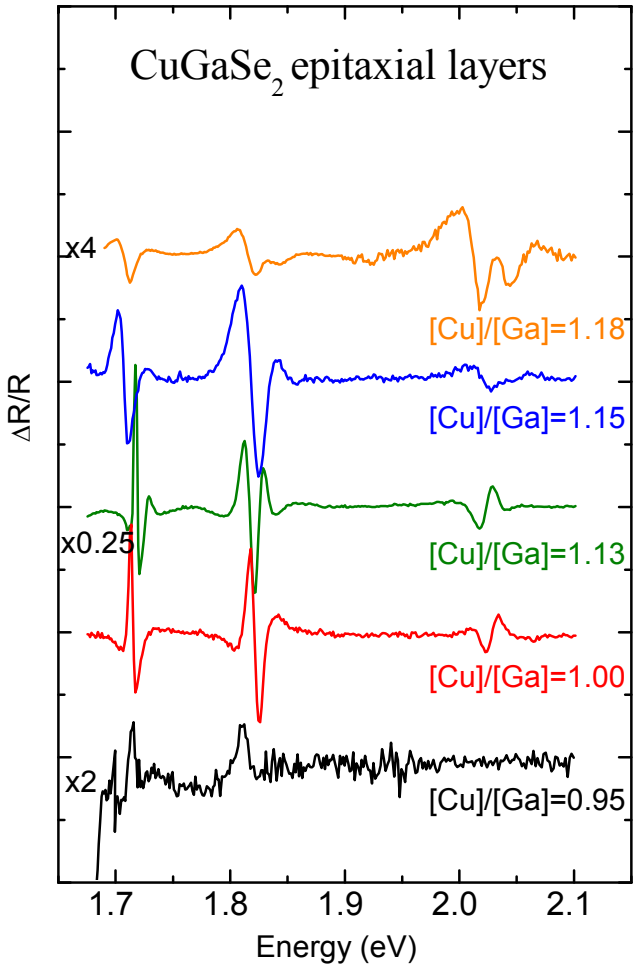

Figure 6.33 Composition dependent PR-spectra of MOVPE grown $CuGaSe_2$ at 20K

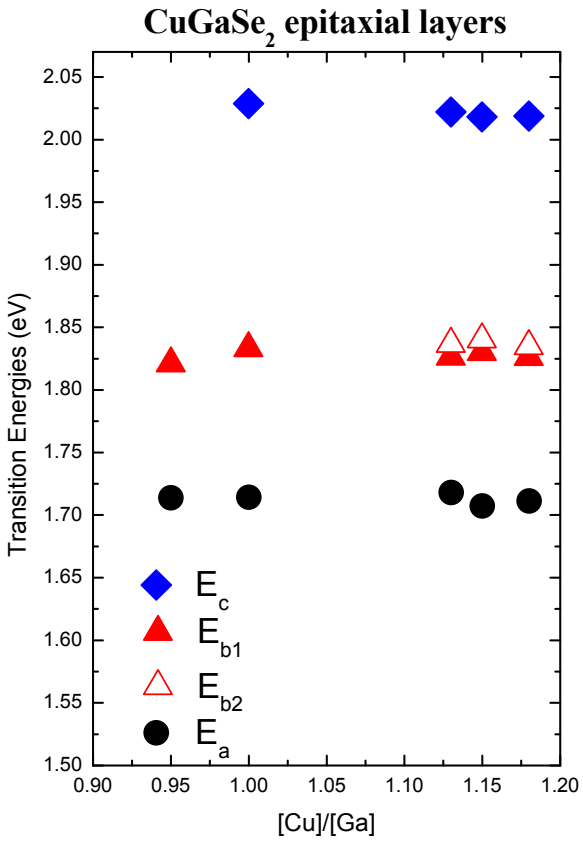

Figure 6.34 Compositional dependence of the three valence-split bands, E_a, E_b and E_c of MOVPE grown $CuGaSe_2$ at 20K

6.2.5 Compositional Dependence of $CuIn_{1-x}Ga_xSe_2$ chalcopyrite absorbers

The compositional dependence of the quaternary $CuIn_{1-x}Ga_xSe2$ chalcopyrite absorbers is studied in this section. The study of the quaternary chalcopyrites is not terminus for the present doctoral thesis; it gives though complementary information on the chalcopyrite absorbers.

In Figure 6.35, the room (300 K) PR spectra of $CuIn_{1-x}Ga_xSe_2$ (CIGS) epitaxial layers with different Ga fractions (x=0.00-1.00) are presented [6.22]. In the room temperature (RT) spectra of the CIGS layers with x<0.80, only the E_a transition is observed. With the increase of the Ga fraction, the E_a band energy shifts to higher energies, varying from 1.02eV (for $CuInSe_2$) to 1.68eV (for $CuGaSe_2$) in agreement with the Ellipsometry results on CIGS reported in [6.21]. With the decrease of temperature,

band broadening is reduced, both the E_a and E_b transitions are shifted to higher energies, and the E_b transition is clearly resolved probably because of the different temperature dependence of the E_a and E_b gaps [6.22]. The band energies were fitted using TDFFs. The E_a-gap energies at 300 in dependence of Ga content are listed in Table 6.7.

Ga-fraction X_{EDX} (Ref. [6.22])	**corrected Ga-fraction x**	**layer thickness d (nm)**	**fundamental gap-energy E_a (E_0(A)) (eV) 300 K**	**Absorption coefficient α (x10^5) (cm^{-1}) E=2eV (300 K)**
0.00		450	1.021	
0.08	0.08	440	1.083	1.42
0.19	0.19	440	1.141	1.48
0.33	0.22 0.53	360	1.152	1.82
0.50	0.50	390	1.301	1.57
0.60	0.55 0.75	290	1.369	2.06
0.82	0.82	250	1.514	2.78
1.00		450	1.684	

Table 6.7 Fundamental gap-energies E_a at 300 K, thickness d, and absorption coefficient α of CIGS epitaxial layers.

It should be noted, that the values of the Ga-fractions (x=[Ga]/([Ga]+[In]) published in Ref. [6.21] have been corrected here in accordance with the XRD- [6.63] and PL-results on the same films. For comparison, both the x-values measured by EDX, labeled x_{EDX} [6.22], and the corrected x-values (x) are given in Table 6.7.

The E_a and E_b transition energies calculated for the chalcopyrite absorbers from the PR spectra at 300K depend much upon the penetration depth of the modulating laser beam. In particular, according to ellipsometric data of CIGS quaternary compounds [6.64], the beam of 488 nm-Ar^+ laser penetrates only the upper region of the CIGS layers up to a depth of 75 nm. Bearing in mind that, in CIGS films, gallium segregates at the backside of the layer, close to the CIGS/GaAs interface, the obtained gap energies of CIGS films with eventually two phases (films with x_{EDX}=0.33 and 0.60, Table 6.7) are representative of the phase with the lower Ga-content. The corrected Ga-fractions

(labeled x in Figure 6.35 and Table 6.7) will be thus used for the CIGS films from now on. The thickness of the films is also given in Table 6.7.

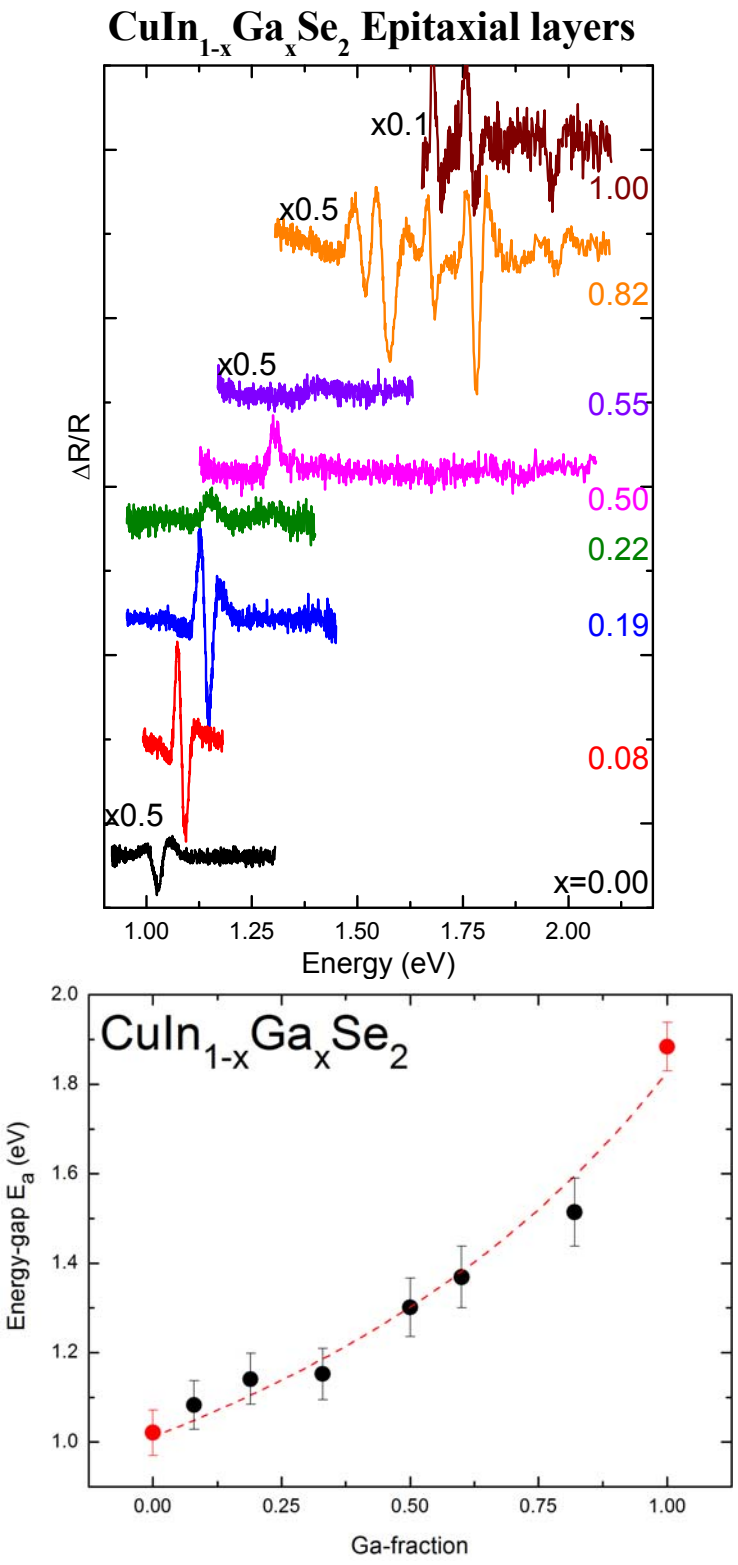

Figure 6.35 Compositional dependence of the PR-spectra of $CuIn_{1-x}Ga_xSe_2$ (CIGS) epitaxial layers at 300 K

B. GROWTH & CHARACTERIZATION STUDIES

6.3 CBD ZnSe grown on Amorphous Glass substrate

For controlling the conditions of growth, ZnSe thin films were initially deposited on amorphous glass substrates by Chemical Bath Deposition (CBD).

Glass substrates are previously placed in an ultrasonic bath with ethanol for 15 minutes and rinsed with distilled water. The conditions of the ZnSe deposition are analytically presented in §4.6. Deposition time varied from 1 to 6 hours. No film formation on amorphous glass substrate was observed with deposition time less than an hour. The film formation did not take place at room temperature, although the solution was kept for a long time. This is because, at low temperatures, most of the Zn^{2+} ions are in bound state due to strong Zn–amine complex formation. Therefore, bath solution was mechanically stirred with magnetic stirrer and thermostatized at 70^{o}C. After deposition, the substrates were taken out of the bath, rinsed with double distilled water, dried in air and preserved in an airtight plastic container. The as-grown films were homogeneous and appeared to have a yellow-golden color.

6.3.1 Structural properties

Zinc selenide thin films can be grown with metastable sphalerite cubic (zinc blende type) or stable wurzite (hexagonal type) structure [6.65]. Previous reports on chemically deposited ZnSe thin films showed that the films can form either cubic zinc blende or hexagonal wurzite type structure. Hence, in order to determine the crystal structure of as-grown and annealed ZnSe films, the XRD patterns of the films were analyzed.

Figure 6.36 shows the XRD patterns of as-grown and annealed films onto amorphous glass substrates. The as-grown films appear amorphous as indicated by the XRD measurements. In the as-grown samples, only the broad hump attributed to the amorphous glass substrate and possibly due to some amorphous phase in Zn-Se bonding is present. For this reason, annealing of the samples was mandatory. Crystallization of the films first appeared at 300^{o}C annealing temperature. The duration of annealing is also a

crucial parameter for the resulting ZnSe layers. Each sample was cut into pieces and each piece was annealed in an open air furnace.

Time of annealing for each ZnSe sample was in the range of 1 to 4 hours, and the X-Ray diffractograms are shown in Figure 6.36. Annealing for 1h did not result in the formation of crystalline ZnSe. The first peaks in the X-Ray diffractograms appeared for annealing time 2h at 300^{o}C. After annealing in atmospheric air ambient, the amorphous Zn-Se phase transformed into stable polycrystalline hexagonal phase [6.66]. In the X-Ray diffractograms, the dominant peak observed at bragg angle 29.335^{o} is assigned to the (101) reflection of the wurzite (hexagonal) type ZnSe and is designated in Figure 6.36 as WZ(101). In some of the diffractograms the zinc-blende (cubic) ZnSe (111) reflection is also present at 27.3^{o} [6.66], and it is designated as ZB(111).

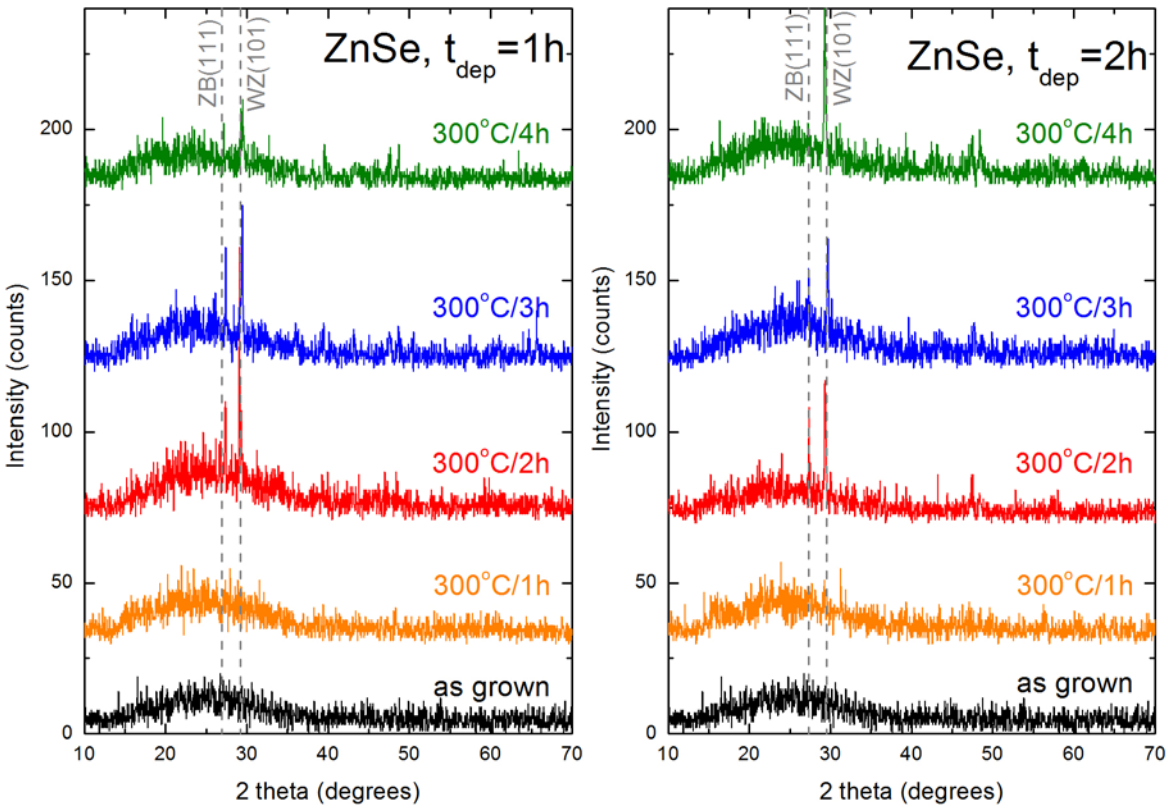

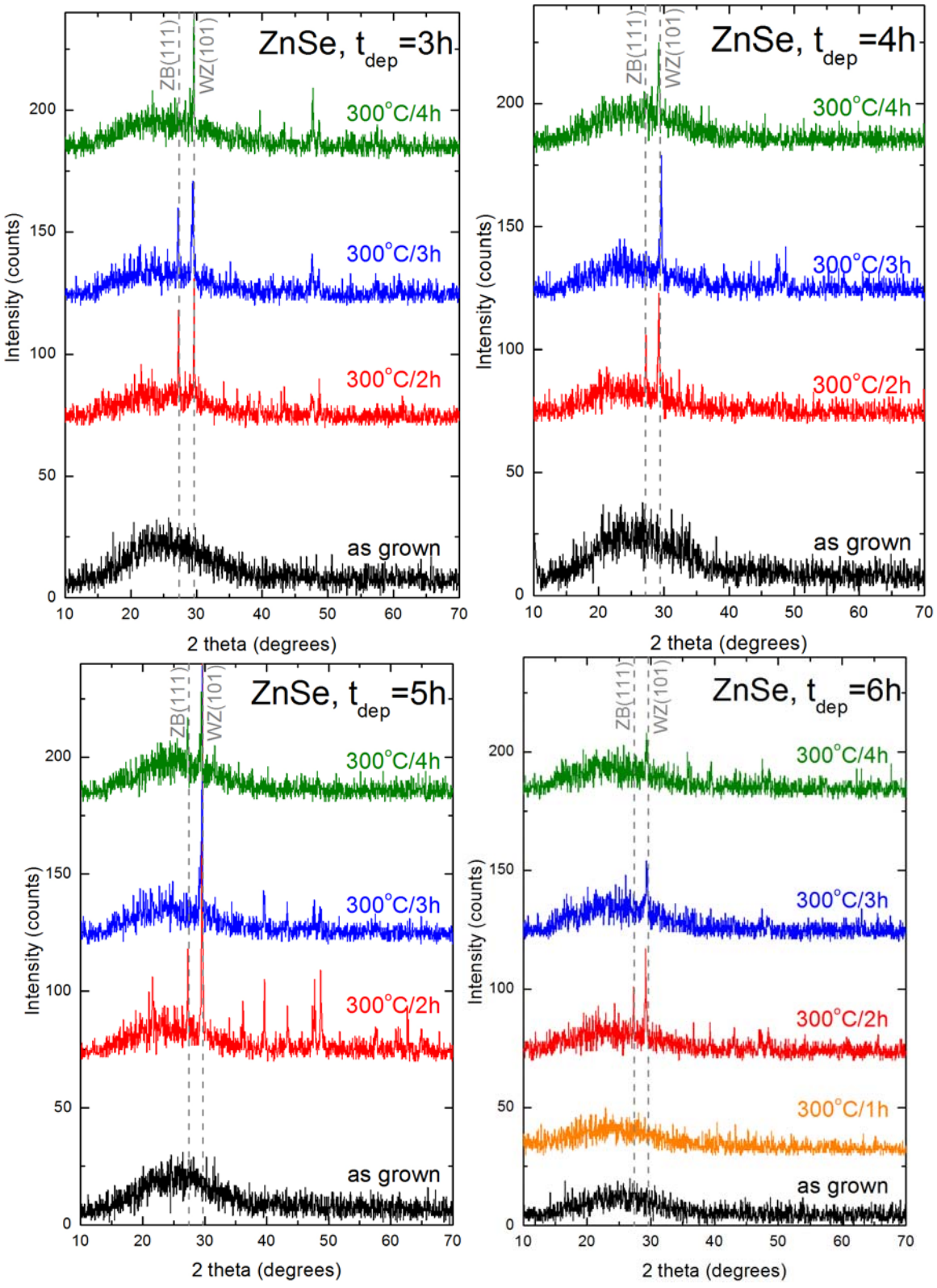

Figure 6.36 XRD diffractograms of CBD ZnSe on glass substrate

of both, as grown and annealed samples

The X-Ray diffractograms were further analyzed and the WZ(101) peaks were fitted with Lorentzians. Parameters, such as Bragg-angle, Full Width at Half Maximum (FWHM), and Intensity, resulting from the fitting, are presented in Figure 6.37. Increasing of deposition and annealing time affects significantly the deposited ZnSe layers. In particular, as time of deposition increases, the Bragg-angle approaches the angle of bulk hexagonal ZnSe (101) reflection. As the annealing time increases, a tendency for the peaks to shift towards lower 2θ values has been observed indicating an increase in interplanar distances. Furthermore, the width (FWHM) of the peaks appears to be narrower, which accounts for improved crystal quality of the layers.

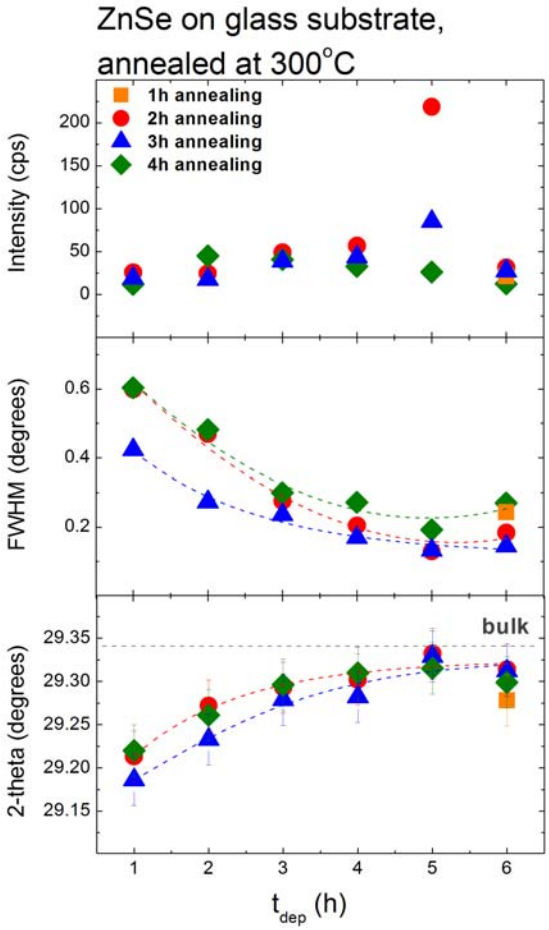

Figure 6.37 XRD parameters (Bragg-angle, FWHM, and Intensity) of the CBD ZnSe on glass substrate in dependence of deposition and annealing time

Strain/stress effects of the deposited ZnSe films have been analysed using Eqs.(3.7) and (3.13). The elastic stiffnesses of ZnSe are C_{11}=95.9GPa, C_{12}=53.6GPa and are given in [6.68]. In the calculation, the Bragg-angle 2θ=29.335^{o} [6.66] of the bulk (strain free) ZnSe was used. The results of strain/stress evaluation in dependence of deposition time of annealed ZnSe films are shown in Figure 6.38. Compressive stresses in-the-plane of the surface developing in ZnSe films on amorphous glass substrates are in the range σ= - (323 – 8) MPa after 2h of annealing, σ= - (395 – 61) MPa after 3h of annealing, and σ= - (308 – 53) MPa after 4h of annealing. The stress appears to relax with the increase of deposition time and, in particular, after 5h of deposition, which accounts for thicker films. ZnSe films annealed at 300^{o}C for 2h appear to be already overall less stressed.

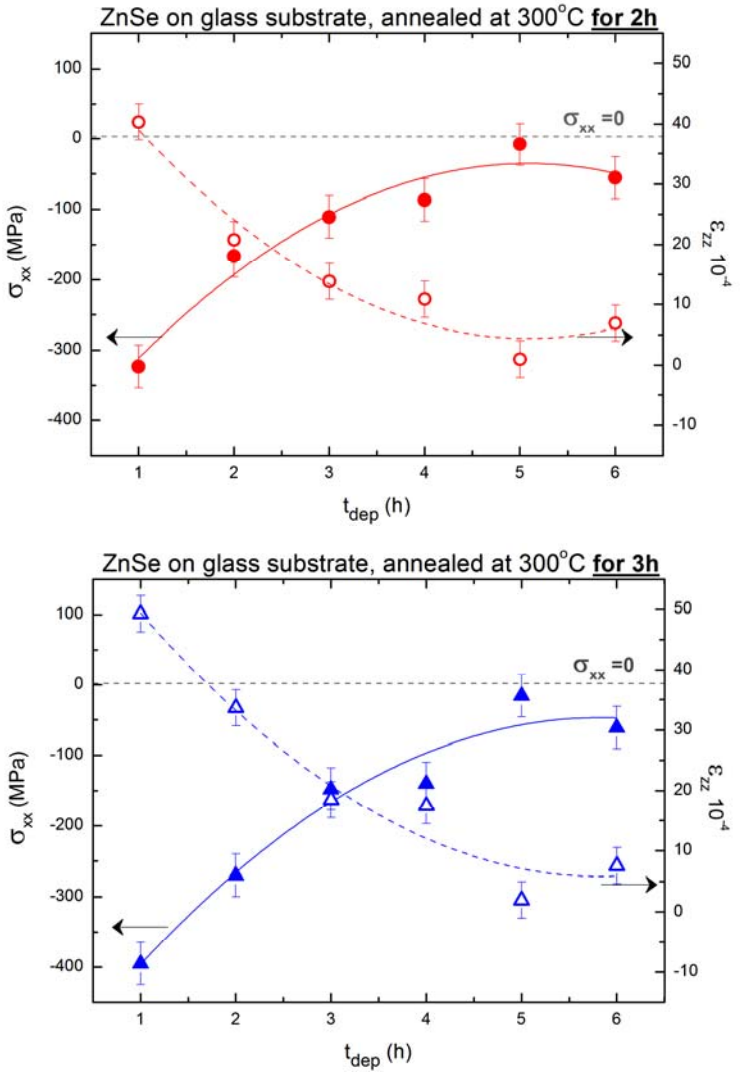

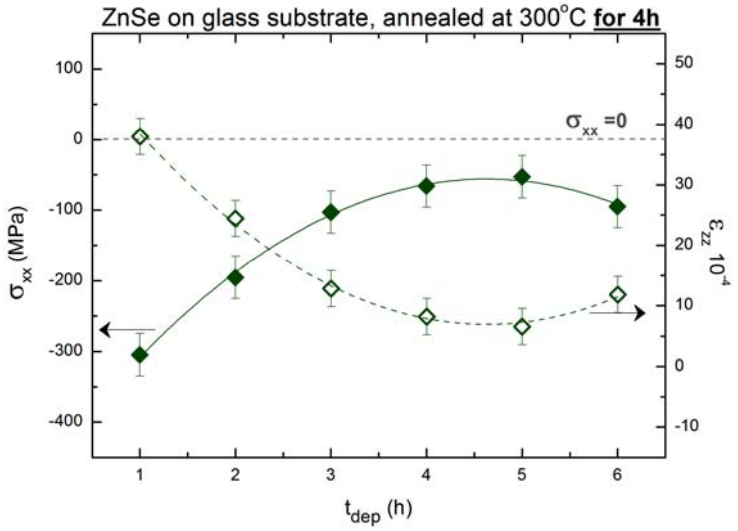

Figure 6.38 Strain/Stress in dependence of deposition time of ZnSe layers on amorphous glass substrate annealed at 300°C for 2h (red circles), 3h (blue triangles), and 4h (green rhombus)

XRD peak width varies inversely with crystallite size, according to Eq.(6.12). A mean crystallite size can be obtained by using the Scherrer formula [6.67]:

$$h = \frac{0.9\,\lambda}{B\cos\theta} \qquad (6.12)$$

In Eq.(6.12), λ is the x-ray wavelength in Å and θ is the Bragg-angle in radians, for a particular reflection. B represents the extra peak-width at half peak-height indicating the line-broadening with respect to a suitable standard.

Using the fitting parameters of the XRD measurements (Figure 6.37) and assuming spherical crystallite formation, the crystallite size has been calculated and is shown in dependence of deposition time in Figure 6.39. As indicated in the figure, the size of the crystallites is increased as the deposition time increases. In particular, the crystallite size for 1h deposition time is in the range of 20-40nm. By agglomeration of smaller size crystallites to crystallite of larger sizes, it reaches a maximum size of 110nm at 5h deposition time. Larger crystallite sizes implicate long range order and improvement of film quality. However, nucleation of large size particles on the substrate surface during film deposition leads to increased surface roughness of the deposited films.

Furthermore, comparison of ZnSe films, after annealing in ambient atmosphere for 2h and 3h, indicates that the creation of larger crystallites reaches a maximum, when deposition time has been 5h. On the other hand, for deposition times more than 5h, agglomeration effects seems to be already saturated and crystallites maintain sizes around 100nm, while annealing for more than 3 h leads to reduction of crystallite sizes independently of the duration of deposition (1-6h) and consequently to reduced film quality probably because of film aging under long-time thermal treatment. This behavior can possibly be conveyed to more effective crystallite formation mechanisms in the chemical bath compared to mechanisms activated by annealing in ambient atmosphere.

Crystallite sizes of ZnSe films with deposition time 3h and subsequent annealing for 4h are comparable with the sizes of crystallites of films with equal deposition time of 3h and subsequent annealing for 2h, whereas ZnSe films deposited and annealed for more than 4h exhibit systematically smaller crystallite sizes. This tendency can also be associated with the lower content of Se-atoms in the ZnSe film deposited for more than 4h as indicated by EDS measurements in the following section. The phenomenon is further intensified by the fact that annealing for more than 3h results also in reduced Se content of the ZnSe films.

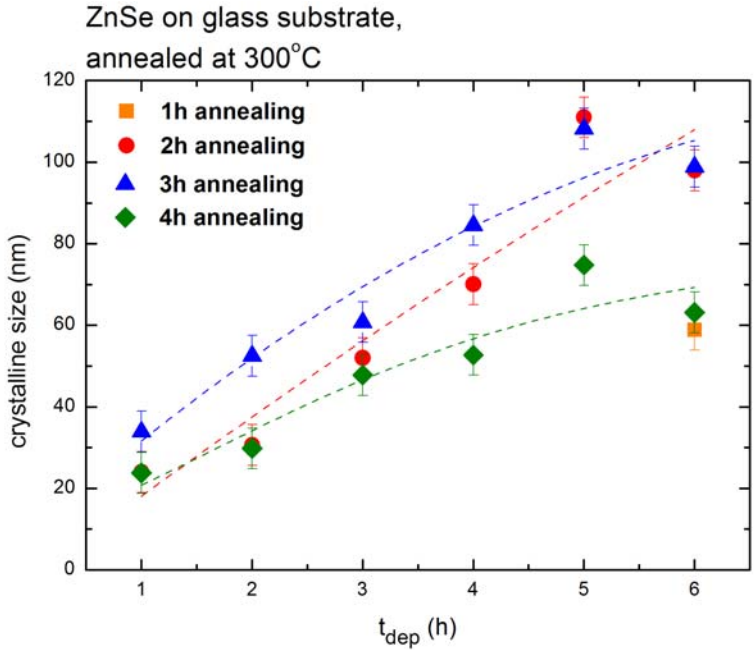

Figure 6.39 Crystallite sizes of the ZnSe films on amorphous glass substrate in dependence of deposition and annealing time

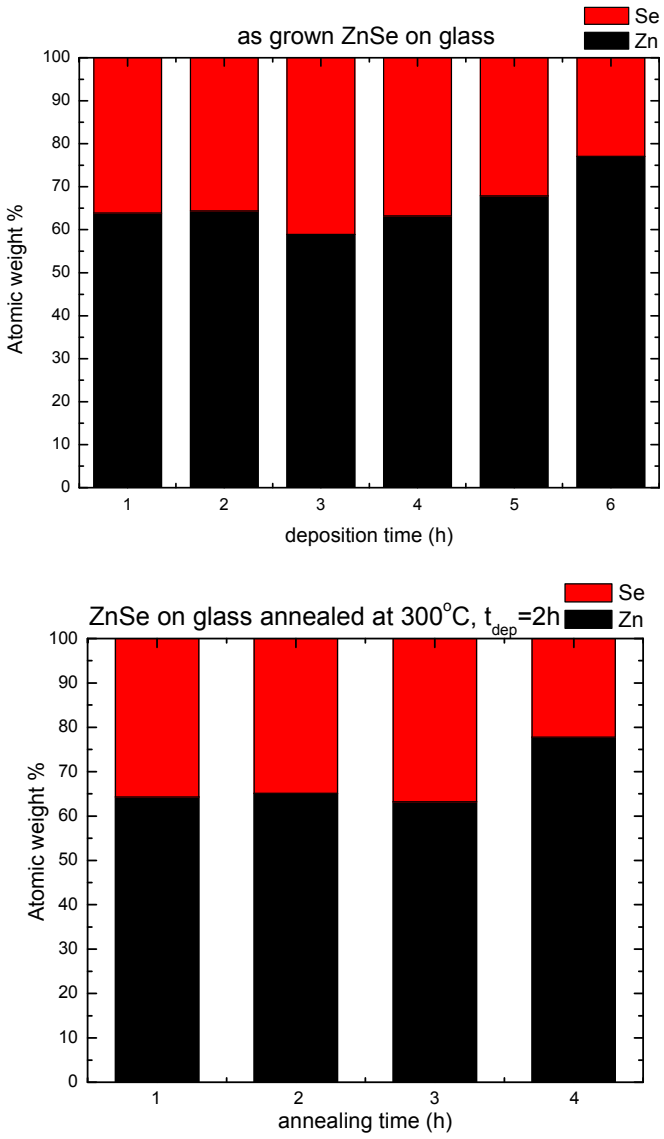

Figure 6.40 EDS results of CBD ZnSe on glass substrate in dependence of (a) deposition time (left) and (b) annealing time (right)

The CBD deposited ZnSe films (ZnSe: 144.35g/mol, Zn (65.39g/mol): 45.3%, Se (78.96 g/mol): 54.7%) are non-stoichiometric. Because of the Se solubility and volatility, Zn is in excess.

Energy Dispersive Spectroscopy (EDS) measurements (Figure 6.40) of the samples showed that for 1-5h deposition time the [Zn]/[Se] ratio remains the same. With further increase of the deposition time part of the Se is dissolved in the solution. Although annealing for 1-3h at 300°C does not significantly affect the [Zn]/[Se] ratio, for

annealing times above 3h, Se vaporizes from the film due to the formation of Se↑, and SeO_2↑ [6.66], according to the following reactions:

$$ZnSe + \frac{1}{2}O_2 \rightarrow ZnO + Se\uparrow$$
$$ZnSe + \frac{3}{2}O_2 \rightarrow ZnO + SeO_2\uparrow \quad (T \geq 400^o C) \tag{6.13}$$

Hence, due to appreciable amount of Se lost (melting point 221°C [6.67]), "quality degradation" of the sample takes place. A similar type of Se loss at and above 400°C for CBD ZnSe films has also been reported by Chaparro et al. [6.70].

For all the above reasons, annealing temperature 300°C and annealing time 2h were chosen for the thermal treatment of CBD grown ZnSe films.

The results of the dependence of the [Zn]/[Se] ratio on the film deposition and annealing time are presented in Figure 6.41. As can be seen, annealing leads to an increase of the [Zn]/[Se] content in the resulting ZnSe films pushing the films further beyond stoichiometry. In fact, the [Zn]/[Se] ratio is significantly increased when ZnSe undergoes annealing at 4h. Also, significant increase in the [Zn]/[Se] ratio takes place when the sample remains in the chemical bath for 5h or more, which is in agreement with previously published data [6.69].

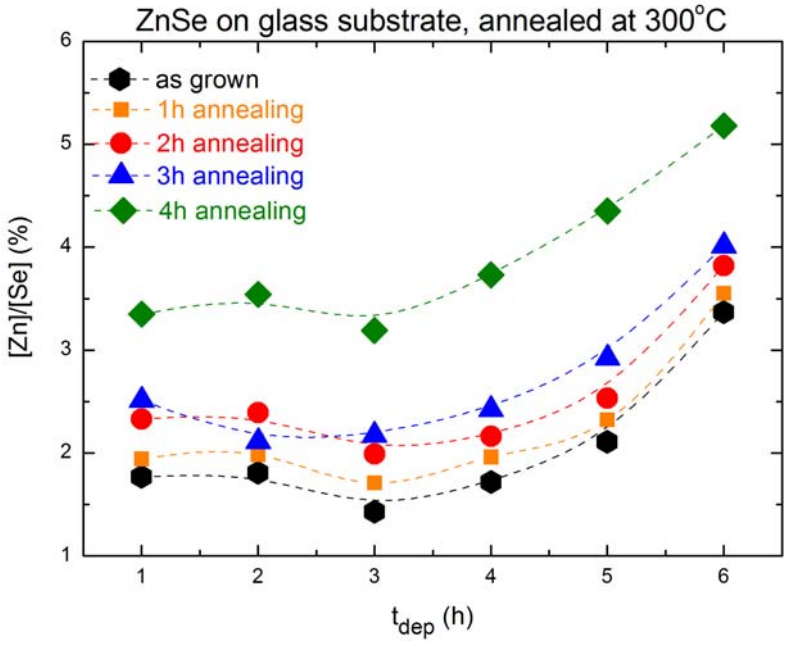

Figure 6.41 [Zn]/[Se] ratio of ZnSe films on amorphous glass substrates in dependence of deposition and annealing time.

Figure 6.42 shows a Scanning Electron Microscopy image of an as-grown ZnSe layer, after one hour of deposition. The image is captured in the region of the sample, where both substrate and deposited layer are apparent. From the image, homogeneous coverage of the glass substrate is concluded.

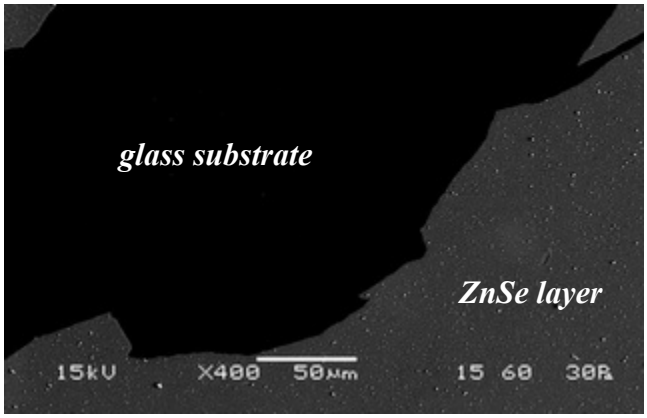

Figure 6.42 SEM-image of 1h CBD deposited ZnSe-layer showing homogeneous coverage of the glass substrate

Figure 6.43 shows scanning electron micrographs of as-deposited ZnSe film at 2000x magnification. The films are uniform and cover uniformly the surface of the glass substrate. In addition, two more observations are made with respect to the film growth mechanism: 1) the films seem to be composed of densely packed grains. Hence, it seems that the growth of ZnSe films by CBD takes place via cluster by cluster deposition, i.e. aggregation of colloidal particles formed in the solution rather than ion by ion deposition on the surface of the glass substrate, which agrees well with the results previously reported [6.71], [6.72], and [6.73]. It is worth to mention that, in the literature, there is no evidence for ion by ion growth of ZnSe. By increasing the duration of deposition from 1 to 6h, the size of the grains appears larger leading to increase of the surface roughness of the deposited layers.

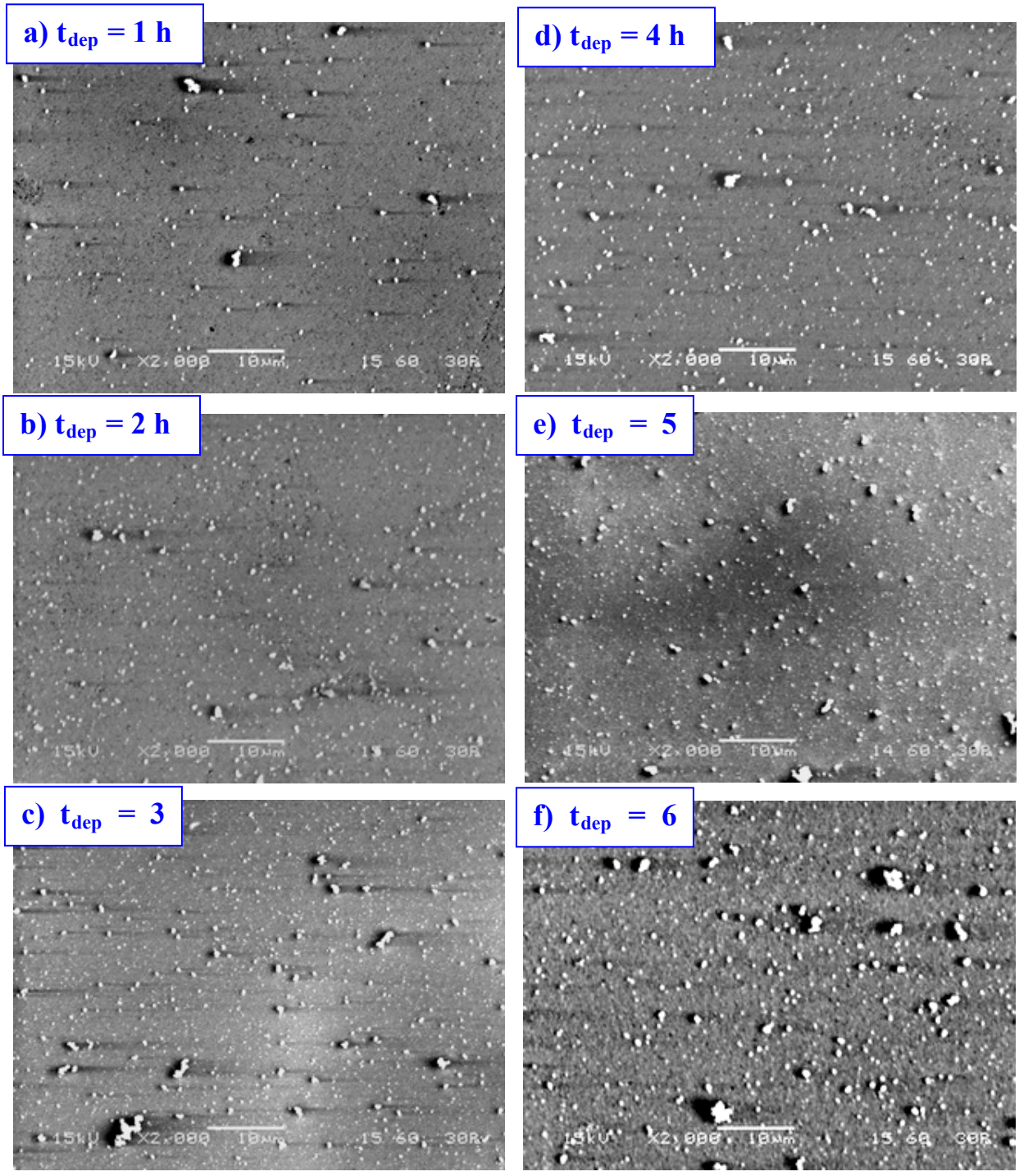

Figure 6.43 SEM images of as-grown ZnSe films with 1 - 6 h deposition time

Figure 6.44 shows the SEM images of ZnSe thin films annealed at 300^{o}C with annealing duration of 1, 3, and 5h (4000x magnification). As-grown ZnSe layers exhibit pinholes scattered in their structure and on surface. Annealing improves the quality of the layers. Pinholes disappear after 2h of annealing. However, after 4h annealing of less thick layers, with deposition time 1h, cracks appear on the surface. This disadvantage is not observed in thicker layers with deposition times 3 and 5h. From the SEM images, it is concluded that, the films exhibit significant quality improvement after annealing at 300^{o}C for 2h.

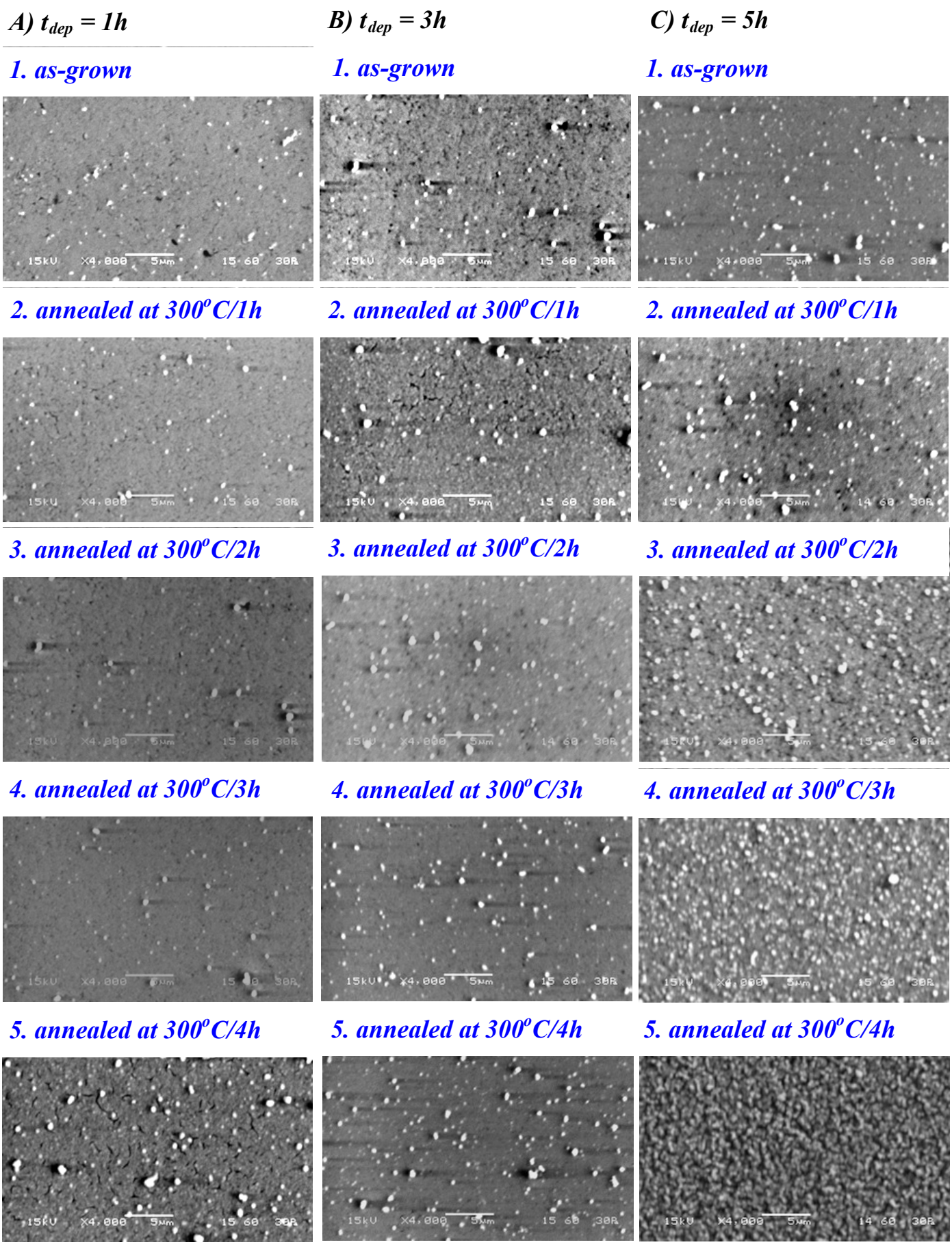

Figure 6.44 SEM images of CBD ZnSe films

in dependence of deposition and annealing time

Film thickness of ZnSe is a critical parameter in the solar cell development procedure. The thickness of ZnSe films deposited by Chemical Bath Deposition depends strongly on the deposition time. Using a profilometer and scanning along a line from the glass substrate to the ZnSe thin film, the thickness of the layers was obtained. The thickness in dependence of deposition time for CBD ZnSe on glass substrate is shown in Figure 6.45. Initially, the film thickness increases linearly and reaches a maximum value (330nm) for 5h deposition time. For longer deposition times, the film thickness shows a slight decrease, as it has already been observed elsewhere [6.66]. Such a phenomenon can be explained by considering the two competing processes in the deposition bath: one process includes the heterogeneous precipitation and homogeneous precipitation of ZnSe, which leads to the film growth, and the other one involves desorption and/or dissolution of the pre-formed ZnSe film, which results into decrease of film thickness. In the initial state of film deposition, the source materials are sufficient and the solution has a high degree of super-saturation, the process of homogenous precipitation (ion-by-ion nucleation and growth mechanism) or aggregation of colloidal particles (cluster by cluster nucleation and growth mechanism) in the solution plays a more important role than the dissolution process, which leads to an increase of ZnSe film thickness. With the deposition time being prolonged, the source material becomes less and less and therefore, after a certain deposition time, the dissolution process predominates over the heterogeneous precipitation on the film and in the solution, resulting into decrease of the ZnSe film thickness.

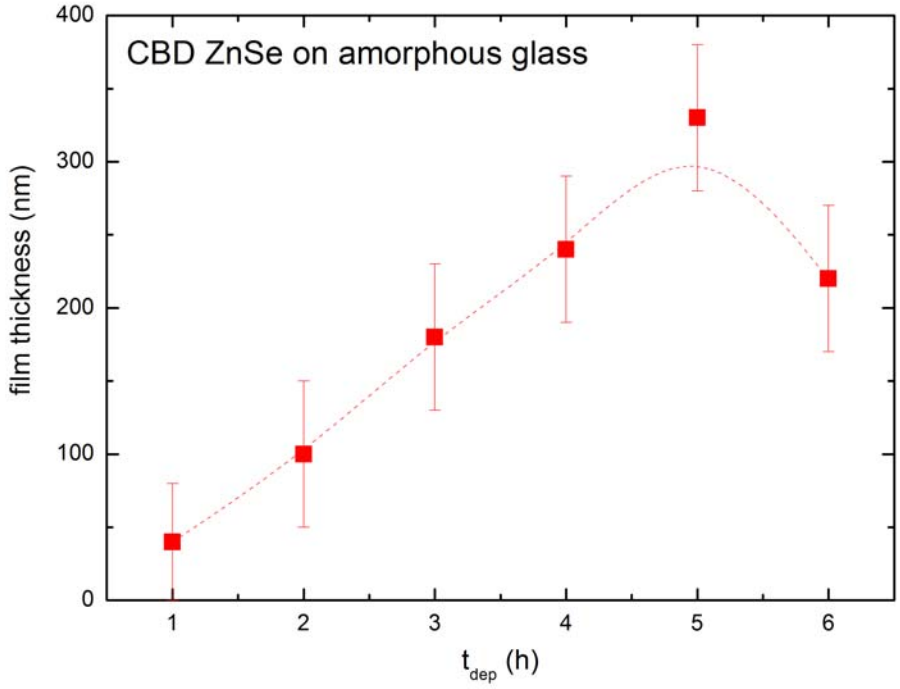

Figure 6.45 Film thickness of ZnSe thin films on amorphous glass substrates in dependence of deposition time

6.3.2 Optical properties

The optical properties of the CBD ZnSe thin films on amorphous glass substrates have been investigated by Optical Absorbance (A). The absorption coefficient, a, is defined by the Beer-Lambert law and is related to the absorbance, in a first approximation, according to:

$$\mathrm{a} = 2.3\frac{A}{d} \tag{6.14}$$

where d is the thickness of the film.

In order to obtain the (optical) band gap, the Tauc model is considered. The main assumption, in this model, is that the edges of the conduction band and valence band are parabolic [6.74] and can be described as:

$$(\mathrm{a}hv) = B(hv - E_g)^m \tag{6.15}$$

where E_g is the optical band-gap, B is an energy-independent constant between 10^7 and 10^8 m^{-1}, and m is an index which characterizes the optical absorption process and is theoretically equal to 2 and 0.5 for indirect and direct allowed transitions, respectively.

Figure 6.46 (a) – (f) below shows $(\alpha h\nu)^2$ vs. photon energy (tauc-plot) for the ZnSe films on amorphous glass substrates, with deposition times 1-6h and annealing times 1-4h depending on the growth parameters selected for each film. The tauc-plots have been obtained by absorbance measurements using Eq.(6.15) via Eq.(6.14) and data from Figure 6.45 for the film thickness *d* (in Eq.(6.14)). The variation of $(\alpha h\nu)^2$ vs. hν is linear at the absorption edge, which confirms the direct band gap transition in ZnSe. The values of the direct optical band-gap E_g are obtained from the intercept of $(\alpha h\nu)^2$ vs. hν curves plotted and are shown in the inset of the graphs.

The band gap energy, E_g, of the ZnSe thin films ranges from 2.68 to 2.98eV. Most films exhibit a slight 'blue- shift' in their energy band gap with respect to the standard bulk energy gap (Eg = 2.7 eV) [6.75], which can be attributed to the compressive stress present in the grown ZnSe films [6.76].

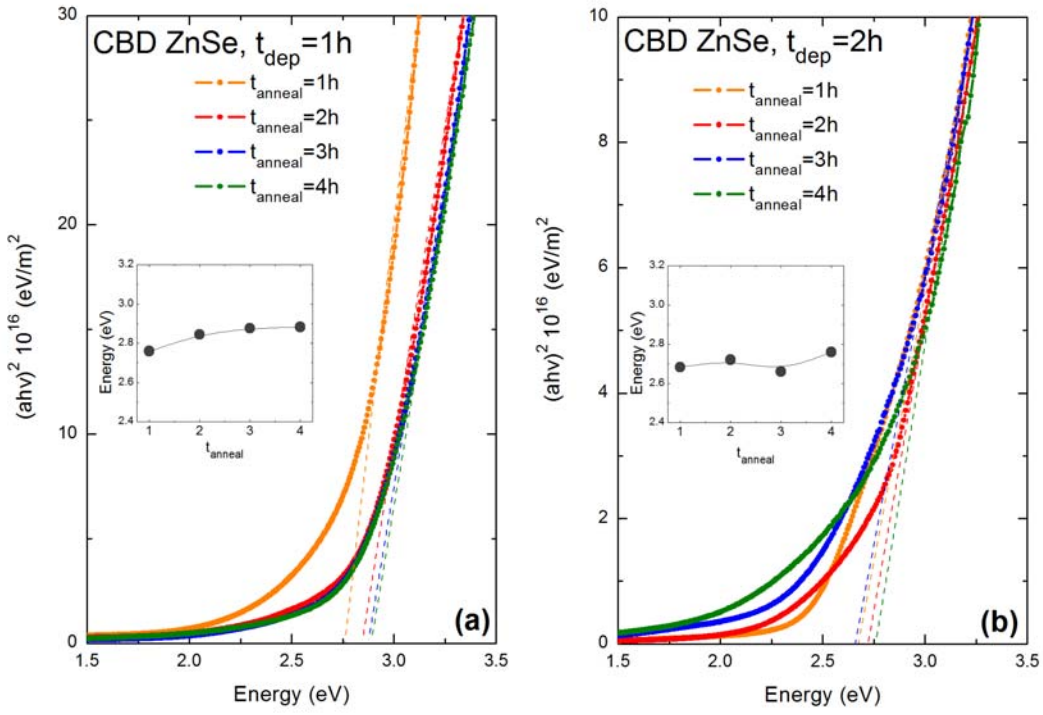

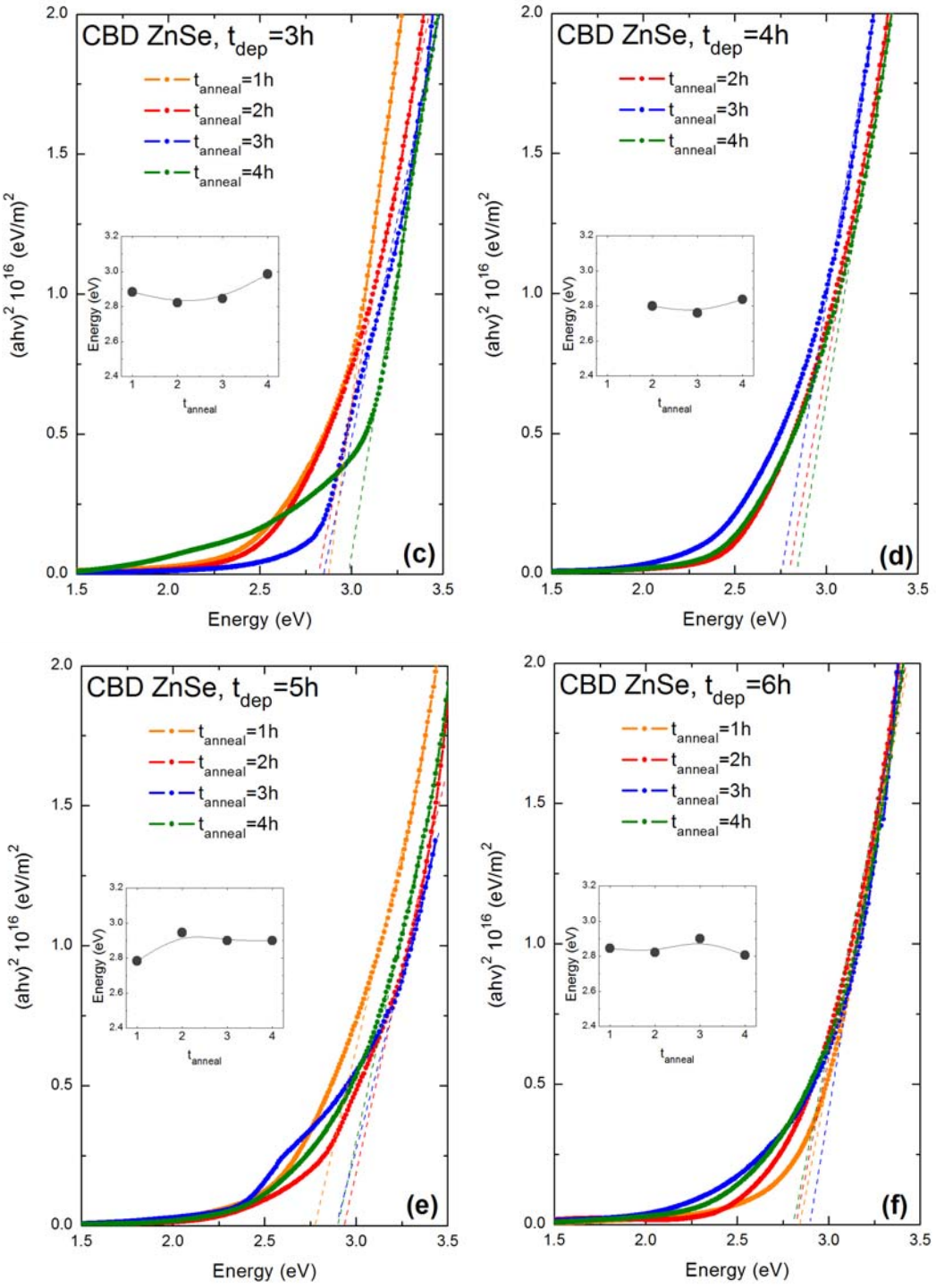

Figure 6.46 Plot of $(\alpha hv)^2$ versus photon energy (hv) of the ZnSe thin films on amorphous glass substrates, with deposition time (t_{dep}) (a) t_{dep}=1h, (b) t_{dep}=2h, (c) t_{dep}=3h, (d) t_{dep}=4h, (e) t_{dep}=5h, and (f) t_{dep}=6h, and for annealing time (t_{anneal}) that varies from 1 to 4h.

6.4 CBD ZnSe on Epitaxial Chalcopyrite Absorbers

After deposition of ZnSe on glass substrate, chemical bath deposition of ZnSe was also performed on epitaxial chalcopyrites. ZnSe is used as a buffer layer between the chalcopyrite absorber and the ZnO window layer. In substrate configuration of solar cell devices, ZnSe is deposited on polycrystalline chalcopyrite absorber. Deposition on epitaxial chalcopyrite absorber aims to clarify the influence of the underlying absorber layer on nucleation and thickness of the deposited ZnSe epilayer.

6.4.1 Structural properties

Figure 6.47 shows the XRD patterns of a) epitaxial $CuGaSe_2$ layer grown on GaAs (100), b) as-grown ZnSe deposited by Chemical Bath Deposition onto epitaxial $CuGaSe_2$ substrate, and c) annealed ZnSe layer on $CuGaSe_2$ substrate.

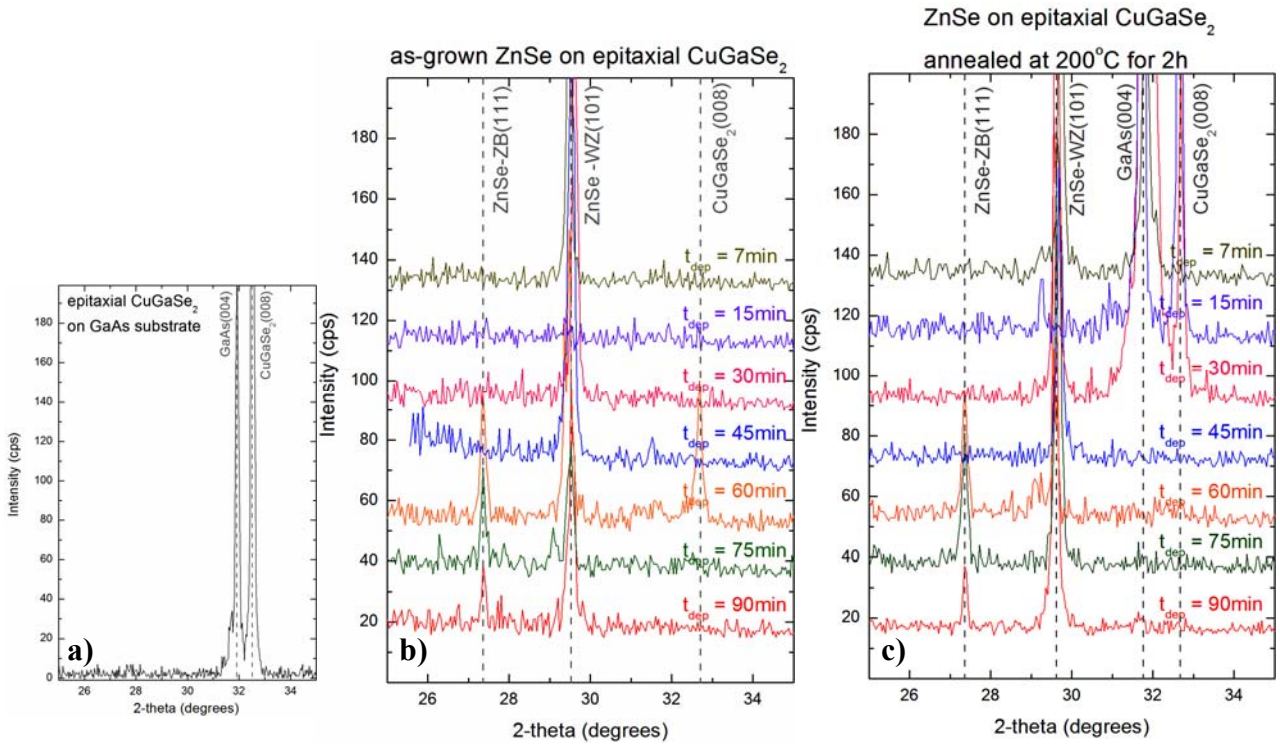

Figure 6.47 XRD patterns of: a) $CuGaSe_2$ epitaxial chalcopyrite on GaAs, b) as-grown CBD ZnSe on epitaxial $CuGaSe_2$ chalcopyrite substrate, and c) CBD ZnSe on epitaxial $CuGaSe_2$ chalcopyrite substrate, annealed at 300°C for 2h.

In this case, formation of ZnSe has been registered for deposition time less than 1h. The highly ordered structure of the epitaxial chalcopyrite seems to assist the fast and ordered growth of the ZnSe layer. When deposited on epitaxial $CuGaSe_2$, the ZnSe layers grow already along the (101) plane, as indicated by the reflection observed at Bragg-angle 29.335^o. For deposition time greater than 1h (60min), the reflection from the cubic ZnSe (111) crystallographic plane is also observed at 27.3^o [6.66]. The as-grown samples have been annealed in order to improve further the crystal quality of the layers. The conditions of annealing were chosen according to the results of the control experiments of ZnSe growth on amorphous glass substrate. In particular, the annealing temperature was 300^oC and the duration of annealing was 2h.

The X-Ray diffractograms were fitted with Lorentzians. Parameters, such as Bragg-angle, Full Width at Half Maximum (FWHM), and Intensity resulting from the fitting, are presented in Figure 6.48. The deposition time affects the thickness of the resulting ZnSe layers. In particular, as the time of deposition increases, the Bragg-angle of as-grown ZnSe layers approaches the angle of the bulk indicating relief of mismatch strain by formation of dislocations [6.77]. On the other hand, in the annealed films, the Bragg-angle appears almost equal to the angle of the bulk, which implies that high temperature treatment of the films results in strain/stress relaxation. Furthermore, comparing the FWHM of the XRD peaks, the annealed films exhibit narrower peaks with reference to the as-grown ones, which is indicative of the improved crystal quality of the films after subsequent annealing.

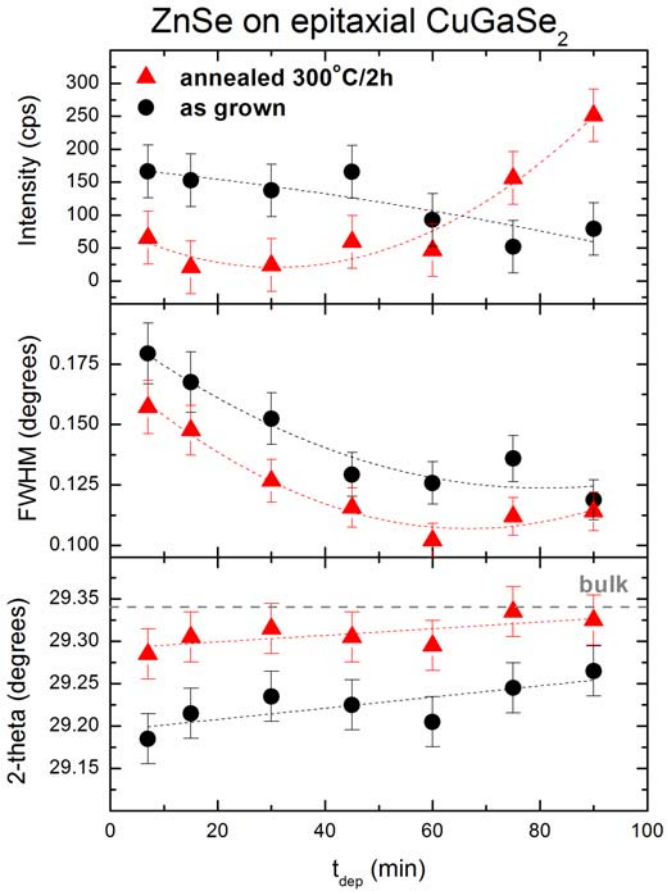

Figure 6.48 XRD parameters (Bragg-angle, FWHM, and Intensity) of the CBD ZnSe on epitaxial $CuGaSe_2$ of as-grown (black bullets) and annealed (red circles) films

Strains/stresses of the CBD ZnSe films on chalcopyrites have been calculated using Eqs.(3.7), (3.13), the elastic stiffnesses of ZnSe C_{11}=95.9GPa, C_{12}=53.6GPa given in [6.68], and the Bragg-angle $2\theta=29.335^{o}$ [6.66] of the bulk (strain free). The results of strain/stress evaluation in dependence of deposition time of as-grown and annealed ZnSe films on epitaxial chalcopyrites are shown in Figure 6.49. Compressive, in-plane stresses developing in as-grown films are between -398 and -185MPa. The stress is partially relaxed with increasing the deposition time, which is a result of the increasing film thickness. After 2h of annealing, the stress relaxes, as expected; its value is between -132 and 0MPa. It seems, that, after 75min deposition followed by 2h annealing at 300°C, the ZnSe layer is fully relaxed through relief of mismatch strain. Such a relief of the lattice strain is acquired through the formation and propagation of dislocations far away from the heterointerface.

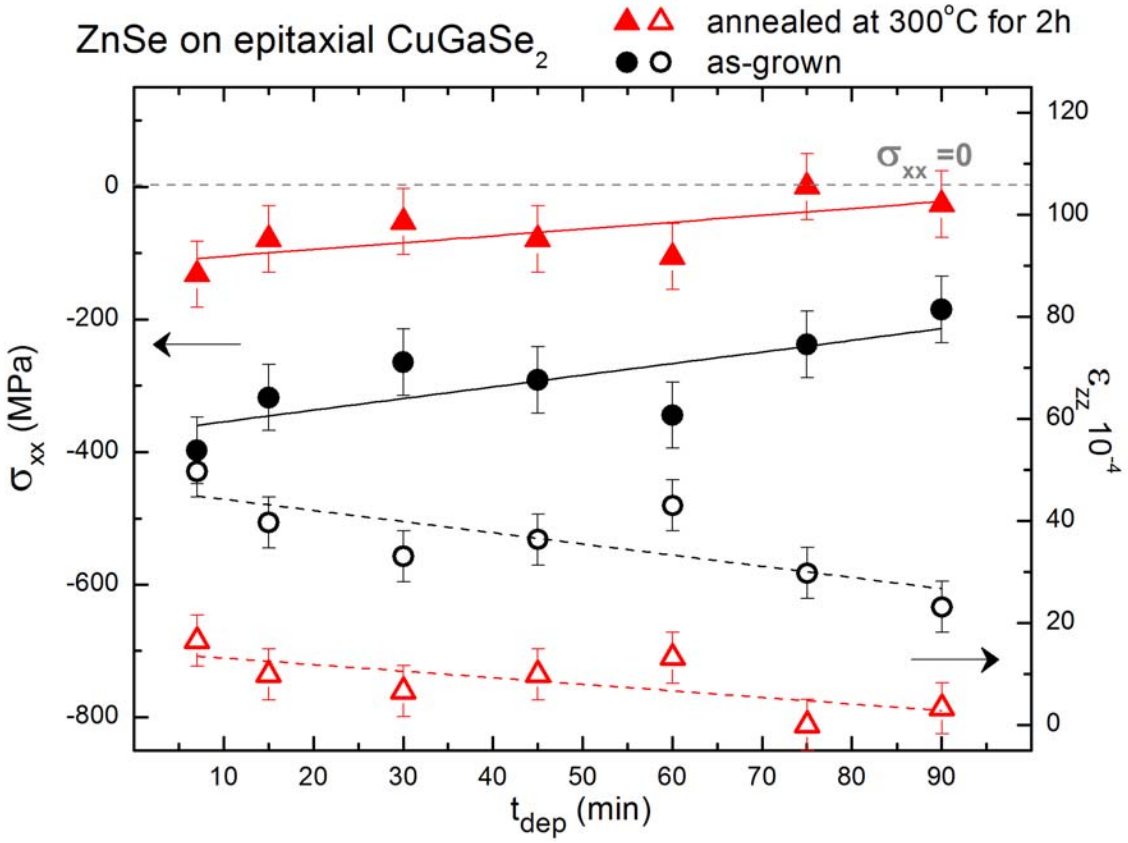

Figure 6.49 Strain/Stress in dependence of deposition time of a) as-grown (black circles) and b) annealed at 300°C /2h (red triangles) ZnSe layers on epitaxial chalcopyrites

XRD peak width varies inversely with crystallite size according to Eq.(6.12). Using the fitting parameters of the XRD measurements (Figure 6.48) and assuming spherical crystal formation, the crystallite size has been calculated and is shown in Figure 6.50. As indicated in the figure, the size of the crystallites is increased as the deposition time increases. In particular, crystallite sizes of as-grown ZnSe films are in the range of 91-141nm and reach a maximum after 60min deposition time.

Furthermore, comparison of crystallite sizes of as-grown and annealed films indicates, that, after annealing, crystallite sizes are slightly reduced independently of deposition time, thus the good crystal quality of the deposited films may be possibly affected, though the surface roughness is reduced.

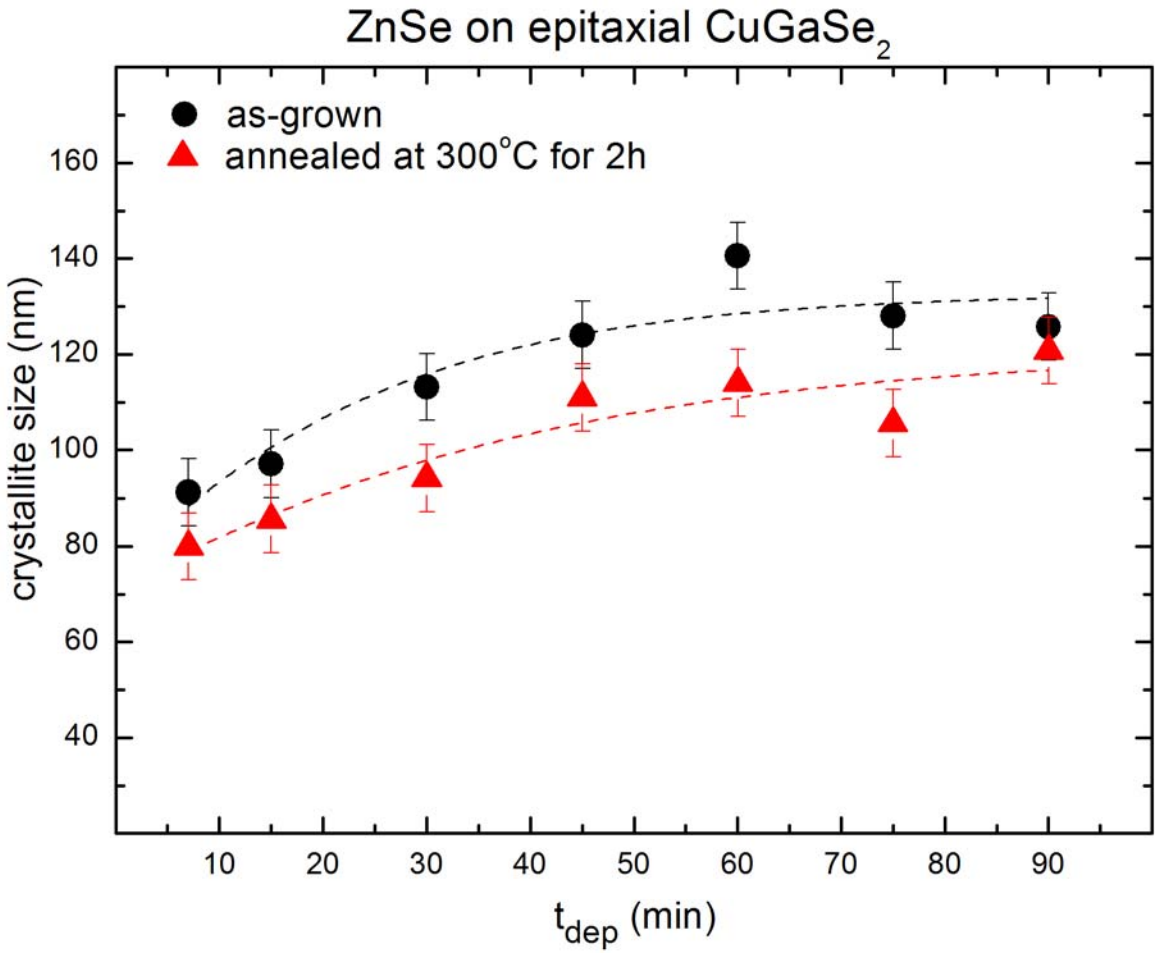

Figure 6.50 Crystallite size of a) as-grown (black circles) and b) annealed at 300°C for 2h (red triangles) ZnSe films on epitaxial chalcopyrites in dependence of deposition time

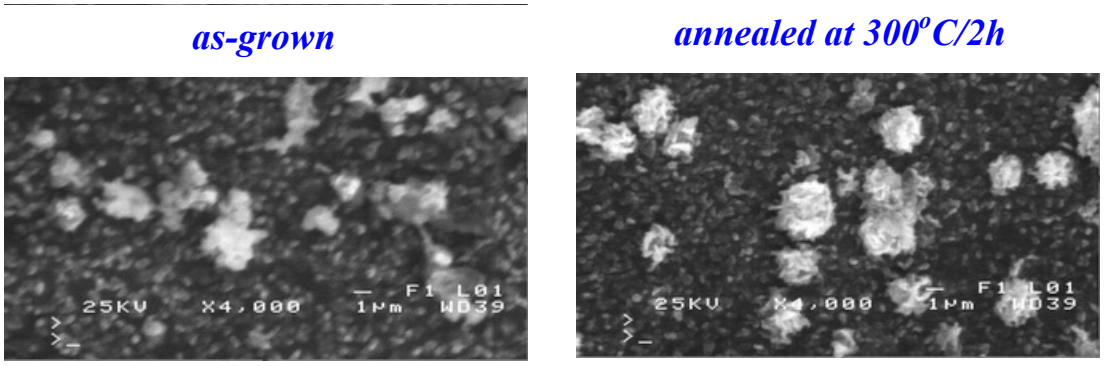

Figure 6.51 SEM-images of as-grown (left) and annealed (right) ZnSe-layer on epitaxial chalcopyrite

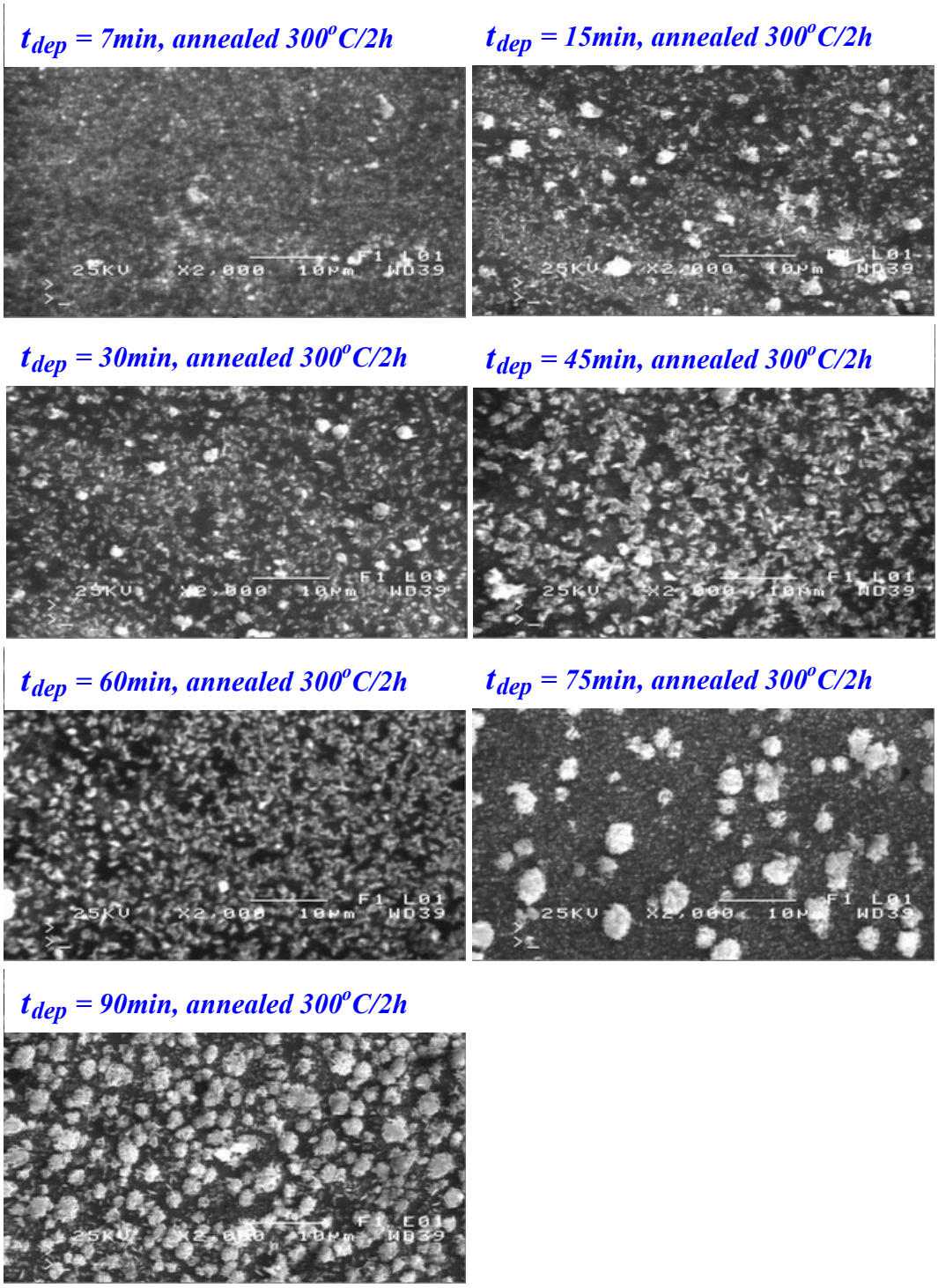

Figure 6.52 SEM images of annealed ZnSe on epitaxial $CuGaSe_2$ for deposition time 7-90 min

Figure 6.51 shows SEM images of as-grown and annealed ZnSe layer on epitaxial $CuGaSe_2$. Annealing affects slightly grain sizes and most probable induces "material fatigue" in the highly oriented ZnSe layers grown on epitaxial chalcopyrites.

Figure 6.52 shows SEM images of annealed ZnSe layers with deposition times varying from 7 to 90min. From the images, it is obvious, that the morphology of the ZnSe layers is strongly related to the epitaxial nature of the underlying chalcopyrite layer. The thickness of the deposited layer depends on the duration of deposition. At deposition time of 7min, a thin homogeneous layer is grown on the $CuGaSe_2$ surface. By increasing the deposition time, the ZnSe layer covering the chalcopyrite surface becomes thicker; in addition, larger ZnSe grains are formed, among them some even larger sparsely spread on the surface. Those larger grains become more compact as deposition time increases.

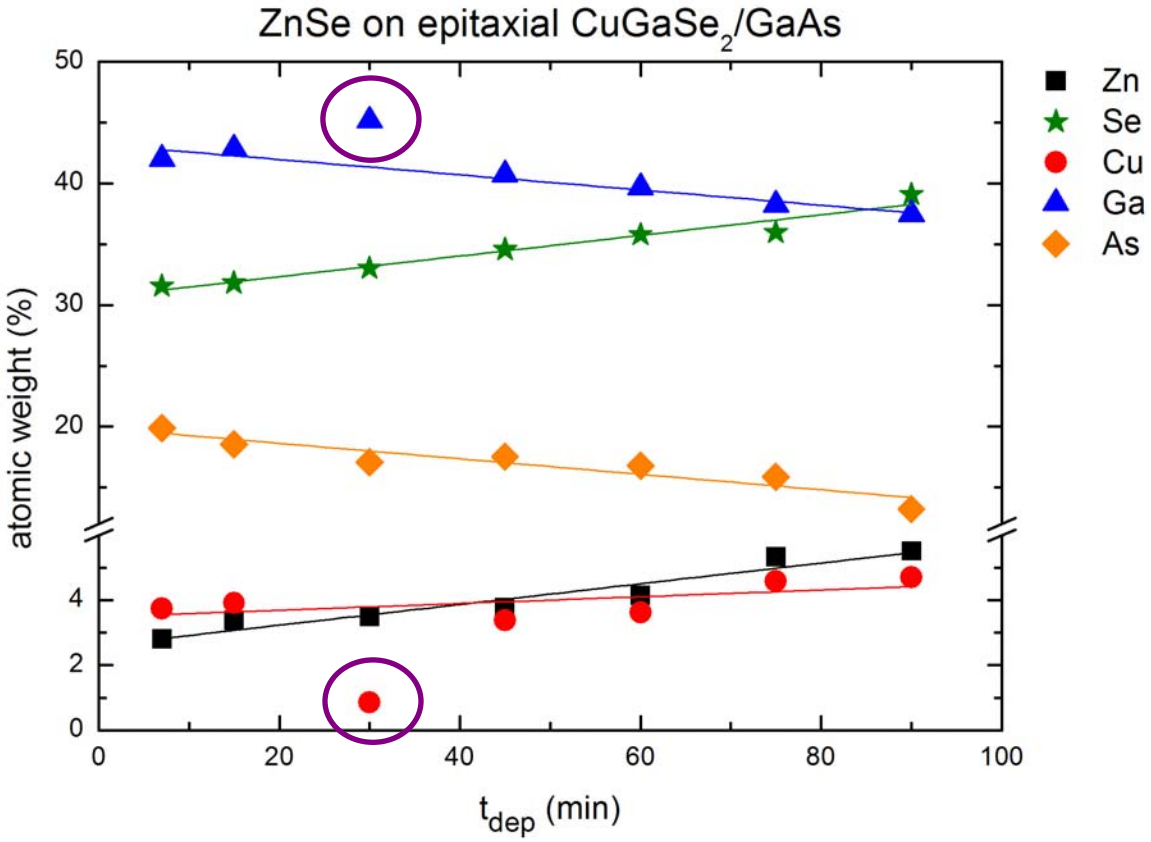

Figure 6.53 Elemental composition of ZnSe layers on epitaxial $CuGaSe_2$/GaAs

EDS measurements were performed on annealed ZnSe layers deposited on epitaxial $CuGaSe_2$/GaAs chalcopyrites. In Figure 6.53, the % atomic weight of elements:

Zn, Se, Cu, Ga, As are presented for samples with different deposition times. In particular, the % atomic weight of Zn and Se are growing with the increase of deposition time. This effect is attributed to the growing thickness of the layers in accordance with deposition time. The same conclusion can be drawn from the decreased atomic weight of Ga in dependence of deposition time. The presence of As in the EDS measurement indicates that the electron beam penetrates both ZnSe and $CuGaSe_2$ layers and reaches the GaAs substrate of $CuGaSe_2$. Deconvolution of the atomic weight % originating from the three different (ZnSe, $CuGaSe_2$, and GaAs) layers is not feasible, mostly because Ga is part of both, $CuGaSe_2$ and GaAs, and Se, part of both, ZnSe and $CuGaSe_2$ layers. Moreover, the slightly growing tendency of Cu can be explained by the [Cu]/[Ga] ratio of the $CuGaSe_2$ layers. In particular, the epitaxial chalcopyrites used to deposit ZnSe with deposition times 45, 60, 75, and 90min are Cu-rich, with [Cu]/[Ga]=1.10, 1.12, 1.13, and 1.10, respectively. The circled data points, in Figure 6.53, have been excluded from the analysis, since the $CuGaSe_2$ layer used for 30min deposition was Cu-poor, with [Cu]/[Ga]=0.96. The [Cu]/[Ga] ratio can explain the low value of the Cu atomic weight %, and the high value of the Ga atomic weight %.

The thickness of the ZnSe layers is a critical parameter in the development of thin film chalcopyrite solar cells. Thickness calibration was performed also on ZnSe layers on epitaxial chalcopyrites. Thickness, in this case, could not be measured with a profilometer due to the small size of the samples. Instead, Scanning Electron Microscopy (SEM) on the crossection of the samples was employed. In Figure 6.54, SEM images of the sample cross-section used to determine the layer thickness are presented.

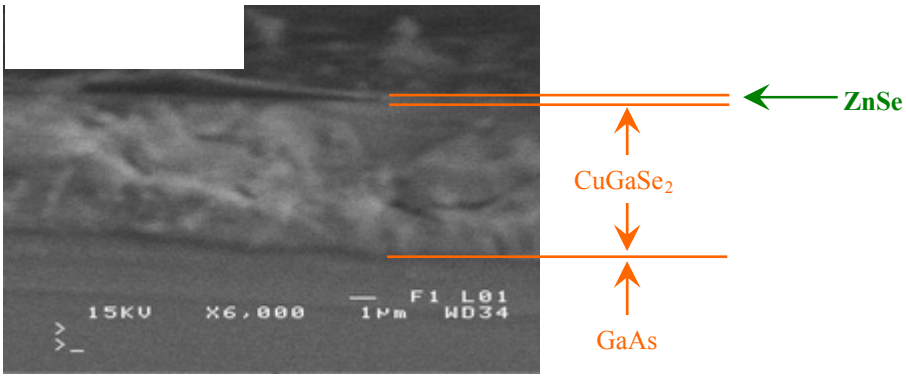

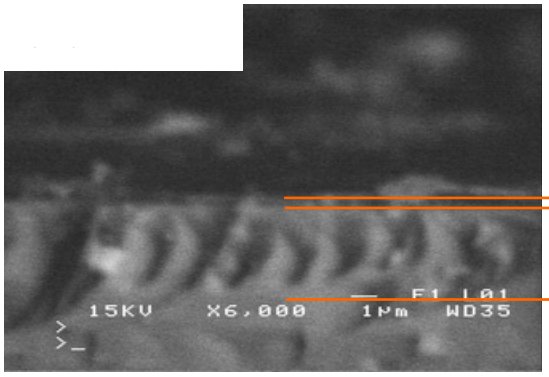
15KV X6,000 1µm WD35
F1 L01
ZnSe
CuGaSe2
GaAs

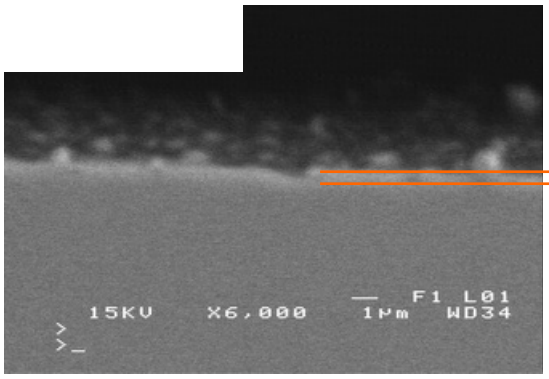
15KV X6,000 1µm WD34
F1 L01
ZnSe
CuGaSe2

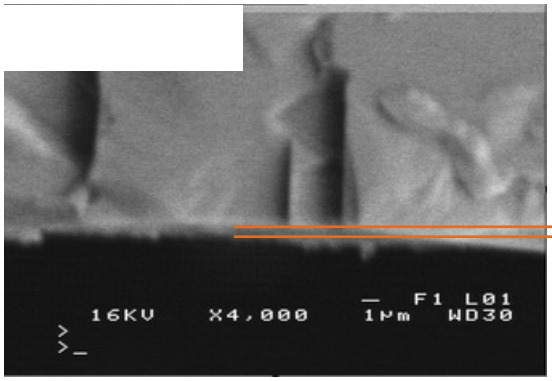
16KV X4,000 1µm WD30
F1 L01
CuGaSe2
ZnSe

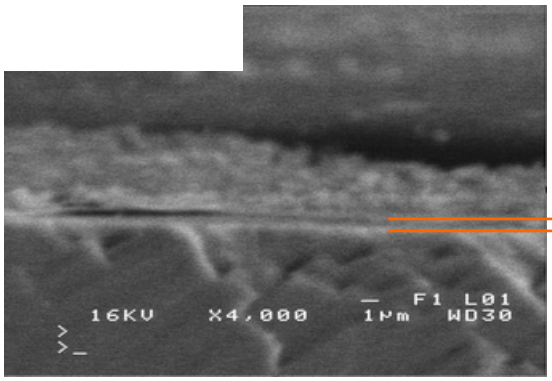
16KV X4,000 1µm WD30
F1 L01
ZnSe
CuGaSe2

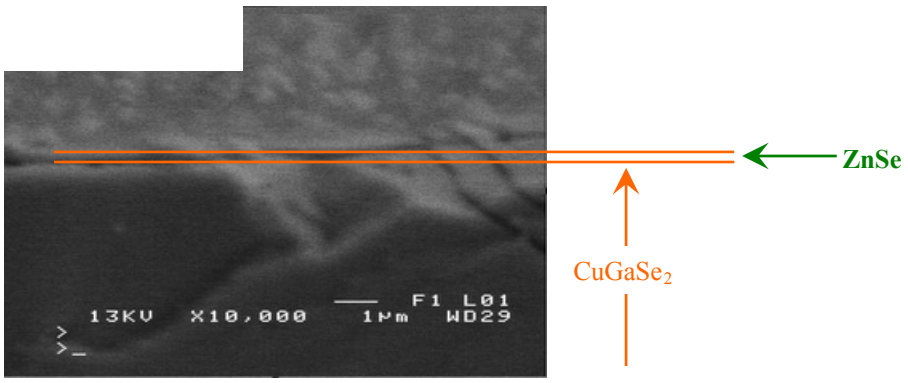

Figure 6.54 SEM images of the crossection of ZnSe on $CuGaSe_2$/GaAs. (different layers are distinguished using lines)

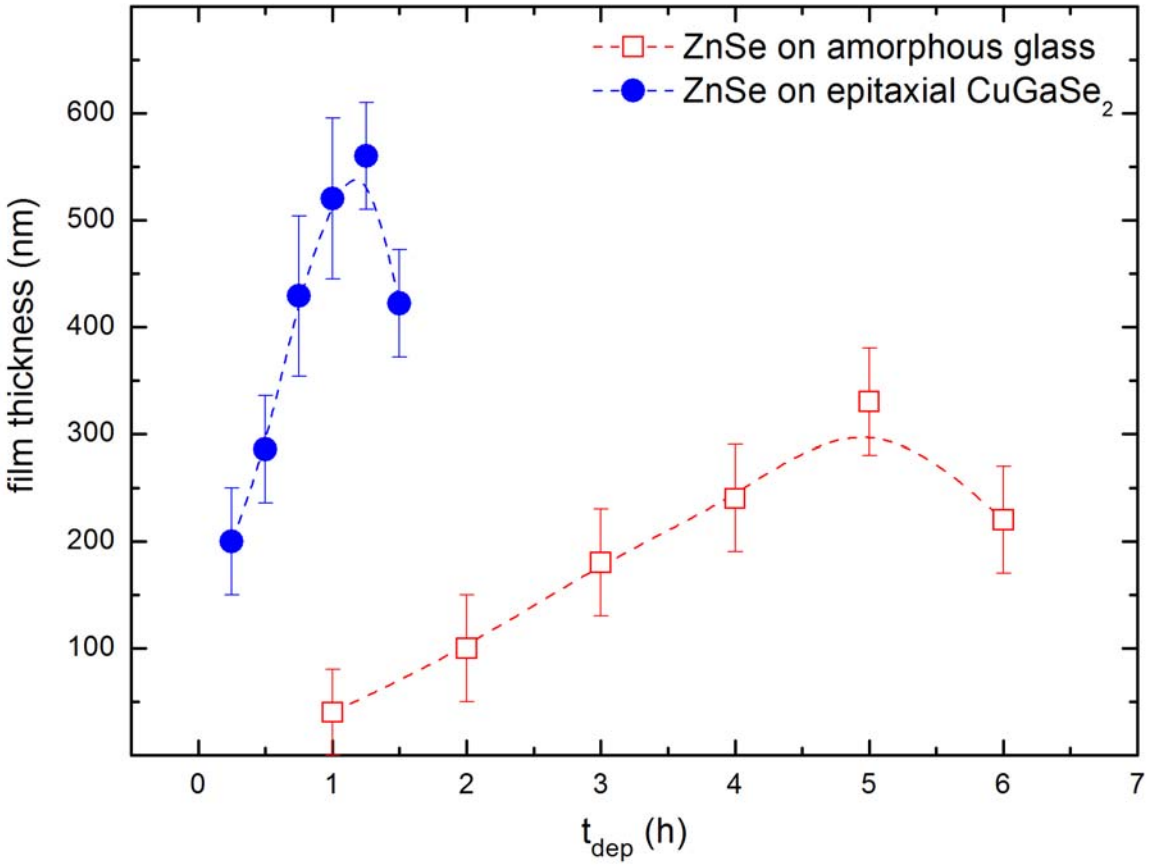

Figure 6.55 Film thickness of ZnSe on epitaxial $CuGaSe_2$/GaAs in dependence of deposition time. The thickness of ZnSe on glass substrate is also presented.

The results of thickness measurements of ZnSe on chalcopyrite by SEM are presented in Figure 6.55 along with the results of the thickness measurements of ZnSe on

amorphous glass substrate by profilometry. Initially, film thickness is increasing linearly and reaches a maximum of 560nm after 75min deposition time. For longer deposition tines, the film thickness shows a decrease, as it has already been observed and explained in case of ZnSe on glass substrate (§6.3.2).

ZnSe films grown on epitaxial $CuGaSe_2$ exhibit high growth rates compared to those grown on amorphous glass substrate. This behavior can be partially attributed to the epitaxial nature of the underlying chalcopyrite layer which reinforces the deposition process. In particular, the formation time of the first precipitate in the solution and the growth rate are substrate dependent. In Figure 6.56, growth rates corresponding to chemical bath deposition of ZnSe on three substrates with different conductivity are presented by Chaparro *et. al.*[6.78]. The curve with number 1 corresponds to unpolished metal substrate, the curve number 2 corresponds to polished metal substrate, whereas, the curve number 3 to an isolator substrate. It is evident that roughness and conductivity of the substrate have a positive effect on the growth rate. From Figure 6.56 it is obvious, that, on conductive substrates, ZnSe nuclates with tremendously higher rates compared to growth rates on isolating substrates.

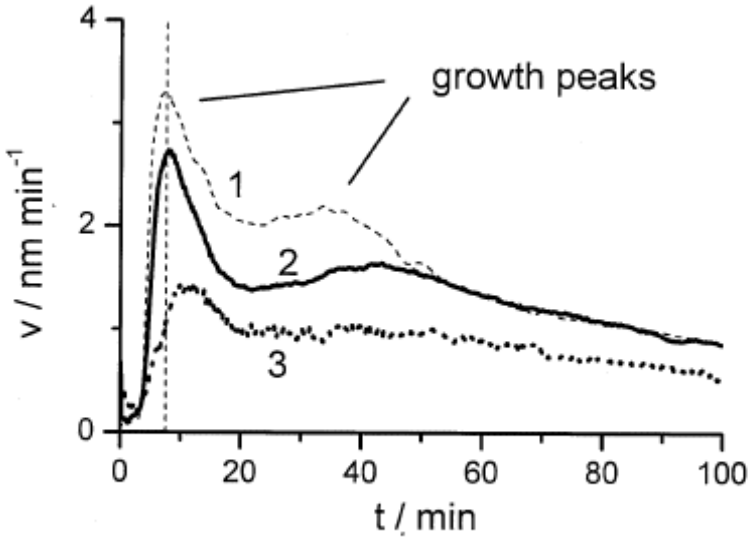

Figure 6.56 Growth rate corresponding to chemical deposition of ZnSe on three substrates with different conductivity [6.78]

In our case, ZnSe on amorphous glass (isolator) substrate has a growth rate of 72nm/h (=1.2nm/min) calculated from the slop of the linear part of Figure 6.45. This

growth rate is comparable to the first peak observed in curve number 3 of Figure 6.56. For the semi-conductive epitaxial $CuGaSe_2$ layer, the growth rate of ZnSe is 6.4nm/min calculated from slop of the linear part of Figure 6.55. In the case of ZnSe deposition on polycrystalline $CuGaSe_2$, the Mo coating of the glass substrate facilitates the ZnSe growth improving growth rates. This is the main reason, that the thickness of ZnSe on polycrystalline chalcopyrite is launched for deposition time of only 15min.

6.5 CBD ZnSe on Polycrystalline Chalcopyrite Absorbers

Having examined growth of ZnSe on epitaxial chalcopyrites, growth of ZnSe was attempted on polycrystalline chalcopyrite substrates. The aim is to complete the process (ZnSe-buffer layer, ZnO-window layer, and Al-front ohmic contact) in order to achieve a prototype solar cell with the n-type part of the p-n junction processed by low-cost, low-temperature, non-polluting chemical and electrochemical techniques.

6.5.1 Structural properties

For the deposition of ZnSe on polycrystalline chalcopyrite, four different chalcopyrite layers were used, among them one quaternary and three ternary layers, as follows:

a) polycrystalline $CuGaSe_2$ chalcopyrite absorber with [Cu]/[Ga]=1.00,

b) polycrystalline $CuGaSe_2$ chalcopyrite absorber with [Cu]/[Ga]=1.13,

c) polycrystalline $CuInS_2$ chalcopyrite absorber with [Cu]/[In]=1.10, and

d) polycrystalline $CuIn_{1-x}Ga_xSe_2$ chalcopyrite absorber with x=0.04

The polycrystalline chalcopyrites are deposited on Mo-coated glass, which in an integrated solar cell serves as the back ohmic contact. Furthermore, Cu-rich absorbers have been chosen, since Cu excess is beneficial to electrical characteristics of the resulting solar cell. Absorbers prepared without Cu excess are generally semi-insulating which is assumed to be due to a high concentration of sulphur vacancies acting as compensating donors [6.79].

Before deposition of ZnSe, etching of the substrates was mandatory to remove oxides and CuSe or CuS phases from the chalcopyrite surface. It has been reported, that

after KCN treatment of the chalcopyrite absorber surface, the efficiency of the solar cell can be tremendously increased [6.80]. The procedure of chemical etching is described in detail in Appendix A.

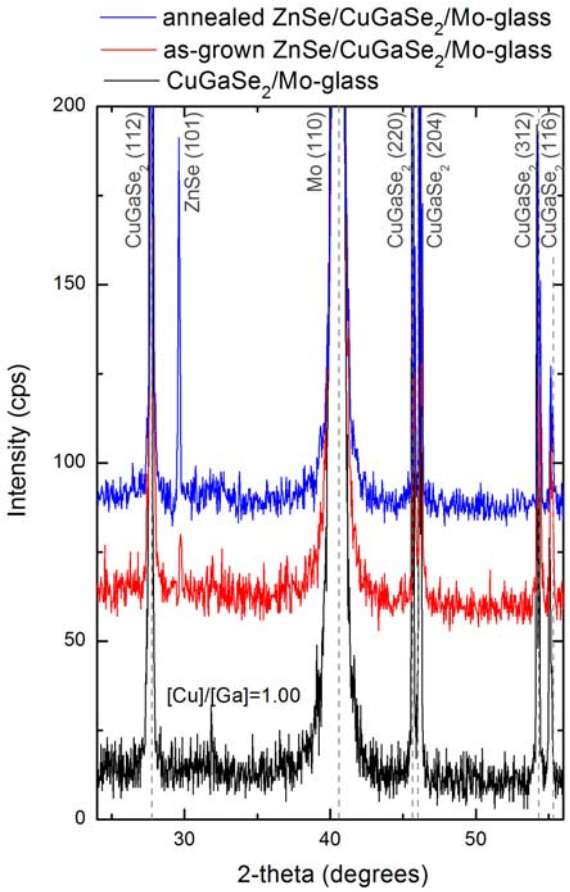

Figure 6.57 XRD-patterns of bare polycrystalline $CuGaSe_2$ absorber (black), as-grown ZnSe on the absorber (red), and annealed ZnSe on the absorber (blue), with [Cu]/[Ga]=1.00

Immediately after KCN etching, the absorbers were submerged in chemical solution for ZnSe deposition. $CuGaSe_2$ chalcopyrite with [Cu]/[Ga]=1.00 remained in the solution for 15min. XRD-patterns of bare polycrystalline $CuGaSe_2$ absorber (black), as-grown ZnSe on the absorber (red), and annealed ZnSe on the absorber (blue), with [Cu]/[Ga]=1.00, are demonstrated above. As observed in Figure 6.57, as-grown ZnSe on $CuGaSe_2$ ([Cu]/[Ga]=1.00) was formed during CBD processing and crystallized after

annealing of the sample at 300°C for 2h. Reflection from the (101)-plane of the hexagonal ZnSe was observed at 2θ=29.18° with FWHM=0.14°, which corresponds to crystallite size of 103nm.

The thickness of the ZnSe film was measured by Scanning Electron Microscopy on the crossection of the sample, in a later step of the process to integrate a solar cell. The ZnSe layer is denoted with green colour in Figure 6.58.

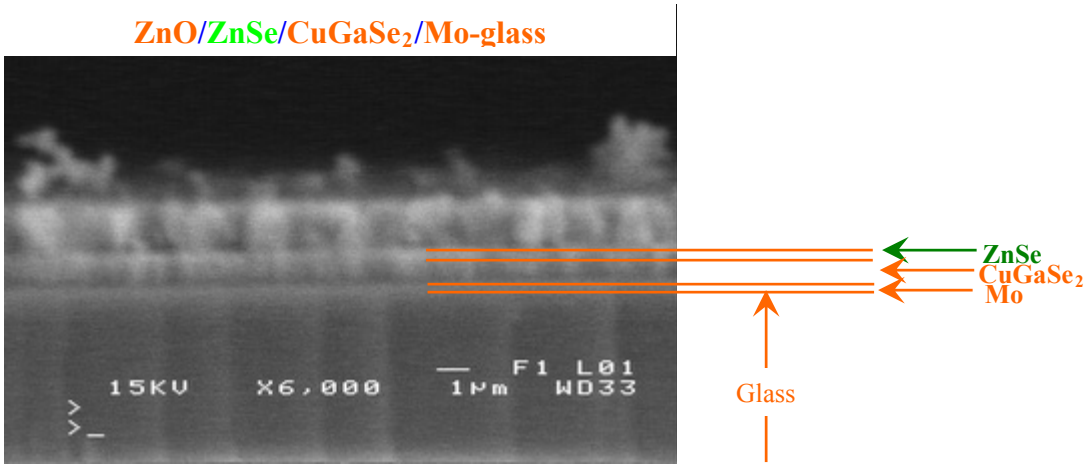

Figure 6.58 SEM-image of the cross-section of ZnO/ZnSe/$CuGaSe_2$/Mo-glass heterostructure. The image was captured in a later step of the solar cell process, where a ZnO layer has been also deposited on top of ZnSe. The ZnSe layer after 15min deposition is indicated with green color.

The thickness of the ZnSe layer was calculated to 290 ± 75 nm. The thickness of this ZnSe layer deposited on polycrystalline $CuGaSe_2$ is somewhat higher than the ZnSe layer with deposition time 15min on epitaxial $CuGaSe_2$. Assuming that ZnSe on polycrystalline $CuGaSe_2$ would have a faster growth rate (due to the Mo sheet at the back of the $CuGaSe_2$ layer) compared to the ZnSe growth rate on epitaxial $CuGaSe_2$, the deposition time for further processing of ZnSe layers on polycrystalline chalcopyrite substrates were chosen accordingly.

After etching, the polycrystalline $CuInS_2$ chalcopyrite with [Cu]/[In]=1.10 remained in the solution for 7min, the polycrystalline $CuGaSe_2$ chalcopyrite with [Cu]/[Ga]=1.13 remained in the solution for 4min, and the quaternary $CuIn_{1-x}Ga_xS_2$ with x=4% remained in the solution for 2.5min. Reports of ZnSe on $CuInS_2$ show complete

coverage of the chalcopyrite substrate after deposition of 2-3min [6.81]. Figure 6.59 shows, on the left: the XRD-patterns of bare polycrystalline $CuInS_2$ (black) with [Cu]/[In]=1.10 and annealed ZnSe on the $CuInS_2$ absorber, and on the right: the XRD-patterns of bare $CuGaSe_2$ absorber (black) with [Cu]/[Ga]=1.00, as-grown ZnSe on the $CuGaSe_2$ absorber (red), and annealed ZnSe on the same absorber (blue). ZnSe crystallite size is 92.9nm and 99.6nm on $CuInS_2$ and $CuGaSe_2$ chalcopyrites, respectively.

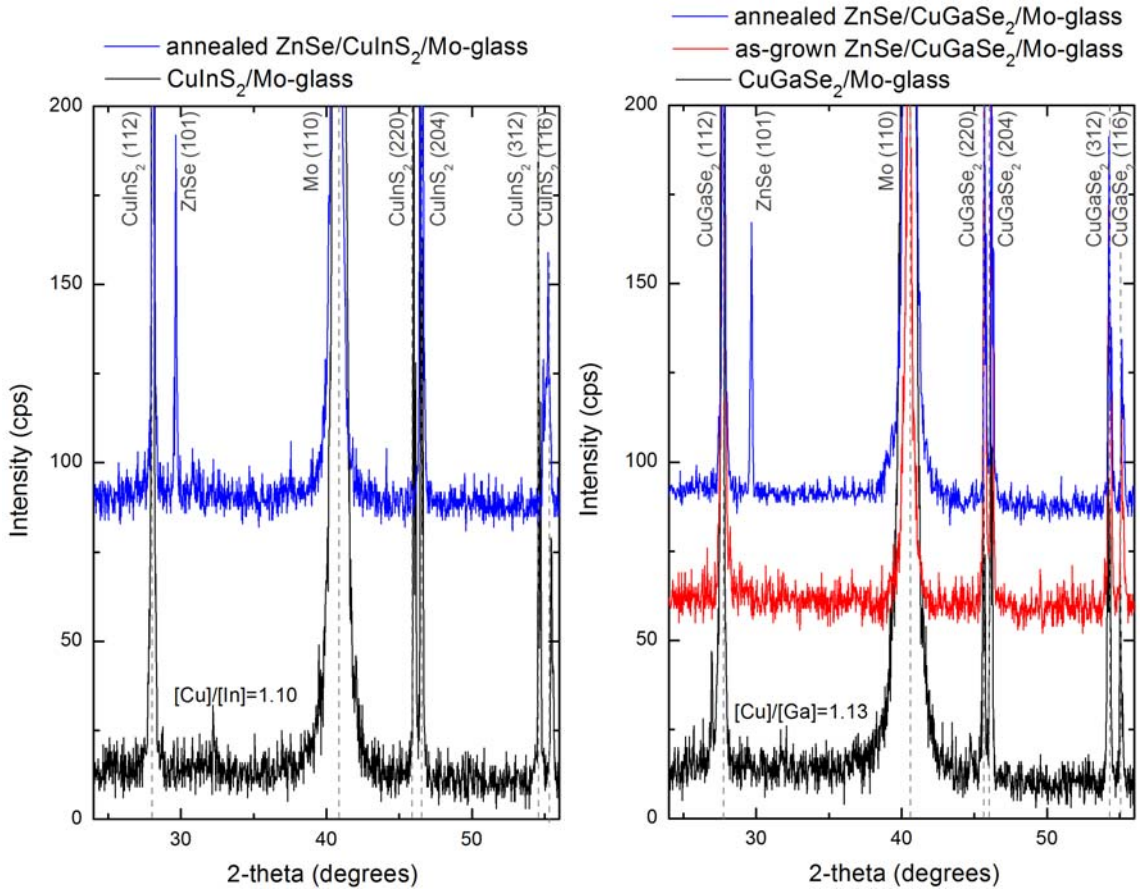

Figure 6.59 On the left: XRD-patterns of bare polycrystalline $CuInSe_2$ absorber (black) and annealed ZnSe on the absorber (blue) with [Cu]/[In]=1.10
On the right: XRD-patterns of bare polycrystalline $CuGaSe_2$ absorber (black), as-grown ZnSe on the absorber (red), and annealed ZnSe on the absorber (blue) with [Cu]/[Ga]=1.13

Film thickness measurements on the other two samples, $CuGaSe_2$ with [Cu]/[Ga]=1.13 and $CuIn_{1-x}Ga_xSe_2$ with x=0.04, by SEM, on the crossection of the

sample, could not been performed. Also, measurement of film thickness with an optical method such as null-ellipsometry could not be carried out without exact modeling of the heterostructure, because ellipsometry measures an effective film thickness including both, the chalcopyrite and the ZnSe layers. To overcome this difficulty, the film thickness of very thin layers (<100nm) was measured by Atomic Force Microscopy (AFM). In particular, after scanning the surface from the chalcopyrite to the ZnSe layer, a profile image was taken to calculate the film thickness as shown in Figure 6.60 and Figure 6.61.

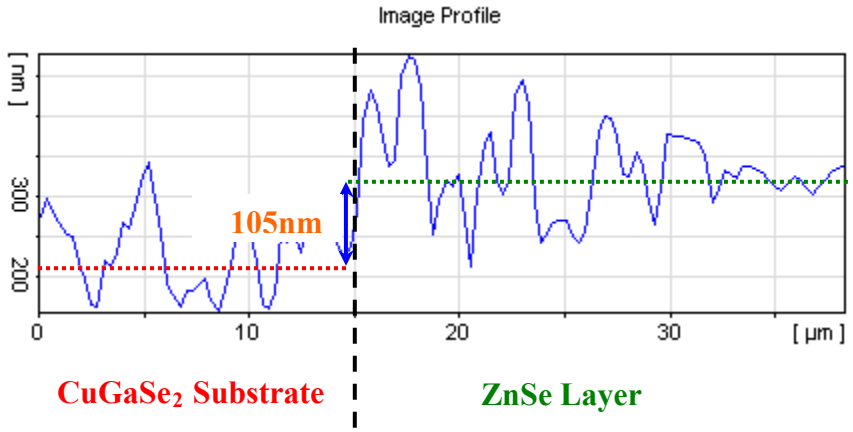

Figure 6.60 Profile Image (AFM) scanning from the $CuGaSe_2$ to the ZnSe layer (deposition time 4m).

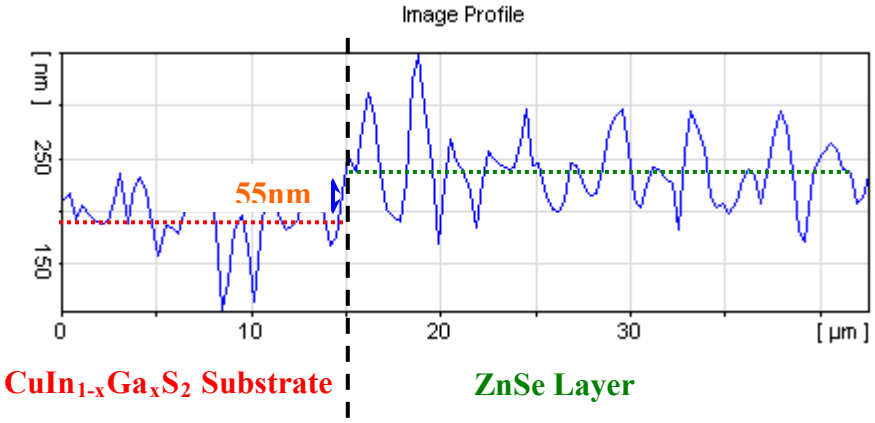

Figure 6.61 Profile Image (AFM) scanning from the $CuIn_{1-x}Ga_xSe_2$ to the ZnSe layer (deposition time 2.5m).

The thickness of the two layers were calculated to 105nm and 55nm for deposition times 4 and 2.5 minutes, respectively. The results of the ZnSe film thickness on

polycrystalline chalcopyrites along with the results of the thickness of ZnSe on epitaxial chalcopyrites are presented in Figure 6.62.

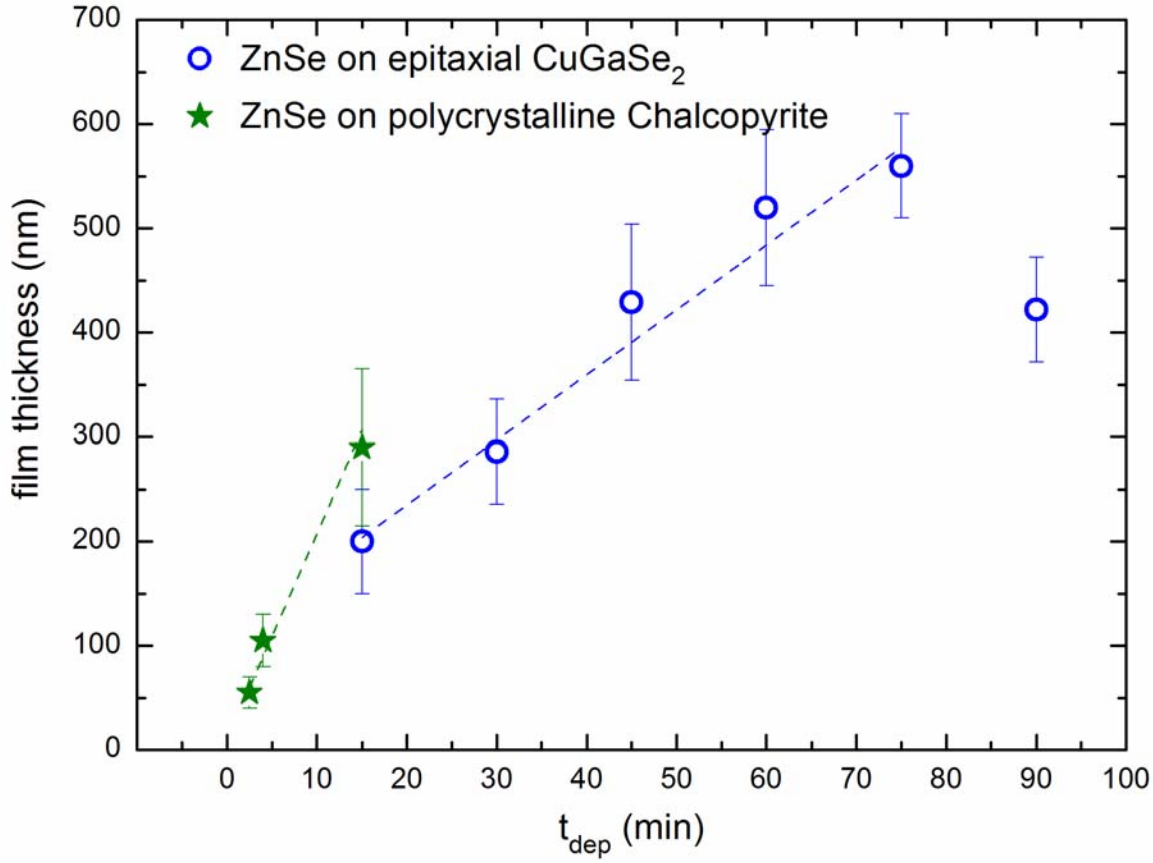

Figure 6.62 Film thickness of ZnSe on polycrystalline $CuGaSe_2$ after 15min deposition time. Also, in the diagram, thickness of ZnSe on epitaxial $CuGaSe_2$.

AFM images of the chalcopyrite and the ZnSe layer are shown in Figure 6.63. It is obvious, that the morphology of the surface of the thinner layer (ZnSe on $CuIn_{1-x}Ga_xS_2$, deposition time 2.5min) is similar to that of the underlying chalcopyrite, whereas the thicker one (ZnSe on $CuGaSe_2$, deposition time 4min) has a different surface morphology than the chalcopyrite.

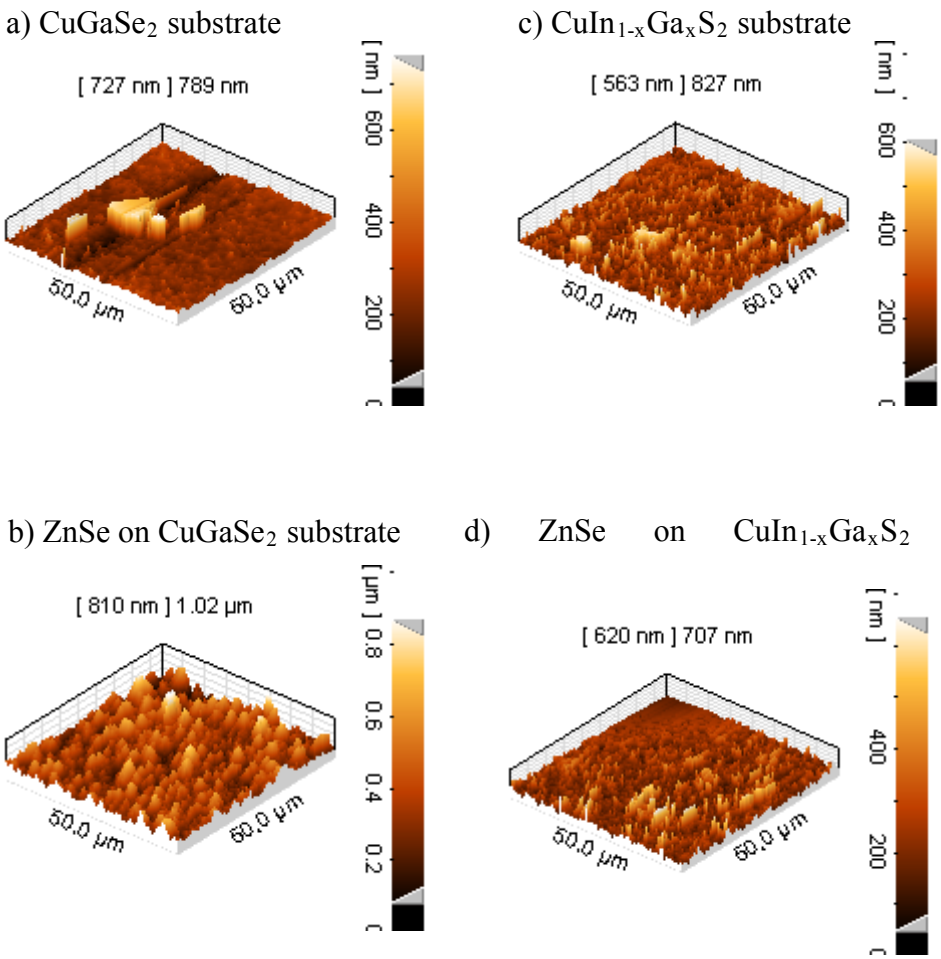

Figure 6.63 AFM images of the chalcopyrite (a and b) and the ZnSe layer (c and d)

6.6 *COMPARISON of EBE ZnSe on Chalcopyrite with CBD ZnSe on Chalcopyrite*

(The EBE ZnSe is a topic of a PhD-Thesis of Semiconductor Thin Film Technology by Dipl. Chem. Ing., Dipl. Phys. G. Roupakas, -the thesis is still processing).

SEM and AFM images of ZnSe deposited on glass/Mo/$CuGaSe_2$ substrates are shown in Figure 6.64. The SEM micrograph (Figure 6.64, left) reveals that the ZnSe film is polycrystalline, highly homogenous, and covers uniformly the underlying chalcopyrite absorber. Mapping of the film surface with AFM (Figure 6.64, right) indicates that

surface roughness is limited to 80 nm; the mean surface roughness is 80 nm, which along with the results of SEM microscopy supports the assessment of good film quality.

In Figure 6.65, the x-ray diffractogram of a ZnSe thin film deposited on a $CuGaSe_2$/Mo/glass substrate at 400 ^oC is shown. A highly intensive narrow peak at 27.23 degrees Bragg-angle is assigned to the reflection at the (111) crystallographic plane of cubic ZnSe. It is followed by two additional, rather weak peaks at higher Bragg angles of 45.41 and 53.73 degrees assigned to the reflection at the (220) and (311) crystallographic planes, respectively. The peak at 27.66 degrees, next to the (111)-peak of ZnSe, originates from the chalcopyrite absorber; it is assigned to the (112) reflection of $CuGaSe_2$. Further reflection peaks of $CuGaSe_2$ appear as doublets at Bragg-angles of 45.75 and 46.20 degrees, the (220)- and (204)-peaks, and at 54.29 and 55.17 degrees, the (312)- and (116)-peaks. The plane spacing d calculated from the (111)- reflection peak according to Eq.(5.1), with θ =27.23 degrees, and λ=1.5406 Å, is d=3.273 Å. The corresponding lattice constant for a material of cubic symmetry defined upon reflection on a (hkl)-plane [6.82] is given by Eq(6.16):

$$\frac{1}{d^2} = \frac{h^2 + k^2 + l^2}{\alpha^2} \tag{6.16}$$

The calculated value is α=5.669 Å and it is almost equal to the value of bulk ZnSe α(ZnSe) =5.6687 Å referred in the literature [6.83]. However, for a thin polycrystalline film deposited on a polycrystalline substrate, this value is influenced by grain sizes and stress, two effects that may be of competitive nature and cancel each other. The lattice constant of bulk $CuGaSe_2$ is $\alpha(CuGaSe_2)$ =5.614 Å. The lattice mismatch between ZnSe and $CuGaSe_2$ is 0.96%; the ZnSe layer is compressively strained.

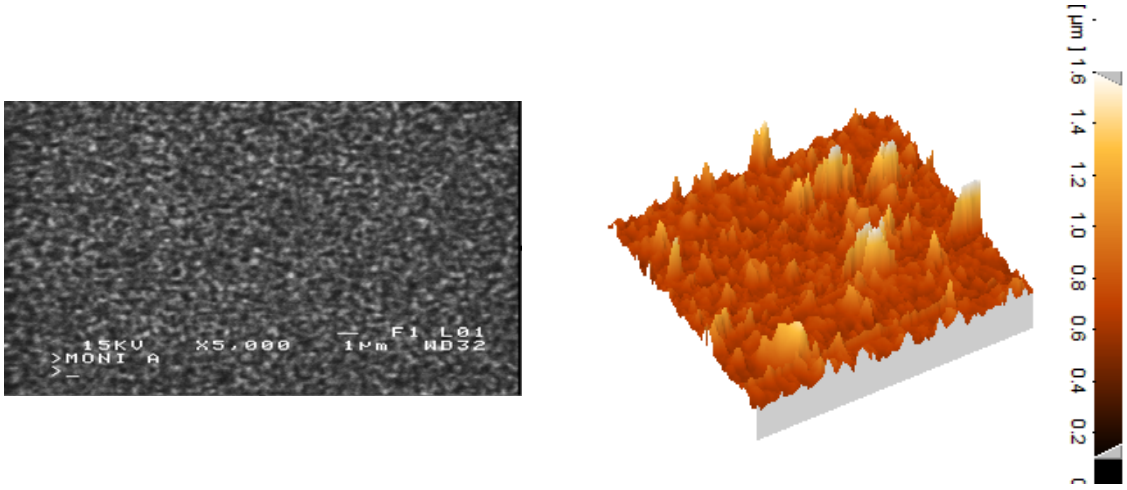

Figure 6.64 SEM (left) and AFM (right) images of ZnSe on $CuGaSe_2$

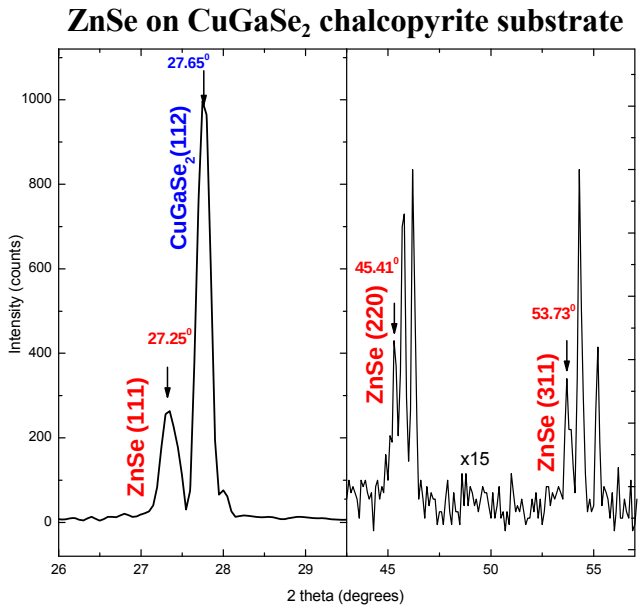

Figure 6.65 X-ray diffractogram of EBE ZnSe on $CuGaSe_2$

The energy band gap of the deposited films has been measured directly by room temperature photoreflectance (PR) spectroscopy. A representative PR-spectrum of the deposited ZnSe films is shown in Figure 6.66. The spectrum was fitted with TDFF. According to the fitting results, a mean value of the (fundamental) energy band gap of E_g= 2.69 eV has been determined. Apart from this, the application of the otherwise only at low temperatures useful PR spectroscopy already at room temperature supports the

results of XRD, SEM, AFM, and Raman studies underlining the very good crystal quality of the deposited films.

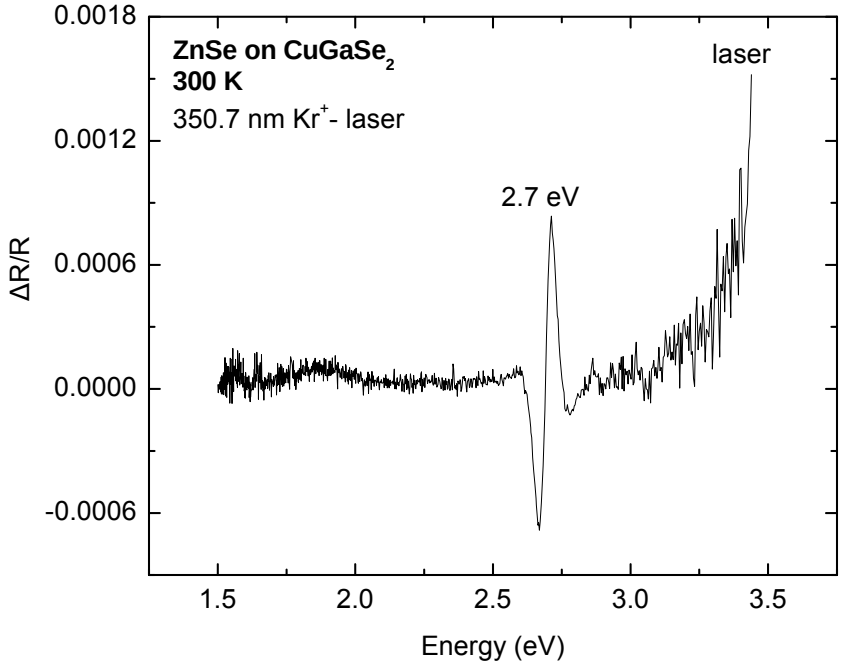

Figure 6.66 PR spectrum of EBE ZnSe on $CuGaSe_2$

6.7 PLD Al/In:ZnO/i-ZnO on ZnSe/Polycrystalline-Chalcopyrite Absorbers

Having deposited ZnSe on polycrystalline chalcopyrites, ZnO should be grown on top of ZnSe, and an Al contact should also be deposited on ZnO to obtain an integrated solar cell. The ZnO layers and the Al ohmic contact were grown by Pulsed Laser Deposition (PLD), with conditions established to be ideal elsewhere [6.84], as described in §4.7.

ZnO layer has in Thin Film Solar Cells a double role; it is the window layer transmitting the incident light generating photocarriers in the absorber and it is also a contact layer enabling collection of the charge.

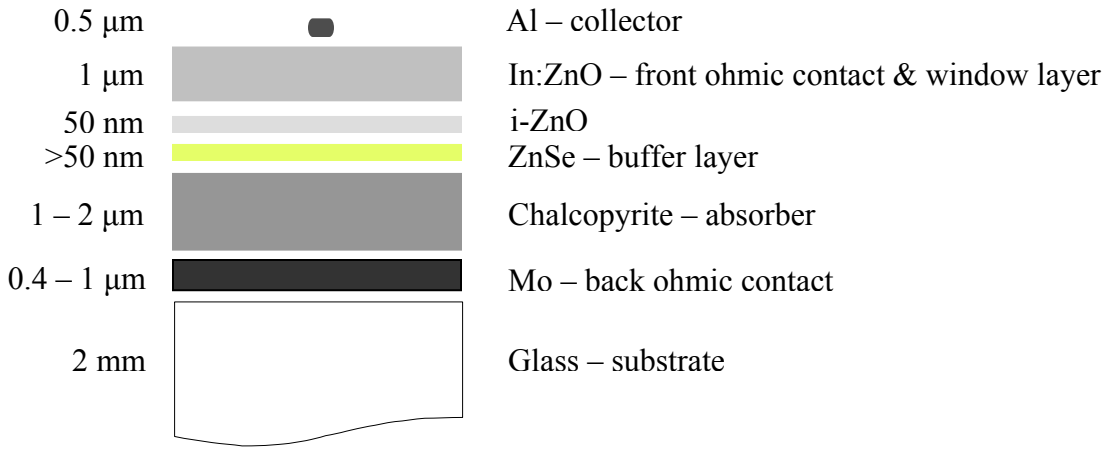

Figure 6.67 Schematic design of a chalcopyrite thin film solar cell

As shown in Figure 6.67, before the deposition of a doped ZnO layer (n-ZnO), the deposition of a thin layer of intrinsic ZnO (i-ZnO) is required. This i-ZnO layer increases the open circuit voltage and is a standard step in the solar cell growth procedure.

In the XRD patterns (Figure 6.68 and Figure 6.69) of two solar cells, reflections from the Mo back ohmic contact and from the (112), (220), (204), (312), and (116) planes of the $CuGaSe_2$ and $CuInGaSe_2$ chalcopyrite, respectively, are present. Also, the (101) plane reflection of ZnSe and the (002) plane reflection of the ZnO are apparent in both patterns. The ZnSe layer on $CuGaSe_2$ was deposited for 15min, whereas, the ZnSe layer on $CuInGaSe_2$ was deposited for only 4min.

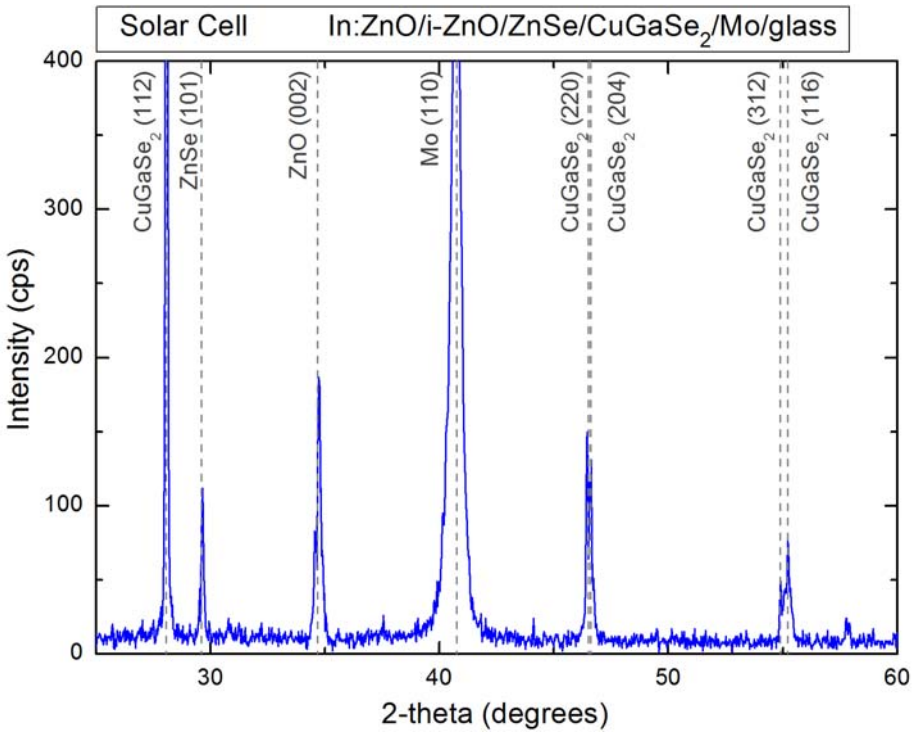

Figure 6.68 XRD pattern of a solar cell with In:ZnO/i-ZnO/ZnSe/GuGaSe$_2$/Mo/glass layers

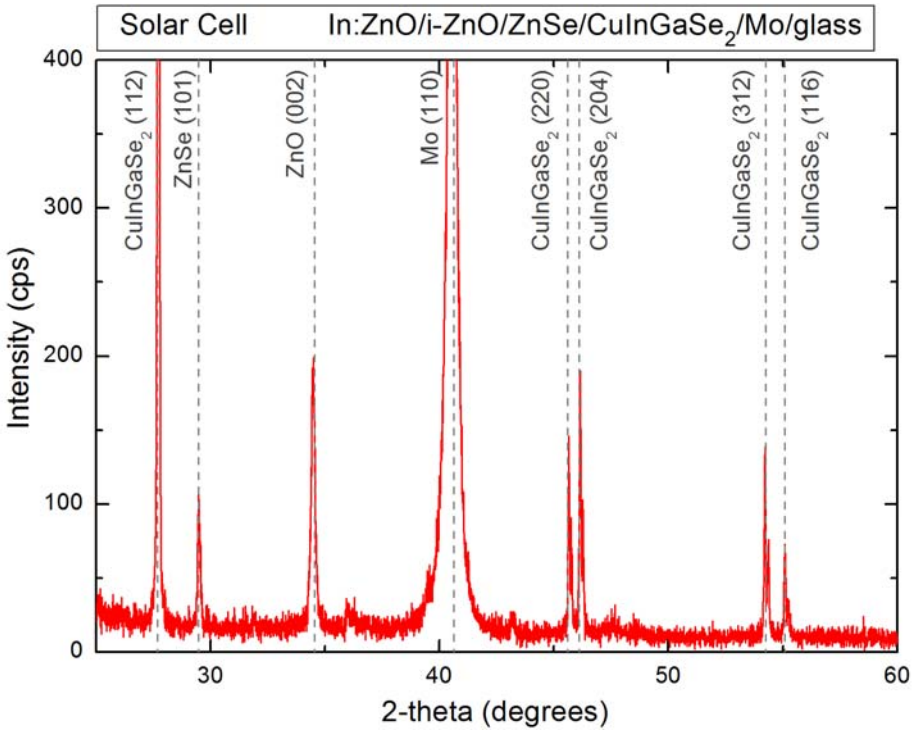

Figure 6.69 XRD pattern of a solar cell with In:ZnO/i-ZnO/ZnSe/Gu(In,Ga)Se$_2$/Mo/glass layers

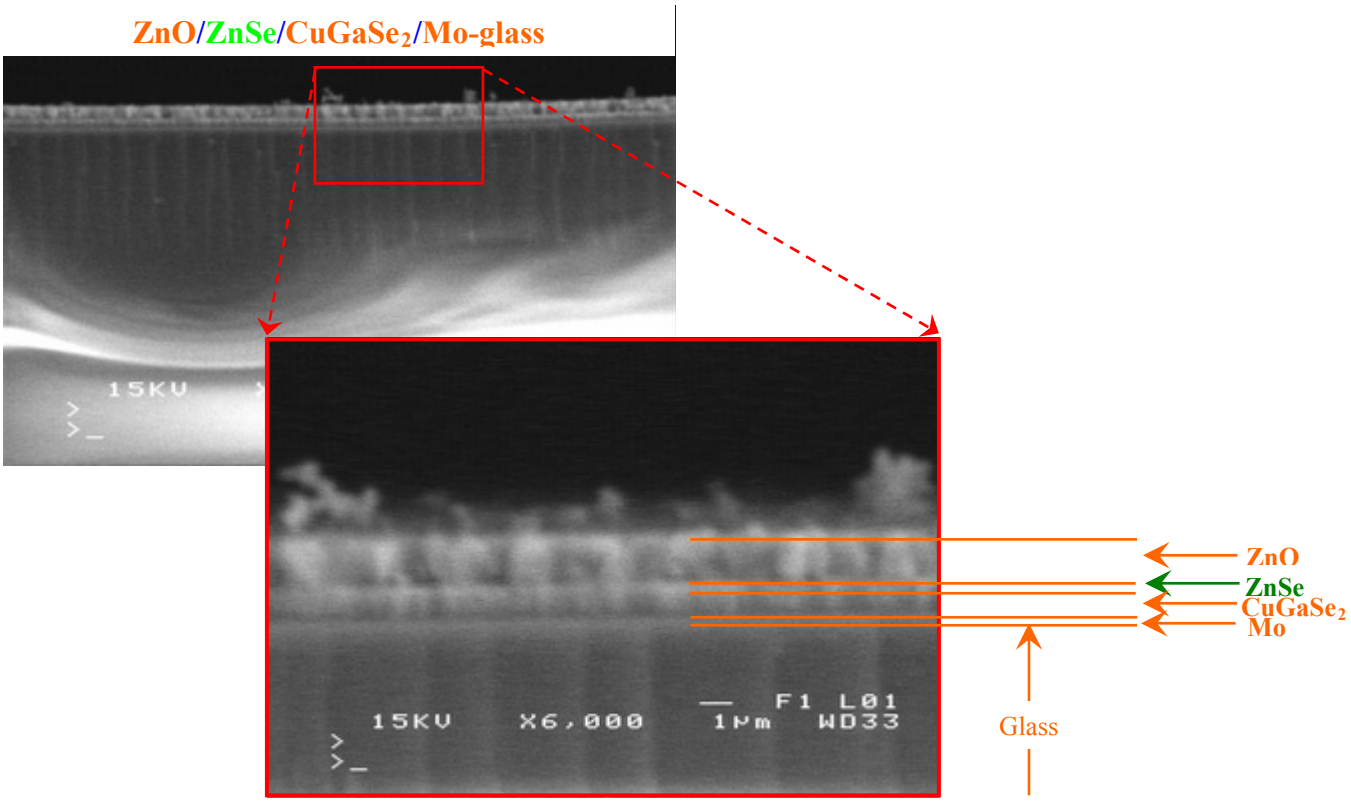

Figure 6.70 SEM-image on the crossection of ZnSe/$CuGaSe_2$/Mo-glass sample after 15min deposition

In the Scanning Electron Microscopy image (Figure 6.70) of the crossection of the sample, all the different layers are apparent: the glass substrate, the Mo coating, the $CuGaSe_2$ absorber, the ZnSe buffer layer, and the ZnO window layer. The thickness of all different layers was be estimated from the image as follows: Mo 100 ± 25 nm, $CuGaSe_2$ 750 ± 75 nm, ZnSe 290 ± 75 nm, i-ZnO and In:ZnO 1170 ± 75 nm.

In Figure 6.71, a real photograph of the solar cell with Cu(In,Ga)Se_2 chalcopyrite absorber is shown. SEM images of the surface of the different layers are demonstrated in Figure 6.72, Figure 6.73, and Figure 6.74. The surface morphology of the ZnSe layer on polycrystalline chalcopyrite is totally different from the morphology of ZnSe on glass substrates and epitaxial chalcopyrites. It is concluded, that the nature of the substrate greatly affects the morphology of the deposited layer [6.85]. In particular, the ZnSe layer on polycrystalline Cu(In,Ga)Se_2 chalcopyrite is homogeneous and highly compact.

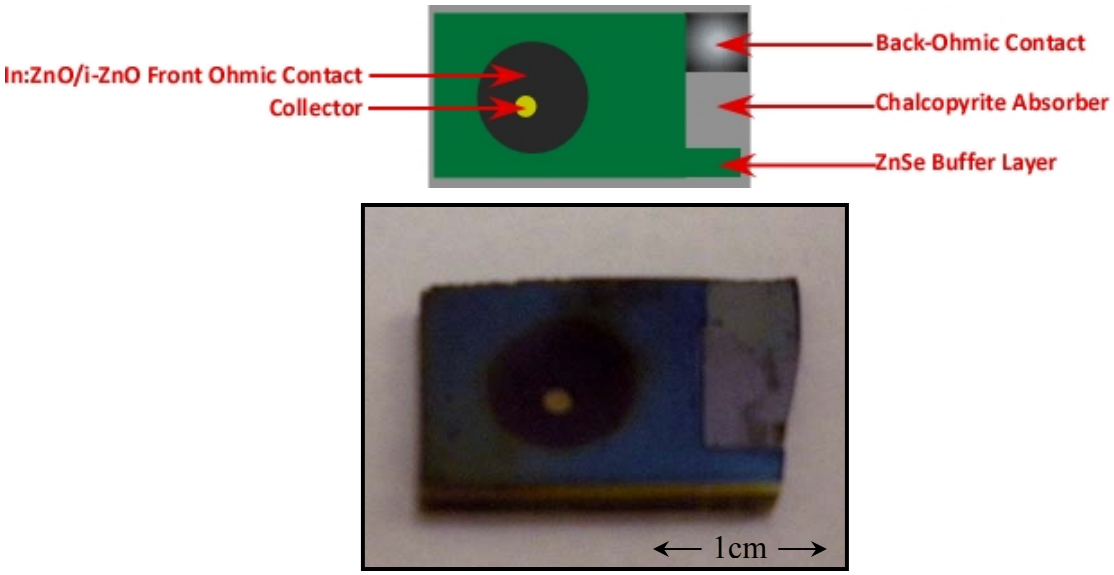

Figure 6.71 Photograph of the In:ZnO/i-ZnO/ZnSe/Cu(In,Ga)Se_2/Mo/glass solar cell (down) and schematic drawing of the sub-layers of the heterostructure used for cell development (up).

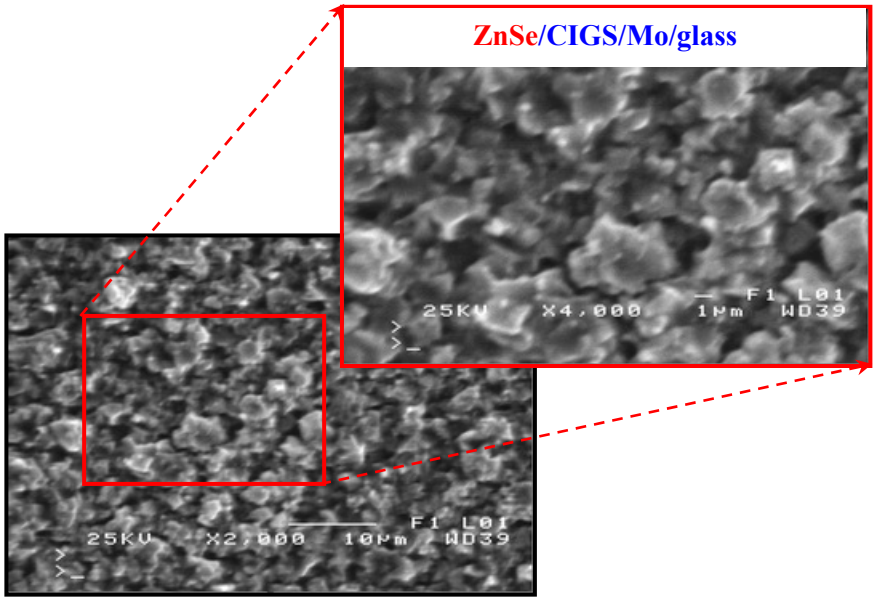

Figure 6.72 SEM images with x2000 and x4000 magnifications of the surface of ZnSe-layer on Cu(In,Ga)Se_2/Mo/glass

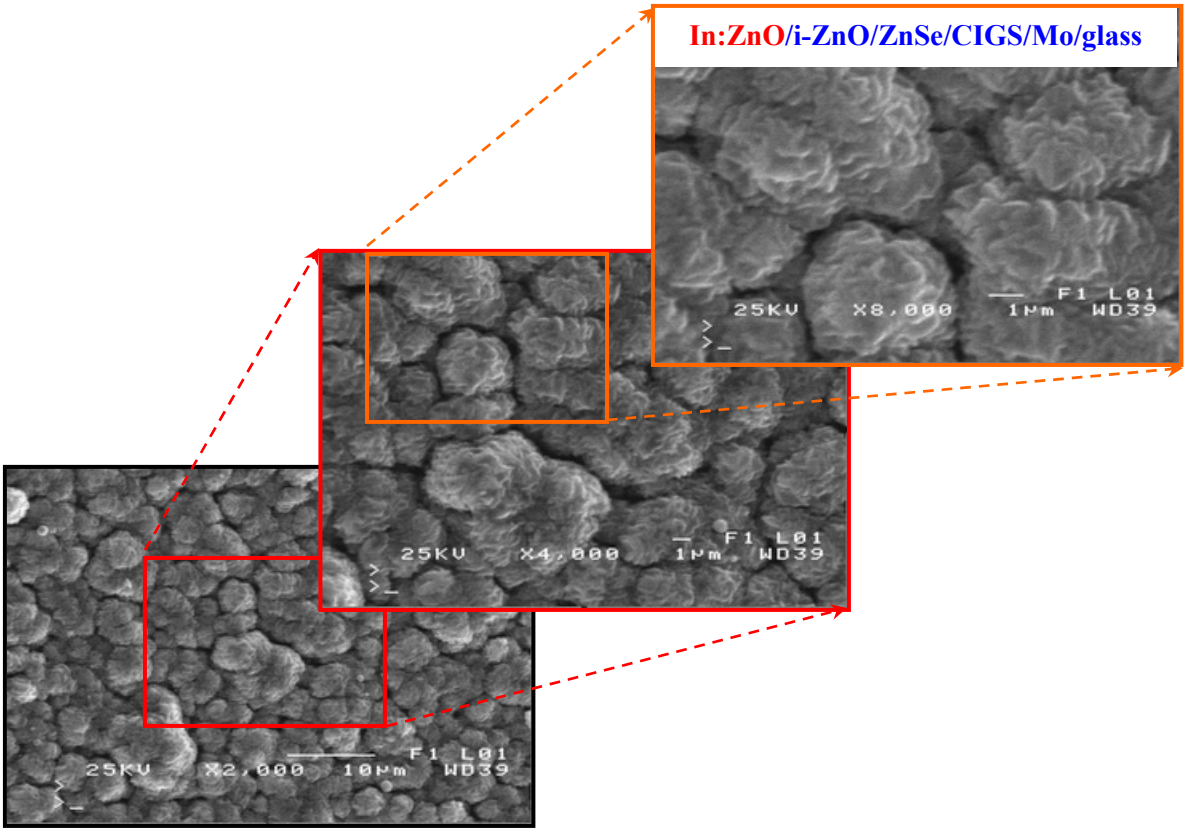

Figure 6.73 SEM images with x2000, x4000, and x8000 magnifications of the surface of In:ZnO layer on i-ZnO/ZnSe/CuInGaSe$_2$/Mo/glass

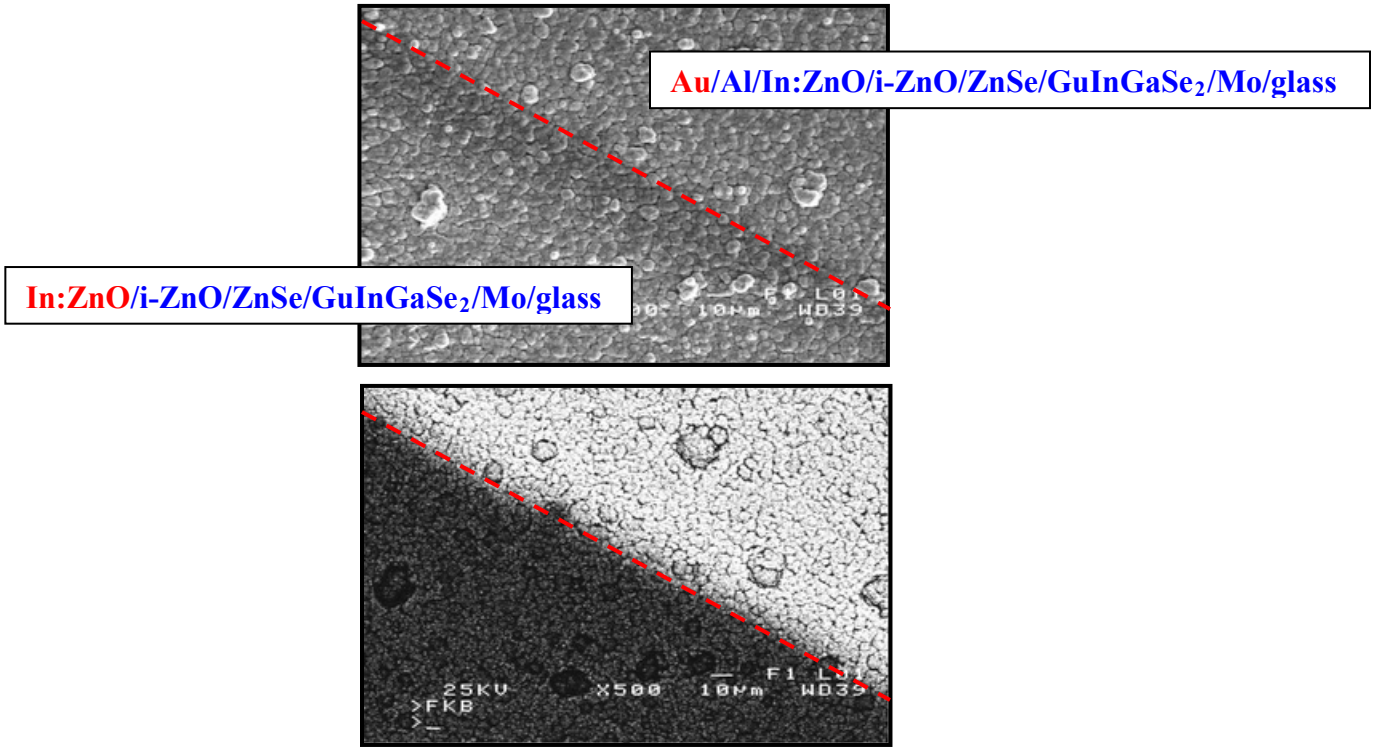

Figure 6.74 SEM image of the interface of In:ZnO and the Au/Al collector (up). Image from the compositional mode of SEM (down)

The In:ZnO layer has large grains densely packed. EDS measurements of the doped ZnO layer showed 3% In content. While scanning the surface of the solar cell and moving from the In:ZnO to the Au/Al collector, no difference in surface morphology is observed (upper part of Figure 6.74). However, using the COMPO mode of the Scanning Electron Microscope, which is used to color areas of the sample with different composition, the two regions have been clearly detected, as seen in the lower part of Figure 6.74. The bottom left region consists of the elements In, Zn and O, which constitute the In-doped ZnO layer, whereas the top right region consists of the elements Au and Al, which constitute the Au/Al carrier collector. Au is deposited on top of Al to prevent oxidation of the Al, as previously mentioned.

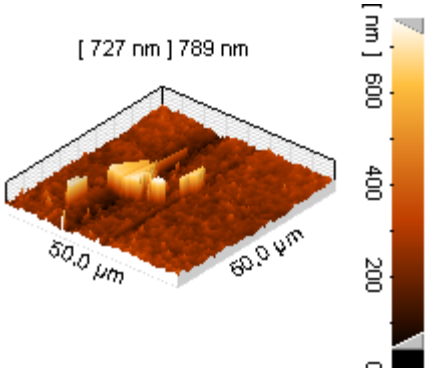

a) $CuGaSe_2$

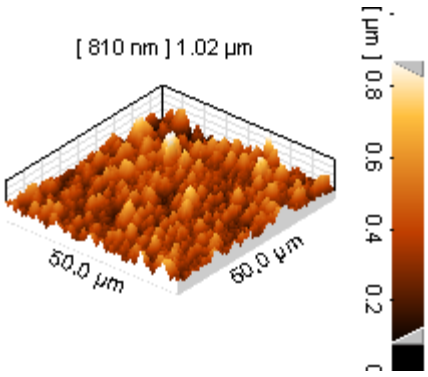

b) ZnSe

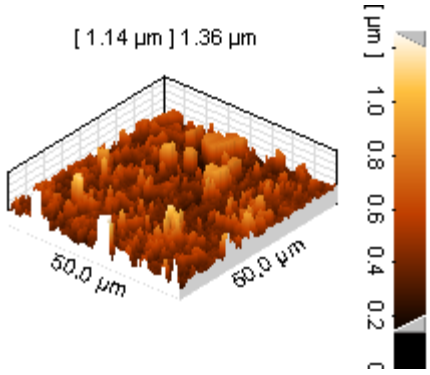

c) ZnO

Figure 6.75 AFM images of the surface of a) the $CuGaSe_2$ chalcopyrite absorber, b) the ZnSe buffer layer, and c) the ZnO window layer

The surface morphology can also be investigated with Atomic Force Microscopy. The roughness of each layer (chalcopyrite/ZnSe/ZnO) is calculated from the AFM images shown in Figure 6.75. The surface roughness of the chalcopyrite $CuGaSe_2$ absorber is 91.1nm, the ZnSe buffer layer is 118nm, and the ZnO window layer is 152nm. Increased roughness of the top ZnO layer (actually, controlled modification of the cell surface for light capture) is desired to prevent reflection and boost absorption of the incident sunlight.

6.8 ECD ZnO grown on ZnSe/Polycrystalline-Chalcopyrite Absorbers

ZnO was electrochemically deposited, initially on Mo-coated glass, and then on ZnSe buffer on CIGS polycrystalline chalcopyrite on Mo coated glass substrate. The deposition time was chosen 1hour. XRD peaks of the ZnO on Mo-coated glass appeared only after 2h annealing at 250^{o}C with three different orientations (100), (002), and (101) of the hexagonal system. Contrary to that, ZnO deposited electrochemically on ZnSe/Cu(In,Ga)Se_2/Mo-glass has a single orientation along the (101) crystallographic plane in coherency with the orientation of the ZnSe.

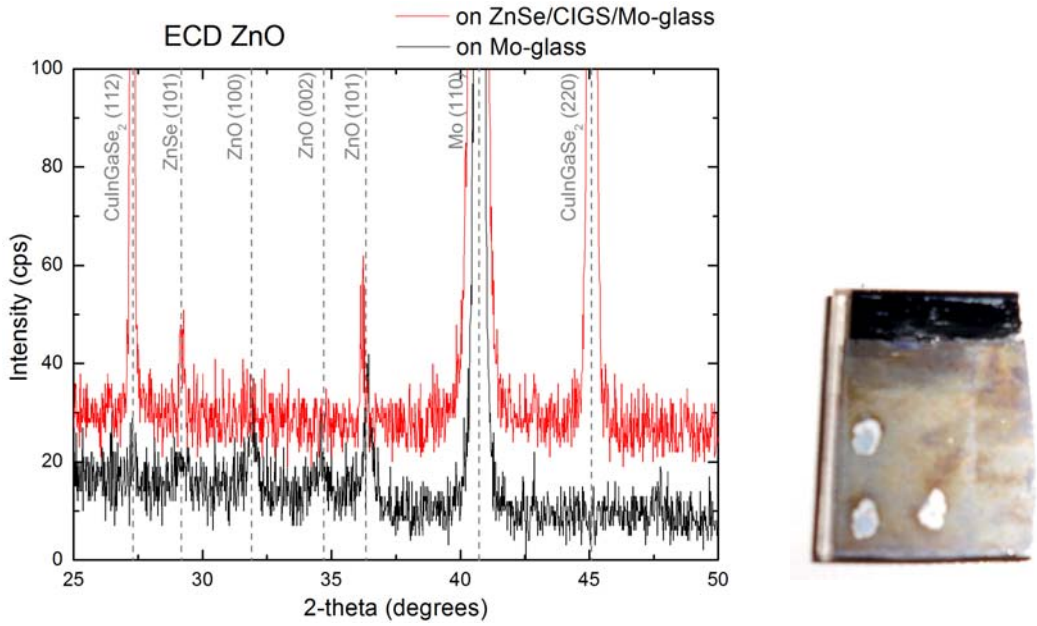

Figure 6.76 Left: XRD pattern of ZnO on Mo-glass (black) and ZnO on ZnSe/Cu(In,Ga)Se_2/Mo-glass (red);
Right: Photograph of the i-ZnO/ /ZnSe/Cu(In,Ga)Se_2/Mo-glass solar cell

6.9 ECD ZnO Nanorods on glass Substrates

Alternatively to PLD ZnO, ZnO nanorods have recently been employed as front ohmic contact and window layer in thin film solar cells. ZnO nanostructures have gained ground in their use as antireflecting coatings in solar cell device applications, because of their high transparency in the solar energy range. Besides large exciton binding energy of 60meV [6.86], ZnO single crystal nanorods (NRs) have less deep defects than their respective thin-film structures. They can be grown with high crystal quality by low-cost techniques, for example electrodeposition [6.87], and exhibit excellent crystalline properties without the need of further annealing.

An AntiReflecting Coating (ARC) is an essential part of a solar cell and is employed to reduce reflection. Thickness and refractive index are key issues of an ARC. Most solar cells are provided with a conventional ARC made by a quarter wavelength thickness dielectric layer, e.g., MgF2, SiN, TiO2, or ZnS. It reduces the reflectivity in a certain wavelength range via destructive interference of waves reflected from the top and the bottom of the ARC [6.88]. The wavelength sensitivity can be reduced by the use of a gradient refractive index layer [6.89], multiple layers [6.90], or trapping the incident light by structuring the surface of a solar cell using the moth-eye effect. Inspired by nature, researchers have developed an alternative to thin film ARCs via subwavelength-structured arrays (Figure 6.77). The surfaces of cornea of some night-flying moths are covered with arrays of subwavelength structures which confer an antireflective effect [6.91], known as the Moth-Eye effect. Incident light cannot resolve the individual features on the surface and so the patterns exhibit an effective refractive index dependent on the ratio of the corneal material to air. The shape of the features causes this ratio to gradually increase from air into the cornea, leading to a gradual increase in effective refractive index. This eliminates the discontinuity in refractive index at the interface and so minimizes reflection. Studies show that these surfaces exhibit low reflectivity over broad ranges of wavelength and angle of incidence [6.92] and so can be more effective than thin film ARCs in reducing reflection.

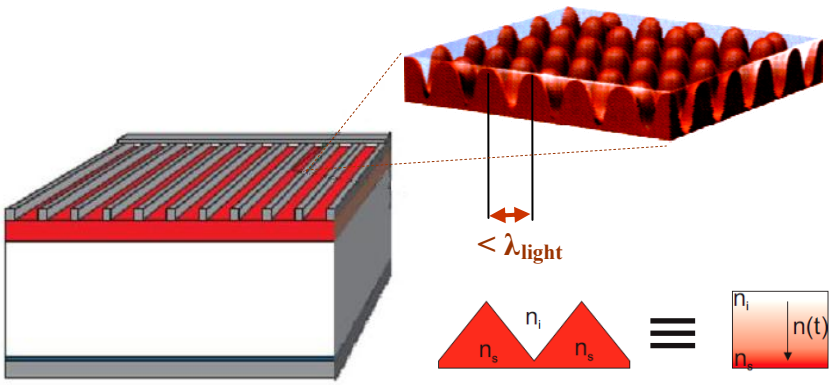

Figure 6.77 ARCs with subwavelength-structured arrays

When vertically deposited on an absorber, ZnO nanorods lead to continuously varying refractive index profiles resulting in broadband suppression of reflection via a subwavelength structure resembling the Moth-Eye effect [6.93]. Vertically deposited ZnO nanorods are, therefore, a promising antireflective coating for both substrate and superstrate solar cell configurations.

In this work, the optical properties of ZnO nanorods prepared by electrochemical deposition using three different solutions as described in 4.8.

6.9.1 Low Dimensional Systems

In treating low-dimensional systems, three categories are usually considered: the so-called two-dimensional (2D) systems which include thin films, layer structures, quantum wells and superlattices, the one-dimensional (1D) systems such as semiconductor wires and rods, and zero-dimensional (0D) systems such as clusters, quantum dots and colloids.

In the regime of strong confinement, the electrons and holes can be thought as confined independent particles. Excitons are not formed and separate size quantization of the electron and hole is the dominant factor. The optical spectra should then consist of a series of lines due to transitions between subbands. The shift in energy as a function of nanostructure size is given by Eq. (6.17) [6.94], [6.95]:

$$\Delta E = \frac{\hbar^2 \pi^2}{2\mu D^2} \tag{6.17}$$

where $\hbar$ is Plank's constant, D the characteristic dimension of the nanostructure, and μ is the reduced effective mass given by:

$$\frac{1}{\mu} = \frac{1}{m_e^*} + \frac{1}{m_h^*} \tag{6.18}$$

m_e^* and m_h^* are the effective electron and hole mass, respectively.

6.9.2 Structural Properties

The results of the structural analysis by XRD, SEM, and AFM imply very good crystal quality of the grown samples, which is also correlated and further discussed with their optical properties in section 6.9.3 Optical Properties.

6.9.2.1 X-Ray Diffraction (XRD)

Figure 6.78 shows the XRD Diffractogram of ZnO NRs typical of the grown samples. The most intense reflection-peaks originate from the (002) plane of the wurzite structure, less intense peaks appear from the (101), (102), and (103) planes. Peaks originating from the glass substrate are assigned to SnO_2. The reflections from the (002) plane are strong and narrow. It is concluded, that high quality hexagonal single crystal ZnO NRs are formed as demonstrated in the SEM image inserted in Figure 6.78.

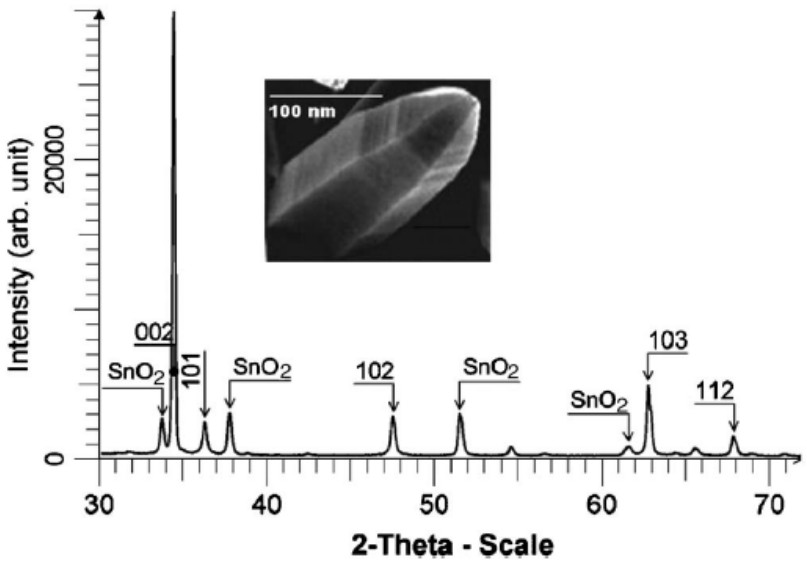

Figure 6.78 XRD pattern of as-grown ZnO NRs electrodeposited at 75 °C on a ZnO coated FTO glass in solution of a) $Zn(NO_3)_2$, sample 0719-1, b) $Zn(NO_3)_2$ and HNO_3, sample 0719-2, and c) $Zn(NO_3)_2$ and NH_4NO_3, sample 0719-3. Indices of the respective Bragg-reflections are specified above the peaks. A SEM image, in the inset, shows an enlarged single-crystal ZnO-nanorod.

6.9.2.2 Scanning Electron Microscopy (SEM)

SEM images confirm the presence of high-quality hexagonal ZnO nanorods with a high aspect ratio (length/in-plane dimension).

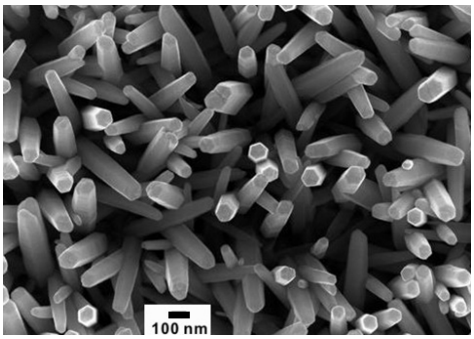

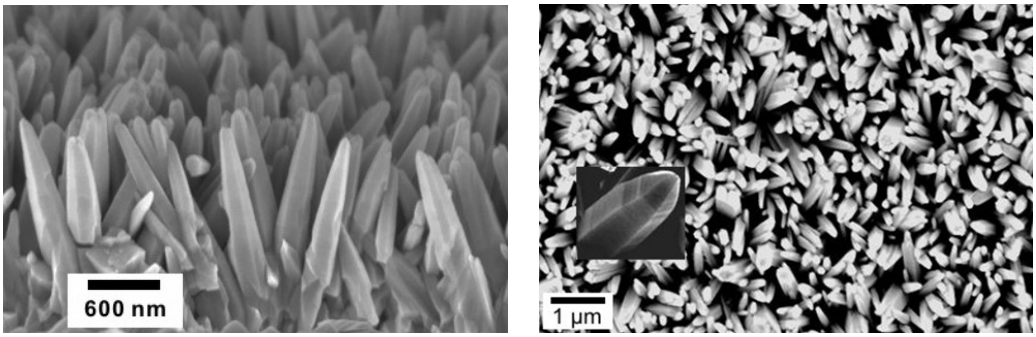

Figure 6.79 SEM images of as-grown ZnO NRs (in the inset, an enlarged image of a nanorod)

6.9.2.3 Atomic Force Microscopy (AFM)

Figure 6.80 a), b), and c) show the AFM images of the ZnO nanorod surface for the three different kinds of samples. The colour pallet, in all three images, is in the same scale 0-400nm. The surface roughness (Root Mean Square, RMS) ranges from 31 to 46 nm. Sample 0719-2 with the greatest density of summits (2.60 per μm^2), as indicated inTable 6.8, is also the one with the highest roughness. The nanorods of sample 0719-3 appear broader than those in the other two samples, probably because the NH_4NO_3 solution has an impact on both, vertical and lateral growth rates [6.96].

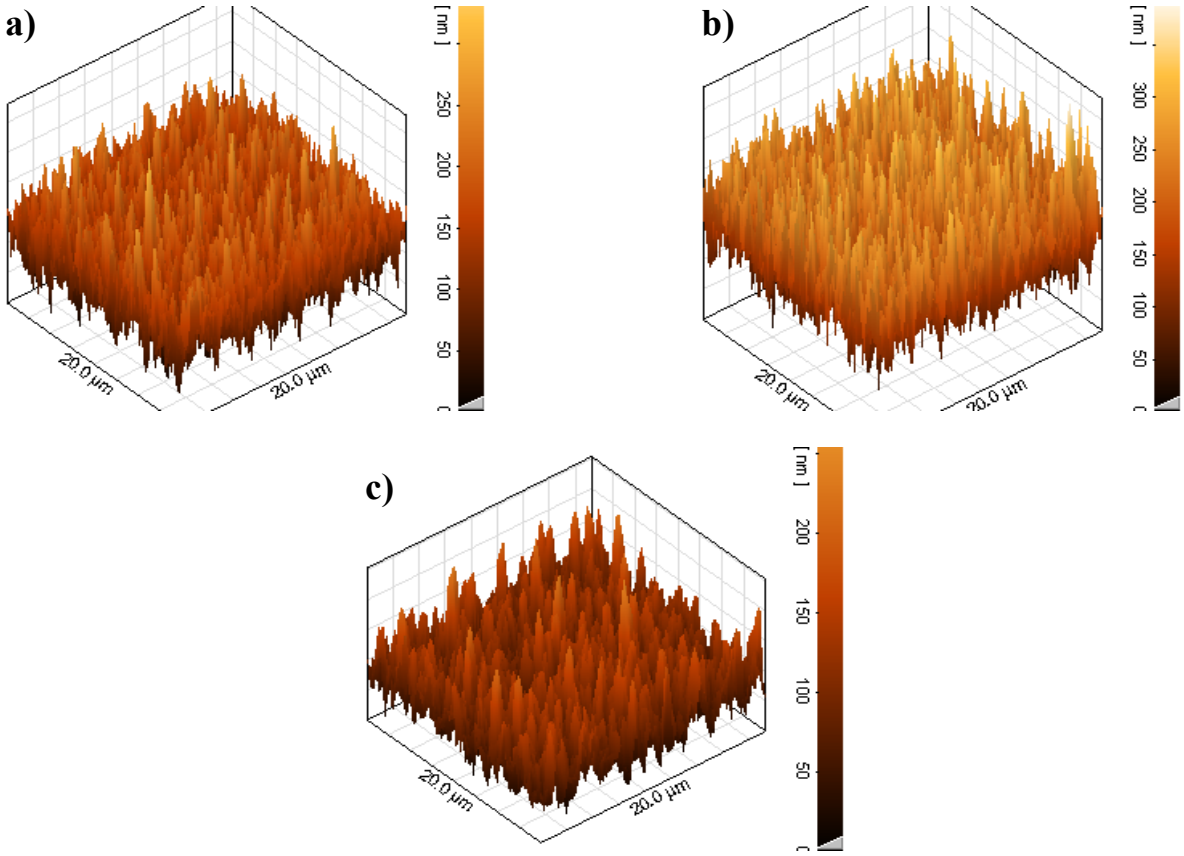

Figure 6.80 AFM images of the ZnO-nanorod samples studied a) 0719-1 b) 0719-2, and c) 0719-3

Table 6.8 Results from the AFM analysis of ZnO-nanorod samples: 0719-1, 0719-2, and 0719-3.

	Max. Height (nm)	**Roughness (nm)**	**Density of Summits(cm^{-2})**
Sample 0719-1	331	37.3	2.44×10^{8}
Sample 0719-2	386	45.9	2.60×10^{8}
Sample 0719-3	253	21.6	2.02×10^{8}

6.9.3 Optical Properties

6.9.3.1 Transmittance

The transmittance and reflectance spectra of the ZnO NRs were measured in the range 0.5-5.0 eV (250–2500 nm), as shown in Figure 6.81. The three kinds of the grown samples become transparent in the energy region 0.5-3.4 eV, which is ideal for solar cell device applications. The transmittance, in the critical visible- and ultra-violet-range, is over 70%. The reflectance, in the same spectral range, is only 5%. Sample 0719-3 exhibits a higher reflectance than the other two samples, which can be attributed to its smaller surface roughness of only 21.6 nm.

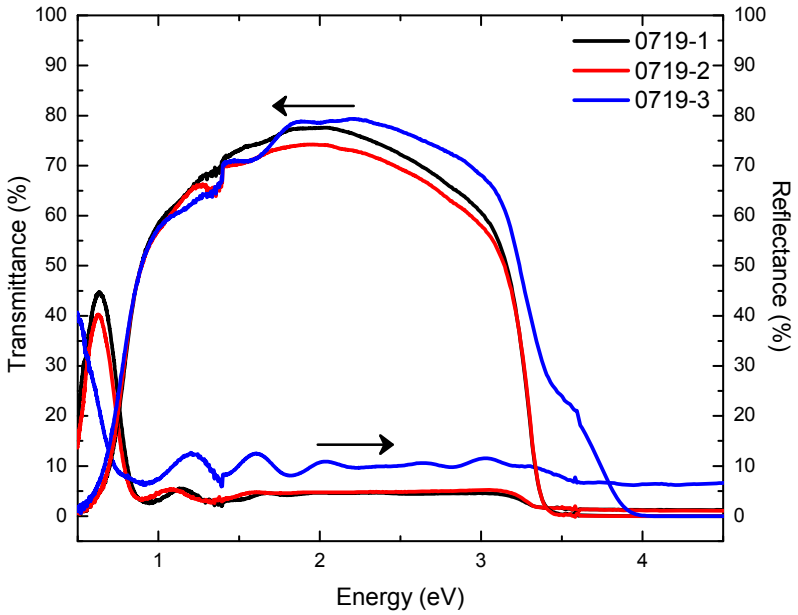

Figure 6.81 Transmittance and Reflectance spectra of samples 0719-1, 0719-2, and 0719-3

Analysis of the dependence of absorption coefficient on photon energy was carried out in order to determine the energy band-gap. The optical gap of the samples was obtained from Eq.(6.19) [6.97]:

$$(ahv) = B(hv - E_g)^m \tag{6.19}$$

where E_g is the optical band-gap, B is an energy-independent constant between 10^7 and 10^8 m^{-1}, and m is an index that characterizes the optical absorption process and is theoretically equal to 2 and 0.5 for indirect and direct allowed transitions, respectively.

The absorption coefficient α is calculated from the transmittance spectra with Eq. (6.20), [6.98] :

$$\alpha = -\frac{1}{d}\ln T \tag{6.20}$$

where d is the sample thickness and T is the normalized transmittance.

In ZnO NRs, the direct transitions are optical transitions that occur in crystalline semiconductors. It is well known, that direct transitions across the band gap are feasible between the valence and the conduction band edges in k space. In this transition process, the total energy and momentum of the electron–photon system must be conserved.

Figure 6.82 shows the plot of $(\alpha h\nu)^2$ vs. photon energy (tauc-plot). The values of the direct optical band-gap E_g of the ZnO NRs were obtained from the intercept of $(\alpha h\nu)^2$ vs. hν curves plotted. E_g values and B constants are given in Table 6.9. As can be seen, the energy band gaps vary from 3.32 eV (sample 0719-1) to 3.75 eV (sample 0719-3). The widening of the optical gap is tentatively attributed to the different growth conditions, e.g. the different chemical solutions of the electrodeposited ZnO NRs.

Table 6.9 Optical gap E_g and constant B of ZnO NRs calculated from the plot of $(\alpha h\nu)^2$ versus (hν)

	B ·10^7 (m^{-1})	**Eg (eV)**
0719-1	9.45	3.32
0719-2	10.87	3.34
0719-3	8.45	3.75

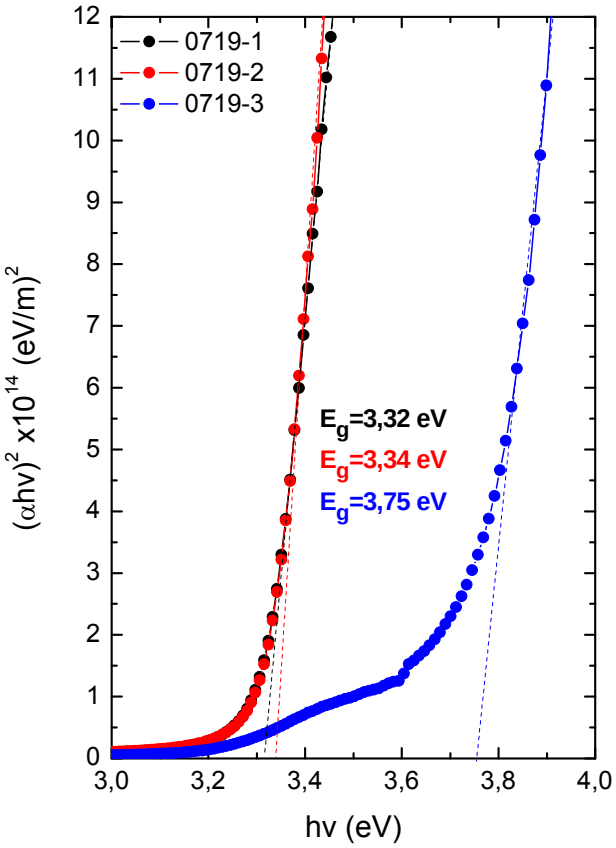

Figure 6.82 Plot of $(\alpha hv)^2$ versus photon energy (hv) of the ZnO nanorods

6.9.3.2 Photoreflectance Spectroscopy

Photoreflectance (PR) spectra have been measured at room temperature (RT) for the three different kinds of samples. The PR-spectra were fitted with two different Third Derivative Functional Forms (TDFFs), one with lower and one with higher energy, corresponding to the E_a and the E_b transition energies of the wurzite type ZnO-nanorods, respectively.

In addition, spatially resolved PR spectra have been measured at three different spots of each sample. The three different spots were selected vertically with their distance from the solution surface being 0.25, 0.75, and 1.25 cm, as shown in Figure 6.83.

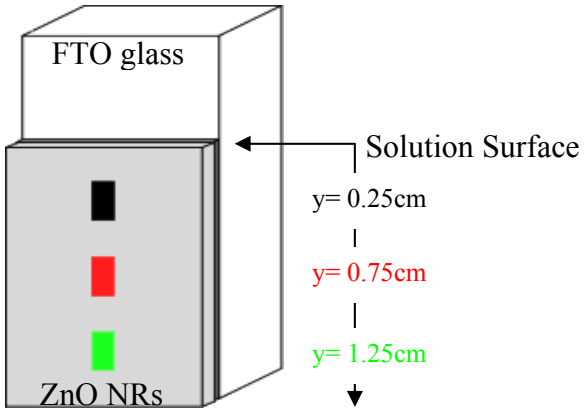

Figure 6.83 Beam spots on the samples in Photoreflectance measurements

On each sample spot, a pair of transitions originating from the ZnO NRs was observed at lower and higher energies (Table 6.10) and was assigned to the excitonic transition energies $E_{0B}(ex)$ and $E_{0A}(ex)$, respectively. In a PR experimental configuration with non-polarized light beam at an angle of incidence 45^{o}, the contribution of the electric field component parallel to the c-axis of the sample, which in this case coincides with the vertically grown ZnO-nanorods, is not significant. In accordance with that, transition energy E_{0C}, mostly excited with parallel polarized light, has not been observed.

The ground state exciton energy is enhanced compared to the free exciton energy of 3.30 eV in the bulk. Potential reasons for this enhancement are the 1D-confinement, [6.99] the grain size, the aspect-ratio, and the strain/stress distribution during deposition.

Apart from this, the energy band gap of sample 0719-1 increases with increasing the distance from the surface of the solution during deposition (Figure 6.84). The two energy peaks appear almost unresolved in the spectrum recorded at the upper part of the sample, close to the top of the chemical bath, and clearly resolved while approaching the lower part of the sample, at the bottom of the bath. The spectra, at y=0.25 and 0.75cm from the top, consist of two excitonic gap-energies: (y=0.25cm, $E_{0B}(ex)$=3.306eV and $E_{0A}(ex)$=3.320eV), (y=0.75cm $E_{0B}(ex)$=3.392eV and $E_{0A}(ex)$=3.400eV), respectively. The spectrum at y=1.25cm is more complicated. Two different pairs of excitonic gap-energies were fitted using four TDFFs (y=1.25cm, $E^{1}_{0B}(ex)$=3.437eV, $E^{1}_{0A}(ex)$=3.441eV, $E^{2}_{0B}(ex)$=3.455eV, $E^{2}_{0A}(ex)$=3.466eV) indicative of possible

inhomogenities in size and/or shape of the deposited nanorods at the respective sample spot where the incident light beam has been focused.

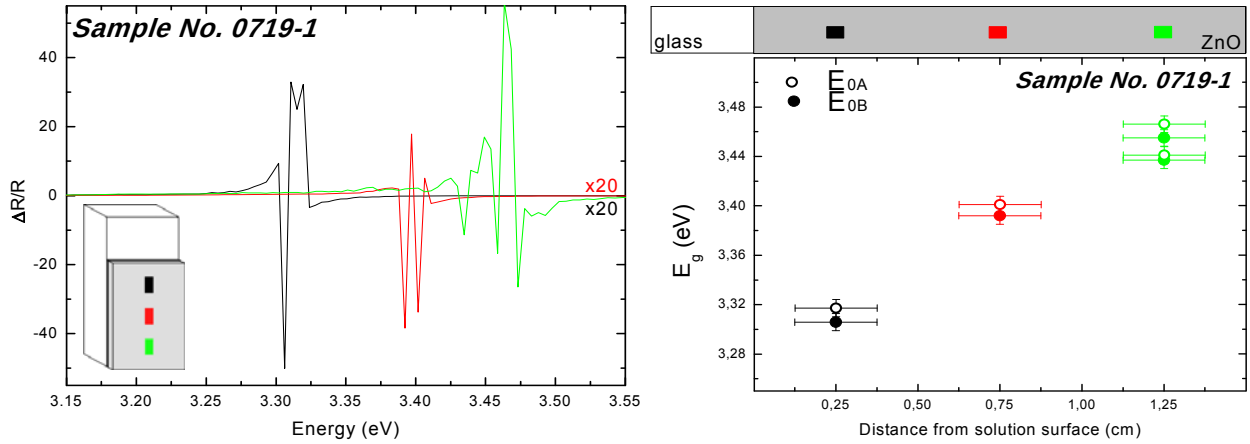

Figure 6.84 PR Spectra in dependence of the distance from the solution surface (left), and diagram of the fitted band gap energies (right) for sample 0719-1

The in-plane dimension of the ZnO-nanorods can be calculated from the energy up-shift of the gap of the nanorods $E^{ZnO\text{-}NRs}$ *(as experimentally measured)* with respect to the gap of the bulk $E^{bulk\text{-}ZnO}$*(as known from the literature* [6.100]*)* using Eqs. (6.17) and (6.18). The energy up-shift is defined as [6.95]:

$$\Delta E = E^{ZnO\text{-}NRs} - E^{bulk\text{-}ZnO} \qquad (6.21)$$

The effective electron and hole masses of bulk ZnO used in the calculation are: $m_e^* = 0.24\, m_e$ and $m_h^* = 0.59\, m_e$, respectively [6.101]. The in-plane dimension is in the range of 3.71 – 19.17nm. This corresponds to the dimension of the upper segment of the NRs, as viewed by SEM, which means that the reflected light stems from the upper most part of the sample. This is expected, since light propagating in the direction top-to-bottom is trapped due to the nanostructure. This can be also a reason for the absence of i-ZnO bands in the spectra; another one could be the very small thickness (40 nm) of the i-ZnO layer. The transition energies E_{0A} and E_{0B} show a strong dependence on the in-plane dimension of the NRs, as expected. In particular, the energy gap of sample 0719-1, grown in $Zn(NO_3)_2$ solution, is widened as the in-plane dimension of the NRs decreases (Figure 6.85). The PR spectrum, at a distance of y=1.25cm from the top, may be interpreted as

originating from the superposition of the PR spectra of nanorods with in-plane dimension of D=3.71 and 4.23nm.

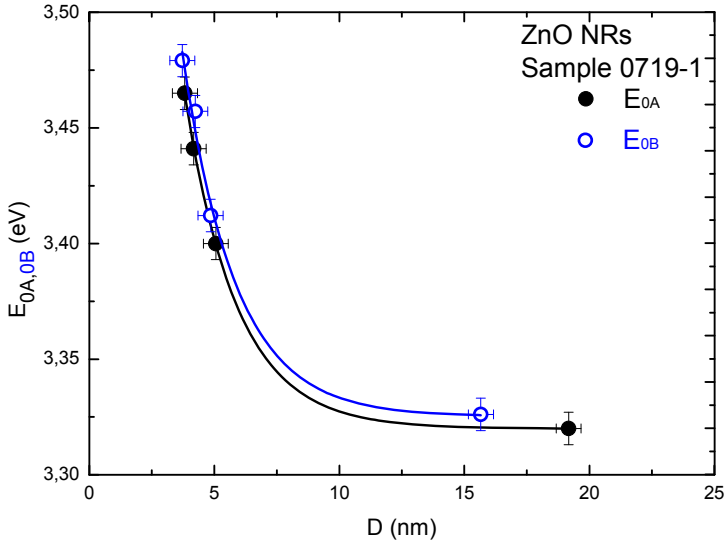

Figure 6.85 Dependence of E_{0A} and E_{0B} gap energies on the in-plane dimension D of the ZnO NRs of sample 0719-1

A similar dependence of the PR spectra was observed on sample 0719-2. The spectra at y=0.75 and 1.25cm distance from the solution surface consist of two excitonic gap-energies: (y=0.75, E_{0B}(ex)=3.373eV and E_{0A}(ex)=3.444eV) and (y=1.25, E_{0B}(ex)=3.338eV and E_{0A}(ex)=3.342eV). The spectrum at y=0.25cm consists of four excitonic gap-energies: (y=0.25, E^1_{0B}(ex)=3.463eV, E^1_{0A}(ex)=3.482eV, E^2_{0B}(ex)=3.472eV, E^2_{0A}(ex)=3.483eV) attributed to inhomogenities in size and/or shape of the deposited nanorods similar to the case of sample 0719-1. In case of sample 0719-2, however, opposite to the case of sample 0719-1, the exciton transition energies decrease while increasing the distance from the solution surface (Figure 6.86).

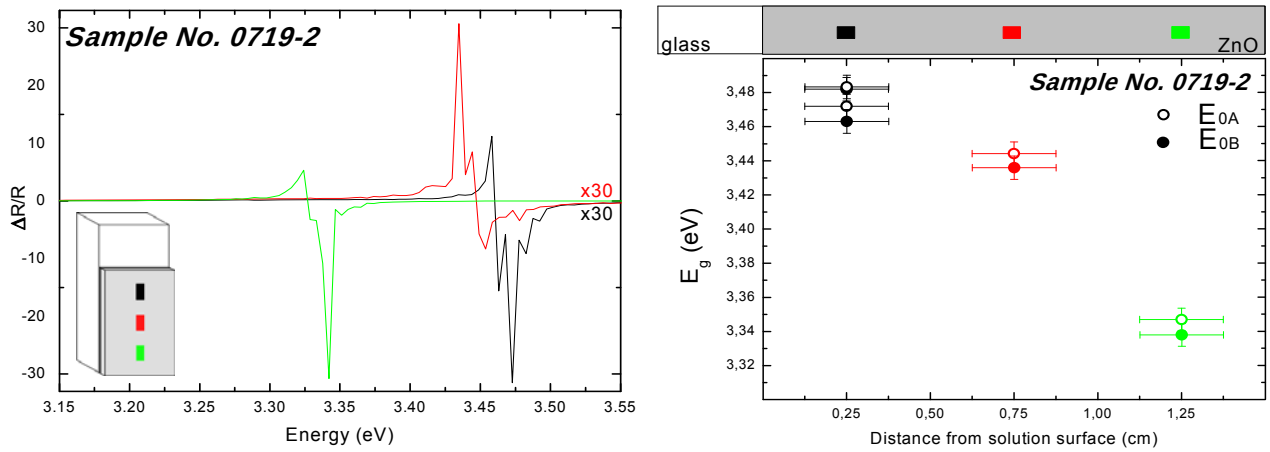

Figure 6.86 PR spectra in dependence of the distance from the solution surface (left), and diagram of the fitted band gap energies (right) for sample 0719-2

Similar to the previous case, the in-plane dimension of the NRs has been calculated in the range 3.46 – 8.87nm. The PR spectrum, at a distance of y=0.25cm from the top, is a superimposition of the PR-spectra of ZnO NRs with D=3.46 and 3.61nm.

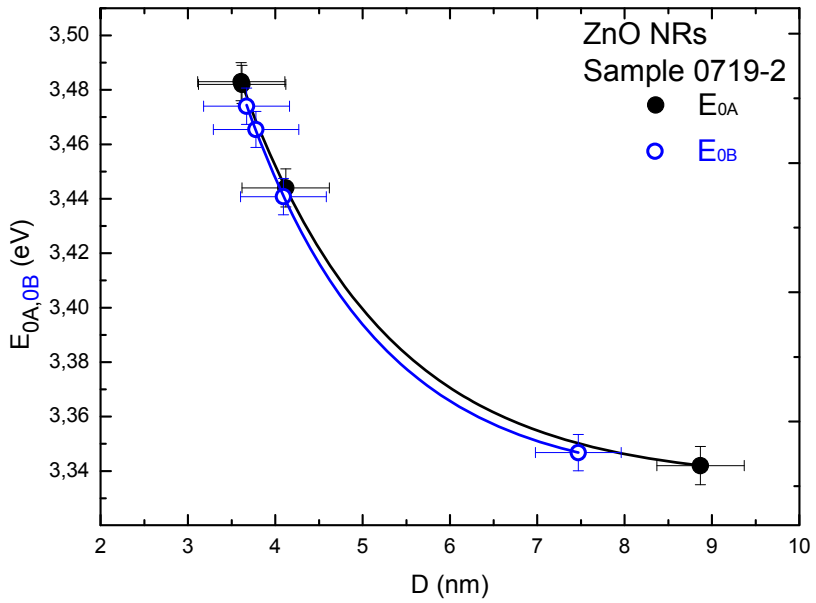

Figure 6.87 Dependence of E_{0A} and E_{0B} gap energies on the in-plane dimension D of the ZnO NRs of sample 0719-2

In both, 0719-1 and 0719-2 samples, a significant dependence of the energy gap on the distance from the solution surface has been observed. Since this energy dependence is different in the two samples studied, it is tentatively associated with a concentration gradient in the solution, during deposition, rather than a temperature gradient. A temperature gradient is expected to have the same influence on both samples. On the contrary, a concentration gradient in solutions with different precursors, e.g. ($Zn(NO_3)_2$ for deposition of sample 0719-1 and $Zn(NO_3)_2$+HNO_3) for deposition of sample 0719-2, may lead to different growth modes and is, therefore, a more plausible explanation.

Table 6.10 Band-gap energies calculated from a) the transmittance spectra and b) the photoreflectance spatially resolved spectra of samples 0719-1, 0719-2, and 0719-3.

	$^{a}E_g$ (eV)	$^{b}E_{0B}$(ex)(eV)	$^{b}E_{0A}$(ex)(eV)	y (cm)
0719-1	3.32	3.306	3.320	0.25
		3.392	3.400	0.75
		3.437	3.441	1.25
		3.459	3.464	
0719-2	3.34	3.463	3.482	0.25
		3.472	3.483	
		3.437	3.444	0.75
		3.338	3.342	1.25
0719-3	3.75	-	-	

Based on the measured energy shifts, the strengths of interband transitions can be calculated from Eq.(2.18) via Eqs.(2.16) and (2.17). Using the transition energies listed in Table 6.10, and the value of Δ_{SO}= -19meV referred in the literature [6.100], the transition strengths, in each sample, have been calculated and are given in Table 6.11.

Table 6.11 Transition Strengths at E_{0A}, E_{0B}, and E_{0C} gaps

	$C_{0A\perp}$:	$C_{0B\perp}$:	$C_{0C\perp}$:	$C_{0A\parallel}$:	$C_{0B\parallel}$:	$C_{0C\parallel}$	y (cm)
0719-1	1	0.98	0.02	0	0.04	1.96	0.25
	1	0.79	0.21	0	0.42	1.58	0.75
	1	0.52	0.48	0	0.96	1.04	1.25
	1	0.58	0.42	0	0.84	1.14	
0719-2	1	0.67	0.33	0	0.66	1.34	0.25
	1	0.96	0.04	0	0.08	1.92	
	1	0.72	0.28	0	0.56	1.44	0.75
	1	0.52	0.48	0	0.96	1.04	1.25

Photoreflectance measurements could not be performed on sample 0719-3. As indicated by the transmittance measurements, the band gap energy (E_g=3.75eV) is higher than the laser energy of 3.67 eV (337.5nm) used for excitation. According to the above mentioned observations, the addition of NH_4NO_3 in the solution has an impact, not only on the growth rate, but on the size of the ZnO nanorods as well. The in-plane dimension of the NRs is reduced leading to an up-shift of the energy gap with the consequence that the photoreflectance, excited only by pumping with equal or above band-gap light, cannot be recorded in case of sample 0719-3.

By comparison of the gap energies calculated from the Transmittance spectra (indirect method) and the gap energies obtained by fitting the PR spectra (direct method), it is apparent, that PR spectroscopy is a high resolution method due to its derivative-like nature. Besides, by using PR, it has been easy to identify the spatial dependence of gap energies originated by spatially different conditions of growth, since, in PR experiments, the light beam diameter on the sample is 1-2mm. On the contrary, in Transmittance experiments, only an approximate value of gap energy can be calculated from the slope of the absorption edge and that averaged over a larger sample area because of the significantly larger beam diameter of 8-10 mm.

From the energy shift ΔE (Eq.(6.21)), the carrier concentration can also be calculated. The total number of carriers is given by [6.102]:

$$n = \frac{8\pi\mu^{3/2}}{h^3} \cdot \frac{2\sqrt{2}}{3} \left(\Delta E\right)^{3/2} \tag{6.22}$$

where μ is the reduced effective mass and h is the Plank's constant. A mean carrier concentration, calculated for both samples with Eq.(6.22), was found to be: $\sim 2.28 \cdot 10^{19}\,\mathrm{cm}^{-3}$, for sample 0719-1, and $\sim 2.52 \cdot 10^{19}\,\mathrm{cm}^{-3}$, for 0719-2. This slight increase in the carrier concentration of sample 0719-2 may result from the n-type doping of the samples with nitrogen [6.87]. Since the solution used for the growth of sample 0719-2 contains both, $Zn(NO_3)_2$ and HNO_3, there might be a slight increase in carrier population supplied by nitrogen doping.

6.9.4 Electrical Properties

Figure 6.88 shows the EQE of a CIGS solar cell without ARC and with Al-doped ZnO nanorod arrays ($Zn(NO_3)_2$ / HNO_3 bath), respectively. This coating leads to a decrease of the weighted global reflectance of the solar cells from 8.6 to 3.5%. The bumps in quantum efficiency, which are related to the interference fringes printed in the figure, were improved by the use of Al-doped ZNAs which leads to a 5.8% increase in short circuit current without significant effect on their open-circuit voltage and fill factor (FF), which is comparable to that of a conventional solar cell with an optimized single layer MgF_2 antireflective coating.. The performance improvement in CIGS solar cell by the use of Al-doped V-ZNAs ARC is comparable to the CIGS solar cell provided with an undoped V-ZNAs ARCs [6.103]. Since the spectral reflectance in the range of 350-1150 nm is similar for the two different V-ZNAs on CIGS solar cells, their performances for enhancing the EQE by quashing the surface reflection via a subwavelength structure are commensurate.

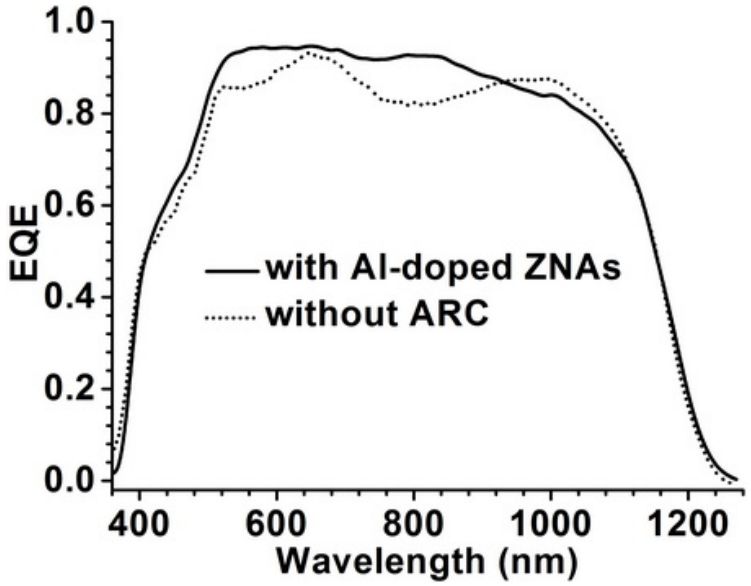

Figure 6.88 External quantum efficiency of a CIGS solar cell without (dot line) and with (solid line) Al-doped ZnO NRs.

6.10 Chalcopyrite based Thin Film Solar Cells

6.10.1 I-V Characteristics of Solar Cells

6.10.1.1 with PVD ZnSe/$CuGaSe_2$/Mo/glass

On the ZnSe/$CuGaSe_2$/Mo/glass heterostructure, a ZnO (window layer) and an Al grid (front ohmic contact) were deposited to complete a prime CGS-solar cell. The I-V characteristic of the heterostructure is shown in Figure 6.89.

The measured current density as a function of the applied voltage (forward bias) is very slim. This fact is attributed to the relatively thick (≈80 nm) ZnSe buffer layer. As already mentioned, the buffer layer thickness is of great importance for the current transport, and, for solar cells with CdS buffer layer, it is chosen to be 30 to 50nm.

On the other hand, without a buffer layer, the band alignment (§ 3.1) is not possible and the solar cell cannot operate.

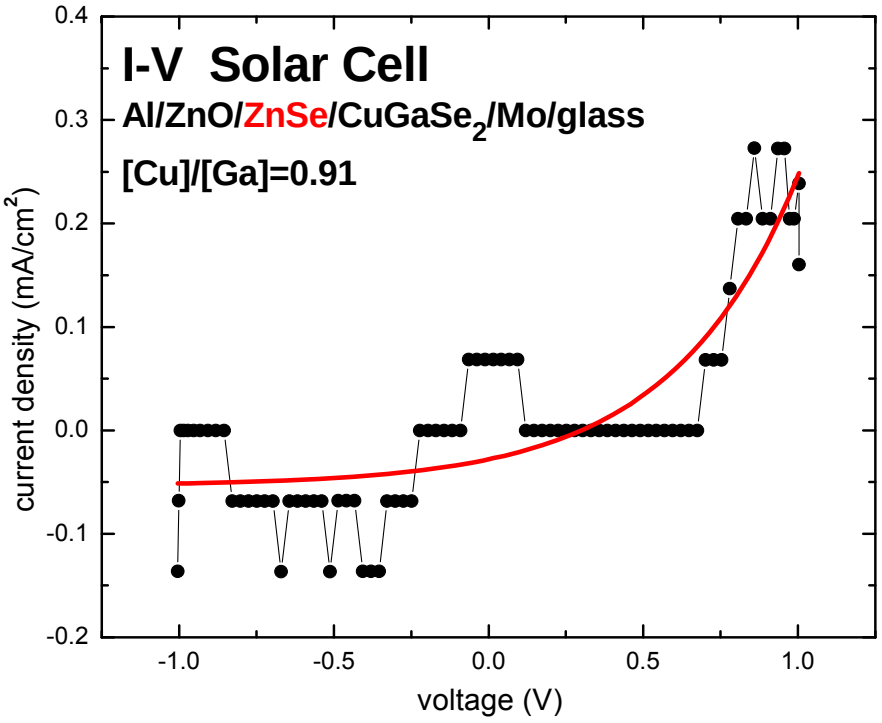

Figure 6.89 I-V characteristic of a CGS-solar cell with PVD ZnSe buffer layer

6.10.1.2 with CBD ZnSe/CuGaSe$_2$/Mo/glass

Thin film solar cells with ZnSe buffer layer grown on polycrystalline substrates, as described in §6.5 have been electrically characterized using a sun simulator (§5.3) at the Center of Renewable Energy Sources and Saving (CRES). To record the characteristic I-V curve, the set-up used in the measurement of commercial solar cells was used.

After several attempts aiming to improve the design of the solar cell and especially to minimize the thickness of the buffer layer, a characteristic I-V in the dark was successfully recorded on two of the solar cells:

a) on the Au/Al/In:ZnO/i-ZnO/ZnSe/CuGaSe$_2$/Mo/glass solar cell, and

b) on the Au/Al/In:ZnO/i-ZnO/ZnSe/Cu(In,Ga)Se$_2$/Mo/glass solar cell

In both cases, the ZnSe buffer layer was grown by Chemical Bath Deposition on polycrystalline chalcopyrites, CuGaSe$_2$ and Cu(In,Ga)Se$_2$, for 4 min.

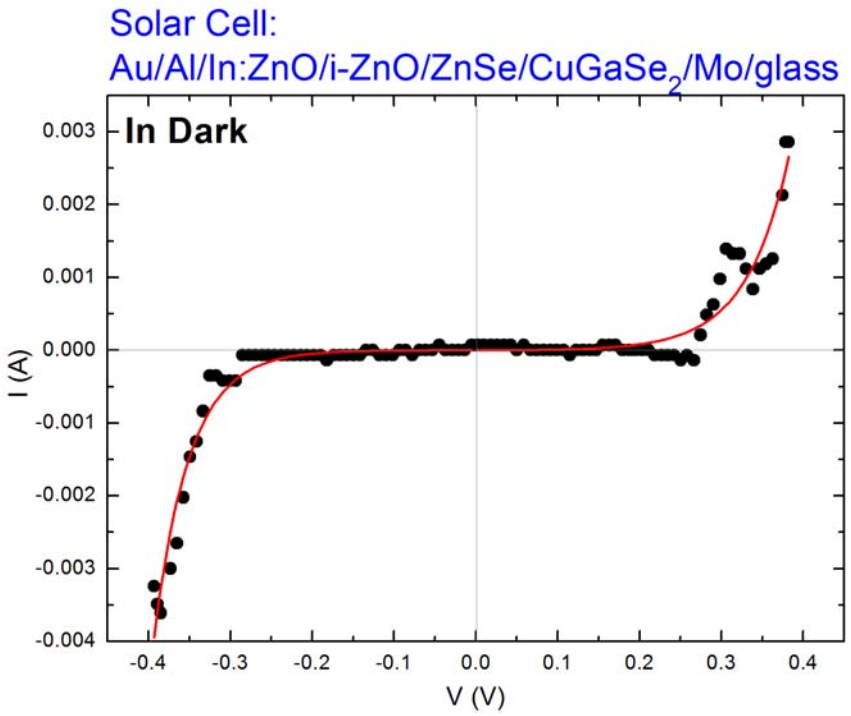

Figure 6.90 I-V Characteristic of Au/Al/In:ZnO/i-ZnO/ZnSe/$CuGaSe_2$/Mo/glass with ZnSe grown for 4min by Chemical Bath Deposition

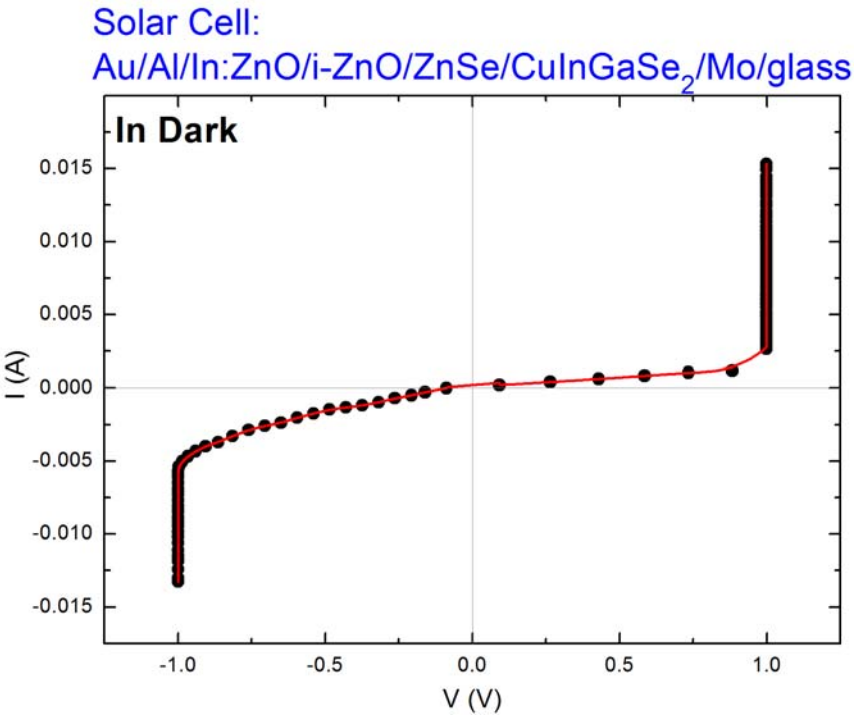

Figure 6.91 I-V Characteristic of Au/Al/In:ZnO/i-ZnO/ZnSe/Cu(In,Ga)Se_2/Mo/glass with ZnSe grown for 4min by Chemical Bath Deposition

The dark current of forward biased solar cell can be expressed by Eq.:

$$I = I_{01} e^{\frac{q(V-R_s I)}{kT}-1} + I_{02} e^{\frac{q(V-R_s I)}{2kT}-1} + \frac{V - R_s I}{R_p} \tag{6.23}$$

where I_{02} and I_{01} stand for recombination and diffusion saturation currents, R_S is the series resistance, R_p is the shunt resistance. The series resistance of large-area solar cells is small and can be negligible.

Eq.(6.23) can be simulated by the circuit depicted in Figure 6.92. V and I are the external voltage and currents which are measured, V_j and I_j being the junction voltage- and junction current-drop, respectively.

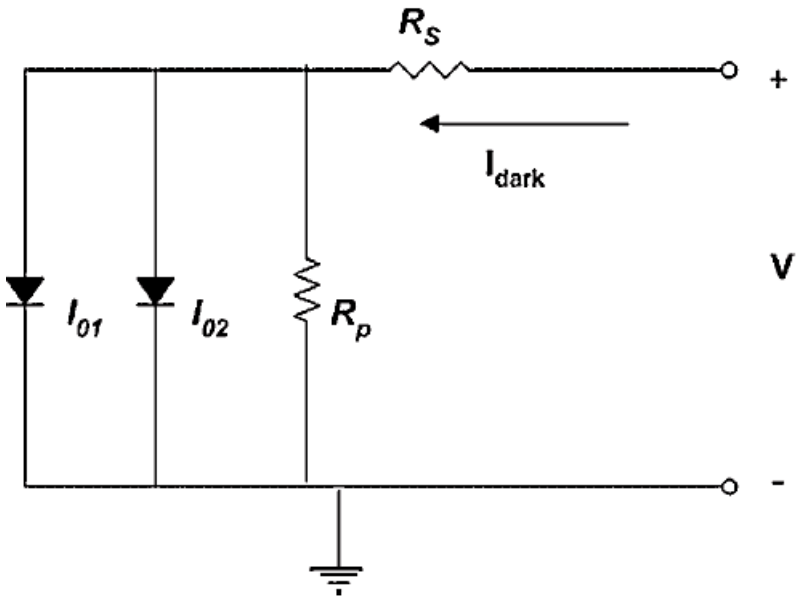

Figure 6.92 Equivalent circuit for solar cell

From Eq.(6.23) the four principal mechanisms which determine the I-V characteristics of a solar cell can be identified.

- The series resistance R_s limits the current I for a particular voltage V or alternatively adds an extra voltage, proportional to the current I, to the junction voltage drop. The R_s effect becomes more important as the current increases.
- The shunt resistance R_p adds an extra path for the current. The shunt current is added to the junction current. This current increases linearly with the voltage,

while the junction current increases exponentially. Consequently, the shunt current should be considered only for low voltage values.

- The recombination current I_R and diffusion current I_D are the intrinsic mechanisms in the junction.

To overcome process incompatibility between the growth methods of the layers, electrodeposition was applied to grow the ZnO window layer. A thin layer of i-ZnO was deposited on a ZnSe/Cu(In,Ga)Se_2/Mo-glass heterostructure. On top, three points Pt serving as collectors were deposited. I-V characteristics were successfully recorded in dark (Figure 6.93) and under illumination (Figure 6.94) with low intensity radiation in the order of 100 W/m^2 under STM (Standard Test Measurement) conditions of AM 1.5. The fillfactor of the cell of ca. 1cm^2 active area is:

$$ff = \frac{I_m V_m}{I_{SC} V_{OC}} = \frac{1\times10^{-3} A \times 0.5\, V}{1.4\times10^{-3} A \times 0.68\, V} = 52.5\%$$

which yields efficiency of:

$$\eta = \frac{P_m}{P_{in}} = \frac{\frac{0.5\times10^{-3} W}{10^{-4} m^2}}{\frac{100\, W}{m^2}} = 5\%$$

This is an absolutely satisfactory value for cells with n-type buffer- and window-layer processed by low cost chemical and electrochemical techniques.

Operation of the cell under high illumination intensity requires adequate dimensioning of the ZnO layer thickness, which will be aquired at a next step of the Low Cost – Best Efficiency CIS/CIGS Thin Film Solar Cell Technology Development.

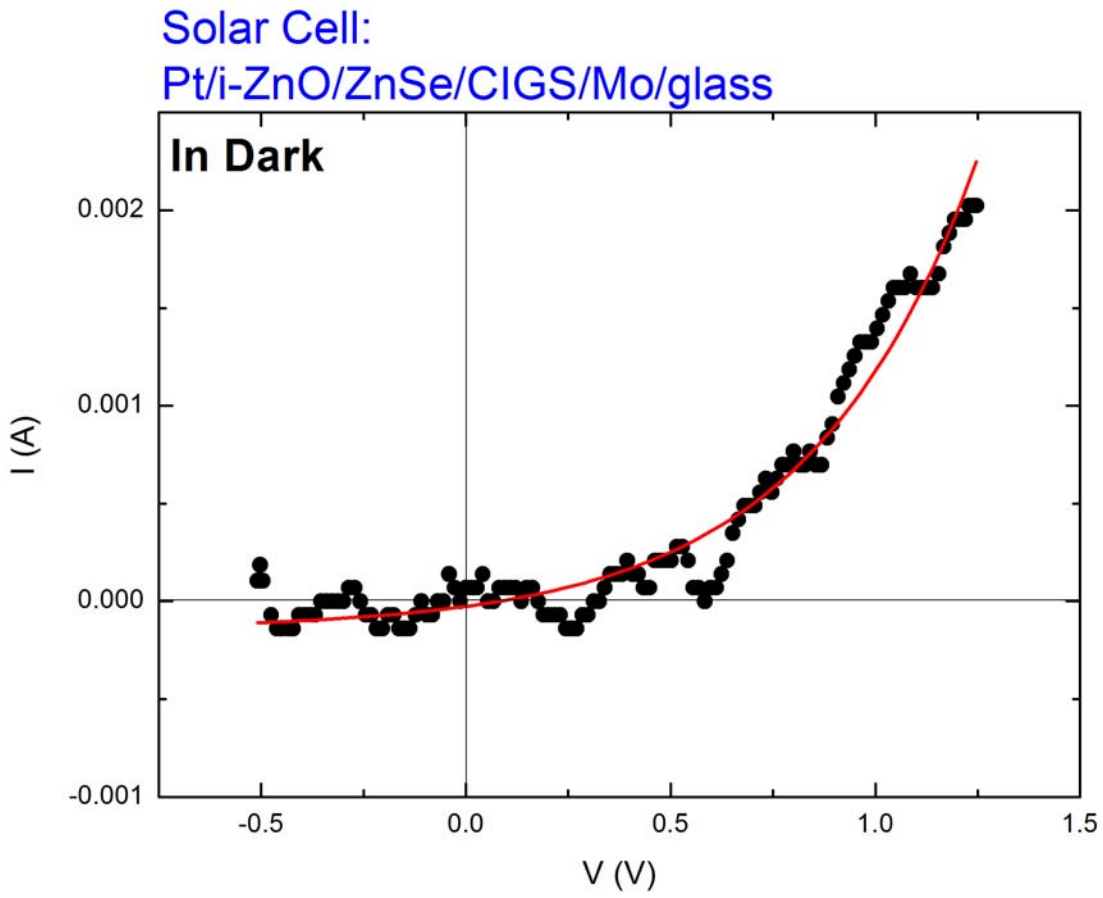

Figure 6.93 I-V Characteristic in dark of Pt/i-ZnO/ZnSe/Cu(In,Ga)Se_2/Mo/glass with ZnSe grown for 2.5min by Chemical Bath Deposition and ZnO grown for 1h by Electrochemical Deposition.

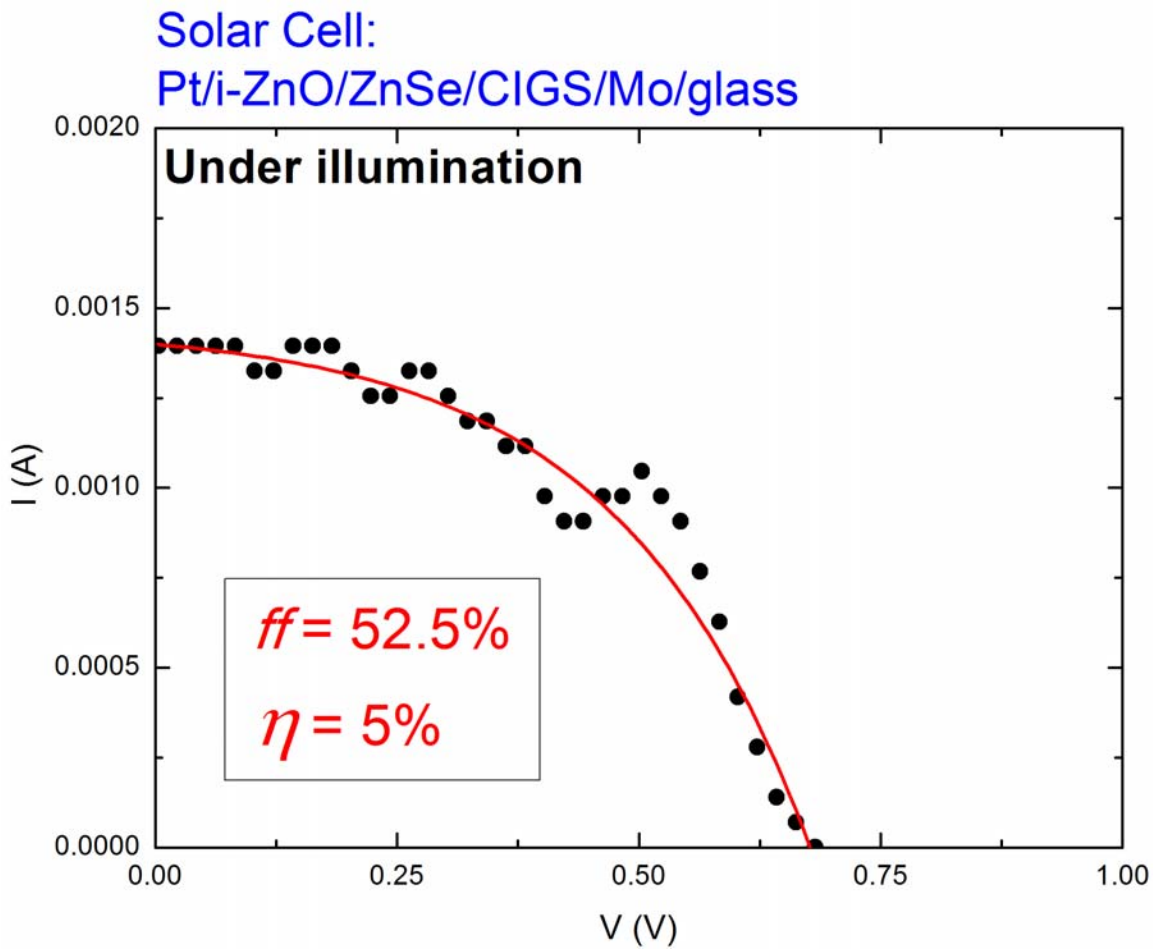

Figure 6.94 I-V Characteristic illumination of Pt/i-ZnO/ZnSe/Cu(In,Ga)Se_2/Mo/glass with ZnSe grown for 2.5min by Chemical Bath Deposition and ZnO grown for 1h by Electrochemical Deposition.

It should be noted, that in the series of measurements of the I-V characteristics, several difficulties have been encountered in the use of the sun simulator set-up. The most crucial one was the contact for the front solar cell collector. To contact the front collector, the standard set-up uses 3-point crown spring probes like the one shown in Figure 6.95. Unfortunately, that kind of probes is not suitable for the prototype thin films solar cells under development and result very often in scratching the solar cell. Scratching results in a short-cut of front and back contact and the cell is irreparably damaged.

To overcome this problem, a more suitable device needed to be constructed. The self-constructed device uses for the front collector, a rounded two-part spring probe. Controlled by two springs, it smoothly touches the surface of the front collector and can be adapted to cells with different collector design.

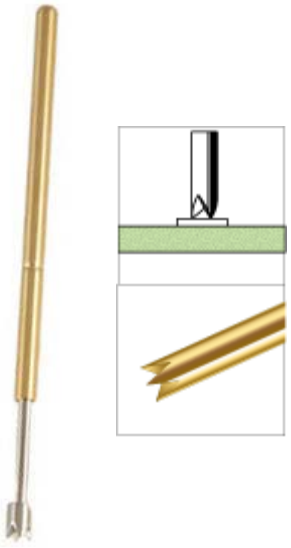

Figure 6.95 3-point crown spring probes used for the electrical connection of commercial solar cells

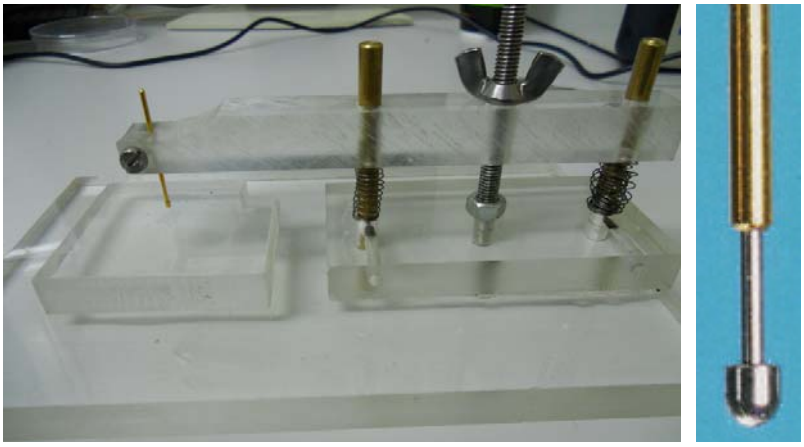

Figure 6.96 Self-constructed device with rounded spring probe used for recording the I-V characteristics

6.10.2 Electroreflectance(ER)of Al/ZnO/CdS/CuIn$_{1-x}$Ga$_x$Se$_2$/Mo/glass Solar Cell

ElectroReflectance (ER) measurements are used to characterize solar cells. This method is a good tool to measure optical properties like band gap energy of absorber, buffer, and window layers, possible secondary phases in the vicinity of the heterojunction, and defects in the semiconductors.

Thin film ElectroAbsorption (EA) which is the relative change of the transmission $\Delta T/T$ occurs as a parallel process to ER as the modulated transmitted light is reflected at the back surface of the sample. Its origin gives rise to a peak of up to 50 meV below the ER signal of the band gap depending on the sample thickness. This EA signal, many times, makes an exact analysis of ER spectra impossible because of the overlap of the two structures. The line shape of interband EA signals can be calculated for a well-known single crystal semiconductor like GaAs prepared with planar surfaces and with known field distribution in the space-charge region [6.104], but not for the presented ZnO/CdS/Cu(In,Ga)S_2/Mo/glass thin film solar cell with rough surfaces. ER can only be discriminated from EA by variation of the angle of incidence [6.105]. The EA signal disappears for high angles of incidence relative to the plane normal due to the exponential dependence of the absorption on optical path length. Another effect is, that, by varying the angle of incidence, the ER signal changes in symmetry, which is caused by interference effects at the ZnO and CdS window layers of the solar cell [6.106]

Acceptor to donor transitions also appear as an EA peak below the band gap energy since the photocurrent and, therefore, the population of the acceptor states is modulated by V_{ac} (ac-voltage applied to the solar cell). This model is introduced by Glembocki et al. [6.107]. The result is an absorption change below the band gap energy corresponding to the energetic levels of donors and acceptors.

In the present work, the optical and structural properties of a Thin Film Solar Cell are being investigated. The design of the solar cell is shown in Figure 6.97. The ER measurements were performed in a temperature range from 10 – 300K, using a closed-cycle He-cryostat. The experimental set-up of the ER is detailed described in §5.2.2.5.

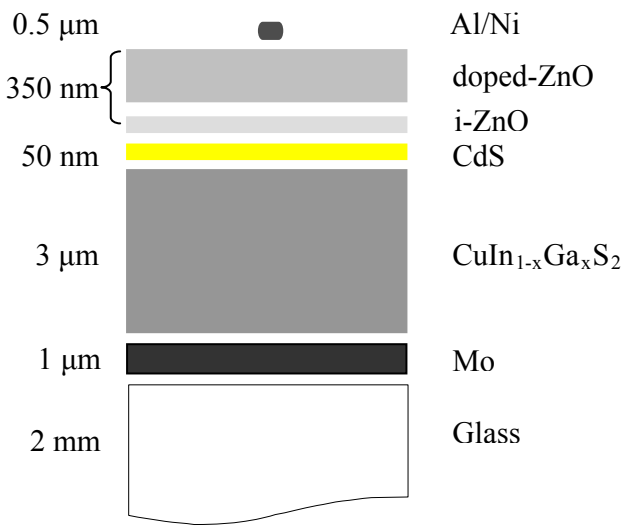

Figure 6.97 Schematic drawing of a Chalcopyrite Thin Film Solar Cell design

The ER spectra recorded at each temperature show sharp intense peaks corresponding to the transition energies of the absorber ($CuIn_{1-x}Ga_xS_2$), the buffer layer (CdS), and the front ohmic contact-window layer (ZnO), as shown in Figure 6.98 (T=300K) and Figure 6.99 (T=10K).

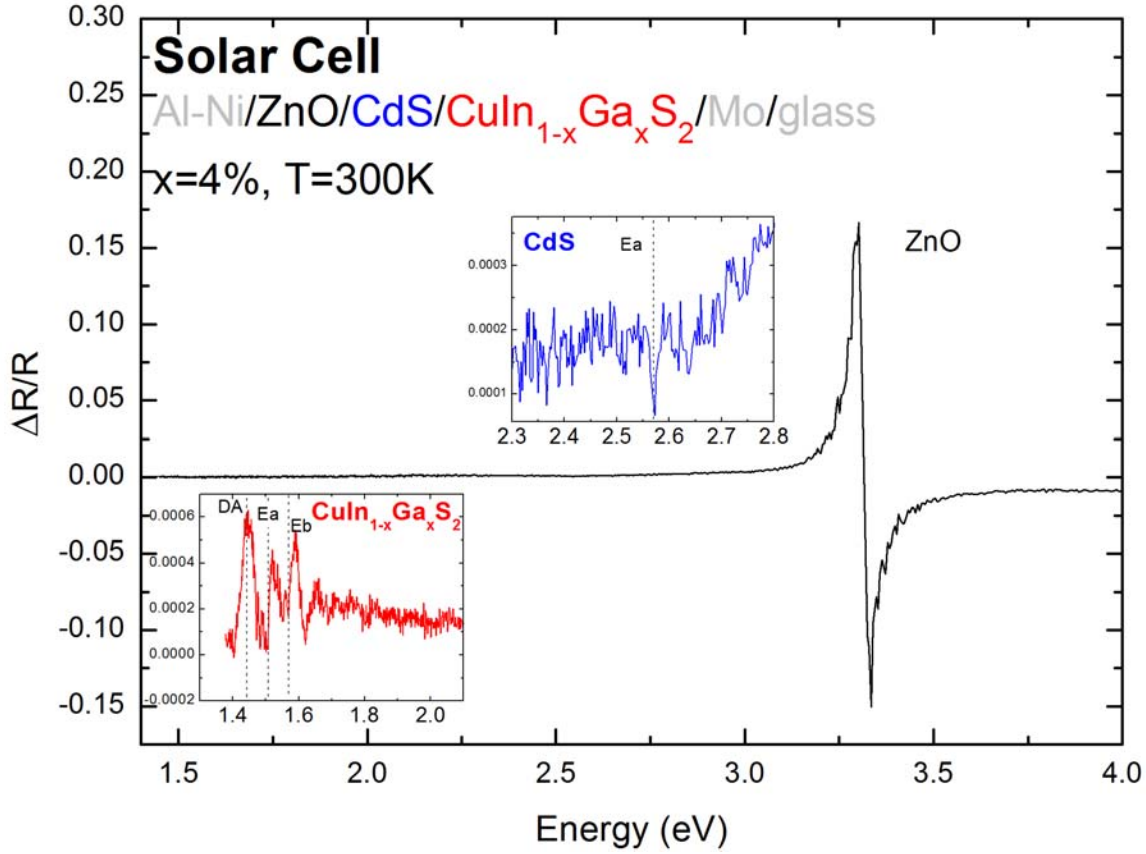

Figure 6.98 ElectroReflectance (ER) spectrum of a ZnO/CdS/$CuIn_{1-x}Ga_xS_2$ at Room Temperature

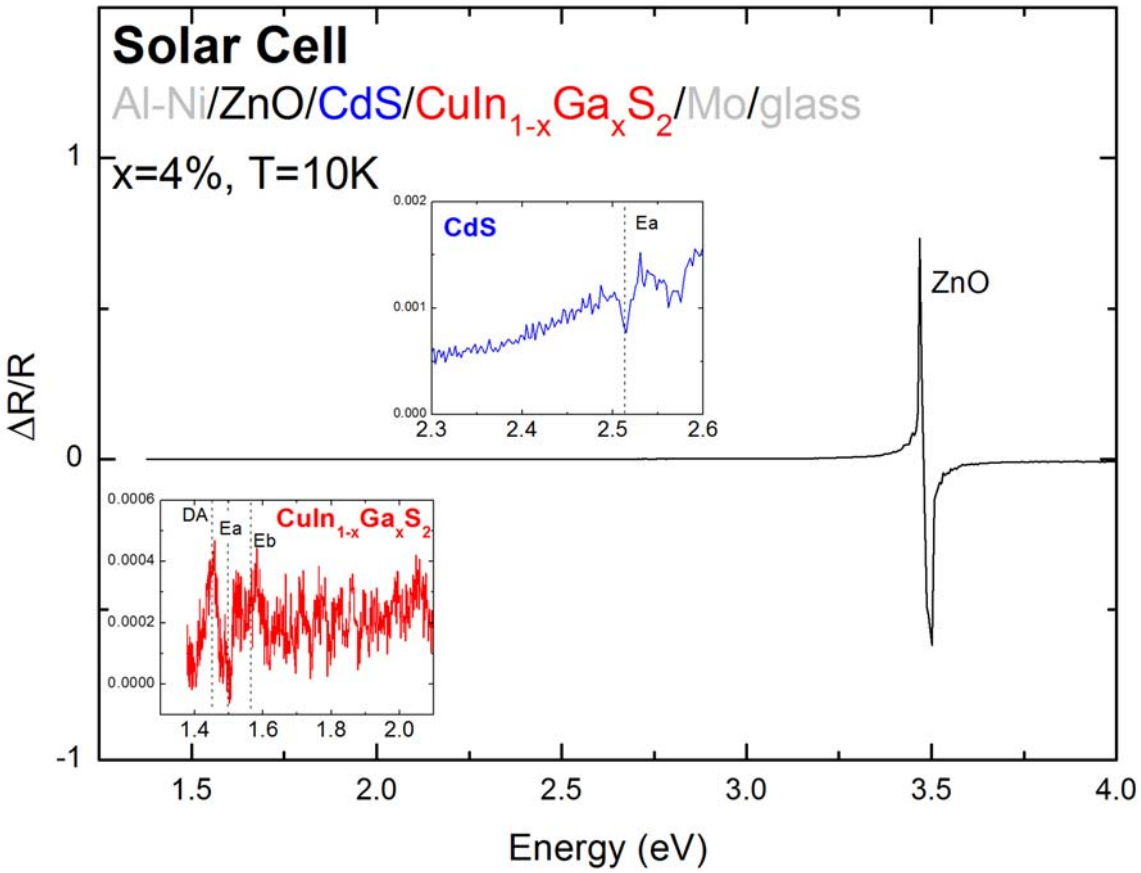

Figure 6.99 ElectroReflectance (ER) spectrum of a ZnO/CdS/$CuIn_{1-x}Ga_xS_2$ at Low Temperature (T=10K)

6.10.2.1 The $CuIn_{1-x}Ga_xS_2$ absorber

The scope of the present paragraph is to determine the band-gap energies, and thus the spectral range for optical absorption of $CuIn_{1-x}Ga_xS_2$ (CIGS) polycrystalline films and CIGS-based solar cells and to analyse the effects of the substitution of In by Ga for composition (x=[Ga]/([In]+[Ga] = 0.04) of the absorber film.

The chalcopyrite band diagram is described in detail in §2.1.3.1. The energy band gap of the quaternary $CuIn_{1-x}Ga_xS_2$ is expected to lie within the band gap of the ternary end members, $CuInS_2$ and $CuGaS_2$. On $CuInS_2$, at 300 K, three split valence bands have never been observed. In particular, only one polarization independent spectrum was observed at 300 K, while, at low temperatures, the band-gap of $CuInS_2$ was found to be a polarization-independent doublet split by 19meV [6.50], [6.108]. In the case of the other ternary end member, $CuGaS_2$, there is strong polarization dependence with the E_a

transition predominant for light polarization parallel to the optical axis and the E_b transition polarized perpendicular to the optical axis [6.108]. The polarization dependence is indicative of a crystal field splitting, which, for $CuGaS_2$, has been calculated to be 120meV (300 K) from the evaluation of the corresponding ER spectra [6.42]. According to the above, with the Ga addition to the ternary $CuInS_2$, the quaternary $CuIn_{1-x}Ga_xS_2$ at 300 K is expected to give ER spectra indicative of a gradual increase of the crystal field splitting from 0 (for $CuInS_2$) to 120meV (for $CuGaS_2$).

ER spectra in the energy region of the $CuIn_{1-x}Ga_xS_2$ absorber consist of: (a) a peak below the energy band gap, either originating from the EA or a DA transition, and (b) two peaks with third derivative line shapes attributed to the E_a and E_b transition energies of the quaternary compound. The energy separation between those two transitions is 50meV at RT and 65meV at 10K. The energy separation may be additionally increased in the presence of elastic strain. The energy gaps of $CuIn_{1-x}Ga_xS_2$ films known from the literature [6.50] range from 1.53 to 2.40 eV, which are the band gap energies of the ternary $CuInS_2$ and $CuGaS_2$, respectively. The E_a and E_b band gap energies in dependence of temperature are shown in Figure 6.100.

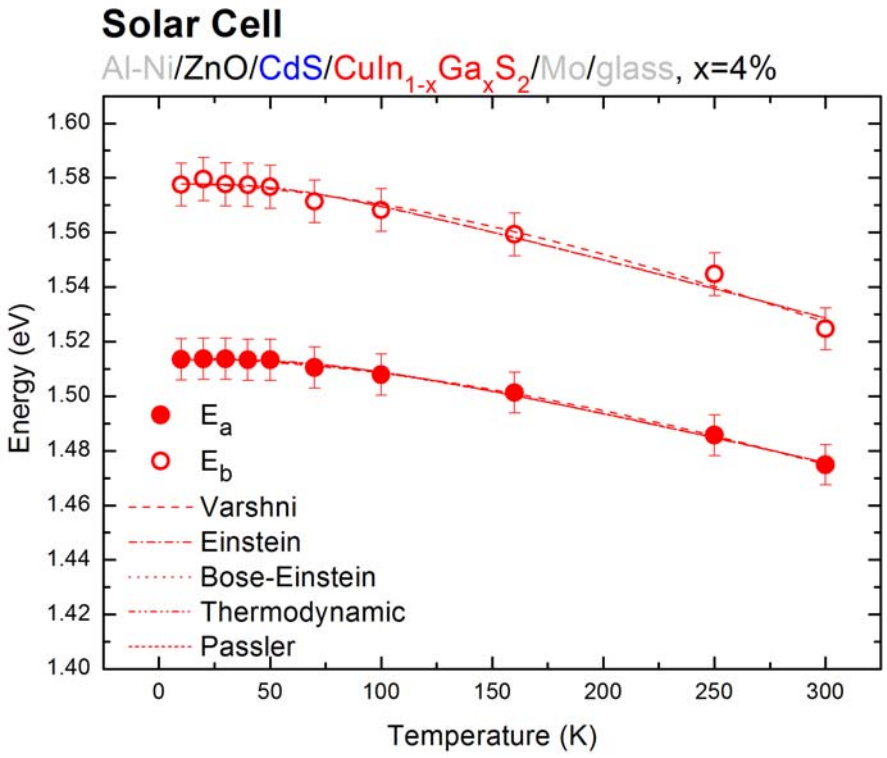

Figure 6.100 E_a and E_b band gap energies in dependence of temperature of $CuIn_{1-x}Ga_xS_2$ quaternary polycrystalline absorber

The results of the bandgap dependence on temperature are discussed in the frame of the five models used for the fitting. The effective phonon temperature (Ξ: obtained by Einstein model (Eq.(2.20)), Θ_B: obtained by Bose-Einstein model (Eq.(2.21)), Θ: obtained by the Pässler model (Eq.(2.23))), is calculated to be 248K. Varshni parameters a and b are very close to those (a=4.3 10^{-4} eV/K, and b=231.54K) published elsewhere [6.109] for $CuInS_2$.

The electron-phonon coupling parameter S, obtained by Eq.(2.22), ranges from 1.131 to 1.257. Further, from Eq.(6.3) the ratio $-\left[\frac{dE_g}{dT}\right]_{\max}$ can be calculated and compared to the parameters K/Ξ and δ, for the magnitude of the limiting slope and $\frac{\langle \hbar \cdot \omega \rangle}{k_B} = \Xi = \Theta = \Theta_B$ for the effective phonon temperature. Comparing the parameter values listed in Table 6.12, it is concluded that within deviations of max. 3%, the theoretical relations are fulfilled.

The calculated value of $-(dE_g/dT)_{max}$ is also listed in Table 6.12 and is close to the parameter δ obtained by the Pässler model. Assuming that mobility μ is determined by lattice scattering, its value can be expressed by Eq.(6.4).

The hole mobility was calculated at Room Temperature (T=300K). In the calculation the effective hole mass of the ternary $CuInS_2$ $m_h^* = 1.3 \cdot m_e$ [6.110] was used. The hole mobility was calculated in the range from 37.96 to 43.79 cm^2/Vs.

At room temperature, six optical phonon modes in $CuIn_{1-x}Ga_xS_2$, with x=0.04, have been reported [6.111] by means of Raman spectroscopy. The frequencies of these modes vary: for $CuGaS_2$, from the lowest value at 95cm^{-1} (12meV) referring to the E_{TO} mode up to the highest value at 355cm^{-1} (44meV), whereas for $CuInS_2$, from 63cm^{-1} (8meV) to 292cm^{-1} (36meV). From fitting with the Pässler model, effective phonon energies $\langle \hbar\omega \rangle$ have been calculated to be 21.4 and 15meV.

		Varshni			Einstein			Bose-Einstein				Thermodynamic			Pässler				$-\left[\frac{dE_g}{dT}\right]_{max}$	$\frac{\langle \hbar \cdot \omega \rangle}{k_B}$
		$E_g(0)$ (eV)	a (meV/K)	b (K)	$E_g(0)$ (eV)	K (meV)	Ξ (K)	E_B (eV)	a_B (meV)	Θ_B (K)	$E_g(0)=E_B-a_B$ (eV)	$E_g(0)$ (eV)	S	$\langle \hbar \cdot \omega \rangle$ (meV)	$E_g(0)$ (eV)	δ (meV/K)	Θ (K)	p	(meV/K)	(K)
$CuIn_{1-x}Ga_xS_2$	E_a	1.514	0.428	690	1.513	48	248	1.537	24	248	1.513	1.513	1.131	21.4	1.514	0.201	248	2.35	0.195	248
	E_b	1.578	0.438	475	1.578	39	174	1.597	19	174	1.578	1.578	1.257	15.0	1.578	0.225	178	2.25	0.217	174
CdS	E_a	2.542	0.184	217	2.541	35	227	2.559	18	228	2.541	2.541	1.548	19.1	2.541	0.156	242	1.95	0.267	222
ZnO	E_a	3.422	1.048	544	3.415	89	538	3.698	0.283	538	3.415	3.415	6.118	46.5	3.417	1.139	537	2.69	1.054	539

Table 6.12 Fitting parameters of the E_a, and E_b bandgap energies of the $CuIn_{1-x}Ga_xS_2$ absorber (x=0.04), the CdS buffer layer and the ZnO window layer with five different models: Varshni, Einstein, Bose-Einstein, Thermodynamic, and Pässler

The number of holes N or density of states can be calculated using Eq. (6.24) [6.112]:

$$N = \int_0^{\Delta E} dn = \frac{8\pi}{h^3}\frac{2\sqrt{2}}{3} m_{VC}^{*\,3/2} \Delta E^{3/2} \tag{6.24}$$

where n is the number of free electrons in cm^{-3}, $m_{VC}^{*} = \frac{m_h^* m_e^*}{m_h^* + m_e^*}$ is the reduced effective mass of an electron with effective mass m_e^* and a hole with effective mass m_h^*, ΔE is the shift of the energy band edge. In this expression, the electron-defect and electron-electron interaction are neglected.

Considering only the lower energy gap E_a of the quaternary $CuIn_{1-x}Ga_xS_2$ (CIGS) compound, ΔE represents the energy shift between the band edge of the quaternary and the edge of the ternary $CuInS_2$ (CIS) compound,

$$\Delta E = \Delta E_a = E_a^{CIGS} - E_a^{CIS} \tag{6.25}$$

In the calculation of the carrier concentration, the effective masses of electrons and holes of $CuInS_2$, $m_e^*=0.03m_e$ [6.113] and $m_h^*=1.3m_e$ [6.110], respectively, were used, since the electron and hole effective masses of the quaternary compound are not known. The E_a band gap of $CuInS_2$ is known to be 1.5eV [6.6]. Starting with Eq.(6.24) via Eq.(6.25), a carrier concentration $N=1.52\ 10^{18}/cm^3$ was calculated.

Ga addition in the absorber layer followed by Ga accumulation at the interface to the Mo/glass substrate [6.114] as well as lattice mismatch between the different layers, in the thin film solar cell, could lead to strain development in the quaternary chalcopyrite $CuIn_{1-x}Ga_xS_2$ absorber. Strain/stress evaluation is accomplished according to the relationships described in §3.2.3. Strain ε_{zz} is obtained by Eq.(3.16), using the experimentally obtained values of E_a and E_b of the quaternary $CuIn_{1-x}Ga_xS_2$ (strained layer) and the values of E_a and E_b band gap energies of the bulk $CuInS_2$ (unstrained) reported in [6.6]. In the calculation, also the elastic stiffnesses of $CuInS_2$ C_{11}=83.7GPa and C_{12}=54.4GPa [6.115] were used, because those of the quaternary compound are not reported in the literature. In addition, for the shear deformation potentials b of all I–III–VI_2 compounds and alloys, appropriate values have been reported according to Eqs.(6.8) and (6.9). Shay and Tell have estimated, for $CuInS_2$, a 45% *d*-character in the *p-d*

hybridization, which, according to Eqs.(6.8) and (6.9), yields a shear deformation potential of b=-2.375eV.

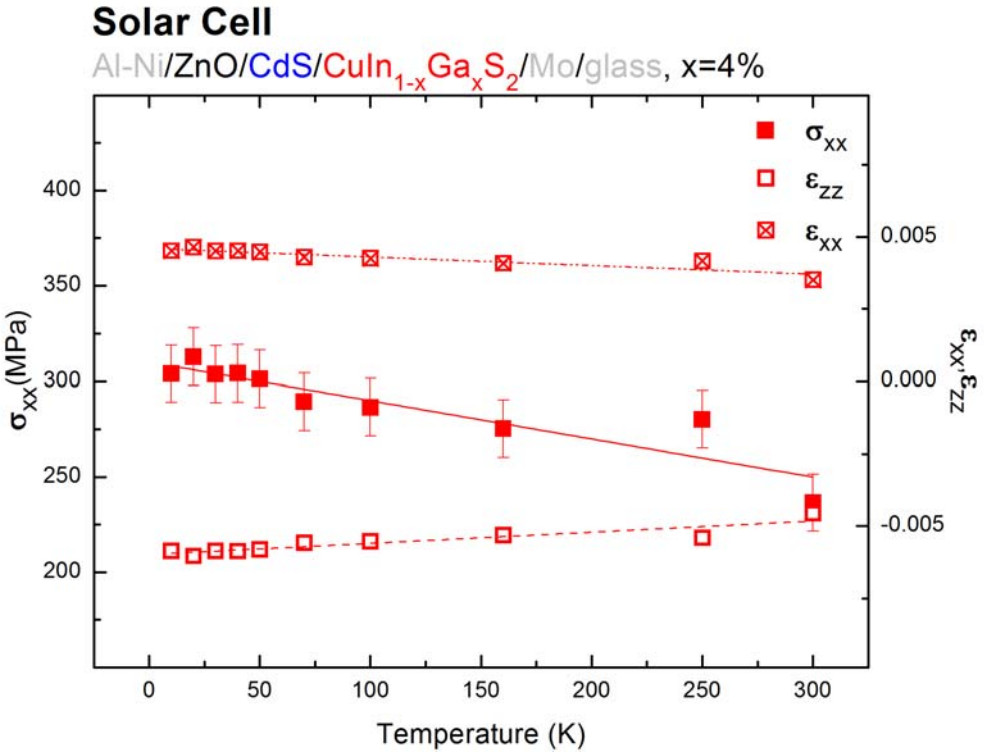

Figure 6.101 Temperature dependence of the strains ε_{xx} and ε_{zz}, and stress σ_{xx} of a thin film solar cell with quaternary $CuIn_{1-x}Ga_xS_2$ absorber compound with x=0.04.

Strains ε_{xx} and ε_{zz} along with stress σ_{xx} in dependence of temperature are shown in Figure 6.101. The stress varies from 236MPa at RT to 304MPa at 10K. The positive sign depicts tensile stress. Stress seems to decrease with the increase of temperature with a rate of 0.2MPa/K. According to previously mentioned theoretical models, the chalcopyrite compound should appear to be strain/stress free at growth temperature. However, this is not the case here. A possible reason is the origin of the stress that develops in the absorber layer. The stress can be partially attributed to the lattice mismatch between the substrate (Mo) and the chalcopyrite and partially to the additional Ga in the $CuInS_2$ structure.

Depending on the growth mechanism, regions within the chalcopyrite compound exhibit differences in the distribution of gallium across the film. This has been confirmed by energy dispersive x-ray fluorescence (EDX) and x-ray diffraction (XRD) studies of the same films reported elsewhere [6.116]. The $CuIn_{1-x}Ga_xS_2$ compound with x = 0.04,

grown from the Cu-free precursor, though it exhibits good film properties, has inevitably a strong gradient in the Ga distribution perpendicular to the substrate.

The study of the kinetics of film formation in a two-step process shows that the gallium concentration is high close to the back contact and decreases towards the film surface [6.116]. This leads to differently distribution of Ga which can be can be split to a 'Ga-rich' and a 'Ga-poor' region of the absorber layers. The Ga distribution in the absorber layer, forming a 'Ga-rich' and a 'Ga-poor' region, could lead to additional strain due to the lattice mismatch between the two sub-regions.

6.10.2.2 The CdS buffer layer

The band gap energy of the buffer layer of the solar cell was also recorded using ER. Evaluation of the band gap was not possible at all temperatures, mostly because, the peak corresponding to the band gap of CdS was shadowed by the intense peak of ZnO. However, the CdS band gap could be evaluated at low (10, 20, 30, 40, 50, and 70K) and near room temperature (250 and 300K). The results of the evaluation are presented in Figure 6.102.

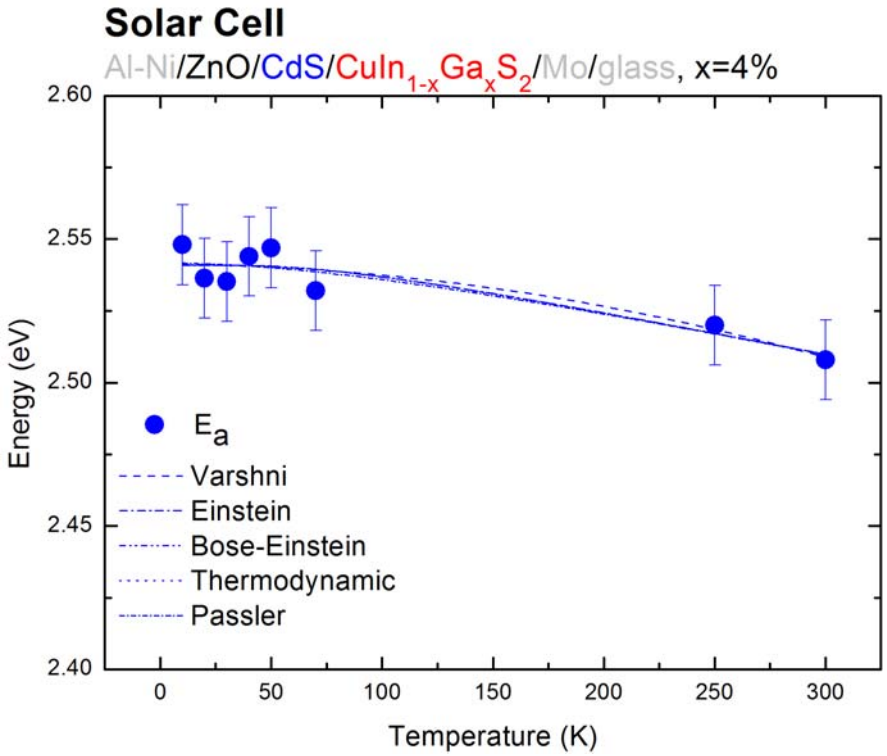

Figure 6.102 CdS band gap of a ZnO/CdS/CuInGaS$_2$/Mo/glass solar cell heterostructure in dependence of temperature

The band gap energy of the CdS-buffer layer, at RT, as measured by ER, was 2.508eV, which is lower than the reported value 2.517eV [6.117]. The shift of the CdS band gap to lower energy reveals that the buffer layers deposited on top of the absorber layer is strained. The lattice constant of CdS (a_{CdS} = 4.14 A° [6.118]) is much smaller than the lattice constant of the $CuIn_{1-x}Ga_xS2$ absorber studied (a_{CIGS}=5.5094Å for x = 0.04 [6.119]). CdS layer exhibits, therefore, tensile stress. It is well known that under the influence of tensile stress, the band-gap is narrowed [6.120].

6.10.2.3 The ZnO Window layer

The band gap energy of the ZnO window layer was also determined using ER. The energy gap in dependence of the temperature is shown in Figure 6.103. The experimental data were fitted with the five different models, described in §2.1.3.2. The results of the fitting are demonstrated in Table 6.12.

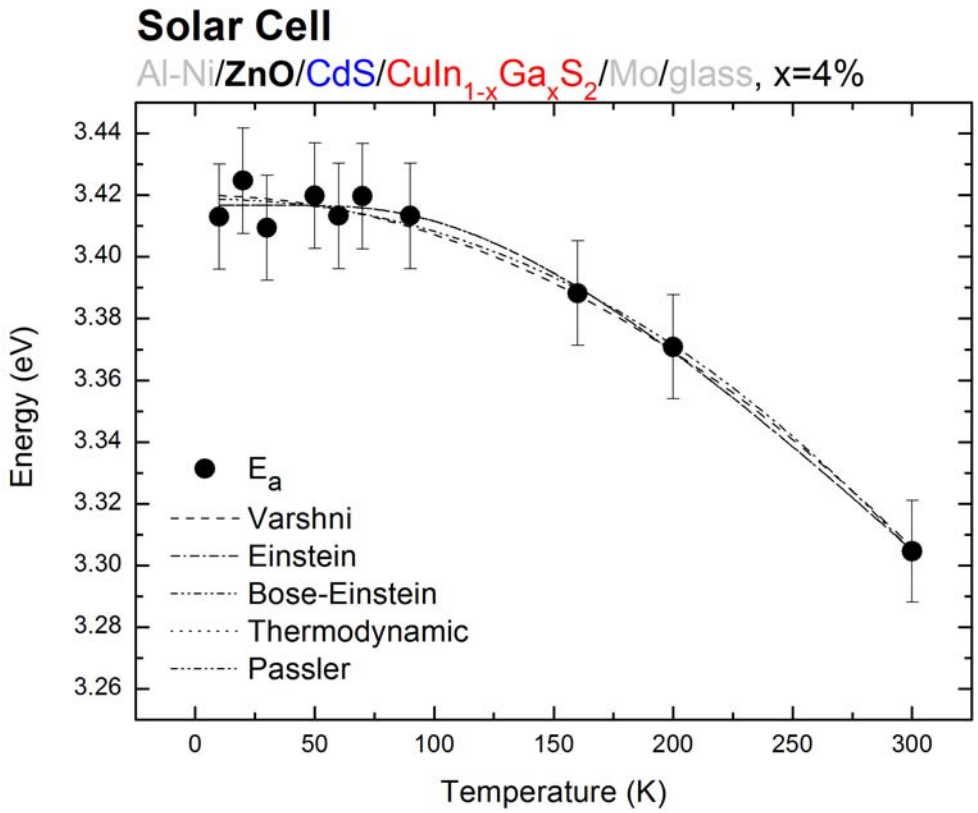

Figure 6.103 ZnO band gap of a ZnO/CdS/CuInGaS$_2$/Mo/glass solar cell in dependence of temperature

At room temperature, four optical phonon modes in ZnO have been reported [6.86] by means of Raman spectroscopy. The frequencies of these modes vary from the lowest value at 380cm^{-1} (47meV) referring to the A_1(TO) mode up to the highest value at 587cm^{-1} (72meV). From fitting with Pässler model, effective phonon energy $\langle \hbar\omega \rangle$ has been calculated to be 46.5meV and is in total agreement with the A_1(TO) mode of ZnO reported elsewhere [6.86].

7. Conclusions

This PhD thesis focuses on:

A. the investigation of the structural and optical properties of chalcopyrite semiconductors used as absorbers in the photovoltaic technology
B. the growth and investigation of structural and optical properties of ZnSe buffer layers used alternatively instead of the toxic CdS

The single crystal chalcopyrite absorbers were grown by Chemical Vapor Transport (CVT) and were provided by the Technical University of Berlin. The epitaxial chalcopyrite layers were grown by Metal-Organic Vapor Phase Epitaxy (MOVPE) and the polycrystalline chalcopyrite thin films by Physical Vapor Deposition (PVD), at the Helmholtz-Centre Berlin for Materials and Energy.

The polycrystalline ZnSe buffer layers were grown by CBD, at the National Technical University of Athens, in the frame of the present work.

The structural properties of the ternary chalcopyrites were investigated by X-Ray Diffraction (XRD) and micro-Raman Spectroscopy. The dominant orientation of the $CuGaSe_2$ epitaxial layers is the [008] and appears at $2\theta = 65.83^o$, whereas for the $CuGaSe_2$ polycrystalline layers is the [112] and appears at $2\theta = 27.67^o$. It has been observed that the orientation of both, the epitaxial and the polycrystalline layers, does not depend on the Ga fraction. Furthermore, the epitaxial layers with [Cu]/[Ga] near stoichiometry are of better quality, a fact that is depicted by the decrease of FWHM and the intensity increase of both, the XRD- and the Raman-spectra. For very Cu-rich chalcopyrites, the crystal quality decreases drastically. Analog to the previous, it is found that the crystal quality of the polycrystalline $CuGaSe_2$ chalcopyrites decreases for Ga-rich absorbers.

The structural and optical properties of ternary ($CuGaSe_2$, $CuInSe_2$, $CuGaS_2$, $CuInS_2$) and quaternary ($CuIn_{1-x}Ga_xSe_2$) chalcopyrite single crystals and epitaxial layers were analyzed in detail by Modulated Reflectance Spectroscopy. Mismatch strains in the epitaxial layers have been quantified. Energy shifts due to anion and/or cation replacement and to the temperature dependence of transition energies in the ternary and quaternary alloys have been exploited. Light polarization has been used to reinforce the selection rules of the optical transitions.

The band gap of ternary chalcopyrite semiconductors, bulk and epitaxially grown selenides $CuInSe_2$ and $CuGaSe_2$, has been studied over a wide temperature range, from room temperature (300K) down to 10K. Energies and widths of the E_a, E_b, and E_c bands have been determined. The non-cubic crystal field and the spin-orbit interaction have been calculated. The results indicate s-shaped temperature dependence below 100K, most pronounced in $CuGaSe_2$ epitaxial layers, and anomalous temperature dependence below 50K, in $CuInSe_2$. Based on the calculation of admixture coefficients, the latter is attributed to the predominant d-character of p-d hybridization of the upper valence band. Besides, the results of the present study point to significantly different temperature dependence of the E_a, E_b, and E_c bands of single crystals and epitaxial layers, which is attributed to structural differences inclusive the incorporation of defects and symmetry breaking. They also point to significantly different temperature dependence of the E_a, E_b, and E_c bands within one and the same kind of material with respect to its bulk or layered structure, which is associated with different electron-phonon coupling mechanisms dominating electronic transitions at temperatures below 100 K, differences in the spin-orbit interaction, and evolution of strain fields in the layers. The experimental results are fitted with 6 different models and important transport properties are calculated, among them minority carrier (hole) mobility. Average phonon frequencies are obtained within the frame of the Varshni, Bose-Einstein, Einstein, thermodynamic, and the Manoogian models and phonon mode assignment is attempted based on the results of this study and also the results of Photoluminescence and Raman studies known from the literature. For the epitaxially on GaAs(001) grown $CuInSe_2$ and $CuGaSe_2$ layers, the shear deformation potential is calculated. Strain/stress effects originating from mismatch- and thermal-strain between substrate and epilayer are quantified and are discussed extensively. A

temperature for full strain relaxation is calculated, which is in total agreement with the temperature of epitaxial layer growth.

The compositional dependence of the optical properties (transition energies) of ternary chalcopyrite absorbers was studied. Complementary to this work, the compositional dependence of quaternary $CuIn_{1-x}Ga_xSe_2$ chalcopyrite absorbers was also studied. The optical functions and the energies of the fundamental band-gaps of $CuIn_{1-x}Ga_xSe_2$ (CIGS) epitaxial layers for solar energy conversion applications have been determined in a wide compositional range (x=0.00-1.00).

Polycrystalline ZnSe buffer layers grown by EBE, in the frame of a PhD-thesis within the work-group of Assist. Prof. Dr. Dimitra Papadimitriou, Supervisor of the present thesis, are reviewed for comparison reasons. The layers were deposited initially on glass, to control the growth procedure and the critical parameter of the layer thickness. Afterwards, ZnSe buffer layers were deposited on chalcopyrite substrate. The solar cell was completed by deposition of ZnO window layer and Al front ohmic contact. Structural and optical characterization of both, ZnSe/glass and ZnSe/$CuGaSe_2$/Mo/glass, was performed by XRD, SEM, AFM, Raman, PR, and null-ellipsometry.

EBE ZnSe on glass: According to the results of structural analysis, the films are polycrystalline, cubic with (111) faces. Films deposited at higher temperatures show improved crystal quality: they consist of larger size crystallites, have better homogeneity, smoother surfaces, and cover uniformly the underlying glass substrate. According to the results of optical analysis, there might be a certain degree of contamination at the film-substrate interface through incorporation of particles from the glass substrate at higher temperatures.

EBE ZnSe on $CuGaSe_2$/Mo/glass: According to the results of the structural investigation, the films are polycrystalline with (111) oriented smooth surfaces, highly homogenous, and cover uniformly the underlying chalcopyrite layer. The films exhibit moderate stresses lower than 1 GPa that can be reduced by optimization of the deposition process. The optical film properties as determined by Null-Ellipsometry and PR spectroscopy yield n=2.580, the refractive index, $\alpha=6.2x10^3$ cm^{-1}, the absorption

coefficient, and E_g=2.69 eV, the energy band gap. The film thickness measured in-situ by crystal monitor detector and ex-situ by Null-Ellipsometry is in the range 75-85 nm.

Polycrystalline ZnSe buffer layers were grown, in the frame of the present PhD-thesis, by low-cost, large-area, fast deposition-rate CBD. The layers were deposited initially on glass, to control the growth procedure and the critical parameter of the layer thickness. Afterwards, ZnSe buffer layers were deposited on both, epitaxial and polycrystalline chalcopyrite substrates. The cells were completed by deposition of ZnO window layer and Al front ohmic contact.

CBD ZnSe on glass: According to the results of structural analysis, the films are polycrystalline, hexagonal with (101) faces. After deposition, subsequent annealing of the samples was necessary to improve crystal quality. The annealed layers consist of larger size crystallites. According to optical measurements, the band gap of the layers is not significantly affected by deposition time and/or annealing temperature. Film thickness calibration on deposition time has been successfully performed.

CBD ZnSe on epitaxial-$CuGaSe_2$/GaAs: After deposition and subsequent annealing of the samples to improve crystal quality, structural analysis of the ZnSe layers was performed. The layers are non-stoichiometric, polycrystalline, hexagonal with (101) faces. Stoichiometry and crystallite sizes depend strongly on deposition and annealing time. Annealing at 300 ^{o}C for 2 h was found to meet the requirements of best film quality. A film thickness calibration curve was established for ZnSe on epitaxial chalcopyrite.

CBD ZnSe on polycrystalline-chalcopyrite/Mo/glass: The same procedure as described above has been followed to deposit ZnSe on polycrystalline chalcopyrite substrates. A thickness calibration curve was established for ZnSe on polycrystalline chalcopyrite.

PLD ZnO on ZnSe/polycrystalline-chalcopyrite/Mo/glass: ZnO was deposited on ZnSe/polycrystalline-chalcopyrite/Mo/glass by Pulsed Laser Deposition (PLD) to obtain an integrated solar cell. The deposited ZnO is polycrystalline, hexagonal, oriented along (002).

ECD ZnO on ZnSe/polycrystalline-chalcopyrite/Mo/glass: ZnO was electrochemically deposited on ZnSe/CIGS-polycrystalline-chalcopyrite on Mo coated glass substrate. Prior to deposition on ZnSe/CIGS, ZnO was deposited by ECD on Mo/glass substrates to control the deposition parameters. The ECD ZnO on ZnSe/Cu(In,Ga)Se_2/Mo-glass is grown oriented along the (101) crystallographic plane in coherency with the underlying ZnSe-buffer.

ZnO NRs: Vertical high quality ZnO nanorods (NRs) have been deposited from an aqueous solution of $Zn(NO_3)_2$ and HNO_3 or NH_4NO_3, at 75°C, on glass substrates coated by TCO layer and ZnO window-layer of solar cells. The structural properties of the ZnO NRs have been studied by X-ray Diffraction (XRD) and microscopy techniques (SEM and AFM). The optical properties have been investigated by Transmittance and Optical Modulation (Photoreflectance) Spectroscopy. The energy band gap of the structures has been determined directly from the PR-spectra. The decrease of the global reflectance of the solar cells has been achieved by using ZnO nanorods as an antireflective coating (ARC) based on the moth-eye effect. The ZnO NRs ARC boosts the solar cells short-circuit current without significant effect on their open-circuit voltage and fill factor. Variation of the band-gap by varying the conditions of growth is foreseen.

Electrical Characterization: On the above mentioned thin film solar cells, electrical measurements were performed (i.e. I-V characteristics) using the Sun Simulator at the Center for Renewable Energy Sources and Saving (CRES).

For Al/In:ZnO/i-ZnO/ZnSe/Chalcopyrite/Mo/glass heterocells, with ZnSe buffer- and ZnO window-layer processed by CBD and PLD techniques, the I-V characteristics of the p-n junctions were systematically recorded.

A solar cell based on PVD grown ternary chalcopyrite absorber $CuIn_{0.96}Ga_{0.04}Se_2$ with CBD ZnSe buffer-layer and ECD ZnO window-layer processed by low-cost, large-area, fast-rate chemical and electrochemical deposition techniques yielded conversion efficiency η=5% (ff=52.5%) which makes low cost – best efficiency TFSCs quite attractive for further development inclusive ECD processing of the chalcopyrite absorber.

Chalcopyrite TFSCs were also characterised by Electroreflectance Spectroscopy techniques in dependence of temperature. The energy gaps of absorber-, buffer-, and window-layer have been measured and strain/stress effects have been quantified.

8. References

8.1 Chapter 1

[1.1] United Nations Development Program (UNDP) World Energy Assessment, New York (2000)

[1.2] D. Chapin, C. Fuller, G. Pearson, J. Appl. Phys. 25, (1964), 676

[1.3] D. Jenny, J. Loferski, P. Rappaport, Phys. Rev. 101, (1956), 1208

[1.4] D. Cusano, Solid State Electron. 6, (1963), 217

[1.5] J. Lindmayer, J. Allsion, COMSAT Tech. Rev. 3, (1973), 1

[1.6] S. M. Sze, Physics of Semiconductor Devices, Willey-Interscience 2nd edition, New York (1981)

[1.7] D. A. Neaman, Semiconductor Physics and Devices: Basic Principles, Irwin-McGraw-Hill 2nd edition, USA (1997)

[1.8] J. Zhao, A. Wang, M. A. Green, Prog. in Photovolt. 7, (1999), 471

[1.9] http://www.nrel.gov/pv/thin_film/docs/kaz_best_research_cells.ppt

[1.*10*] S. Wagner, J. L. Shay, P. P. Migliorato, H. M. Kasper, *Appl. Phys. Lett. 25, (1974) 434*

[1.11] L. L. Kazmerski, F. R. White, G. K. Morgan, Appl. Phys. Lett. 46 (1976) 268

[1.12] K. L. Copra, P. D. Paulson, V. Dutta, Prog. Photovolt: Res. Appl. 12 (2004) 69

[1.13] T. Nakada, T. Kume, T. Mise, A. Kunioka, Jap. J. Appl. Phys. 37, (1998), L499

[1.14] Jackson P, Hariskos D, Lotter E, Paetel S, Wuerz R, Menner R, Wischmann W and Powalla M 2011 New world record efficiency for Cu(In,Ga)Se_2 thin-film solar cells beyond 20% . Photovolt.: Res. Appl. DOI: 10.1002/pip.1078

[1.15] K. Ramanathan, M. A. Contreras et. al. Prog. Photovolt. Res. Appl. 11, (2003) 225

[1.16] K. Siemer, J. Klaer, I. Luck, J. Burns, R. Klenk, D. Braeunig, Solar Energy Materials and Solar Cells 67 (1-4), (2001) 159

[1.17] N. Romero, A. Bosio, V. Canevari, M. Terheggen, R. L. Vaillant, Thin Solid Films 431-432, (2003) 364

[1.18] S. Major, A. Banerjee, K. L. Copra, Thin Solid Films 108(3), (1983) 333

8.2 Chapter 2

[2.1] J. L. Shay, J. H. Wernick, *Ternary chalcopyrite semiconductors: Growth, electronic properties, and applications, Pergamon Press, Oxford (1974)*

[2.2] J. L. Shay, E. Buehler, J. H. Wernick, Phys. Rev. Lett. 24, (1970) 1301

[2.3] M. I. Alonso, M. Garigga, C. A. Durante Ricon, E. Hernandez, M. Leon, Appl. Phys. A 74, (2002) 659

[2.4] F. W. Ohrendorf, H. Haeuseler, Cryst. Res. Technol. 34(3), (1999) 339

[2.5] H. Neumann, Cryst. Res. Technol. 39(11), (2004) 939

[2.6] H. Tanino, T. Maeda, H. Fujikake, H. Nakanishi, S. Endo, T. Irie. Phys. Rev. B 45(23), (1992) 13323

[2.7] J. Camassel, L. Artus, J. Pascual, Phys. Rev. B 41, (1990) 5717

[2.8] J. Gonzalez, J. C. Chervin, Jpn. J. Appl. Phys. Suppl. 32-3, (1993) 575

[2.9] W. H. Koschel, M. Bettini, Phys. Stat. Sol. B 72, (1975) 729

[2.10] J. Gonzalez, B. J. Fernandez, Phys. Rev. B 46, (1992) 15092

[2.11] C. Ricon, F. J. Ramirez, J. Appl. Phys. 72(9), (1992) 4321

[2.12] M. I. Alonso, K. Wakita, J. Pascual, M. Garrriga, N. Yamamoto, Phys. Rev. B 63, (2001) 075203-1

[2.13] M. Cardona, Modulation Spectroscopy, Academic Press, New York (1969)

[2.14] H. Kuzmany, Solid-State Spectroscopy: An Introduction, Springer-Verlag, Berlin (1998)

[2.15] J. E. Jaffe, A. Zunger, Phys. Rev. B 28(10), (1983) 5822

[2.16] T. Kawashima, S. Adachi, H. Miyake, and K. Sugiyama, "Optical constants of CuGaSe[sub 2] and CuInSe[sub 2]," Journal of Applied Physics, vol. 84, 1998, p. 5202

[2.17] H.Y. Fan, Phys. Rev. 82, (1951) 900

[2.18] P.B. Allen and V. Heine, J. Phys. C: Sol. St. Phys. 9, (1976) 2305-2312

[2.19] Y.P. Varshni, Physica 34, (1967) 149 – 154

[2.20] A. Meeder, A. J ger-Waldau, V. Tezlevan, E. Arushanov, T. Schedel-Niedrig, and M.C. Lux-Steiner, "Temperature dependence of the exciton gap in monocrystalline $CuGaSe_2$," Journal of Physics: Condensed Matter, vol. 15, Sep. 2003, pp. 6219-6227

[2.21] S. Logothetidis, M. Cardona, P. Lautenschlager, M. Garriga, Phys. Rev. B 34, (1986) 2458–2469

[2.22] K.P. O'Donnell, X. Chen, Appl. Phys. Let. 58, (1991) 2924

[2.23] R. Pässler, Phys. Stat. Sol. B 200, (1997) 155

[2.24] A. Manoogian, J. Woolley, Can. J. Phys. 62, (1984) 285-287

[2.25] S. Guha, Q. Cai, M. Chandrasekhar, H.R. Chandrasekhar, H. Kim, A.D. Alvarenga, R. Vogelgesang, A.K. Ramdas, M.R. Melloch, Phys. Rev. B 58, (1998) 7222-7229.

[2.26] P. Yu, Sol. St. Com. 13, (1973) 1883-1887.

[2.27] L. Artus, Y. Bertrand, Sol. St. Com. 61, (1987) 733-736.

[2.28] I. Choi, S. Eom, P. Yu, Phys. Stat. Sol. B 215, (1999) 99-104.

[2.29] T. Hsu and J. Lin, Phys. Rev. B 37, (1988) 4106-4110.

[2.30] M.V. Yakushev, A.V. Mudryi, I.V. Victorov, J. Krustok, E. Mellikov, Appl. Phys. Let. 88, (2006) 011922.

[2.31] H.Y.Xu, D. Papadimitriou, L. Zoumpoulakis, J. Simitzis, M. Lux-Steiner, J. Phys D: Appl. Phys. 41, (2008), 165102

[2.32] C. Rincon, E. Hernández, S.M. Wasim, I. Molina, J. Phys. Chem. Sol. 59, (1998) 1015-1019.

[2.33] J. Shay, H. Kasper, Phys. Rev. Let. 29, (1972) 1162-1164.

[2.34] J.E. Jaffe, A. Zunger, Physical Review B 29, (1984) 1882–1906.

[2.35] J. Serrano, C. Schweitzer, C. Lin, K. Reimann, M. Cardona, D. Fröhlich, Phys. Rev. B 65, (2002) 1-7.

[2.36] J. E. Jaffe, A. Zunger, Phys. Rev. B 27(8), (1983) 5176

[2.37] J. E. Jaffe, A. Zunger, Phys. Rev B 29(4), (1984) 1882

[2.38] C-Y Yeh, Z. W. Lu, S. Froyen, A. Zunger, Phys. Rev. B 46(16), (1992) 10086

[2.39] B. K. Agrawal, P. S. Yadav, S. Agrawal, Phys. Rev. B 50(20), (1994) 14881

[2.40] S. Adachi, T. Taguchi, Phys. Rev. B 43(12), (1991) 9569

[2.41] J. E. Bernard, A. Zunger, Phys. Rev. B 36(6), (1987) 3199

[2.42] J. R. Chelikowsky, M. L. Cohen, Phys. Rev. B 14, (1976) 556

[2.43] J. C. Phillips, Bonds and Bands in Semiconductors, Academic, New York, 1973.

[2.44] D. R. Lide (Ed.), CRC Handbook of Chemistry and Physics, 73rd Edition, CRC Press, New York, 1992.

[2.45] U. Özgür, Y. I. Alivov, C. Liu, A. Teke, M. A. Reshchikov, S. Do˘uan, V. Avrutin, S. J. Cho, H. Morkoç, J. Appl. Phys. 98 (2005) 041301.

[2.46] B. K. Meyer, H. Alves, D. M. Hofmann, W. Kriegseis, D. Forster, F. Bertram, J. Christen, A. Hoffmann, M. Straßburg, M. Dworzak, U. Haboeck, A. V. Rodina, Phys. Stat. Sol. (b) 241 (2004) 231.

[2.47] D. Vogel, P. Krüger, J. Pollmann, Phys. Rev. B 52 (1995) R14316.

[2.48] Ozaki, S., Mishima, T., Adachi, S.: Photoreflectance Spectroscopy of ZnO for Ordinary and Extraordinary Rays. Jpn. J. Appl. Phys. 42, 5465-5471(2003)

[2.49] Meyer, B.K., Alves, H., Hofmann, D.F., Kriegseis, W., Forster, D., Bertram, F., Christen, J., Hofmann, A., Strassburg, M., Dworzak, M., Haboeck, U., Rodina, A.V.: Bound exciton and donor–acceptor pair recombinations in ZnO. Phys. Stat. Sol. (b) 241, 231-260 (2004)

[2.50] Birman, J.L.: Polarization of Fluorescence in CdS and ZnS crystals. Phys. Rev. Lett. 4, 157-159 (1959)

[2.51] Thomas, D., Hopfield, J.J.: Exciton Spectrum of Cadmium Sulfide. Phys. Rev. 116, 573-582 (1959)

[2.52]Thomas, D.: Theoretical and Experimental Effects of Spatial Dispersion on the Optical Properties of Crystals. J. Phys. Chem. Sol. 15, 97 (1960)

8.3 Chapter 3

[3.1] I. Repins, A. Contreras, B. Egaas, C. DeHart, J. Scharf, C. Perkins, B. To, R. Noufi, Prog. Photovoltaics: Res. Appl. 16, (2008) 235

[3.2] J. Abusharma, R. Noufi, S. Johnston, S. Ward, X. Wu, 31st IEEE Photov. Spec. Conf. and Exib. (2005) Florida

[3.3] R. Herberholz, V. Nadenau, U. Ruehl, C. Koeble, H. W. Schock, B. Dimmler, Sol. Energy Mater. Sol. Cells 49, (1997) 227-237

[3.4] S-H. Wei, A. Zunger, Appl. Phys. Lett. 63, (1993) 2549-2551

[3.5] A. Hofmann and C. Pettenkofer, "Surface orientation dependent band alignment for $CuInSe_2$–ZnSe–ZnO," Applied Physics Letters, vol. 98, 2011, p. 113503.

[3.6] S. M. Hu, J. Appl. Phys. 70, (1991) R53-R80

[3.7] J. F. Nye, Physical properties of crystals, Oxford: Claredon

[3.8] E. Anastasakis and M. Cardona, High Pressure in Semiconductor Physics II. Semiconductors and Semimetals vol. 55, (1998), New York: Academic

[3.9] J.L. Shay, J.H. Wernick, Ternary Chalcopyrite Semiconductors: Growth, Electronic properties and Applications, (1975) Oxford: Pergamon Press

[3.10] Noyan I and Cohen J 1987 Residual Stress: Measurement by Diffraction and Interpretation (Springer-Verlag: New York Berlin Heidelberg) p 117

[3.11] Chichibu S, Mizutani T, Murakami K, Shioda T, Kurafuji T, Nakanishi H, Niki S, Fons P J and Yamada A 1998 Band gap energies of bulk, thin-film, and epitaxial layers of $CuInSe_2$ and $CuGaSe_2$ J. Appl. Phys. 83 3678-3689

[3.12] H. Asai, K. Oe, J. Appl. Phys. 54, (1983) 20520-2056

[3.13] J. H. Chen, W. S. Chi, Y. S. Huang, Y. Yin, F. Pollak, G. D. Pettit, J. M. Woodall, Semicond. Sci. Technol. 8 (1993) 1420-1425

[3.14] Y. Harada, H. Nakanishi, S. Chichibu, J. Appl. Phys. 91, (2002) 5909-5914

8.4 Chapter 4

[4.1] T. F. Ciszek, J. Cryst. Growth 70 (1984) 405-410

[4.2] A. Bauknecht, Dissertation: CuGaSe2 fuer die anwendung in der photovoltaik (1999) Freie Universitaet Berlin

[4.3] U. Fiedeler, Dissertation: Rekombination und Diffusion in CuGaSe2 – Solarzellen (2001) Freie Universitaet Berlin

[4.4] N. Rega, S. Siebentritt, I. Beckers, J. Beckmann, J. Albert, M-Ch. Lux-Steiner, J. Cryst. Growth 248 (2003) 169-174

[4.5] A. Bauknecht, S. Siebentritt, J. Albert, and M-Ch. Lux-Steiner, J. Appl. Phys. 89 (2001) 4391-400

[4.6] N. G. Dhere, R. G. Dhere, J. Vac. Sci. Tech. A 23 (2005) 1208-1214

[4.7] D. Hariskos, S. Spiering, M. Powlla, Th. Sol. Films 480-481 (2005) 99-109

[4.8] J. M. Dona, and J. Herrero, J. Electrochem. Soc. 142-3 (1995) 764-770

[4.9] O. Savadogo, Sol. Energ. Mater. Sol. Cells 52 (1998) 361

[4.10] J. M. Dona, J. Herrero, J. Electrochem. Soc. 144 (1997) 4081

[4.11] R. Ortega-Borges, D. Lincot, J. Electrochem. Soc. 140 (1993) 3464

[4.12] A. M. Chaparro, M. T. Gutierrez, J. Herrero, Electrochemica Acta 47 (2001) 977

*[4.13] Postels, B., Bakin, A., Wehman, H.-H., Suleiman, M., Weimann, T., Hinze, D., Waag, A. Appl. Phys. A **91**, 595–599 (2008)*

*[4.14] Chen, J., Aé, L., Aichele, Ch., Lux-Steiner, M.-Ch. Appl. Phys. Let. **92**, 161906 (2008)*

*[4.15] Tang, Y., Chen, J., Greiner, D., Ae, L., Baier, R., Lehmann, J., Sadewasser, S., Lux-Steiner, M.-Ch., J. Phys. Chem. C **115**, 5239-5243 (2011)*

8.5 Chapter 5

[5.1] C. Kittel, Introduction to Solid State Physics.

[5.2] G. R. Wilkinson, Raman spectra of solids in Molecular spectroscopy, (1975) Chemical Society, London

[5.3] P. Bruesch, Phonons theory and experiments, Vol. I and II, (1983) Springer-Verlag, Heidelberg

[5.4] M. Cardona, and G. Guentherodt, Light scattering in solids II, (1982) Springer-Verlag, Berlin

[5.5] R. M. Martin, L. M. Falikov, Light scattering in solids I, (1983) Springer, Berlin

[5.6] M. Cardona, Modulation Spectroscopy, Academic Press, (1969) New York

[5.7] U. Rossow, and W. Richter, Optical characterization of epitaxial semiconductor layers by electromagnetic radiation, Springer-Berlin, (1995) Heidelberg

[5.8] D. E. Aspnes, Surf. Sci. 37, (1973) 418-442

[5.9] B. O. Seraphin, and N. Bottka, Phys. Rev. 139, (1965) A560-A565

[5.10] F. H. Pollak, Surf. Interf. Anal. 31, (2001) 938-953

[5.11] D. E. Aspnes, Handbook on Semiconductors, T. S. Moss, (1980) New York

[5.12] H. Shen, and M. Dutta, J. Appl. Phys. 78, (1995) 2151-2176

8.6 Chapter 6

[6.1] C. Xue, D. Papadimitriou, Y. S. Raptis, N. Esser, W. Richter, S. Siebentritt, and M. Ch. Lux-Steiner, J. Appl. Phys. 94 (2003) 4341-4347

[6.2] F. W. Ohrendorf, H. Haeuseler, Cryst. Res. Tech. 34 (1999) 339

[6.3] Xue C 2003 Structural and Optical Investigation of $CuGaSe_2$ Thin Films for Solar Cells Device Applications (Athens:Doctoral Thesis)

[6.4] Anastassakis E 1991 Light Scattering in Semiconductor Structures and Supperlattices (Plenum Press: New York)

[6.5] Pollak F H and Cardona M 1968 Piezo-Electroreflectance in Ge, GaAs, and Si. Phys. Rev. 172 816-837

[6.6] J. E. Jaffe, and A. Zunger, Phys. Rev. B 28, (1983) 5822-5847

[6.7] S. H. Wei, and A. Zunger J. Appl. Phys. 78, (1995) 3846-56

[6.8] Alonso M I, Garriga M, Durante Rincon C A, Hernandez E and Leon M 2002 Optical functions of chalcopyrite $CuGa_xIn_{1-x}Se_2$ alloys Appl. Phys. A 74 659-664

[6.9] Shay J L and Wernick J H 1975 Ternary chalcopyrite semiconductors: growth, electronic properties and applications (Pergamon Press: Oxford)

[6.10] Parlak C and Eryigit R 2006 Ab initio volume-dependent elastic and lattice dynamical properties of chalcopyrite $CuGaSe_2$ Phys. Rev. B 73 245217 1-10

[6.11] D. E. Aspnes, Surf. Sci. 37, (1973) 418-442

[6.12] S. Chichibu, T. Mizutani, K. Murakami, T. Shioda, T. Kurafuji, H. Nakanishi, S. Niki, P. J. Fons, and A. Yamada J. Appl. Phys. 83, (1998) 3678-89

[6.13] C. Xue, D. Papadimitriou, and N. Esser, Thin Solid Films 451-452, (2004) 189-92

[6.14] H. Y. Xu, D. Papadimitriou, L. Zoumpoulakis, J. Simitzis and M-Ch. Lux-Steiner, J. Phys. D: Appl. Phys. 41, (2008) 165102

[6.15] El-Nahass M M, Farag A A M and Soliman H S 2011 Optical absorption and dispersion characterizations of $CuGaSe_2$ thin films prepared by flash evaporation technique Optics Communications 284 2515–2522

[6.16] Deus P, Neumenn H, Kuhn G and Hinze B 1983 Low-temperature thermal expansion in $CuInSe_2$ Phys. Stat. Sol.(a) 80 205-209

[6.17] J. E. Jaffe, and A. Zunger, Phys. Rev. B 29, (1984) 1882-906

[6.18] J. S. Blakemore, J. Appl. Phys. 53, (1982) R123-R181

[6.19] V. Kumar, and B. Sastry, J. Phys. Chem. Solid 63, (2002) 107-112

[6.20] Harada Y, Nakanishi H and Chichibu SF 2002 Band gap energy bowing and residual strain in $CuAl(S_xSe_{1-x})_2$ chalcopyrite semiconductor epilayers grown by low-pressure metalorganic vapor phase epitaxy J. Appl.Phys. 91 5909-5914

[6.21] M. I. Alonso, M. Garriga, C. A. Durante Rincon, E. Hernandez, and M. Leon, Appl. Phys. A 74, (2002) 659-664

[6.22] S. Theodoropoulou, D. Papadimitriou, N. Rega, S. Siebentritt, and M.-Ch. Lux-Steiner, Thin Solid Films 511-512, (2006) 690-694

[6.23] Y. P. Varshni, Physica 34, (1967)149-154

[6.24] H. Neumann, W. Horig, and E. Reccius, Sol. Stat. Com. 27, (1978) 449-451

[6.25] C. Xue, D. Papadimitriou, Y. Raptis, N. Esser, W. Richter, S. Siebentritt, and M.-Ch. Lux-Steiner, J. Appl. Phys. 94, (2003) 4341-4347

[6.26] S. Shirakata, and H. Miyake. J. Phys. Chem. Sol. 64, (2003) 2021-2024

[6.27] S. Levcenko, N. Syrbu, V. Tezlevan, E. Arushanov, S. Doka-Yamigno, Th. Shedel-Niedrig, and M.-Ch. Lux-Steiner, J. Phys: Cond. Matter 19, (2007) 456222

[6.28] S. Shirakata, and S. Chichibu, J. Appl. Phys. 79, (1996) 2043-2054

[6.29] R. Pässler, "Basic model relations for temperature dependencies of fundamental energy gaps in semiconductors," physica status solidi (b), vol. 200, 1997, p. 155

[6.30] J.B. Caceres and C. Rincón, "Debye Temperature of $A^IB^{III}C^{VI}2$ Chalcopyrites and $CuB^{III}{}_3C^{VI}{}_5$ and $CuB^{III}{}_5C^{VI}{}_8$ Ordered Defect Compounds," Physica Status Solidi (B), vol. 234, Nov. 2002, pp. 541-552.

[6.31] A. Meeder, A. J ger-Waldau, V. Tezlevan, E. Arushanov, T. Schedel-Niedrig, and M.C. Lux-Steiner, "Temperature dependence of the exciton gap in monocrystalline $CuGaSe_2$," Journal of Physics: Condensed Matter, vol. 15, Sep. 2003, pp. 6219-6227.

[6.32] C. Giannini, S. Lagomarsino, F. Scarinci, and P. Castrucci, "Nature of the band gap of polycrystalline β-FeSi2 films," Physical Review B, vol. 45, Apr. 1992, pp. 8822-8824

[6.33] J.H. Schön, F.P. Baumgartner, E. Arushanov, H. Riazi-Nejad, C. Kloc, and E. Bucher, "Photoluminescence and electrical properties of Sn-doped $CuGaSe_2$ single crystals," Journal of Applied Physics, vol. 79, 1996, p. 6961.

[6.34] S. Siebentritt, "Defects and transport in the wide gap chalcopyrite $CuGaSe_2$" Journal of Physics and Chemistry of Solids, vol. 64, Sep. 2003, pp. 1621-1626.

[6.35] C. Rincón and F.J. Ramírez, "Lattice vibrations of $CuInSe_2$ and $CuGaSe_2$ by Raman microspectrometry," Journal of Applied Physics, vol. 72, 1992, p. 4321.

[6.36] I.V. Bodnar, A.G. Karoza, and G.F. Smirnova, "Lattice reflectivity spectra of $CuGaS_2$-$CuGaSe_2$ solid solutions," Physica Status Solidi (b), vol. 84, Nov. 1977, p. k65-k69.

[6.37] C. Xue, D. Papadimitriou, Y.S. Raptis, N. Esser, W. Richter, S. Siebentritt, and M.C. Lux-Steiner, "Compositional dependence of Raman scattering and photoluminescence emission in $Cu_xGa_ySe_2$ thin films," Journal of Applied Physics, vol. 94, 2003, p. 4341

[6.38] B. Minceva-Sukarova, "Raman spectra of thin solid films of some metal sulfides," Journal of Molecular Structure, vol. 410-411, Jun. 1997, pp. 267-270.

[6.39] P. Lautenschlager, P. Allen, and M. Cardona, "Phonon-induced lifetime broadenings of electronic states and critical points in Si and Ge," Physical Review B, vol. 33, Apr. 1986, pp. 5501-5511

[6.40] M. Alonso, K. Wakita, J. Pascual, M. Garriga, and N. Yamamoto, "Optical functions and electronic structure of $CuInSe_2$, $CuGaSe_2$, $CuInS_2$, and $CuGaS_2$" Physical Review B, vol. 63, Jan. 2001, pp. 1-13.

[6.41] B. Tell and P.M. Bridenbaugh, "Aspects of the band structure of $CuGaS_2$ and $CuGaSe_2$" Physical Review B, vol. 12, 1975, p. 3330–3335

[6.42] J. Shay, B. Tell, H. Kasper, and L. Schiavone, "p-d Hybridization of the Valence Bands of I-III-VI_2 Compounds" Physical Review B, vol. 5, 1972, p. 5003–5005.

[6.43] L. Artus, Y. Bertrand, and C. Ance, "Crystal-field and spin-orbit interactions at the fundamental gap of $AgGaSe_2$ chalcopyrite compound" Journal of Physics C: Solid State Physics, vol. 19, 1986, p. 5937–5943.

[6.44] R. Braunstein and E. Kane, "The valence band structure of the III–V compounds" Journal of Physics and Chemistry of Solids, vol. 23, Oct. 1962, pp. 1423-1431.

[6.45] K. Yoodee, J. Woolley, and V. Sa-yakanit, "Effects of p-d hybridization on the valence band of I-III-VI_2 chalcopyrite semiconductors" Physical Review B, vol. 30, Nov. 1984, pp. 5904-5915.

[6.46] N.N. Syrbu, M. Bogdanash, V.E. Tezlevan, and I.G. Stamov, "Exciton - phonon spectra and energy band structure of crystals," Journal of Physics: Condensed Matter, vol. 9, Feb. 1997, pp. 1217-1223.

[6.47] T. Kawashima, S. Adachi, H. Miyake, and K. Sugiyama, "Optical constants of $CuGaSe_2$ and $CuInSe_2$" Journal of Applied Physics, vol. 84, 1998, p. 5202.

[6.48] L. Artus, Y. Bertrand, and C. Ance, "Crystal-field and spin-orbit interactions at the fundamental gap of $AgGaSe_2$ chalcopyrite compound," Journal of Physics C: Solid State Physics, vol. 19, Oct. 1986, pp. 5937-5943.

[6.49] J.E. Jaffe and A. Zunger, "Theory of the band-gap anomaly in ABC_2 chalcopyrite semiconductors" Physical Review B, vol. 29, 1984, p. 1882–1906.

[6.50] J. Shay and B. Tell, "Energy band structure of $I–III–VI_2$ semiconductors," Surface Science, vol. 37, 1973, p. 748–762

[6.51] Y. Harada, H. Nakanishi, and S.F. Chichibu, "Band gap energy bowing and residual strain in $CuAl(S_xSe_{1-x})_2$ chalcopyrite semiconductor epilayers grown by low-pressure metalorganic vapor phase epitaxy," Journal of Applied Physics, vol. 91, 2002, p. 5909.

[6.52] A. Bauknecht, S. Siebentritt, J. Albert, Y. Tomm, and M.-C. Lux-Steiner, "Exitonic Photoluminescence from $CuGaSe_2$ single Crystals and epitaxial layers: Temperature Dependence of the band gap energy," JJAP, vol. 39, 2000, pp. 322-325.

[6.53] K. Yoshino, H. Yokoyama, K. Maeda, T. Ikari, A. Fukuyama, P. Fons, A. Yamada, and S. Niki, J. Appl. Phys. 86, (1999) 4354

[6.54]A. Mudryi, M. Yakushev, R. Tomlinson, A. Hill, R. Pilkington, I. Bodnar', I. Viktorov, V. Gremenok, I. Shakin, and A. Patuk, "Optical spectroscopy of excitonic states in $CuInSe_2$" Semiconductors, vol. 34, May. 2000, pp. 534-537.

[6.55] C. Rincon, E. Hernandez, S. Wasim, and I. Molina, J. Phys. Chem. Solids 59, (1998) 1015

[6.56] P. Deus P, H. Neumann H, G. Kuehn, and B. Hinze B, Phys. Status Solidi a 80, (1983) 205

[6.57] J. Serrano, Ch. Schweitzer, C. T. Lin, K. Reimann, M. Cardona, and D. Frohlich Phys. Rev. B 65, (2002) 125110

[6.58] H. Tanino, T. Maeda, H. Fujikake, H. Nakanishi, S. Endo, and T. Irie, "Raman spectra of $CuInSe_2$" Physical Review B, vol. 45, Jun. 1992, pp. 13323-13330.

[6.59] S. Wei and A. Zunger, "Band offsets and optical bowings of chalcopyrites and Zn-based II-VI alloys," Journal of Applied Physics, vol. 78, 1995, p. 3846.

[6.60] N. Rega, S. Siebentritt, I. Beckers, J. Beckmann, and J. Albert, "MOVPE of epitaxial $CuInSe_2$ on GaAs," Journal of Crystal Growth, vol. 248, 2003, pp. 169-174.

[6.61] A. Baucknecht, S. Siebentritt, J. Albert, and M-Ch. Lux-Steiner, Mat. Res. Soc. Symp. Proc. 668, (2002) H5.14

[6.62] C. Xue, D. Papadimitriou, N. Esser, Thin Solid Films 451 –452 (2004) 189–192.

[6.63] N. Rega, S. Siebentritt, J. Albert, M.-Ch. Lux-Steiner, Mat. Res. Soc. Symp. Proc. 763, (2003)183-88.

[6.64] P. D. Paulson, R. W. Birkmire, and W. N. Shafarman, J. Appl. Phys. 94, (2003) 879-88.

[6.65] JCPDS data files 37-1463 and 15-105.

[6.66] R. Kale and C. Lokhande, "Influence of air annealing on the structural, morphological, optical and electrical properties of chemically deposited ZnSe thin films," Applied Surface Science, vol. 252, Nov. 2005, pp. 929-938

[6.67] B.D. Cullity, Elements of X-ray Diffraction, Addison-Wesley, Reading, 1978

[6.68] M.S. Gaith and I. Alhayek, Estimation of the Degree of Anisotropy and Overall Elastic Stiffness of Advanced Anisotropic Materials, 2006.

[6.69] A. Chaparro, "Morphological and compositional study of CBD-ZnSe thin films by microscopy techniques and angle resolved XPS," Thin Solid Films, vol. 358, Jan. 2000, pp. 22-29.

[6.70] A.M. Chaparro, M.A. Martinez, C. Guillen, R. Bayon, M.T. Gutierrez, J. Herrero, Thin Solid Films 361 (2000) 177.

[6.71] J.M. Dona, J. Herrero, J. Electrochem. Soc. 142 (1995) 764.

[6.72] R.A. Zingaro,D.O.Skolvin, J.Electrochem.Soc. 111 (1964) 42

[6.73] A.M. Chaparro, C. Maffiotte, M.T. Gutierrez, J. Herrero, Thin Solid Films 358 (2000) 22

[6.74] N.F. Mott, E.A. Davis, Electronic properties in non-crystalline materials, Oxford University Press, London, 1971

[6.75] C.D. Lokhande, P.S. Patil, H. Tributsch, A. Ennaoui, Sol. Energy Mater. Sol. Cells 55 (1998) 379

[6.76] B. Rockwell, H. Chandrasekhar, M. Chandrasekhar, A. Ramdas, M. Kobayashi, and R. Gunshor, "Pressure tuning of strains in semiconductor heterostructures: (ZnSe epilayer)/(GaAs epilayer)," Physical Review B, vol. 44, Nov. 1991, pp. 11307-11314.

[6.77] T. Yao, "The effect of lattice deformation on optical properties and lattice parameters of ZnSe grown on (100)GaAs," Journal of Crystal Growth, vol. 81, Feb. 1987, pp. 518-523.

[6.78] A. Chaparro, "Quartz-crystal microbalance study of the growth of Zn(Se,O) thin-films in a chemical bath. A sequential electroless-chemical process" Electrochimica Acta, vol. 47, Dec. 2001, pp. 977-986.

[6.79] R. Klenk, J. Klaer, R. Scheer, M. Luxsteiner, I. Luck, N. Meyer, and U. Ruhle, "Solar cells based on CuInS?an overview," Thin Solid Films, vol. 480-481, Jun. 2005, pp. 509-514.

[6.80]Y. Ogawa, "Influence of KCN treatment on $CuInS_2$ thin films," Applied Surface Science, vol. 92, Feb. 1996, pp. 232-236.

[6.81] M.-Ch. Lux-Steiner, A. Ennaoui, C. Fischer et.al., "Processes for chalcopyrite-based solar cells," Thin Solid Films, vol. 361, Feb. 2000, p. 533–539.

[6.82] B. Hahn, E. Pschorr-Schoberer, E. Griebl, M. Kastner, W. Gebhardt, J. Cryst. Growth 191, 65 (1998).

[6.83] Landolt-Börnstein, Semiconductors, Physics of II-VI Compounds 17 b, ed. O. Madelung, Springer Verlag, Berlin, 1982.

[6.84] M. Tsoutsouva, "Development and properties of contacts in electronic devices", Dissertation, National Technical University of Athens, 2010.

[6.85] L. Larina, D.H. Shin, N. Tsvetkov, and B.T. Ahn, "Growth of Ultrathin Zn Compound Buffer Layer by a Chemical Bath Deposition for $Cu(In,Ga)Se_2$ Solar Cells," Journal of The Electrochemical Society, vol. 156, 2009, p. D469.

[6.86] Ü. Özgür, Ya. I. Alivov, C. Liu, A. Teke, M. A. Reshchikov, S. Doğan, V. Avrutin, S.-J. Cho, and H. Morkoçd, J. Appl. Phys. 98, 2005, 041301

[6.87] J. Chen, L. Aé, Ch. Aichele, and M. Ch. Lux-Steiner, Appl. Phys. Let. 92, 161906 (2008)

[6.88] K. Ramanathan, M. A. Contreras, C. L. Perkins, S. Asher, F. S. Hasoon, J. Keane, D. Young, M. Romero, W. Metzger, R. Noufi, J. Ward, A. Duda, Progress in Photovoltaics: Research and Applications 2003; 11(4): 225–230

[6.89] W. H. Southwell, Optics Letters 1983; 8: 584–586

[6.90] J. A. Dobrowolski, D. Poitras, P. Ma, H. Vakil, M. Acree, Applied Optics 2002; 41: 3075–3083

[6.91] P. Vukusic and J. R. Sambles, Nature, vol. 424, pp. 852-855, 2003

[6.92] S. J. Wilson and M. C. Hutley, Optica Acta, vol. 29, pp. 993-1009, 1982.

[6.93] L. Kasturi, L. Chopra, Suhit Ranjan Das, Thin film solar cells, Springer, New York, 1983, pp. 515–520

[6.94] J. Davies, The Physics of low-dimensional semiconductors, 1998 Cambridge University Press

[6.95] A. D. Yoffe, (1993), Advances in Physics, 42: 2, 173 — 262, First published on: 01 March 1993

[6.96] S. J. Lee, S. K. Park, C. R. Park, J. Y. Lee, J. Park, Y. R. Do, J. Phys. Chem. C 2007, 111, 11793– 11801

[6.97] J.I. Pankove, Optical Processes in Semiconductors, Prentice-Hall Inc, Englewoord Cliffs, NJ, 1971.

[6.98] E. Hecht, Optics. Addison-Wesley, Adelphi University (2002)

[6.99] Y. Gu, Igor L. Kuskovsky,a) M. Yin, S. O'Brien, and G. F. Neumark, Quantum confinement in ZnO nanorods, Appl. Phys. Let. 85 (2004) 3833-3835.

[6.100] S. Ozaki, T. Mishima, S. Adachi, Jpn. J. Appl. Phys. 42 (2003) 5465-5471

[6.101] B. K. Meyer, et. al. Phys. Stat. Sol. (b) 241 (2004) 231-260

[6.102] T.S. Moss, The Interpretation of the Properties of Indium Antimonide, Proc. Phys. Soc. B 67 (1954) 775

[6.103] L. Ae, D. Kieven, J. Chen, R. Klenk, Th. Rissom, Y. Tang and M. Ch. Lux-Steiner, Prog. Photovolt: Res. Appl. 2010; 18:209–213

[6.104] U. Behn and H. Ro¨ppischer, Phys. Status Solidi B 141, 325 (1987)

[6.105] R. Henninger, J. Klaer, K. Siemer, J. Bruns, and D. Bräunig, "Electroreflectance of CuInS[sub 2] thin film solar cells and dependence on process parameters," Journal of Applied Physics, vol. 89, 2001, p. 3049.

[6.106] X. L. Zheng, D. Heiman, B. Lax, and F. Chambers, Appl. Phys. Lett. 52, 287 (1988)

[6.107] O. J. Glembocki, N. Bottka, and J. E. Furneaux, J. Appl. Phys. 57, 432 (1984)

[6.108] Tell B, Shay J L and Kasper H M 1971 Phys. Rev. B 4 2463–71

[6.109] L. L. Kazmeski, C. C. Shieh, Thin. Sol. Film. 41 (1977) 35

[6.110] H. L. Hwang, C. C. Tu, J. S. Maa, C. Y. Sun, Sol. En. Mat. 2 (1980) 433

[6.111] S. Theodoropoulou, "CIGS Thin Film Photovoltaic Technology: Energy band gap and lattice defect analysis in Chalcopyrite Semiconductor Heterostructures", Dissertation NTUA, 2008

[6.112] T.S. Moss, "The Interpretation of the Properties of Indium Antimonide," Proceedings of the Physical Society. Section B, vol. 67, Oct. 1954, pp. 775-782.

[6.113] T. M. Hsu, H. Y. Chang, H. J. Hwang, S. Y. Lee, Ternary Multinary Compd. Mater. Res. Soc. (1988) 12

[6.114] S. Theodoropoulou, D. Papadimitriou, a G. Mamalis, D.E. Manolakos, R. Klenk, and M.-C. Lux-Steiner, "Band-gap energies and strain effects in $CuIn_{1-x}Ga_xS_2$ based solar cells," Semiconductor Science and Technology, vol. 22, Aug. 2007, pp. 933-940.

[6.115] J. Łażewski, P. T. Jochym, and K. Parlinski, Band structure, Born effective charges, and lattice dynamics of CuInS2 from ab initio calculations, J. Chem. Phys. 117, 2726 (2002)

[6.116] Kaigawa R, Neisser A, Klenk R and Lux-Steiner M Ch 2002 Thin Solid Films 415 266–71

[6.117] R. Berkowica and T. Skettrup, "Brillouin scattering, piezobirefringence, and dispersion of photoelastic coefficients of CdS and ZnO," Physical Review B, vol. 11, Mar. 1975, pp. 2316-2326

[6.118] Grahn H T 1999 Introduction to Semiconductor Physics (Singapore: World Scientific)

[6.119] Kato T, Hayashi S, Kiuchi T, Ishihara Y, Nabetani Y and Matsumoto T 2002 J. Cryst. Growth 237–239 2005–8

[6.120] Yao T, Okada Y, Matsui S, Ishida K and Fujimoto I 1987J. Cryst. Growth 81 518–23

9. Appendix A

Chemical etching procedure

For the chemical etsching of the polycrystalline chalcopyrite, two solutions need to be prepared:

S1: 10% KCN solution (25gr KCN in 230ml double distilled H_2O), and

S2: 1M KOH solution (5.6gr KOH in 100ml double distilled H_2O)

The pH of S1 is being adjusted between 10 and 12 by addition of S2.

At room temperature, the chalcopyrite is submerged in S1 for exactly 3min.

After chemical etching the chalcopyrite needs to be washed out first with S2 (pH>10) and then with double distilled H_2O.

In the end, the chalcopyrite needs to be dried out in inert atmosphere (usually N_2).

ATTENTION!

The KCN solution should ***for no reason*** be exposed to air, since the atmospheric CO_2 is being dissolved in the solution, the pH becomes acidic, and HCN is being released. **HCN, if inhaled, can become extremely toxic and therefore fatal!**

10. CURRICULUM VITAE

Personal Information

First Name: Konstantina

Last Name: Anestou

Date of Birth: 01/02/1982

Place of Birth: Athens

Address: Lakonias 43

G-17342, Athens

Phone number: 0030-210-9936645, (mobile) 0030-6949 08 27 34

e-mail: kwnstanes@yahoo.gr

Studies

-2006: PhD in Materials Science and Technology* at the National Technical University of Athens

2006-2005: Master of Science in the Interdisciplinary Postgraduate Program* of the National Technical University of Athens: "Materials Science and Technology"

2005-1999: Diploma in Applied Physics* at the National Technical University of Athens

06-07/2002: Research studies on solid phases by XRF at the National Center of Scientific Research "Demokritos"

-01/06: PhD Thesis on the *"Development and Characterization of Chalcopyrite based Thin Film Solar Cells for Photovoltaic Technology Applications"*, at the National Technical University of Athens, supervised by Assist. Prof. Dr. Dimitra Papadimitriou

10/05-06/06: Master-Thesis on the *"Comparative Studies of Monocrystalline Chalcopyrites for the Photovoltaic Technology"*, at the National Technical University of Athens, under the supervision of Assist. Prof. Dr. Dimitra Papadimitriou

10/04-07/05: Diploma-Thesis on the *"Optimization of Mechanical Properties of Porous Silicon for Micromechanical Applications"*, at the National Technical University of Athens and the National Center of Scientific Research "Demokritos", under the supervision of Assist. Prof. Dr. Dimitra Papadimitriou

Distinctions/prizes

Thomaidion prize for the publications:

K. Anestou, D. Papadimitriou, C. Tsamis and A. Nassiopoulou, "*Stress Characteristics of Suspended Porous Silicon Microstructures on Silicon*", J. Phys.: Conf. Ser. **10** (2005) 309-312.

Foreign Languages

English (Proficiency of Cambridge)

German (Zertifikat Deutsch)

List of Publications

1. K. Anestou, D. Papadimitriou *"Optical modulation techniques applied in the analysis of chalcopyrite semiconductor heterostructures",* J. Phys. D: Appl. Phys. (revised).

2. K. Anestou, D. Papadimitriou, Y.Tang, J. Chen, M.-Ch. Lux-Steiner *"Innovative Anti-Reflective ZnO Coating for improved Solar Cell performance",* E-MRS 2011 Conference Series (2011) (submitted).

3. S. Theodoropoulou, D. Papadimitriou, K. Anestou, Ch. Cobet, and N. Esser "*Optical Properties of $CuIn_{1-x}Ga_xSe_2$ Quaternary Alloys for Thin Film Photovoltaic Technology*", Semicond. Sci. Technol. 24 (2009) 015014

4. D. Papadimitriou, G. Karras, Ch. Cobet, S. Theodoropoulou, K. Anestou, G. Roupakas, W. Richter *"Development of Optomechanical Constructions - Application in the Characterization of Thin Film Solar Cells",* Proc. of the PYTHAGORAS Conference on the Scientific Research at the National Technical University of Athens, Plomari Lesbos (2007), 513-519.

5. K. Anestou, D. Papadimitriou, C. Tsamis and A. Nassiopoulou, "*Stress Characteristics of Suspended Porous Silicon Microstructures on Silicon*", J. Phys.: Conf. Ser. 10 (2005) 309-312.

List of Conferences

1. K. Anestou, D. Papadimitriou, Y.Tang, J. Chen, M.-Ch. Lux-Steiner *"Innovative Anti-Reflective ZnO Coating for improved Solar Cell performance"*, E-MRS 2011 Spring Meeting IUMRS ICAM 2011 & E-MRS / MRS Bilateral Conference on Energy, Nice, May 2011.

2. K. Anestou, D. Papadimitriou, Ch. N. Panagopoulos, D. Yfantis, *"CIS/CIGS Thin Film Photovoltaic Technology: Chemical and Electrochemical Growth of ZnSe buffer layer"* RENES 2010 – 4th National Conference: The Application of Renewable Energy Sources towards an Ambitious and Credible National Action Program", Athens, May 2010.

3. K. Anestou, D. Papadimitriou, C. D. Yfantis, Th. Schedel-Niedrig, M. Ch. Lux-Steiner, U. W. Pohl "*Optical Modulation Techniques Applied in the Analysis of Bulk Semiconductors and Semiconductor Heterostructures"* 6th International Conference on Instrumental Methods of Analysis, Athens, October 2009.

4. D. Papadimitriou and K. Anestou *"Application of Raman Spectroscopic Techniques in the Characterization of Nanostructured Semiconductors and Semiconductor Microstructures"* 72nd DPG International Conference on Solid State Physics and Condensed Matter, Berlin, February 2008.

5. S. Theodoropoulou, D. Papadimitriou, K. Anestou, Ch. Cobet, and N. Esser "*Optical Properties of $CuIn_{1-x}Ga_xSe_2$ Quaternary Alloys for Thin Film Photovoltaic Technology*", XXIII National Conference of Solid State Physics and Materials Science, Athens, September 2007.

6. D. Papadimitriou, G. Karras, Ch. Cobet, S. Theodoropoulou, K. Anestou, G. Roupakas, W. Richter *"Development of Optomechanical Constructions - Application in the Characterization of Thin Film Solar Cells",* PYTHAGORAS Conference on the Scientific Research at the National Technical University of Athens, Plomari Lesbos, July 2007.

7. K. Anestou, D. Papadimitriou, C. Tsamis and A. Nassiopoulou, "*Stress Characteristics of Suspended Porous Silicon Microstructures on Silicon*", 2nd Int. Conference on Microelectronics, Microsystems, Nanotechnology, MMN 2004, Athens, November 2004.

List of talks

Review of Hollography principles and methods.

Academic Experience

1. Supervision of the advanced student-laboratory *"Study of Optical Properties with Null Ellipsometry"* for MSc.-courses in Optical Characterization Methods within the frame of the Interdisciplinary Postgraduate Program of the National Technical University of Athens: "Materials Science and Technology", SS 2007, SS2008, SS2010

2. Supervision of the advanced student-laboratory *"Advanced Optical Spectroscopic Techniques"* for courses in Optical Characterization Techniques within the frame of the School Of Applied Mathematical and Physical Sciences of the National Technical University of Athens, SS 2009.

Seminars

1. *"Photovoltaics: Technology Development and Market Trends"*, organized by National Technical University of Athens, Center of Renewable Energy Sources, German-Greek Chamber of Industry and Commerce, and Hellenic Association of Photovoltaic Companies, NTUA, Athens, October 2010.

2. *"New Researchers Seminars PENED 2003: Methodology and Practice in Research, Technology and Innovation management"*, organized by the General Secretariat for Research and Technology, NTUA, Athens, 2008.